4-22-2015 12:00 AM

Chromatin Structure and Differential Accessibility of Homologous Human Mitotic Metaphase Chromosomes

Wahab A. Khan, *The University of Western Ontario*

Supervisor: Dr. Joan Knoll, *The University of Western Ontario*
Joint Supervisor: Dr. Peter Rogan, *The University of Western Ontario*
A thesis submitted in partial fulfillment of the requirements for the Doctor of Philosophy degree in Pathology

Chromatin Structure and Differential Accessibility of Homologous Human Mitotic Metaphase Chromosomes

(Thesis format: Integrated-Article)

by

Wahab Altaf Khan

Graduate Program in Pathology and Laboratory Medicine

A thesis submitted in partial fulfillment
of the requirements for the degree of
Doctor of Philosophy

The School of Graduate and Postdoctoral Studies
The University of Western Ontario
London, Ontario, Canada

Abstract

The human mitotic metaphase chromosome is a product of complex chromatin restructuring during interphase. Metaphase chromosomes exhibit considerable plasticity in condensation. This is evident as distinct regions of accessible and compact chromatin fiber or epigenetic differences in histone and non-histone proteins. Such differences in chromatin condensation have been extensively described along the length of individual mitotic chromosomes but have not been recognized between homologous loci during metaphase.

This thesis characterizes localized differences in condensation of homologous metaphase chromosomes that are related to differences in accessibility (DA) of associated DNA probe targets. Reproducible DA was observed for ~10% of locus-specific, short (1.5-5 kb) single copy (SC) DNA probes used in fluorescence in situ hybridization. To investigate the physical and structural organization of chromatin at locus-specific sites, we developed correlated atomic force and fluorescence microscopy imaging. Comparison of centromeric DNA and protein distribution patterns in fixed homologous chromosomes indicated that CENP-B and α-satellite DNA were distributed distinctly from one another and relative to observed centromeric ridge topography. At non-centromeic locations, short DNA probes that did not exhibit DA showed greater accessibility to the accessible chromatin topography on both homologs.

Localized differential accessibility between chromosome homologs in metaphase was non-random and reproducible but not unique to known imprinted regions or specific chromosomes. Second, non-random DA was shown to be heritable within a 2 generation family. Third, DNA probe volume and depth measurements of hybridized metaphase chromosomes showed internal differences in chromatin accessibility of homologous regions by super-resolution 3D-structured illumination microscopy. Finally, genomic regions with equivalent accessibility were enriched for epigenetic marks of open interphase chromatin to a greater extent than regions with DA, suggesting that observed

structural differences in accessibility may arise during or preceding metaphase chromosome compaction.

Inhibition of the topoisomerase IIα-DNA cleavage complex mitigated DA by decreasing DNA superhelicity and axial metaphase chromosome condensation. Inter-homolog probe intensity ratios, depth, and volume between chromosomes treated with a catalytic inhibitor of topoisomerase IIα, were equalized compared to untreated cells. These data altogether suggest that DA is a reflection of allelic differences in metaphase chromosome compaction, dictated by the catenation state of the chromosome.

Keywords: Human metaphase chromosomes, Mitosis, Chromosome condensation, Differential accessibility, Fluorescence *in situ* hybridization, Single copy DNA probes, Chromosome structure/topography, Atomic force microscopy, Super resolution microscopy, Chromatin memory, Epigenetics, *In vitro* chromatin modifications

Co-Authorship Statement

Chapter 2: Relating centromeric topography in fixed human chromosomes to α-satellite DNA and CENP-B distribution. *Cytogenet Genome Res*. 2013;139(4):234-42. doi: 10.1159/000348744

Drs. Roderick Chisholm and Seyed Tadayyon assisted with AFM analysis and correlated imaging. Akila Subasinghe built the MATLAB compiler for GVF analysis and Drs. Jagath Samarabandu and Peter Rogan provided feedback on its optimization. Drs. Peter Norton and Linda Johnston provided access to their AFM facilities. Drs. Joan Knoll and Peter Rogan developed and coordinated the study and edited the manuscript. Wahab Khan developed the correlated AFM/FISH-immunofluorescence techniques, and assisted with all aspects of manuscript preparation and data analysis. All authors approved the final manuscript submission for publication.

Chapter 3: Localized, non-random differences in chromatin accessibility between homologous metaphase chromosomes. *Mol Cytogen*. 2014, 7:70 doi:10.1186/s13039-014-0070-y

Drs. Joan Knoll and Peter Rogan conceived and guided the project. Dr. Knoll provided cell lines and assisted with probe FISH signal interpretations. Wahab Khan carried out lymphoblastoid cell culture, single and low copy DNA probe design, FISH, 3D-SIM experiments, and analysis. All authors drafted the manuscript and approved the final submission for publication.

Chapter 4: Reversing chromatin accessibility differences that distinguish homologous mitotic metaphase chromosomes

Drs. Joan Knoll and Peter Rogan guided the project and provided feedback on experimental strategy. Dr. Knoll assisted with probe FISH signal interpretations. Wahab Khan performed *in vitro* chromosome decondensation treatments, FISH, and assisted with 3D-SIM, experiments. All authors drafted the manuscript.

Acknowledgments

I owe a debt of gratitude to many individuals, both scientifically and personally, over the course of this PhD. Foremost, I'd like to thank my advisors Dr. Joan Knoll and Dr. Peter Rogan who have been tremendously supportive. In their laboratories, there was never a lack of guidance or resources to complete the work. Dr. Knoll oversaw many aspects of my research. She helped refine my experiment design, data interpretation, and meticulously clarified my writing. Dr. Rogan provided many useful discussions, challenged me to think about my data in novel ways, and provided insightful ideas for the project. Both of their extraordinary efforts have left an indelible mark in improving and shaping this thesis. They have been a pleasure to work with and learn from.

I would also like to thank my advisory committee, Dr. Subrata Chakrabarti and Dr. Zia Khan for their overall support and feedback. Dr. Khan's course on grant writing was indispensable in preparing for the candidacy exam. Thank you as well to the staff from the 4th floor in Pathology for their prompt assistance in administrative matters.

Work in the Knoll-Rogan laboratories would not have been possible without the help of amazing Research Assistants, John Mucaki and Heather Tarnowski (past member). John helped in countless ways. He looked after cell culture when I was away from the lab, assisted me with instrumentation issues, and helped troubleshoot experiments. As well, thanks to all members of the Knoll-Rogan laboratories for their helpful comments in improving the presentation of the data in this thesis for various conferences and Departmental seminars. Stephanie, thank you for all the snacks you prepared over the years. Natasha thank you for helping me with my work in the early days of DA analysis. Lee, thanks for the rides home in the dead of winter, and Ben thanks for making me realize how little I know about high performance computing (the Summer of code will happen one day).

A special thanks to Dr. Kevin Conway, Chad Steele, Andre Levesque (Nikon Canada), Nathan Claxton (Nikon USA), and affiliates (Marine Biology Labs – Woods Hole; Center for Biologic Imaging – University of Pittsburgh) for lending their expertise and

time in helping me chase around a super-resolution microscope. Woods Hole was a great experience.

To my Mom and Dad – I am eternally grateful for everything you have done to get me to this point. To my dear wife Arfa – thank you for your support and patience during this process and for accompanying me on this adventure. I look forward to our next one!

This thesis was supported by The Ontario Graduate Scholarship, Queen Elizabeth II Graduate Scholarship in Science and Technology, Western Graduate Research Scholarship, Graduate thesis Research and Society of Graduate Studies travel bursaries, Canadian Institute of Health Research travel award, and various Departmental travel funds. Further project funding has been from the Canadian Foundation for Innovation (JHMK and PKR), Canada Research Chairs Secretariat (PKR), Canadian Institute for Photonic Innovations, Ontario Research Fund (JHMK), and the NSERC Discovery Grant 371758-2009 (PKR).

London W.A.K.
April 2015

Table of Contents

List of Tables

List of Figures

List of Appendices

List of Abbreviations

3C	Chromosome conformation capture
3D	Three dimensional
3D-SIM	3-dimensional structured illumination microscopy
4C	Circularized chromosome confirmation capture
5-AZC	5-azacytidine
5C	Carbon-copy chromosome confirmation capture
AFM	Atomic force microscopy
ANOVA	Analysis of variance
AS	Angelman syndrome
AT	Adenine + thymine content
BAC	Bacterial artificial chromosome
BLAST	Basic local alignment search tool
BSA	Bovine serum albumin
bp	Base pair
CENP	Centromere-associated protein (multiple categories such as A,B,C)
GC	Guanine + Cytosine content
CCNV	Common copy number variant
ChIP-seq	Chromatin immunoprecipitation sequencing
CO_2	Carbon dioxide

$C_o t$	DNA concentration multiplied by time
CpG	Cytosine– phosphate–Guanine
DA	Differential accessibility
DAPI	4′,6-diamidino- 2-phenylindole
DNase I	Deoxyribonuclease I
DNase I HS	Deoxyribonuclease I hypersensitivity
DNMT1	DNA methyltransferase I
EM	Electron microscopy
ENCODE	Encyclopedia of DNA elements
FAIRE	Formaldehyde-assisted isolation of regulatory elements
FISH	Fluorescence in situ hybridization
G-bands	Giemsa bands
GIMP	GNU Image Manipulation Program
GVF	Gradient vector flow
H3K9Ac	Histone H3 lysine 9 acetylation
H3K27ac	Histone H3 lysine 27 acetylation
H3K4me1	Histone H3 lysine 4 mono-methylation
H3K4me2	Histone 3 lysine 4 di-methylation
H3K27me3	Histone 3 lysine 27 tri-methylation
HIAR	Heat-induced antigen retrieval

HiC	Chromosome capture followed by high-throughput sequencing
HP1	Heterochromatin protein 1
IgG	Immunoglobulin G
Immuno-FISH	Immunofluorescence combined with FISH
kb	Kilobase pair
LC	Low copy
LINE	Long interspersed nuclear elements
MNase	Micrococcal nuclease
min	Minute
OA	Okadaic acid
PALM	Photoactivated localization microscopy
PBS	Phosphate-buffered saline
PCC	Premature chromosome condensation
PCR	Polymerase chain reaction
PRC2	Polycomb repressive complex 2
R-bands	Reverse of Giemsa bands
RCA	Regulator of chromosome architecture
RPMI	Roswell Park Memorial Institute medium
RT	Room temperature
RUNX	Runt-related transcription factor

scFISH	Single copy fluorescence in situ hybridization
SC	Single copy
SD	Segmental duplicon
SEM	Scanning electron microscopy
SINE	Short interspersed nuclear elements
SMC	Structural maintenance of chromosome
SNP	Single nucleotide polymorphism
SSC	Sodium chloride/sodium citrate buffer
TopoIIα	Topoisomerase IIα
TSA	Trichostatin A
XIST	X inactive specific transcript
YAC	Yeast artificial chromosome

Chapter 1

General Introduction

1.1 Significance of this PhD thesis

It is important that a cell preserve its chromatin state from one cell generation to the next in order to sustain normal development in progeny cells and to avoid disease. This must occur despite most of the nuclear chromatin associated factors disassociating from mitotic chromosomes as they condense. Further, re-association of a complex series of nuclear proteins would need to occur with high fidelity following mitosis. Cellular epigenetic memory argues that several key components that act as markers to recall the chromatin state remain associated to chromosomes. It is not well known how the association of these features to chromatin is implemented in order to maintain epigenetic memory. Our studies demonstrate structural differences between homologous regions in metaphase chromosomes resulting from differentially compacted chromatin. These differences are linked to the level of DNA supercoiling between the homologous targets, but themselves are not an epigenetic mark. Such differences would have implications for directing the binding of nuclear chromatin associated factors that would in turn be important for establishing the chromatin state following mitosis.

1.2 Mitotic Chromosome Condensation – Historical Perspective

The discovery of chromosomes is credited to von Nägeli and Flemming but it was not until the early 1900s that the connection between chromosomes and heredity was clearly proposed (1). The chromosome theory of inheritance postulated that chromosomes have a stable structure, they occur in pairs (i.e. homologs), and that one member of each pair is contributed through either the maternal or paternal lineage. Interestingly, these observations were recognized as being consistent with those of Gregor Mendel and Charles Darwin, who explored the possible mechanisms of how cells pass on their traits from one generation to the next (2). Although it was known in the early 1900s how

chromosomes appeared under the microscope, it was not until much later that researchers began to study the fundamental organizing units of chromosomes and how they moved through mitosis.

Condensation of the mammalian genome into mitotic metaphase chromosomes (Figure 1-1) enables its segregation into daughter cells. This is a critical process, as it preserves the integrity of the genome. Generally chromosome condensation is envisioned as a stepwise process, where negatively charged DNA wraps around a protein octamer composed of two copies each of positively charged histone proteins H2A, H2B, H3, and H4 (3). This forms a nucleosome core which is further packed into increasingly complex chromatin fibers, accounting for approximately a 40:1 compaction ratio (4). Histone H1 binds to linker DNA between nucleosomes and helps stabilize the chromatin fiber (3). At levels of condensation beyond the nucleosome core, it is less certain what accounts for the remaining ~ 500 fold compaction required to form mitotic chromosomes (4). In fact, the fundamental question of how chromatin folds into higher order chromosome structures has been the subject of much debate. Over the years, several models have been proposed that attempt to define how metaphase chromosomes acquire shape, among which the most widely cited is the radial loop model (5,6). Paulson, Laemmli and colleagues in the late 1970s (5,6), using high salt protein extraction which resulted in histone depleted chromosomes, showed loops of radially organized chromatin fibers anchored axially to a central protein scaffold core (7). They showed that chromatin loops are inherent to the organization of the metaphase chromosome. Within a year of the proposed radial loop model, a contrasting study based on experiments using high voltage electron microscopy (EM), postulated that chromatin fibers hierarchically fold into thicker chromatin structures instead of radial chromatin fibers converging on a protein scaffold (8). It was suggested that this successive coiling culminates in metaphase chromosomes and came to be termed the helical coiling model (8).

The radial loop and helical coiling models produced useful information with regard to the fundamental organizing unit of chromosomes; however, they were incompatible with

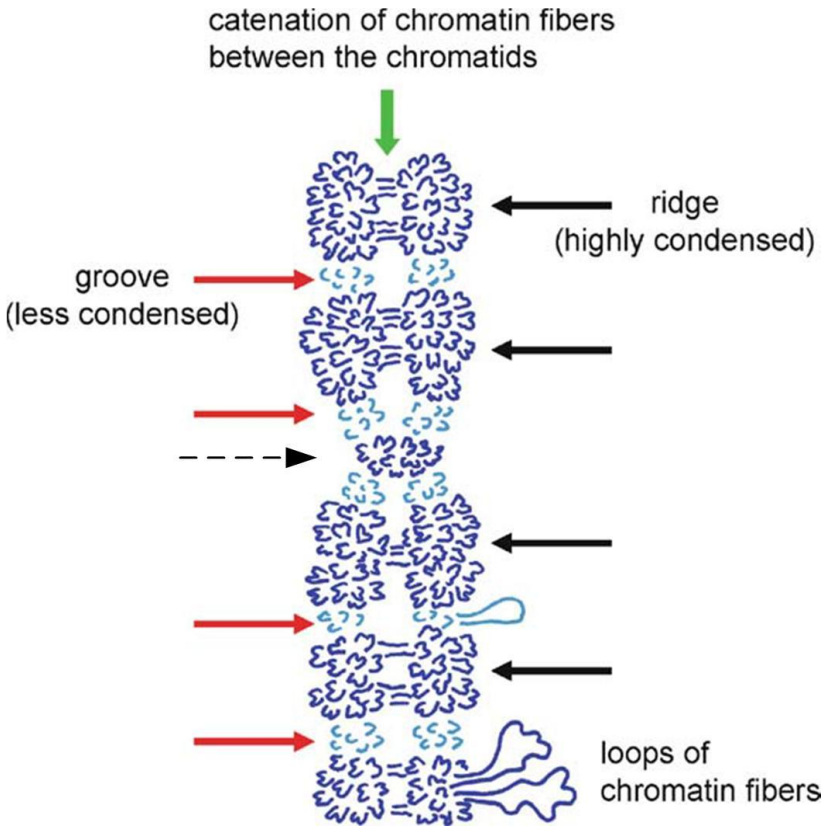

Figure 1-1. Diagram of condensed chromatin fibers within the metaphase chromosome

The metaphase chromosome is non-uniform in structure. It is composed of a pair of sister chromatids with highly condensed (ridges; black arrow) or less condensed (grooves; red arrow) chromatin fiber loops. Sister chromatids are also connected with entangled chromatin fibers (green arrow). Primary constriction indicating centromere location is indicated with black dashed arrow. [*]

[*] Ushiki T, Hoshi O. Atomic force microscopy for imaging human metaphase chromosomes. Chromosome Res. 2008;16(3):383-96. doi: 10.1007/s10577-008-1241-7. Copy of license agreement for Figure re-use is provided from Springer (see appendix).

each other and did not scale well to explain the range of mammalian chromosomes sizes (9). To integrate the two models, Rattner and Lin (1985) proposed that both radial loops and helical coils can coexist in formation of metaphase chromosomes, through condensation of a 200-300 nm fiber (10). They exposed chromosomes to nonionic detergents resulting in a progressive increase in the diameter of the 200-300 nm fiber and revealed that the fiber is composed of 25-30 nm radial loops, forming the final metaphase chromatid. In attempting to determine the path of the fiber within the chromosome, conventional EM combined with axial tomography further refined the radial loop and helical coil models. It was discovered that helical coiling is not strictly a sequential process, in which chromatin is first assembled into lower levels of organization and then subsequent higher order folding. Rather, large scale chromatin folding with increased condensation can occur even at lower structural levels. It was also noted that chromatin loops do not have a consistent radial symmetry about the central chromosome axis. The authors ultimately suggested a diffuse distribution of the scaffold protein which anchors the loops (10). Many models of mitotic chromosome condensation have gained popularity in chromosome biology; some of which have been highlighted here (Figure 1-2). There still remains little progress on a consensus model of chromosome condensation shaping the metaphase chromosome. This gap in knowledge has prompted interest in both interphase and metaphase chromatin organization, with much effort directed at determining the protein composition of mitotic chromosomes.

1.3 Protein Composition of Mitotic Chromosomes

Purification of mitotic chromosomes can be challenging as cytoplasmic proteins adhere to chromosomes through nonspecific electrostatic interactions (11). This issue, termed the ‘hitchhiker problem’, was initially addressed by fractionation procedures or digesting chromosomes with micrococcal nuclease (MNase) (5). The approach of Fukui and colleagues further addressed chromosome purity and yield using density gradient centrifugation followed by a proteome analysis of metaphase chromosomes (12).

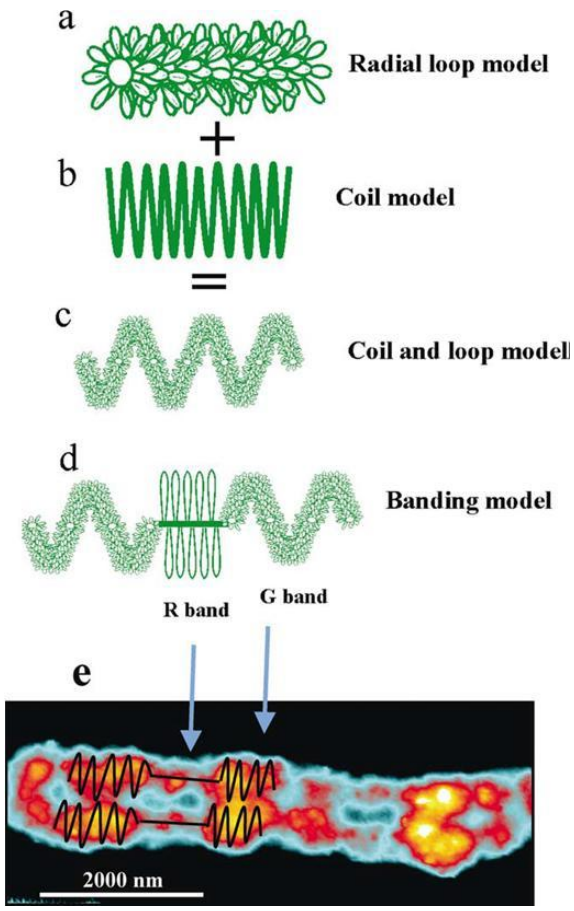

Figure 1-2. Models of mitotic chromosome condensation.

(a-e) Independent models in which the radial loops extending from the longitudinal axis of the chromatin fiber or (b) in which the chromatin fiber is helically folded are shown. (c) The combination of the two give rise to the coil-loop model, where the thick radial loop fiber is helically folded to form the chromatid. (d) Regions of compact and less compact chromatin fiber is coarsely divided into Giemsa dark (G-bands) or Giemsa-light staining regions (reverse band or R-bands), respectively. (e) Topographic cross-section of metaphase chromosome shows a black line from which the radial loops extend to from compact or less compact structures (R-bands) Adapted from (7). †

† Copy of license agreement for figure re-use is provided from Elsevier Limited (see appendix).

From this analysis, the mitotic chromosome was divided into seven categories (a-g) (12). Proteins associating with a) the chromosome arm included the core histones; b) chromosome scaffold included family of condensins (I and II) and topoisomerase IIα; c) chromosome periphery included fibrous proteins such as lamin, fibrillarin, nucleolin; and d) chromosome fiber included cytoskeletal proteins such as tubulin, actin, vimentin (12). The proteome analysis further categorized e) centromeric and f) heterochromatic regions of the chromosome to include kintechore associating proteins such as CENP-A, CENP-C along with heterochromatin proteins CENP-B [(found at the inner kinetochore (13)], cohesin, heterochromatin protein I (HP1), and Aurora B (12). Proteins of the g) telomeric region included the shelterin and Ku family involved in maintenance of chromosome ends (12). Some of these essential protein components that shape the mitotic chromosomes can be broadly grouped into histone, non-histone, or DNA modifying proteins and are discussed below.

1.3.1 Major Histone Proteins

Purified mitotic chromosomes have a protein to nucleic acid ratio of roughly 2:1, by mass, and about half of this protein is comprised of histones (11). The histone-DNA structure of chromatin, initially proposed by Kornberg (14), wraps eukaryotic DNA around repeating units of nucleosomes. As identification of enzymes responsible for the chemical post-translational modifications of histone proteins were deciphered, scientists began to favor the view that a ‘histone code’ exists which alters chromatin structure (15). These post-translational modifications are encoded on the N-terminal tail domain of histone proteins and consist of acetylation, phosphorylation, methylation, and ubiquitination. Of particular note is phosphorylation at serine 10 of histone H3 associated with mitotic chromosome condensation (16). This process has been demonstrated in yeast and is likely important in higher eukaryotes. Molecular pathways downstream of this modification result in a deacetylation at lysine 16 on histone H4. This consequently leads to an interaction of the N-terminal tail of H4 with neighboring nucleosomes promoting chromosome hypercondensation (16). Post-translational modifications driving chromosome condensation are not limited to serine phosphorylation. A combination of

acetylation of lysine, methylation of lysine and arginine, or addition of the protein ubiquitin contributes to a large diversity of histone modifications. Importantly, apart from histone phosphorylation, these distinct amino-terminal post-translational modifications have been recognized to be primarily involved in cellular processes related to gene regulation during interphase (15). Combinations of these modifications can not only influence chromatin fiber folding and gene regulation, but also act as a source of epigenetic information that is potentially passed on through cell division (17).

Besides post translational modifications to the canonical histones, higher order chromatin organization can be affected by histone variants. Histone variants are not modified histones, as they are encoded by multiple copies of non-allelic histone genes that substantially differ in their primary sequence and are among the slowest evolving proteins known (18). Primarily, the influence of histone variant H2A.Z, in place of H2A, on chromatin folding has been extensively studied in higher eukaryotes (19). Compared to H2A, crystallization studies of the nucleosome revealed that the H2Z.A variant has an extended acidic patch consisting of several amino acids. H2Z.A incorporation into chromatin permits high affinity interaction of the N-terminal tail of histone H4 with this acidic patch. This ultimately leads to stronger electrostatic interactions between histone residues and the DNA phosphate backbone, causing increased intra-fiber folding and more compact chromatin structures (20).

The complexity of the histone code can be further extended to chromatin associating polypeptides that add or remove covalent modifications from histone tails. These enzymes which catalyze the addition of one or more acetyl, methyl, and phosphate groups to the histone COOH tail (i.e. ‘writers’ of the histone code) are referred to as histone acetyl transferases, protein methyl transferases and kinases, respectively (15,17). Conversely, since histone modifications are reversible; erasers of these modifications can be grouped into histone deacetylases, lysine demethylases, and families of protein phosphatases (17). Finally, once covalent modifications are catalyzed, they can be interpreted by readers or effector domains of proteins, such as bromodomains or HP1, which remodel specific chromatin states (17). Considerable progress has been made in

this area of chromatin biology, and it is obvious that histone proteins provide a diverse range of variability in the protein composition of mitotic chromosomes (21). A second set of proteins that act in concert with modifications to histones are non-histone proteins. These proteins have been recognized, since the proposal of the radial model hypothesis, to dramatically influence chromatin architecture and metaphase chromosome morphology.

1.3.2 Major Non-histone Proteins

Previously, studies of the mitotic chromosome proteome revealed over 200 proteins isolated from HeLa cells (12). From this analysis, the most stable non-histone proteins involved in building the chromosome architecture were topoisomerase IIα (topoIIα) and two types of structural maintenance of chromosome (SMC) complexes: condensin I and II. Unlike condensins which introduce positive supercoils (i.e. DNA helix is twisted tighter), topoIIα has a dual role in producing positive or negative DNA supercoils (i.e. unwinds DNA) at different stages of the cell cycle (22). TopoIIα can also catenate (knot) and decatenate (unknot) DNA strands. Cytological analyses have revealed that the chromosome scaffold primarily consists of topoIIα and SMC condensin complexes extending from one end of the chromosome to the other (i.e. axial distribution) in a 'barber shop pole-like' pattern (22). These non-histone proteins are essential in organizing higher order structure of mitotic chromosomes, but how this is accomplished is not well understood (9,11). Some of the evidence suggests that formation of metaphase chromosomes undergoes a two-step process (22). First, in prophase the chromatids take shape through formation of the topoIIα axis. This is followed by the axial shortening and thickening of the chromatids by topoIIα during early stages of chromosome condensation and in transition to metaphase. At later stages of condensation, the condensin complex binds to the periphery of the chromatid arm and perhaps through protein-protein interactions allows the two proteins to stack to the center of chromatids; forming the scaffold (23,24). Additionally, experiments in which the condensin complex is depleted; results in a chromosome with no shape and very little condensation (25). Condensin depletion also blocks the recruitment of KIF4A, a protein from the kinesin superfamily, to the chromosome axes and prevents lateral compaction of metaphase chromosomes

(23). In cells where topoIIα is inhibited, metaphase chromosome condensation is reduced, but condensin loading onto the protein scaffold is not affected. This suggests the condensin and topoIIα are working by divergent pathways in shaping metaphase chromosomes (26).

It is also known that chromosome condensation into metaphase can proceed even in the absence of a scaffold, albeit much slower and with lag during anaphase (27). This leaves an open area of research to determine if there are other candidates involved in shaping metaphase chromosome architecture. Provisionally, a chromosome condensation factor termed regulator of chromosome architecture (RCA) has been discovered that acts with condensin in early mitosis to build the mitotic chromosome (28). The nature of RCA is still unknown but its activity is sustained by a family of cyclin-dependent kinases. Another category of chromosomal proteins that are part of the nuclear envelope, such as lamin and fibrillarin, localize to the chromosome periphery (12). Similarly, fibrous proteins such as β-actin and β-tubulin are distributed unevenly to the chromosome periphery (12). The involvement of these fibrous proteins in forming higher order structure remains controversial.

Cohesin, another member of the SMC protein complex, further maintains mitotic chromosome integrity during cell division. Cohesin is established during S phase, where its SMC subunits hold together sister chromatids of newly replicated chromosomes (29). In vertebrates, sister chromatid cohesion is displaced prior to metaphase, which allows the chromatids to resolve. This is important for alignment of chromosomes on the mitotic spindle as well as maintaining tension across the centromere. The latter is thought to counterbalance the pulling force of microtubules (29). Prior to the onset of anaphase, cohesin is removed from the centromere by an endopeptidase called separase, ensuring proper chromosome segregation. Besides maintaining mitotic chromosome integrity, cohesin is thought to be involved in chromosome compaction (30). Using three dimensional (3D) fluorescence *in situ* hybridization (FISH), it was demonstrated that chromatin became more compact after decreasing concentrations of cohesin. This was attributed to a decrease in intrachromosomal interactions between short range chromatin

loops during interphase (30). The authors of this study speculate that this could be one of the steps in the transiting to metaphase chromosome at the onset of mitosis.

1.3.3 DNA-modifying Proteins associated with Chromosome Conformation

Among the chromosome scaffold proteins, topoisomerases have the unique property of interacting with the DNA helix to effect topological simplification or separation of entangled daughter strands during replication (31). Distinct families of topoisomerase facilitate this process that fall into type I and type II enzymes. Type I topoisomerase creates single stranded breaks in the DNA by disrupting its phosphodiester bonds and does not require ATP, whereas type II creates double stranded breaks in the DNA and does require ATP (32). The two types can be further divided into IA, IB, IIA and IIB. In contrast to type IA and IB enzymes, type IIA and IIB DNA topoisomerases facilitate ATP-dependent transport of one intact DNA double helix though another (32). This facilitates topological transformation of the chromosome, resulting in relief of positive and negative supercoils (32). Such conformational changes in the twisting (i.e. writhe) of the double helix are expected, and in fact necessary, as chromosomes undergo compaction in order to ensure proper segregation into daughter cells. Changes to chromosome conformation are further complemented by cytosine DNA methylation. Cytosine methyltransferases affect dinucleotide CpG islands by the addition of a methyl group at GC rich regions positioned at 5’ ends of many genes (33). This is a well-recognized model of epigenetic inheritance during normal development, imprinting and X chromosome inactivation in mammals. With respect to chromatin structure, levels of DNA methylation are dynamically changed via concomitant changes in chromatin or development in humans (34). In abnormal diploid embryos, DNA methylation patterns between homologous metaphase chromosomes can also be variable; such that one of the parental homologs remains under-methylated. This has been attributed to the phenomenon of hemi-methylation, where a strand of newly replicated DNA is not methylated while an old one remains methylated (34).

1.3.4 Centromeric and Telomeric Proteins

Apart from proteins that make up the chromosome scaffold, several evolutionarily conserved centromere proteins (CENP-A, B, and C) are involved in centromere maintenance and kinetochore formation (12). During metaphase, chromatid cohesion is preserved at the centromere through the action of the cohesin SMC protein complex. Prior to anaphase, termination of cohesion from the centromere is imperative for accurate chromosome segregation. This is accomplished through separase, which proteolytically cleaves centromeric cohesion, thereby triggering sister chromatid separation (25). The telomere is another functional component of the chromosome that forms a nucleoprotein cap. Proteome analysis found several proteins common to telomeres that were associated with cell lines in the presence or absence of active telomerase (11,12). Among the most abundant of these were from categories of shelterin proteins, histones, and orphan receptors. Components of the shelterin complex are involved in telomere maintenance and protection from DNA damage (11). The orphan receptors maintain telomeres through recombination rather than telomerase activity (11). Cell lines in the absence of a telomerase maintenance pathway, showed reduced chromatin compaction in telomeric regions. This was postulated to occur through the recruitment of orphan receptors to telomeric sites; thus altering their heterochromatic state (35).

1.4 Role of XIST RNA in Chromatin Structure

X chromosome inactivation is a classic example of the non-uniformity in chromosome compaction and the differential treatment of homologs in the same cell nucleus. Apart from chromosomal proteins, RNAs are known to control chromatin structure, many of which coordinate gene silencing and activation (36). A long non-coding RNA, termed the X inactive specific transcript (XIST) is well recognized for its ability to control expression dosage of genes encoded on the X chromosome in female mammals (37). This involves recruitment of the polycomb repressive complex 2 (PRC2) to turn off gene expression from one of the two pairs of mammalian X chromosomes in each female cell at random (37,38). The mechanism by which XIST recruits PRC2 to effect this change is not entirely understood, but it has been shown by microscopy that XIST encapsulates the

entire inactive X chromosome in a cloud, forming a silencing compartment (37,39). Genes that escape silencing show reduced association with XIST (37), and are seen looping out of the condensed core (39). It should also be noted that the pathway of X chromosome inactivation, leading to epigenetic differences between homologs, is distinct from structural differences in locus-specific inter-homolog chromatin accessibility presented in this thesis.

1.5 Chromatin Accessibility and Organization in the Genome

The complexity of the mitotic proteome is vast. This includes modifications to histones, rebuilding nucleosomes with different histone variants, or recruitment of non-histone proteins that influence chromosome topology, ultimately shaping metaphase chromosomes. Taken together, these mechanisms assist not only in remodeling chromatin and maintaining chromosome architecture, but are critical in controlling chromatin accessibility. Our understanding of chromatin accessibility has permitted identification of epigenetic changes linked to cell regulatory events as well as disease development. The Encyclopedia of DNA Elements (ENCODE) international consortium, has been involved in these important efforts, which have primarily concentrated on annotating epigenetic marks that are established during interphase (40). Chromatin accessibility at the molecular and spatial levels in interphase and with respect to human metaphase chromosomes will be discussed below.

1.5.1 Chromatin Accessibility at the Molecular Level

At the molecular level, chromatin accessibility has been extensively studied by limited treatments with deoxyribonuclease I (DNase I), an enzyme that degrades DNA (i.e. is hypersensitive) primarily in regions with localized nucleic acid decondensation. Increased accessibility has been reported at genomic modules that bind to transcriptional regulatory protein factors and RNA polymerase, including promoters, enhancers, transcription start sites, intergenic regions, and long terminal repeat elements (41). A comprehensive study of the open chromatin landscape using DNase I and chromatin

immunoprecipitation followed by high-throughput sequencing (ChIP-seq) found that relative accessibility in the human genome varies by greater than 100 fold and is consistent across different cell types (42). Moreover, the authors found a strong inverse correlation between deposition of DNA methylation at CpG islands and chromatin accessibility, suggesting cytosine methylation reduces accessibility by displacing transcription factors (42). Investigation of chromatin using MNase in combination with ChIP-seq has implicated nucleosome repositioning with increased accessibility, especially in regions where transcription factor occupancy is high (43), whereas distal elements remained nucleosome rich. Single nucleotide polymorphisms are known to affect this nucleosome positioning by disrupting transcription factor binding (43), suggesting that accessibility of DNA can be determined by the genome sequence itself. It is also recognized that loss of histone H1 is sufficient to reduce chromatin compaction. This is supported by evidence that nuclei devoid of histone H1 are an order of magnitude more sensitive to DNase I (41). It follows therefore that at active genomic loci, the amount of histone H1 is reduced relative to inactive regions.

As described above chromatin accessibility at the molecular level, and primarily in interphase, is determined by the presence or absence of nucleosomes (41–43). Although this may be a major way by which DNA accessibility is regulated, the presence of a diverse set of histone modifications and different isoforms of the histone octamer itself suggest a more complex picture. It raises the possibility that accessibility of DNA at the molecular level may not simply be a paired phenomenon, where nucleosome-free DNA is completely accessible and nucleosome-bound DNA is inaccessible (44). Moreover a molecular approach to studying chromatin accessibility, albeit providing a genome wide view (44), has been less successful at visualizing how this accessibility is regulated within the 3D space of the nucleus.

1.5.2 Spatial Organization of Chromatin during Interphase

The spatial organization of chromatin during interphase was not obvious until the use of whole chromosome or region specific fluorescent DNA probes made it possible to distinguish individual chromosomes (45). It became apparent then that chromosomes in

the interphase nucleus were organized into chromosome territories. This was demonstrated in both fixed and living cells (46,47). Typically, gene-dense chromosome territories cluster at the nuclear center and gene poor territories at the nuclear periphery (34). This organization is non-random, in that genomic loci or even specific chromosomes reside in preferred nuclear locations (46) with no intermingling of juxtaposed chromosome territories (48). Accessibility of genomic loci around the outside of a chromosome territory favors a decondensed chromatin state for clusters with high gene density (46). In some diseases such as cancer-causing chromosomal aberrations (i.e. translocations), the spatial-temporal locations of chromosome territories can be altered. For example in a cell line derived from a patient with Hodgkin's disease, chromosome 19 was involved in complex rearrangements with chromosomes 2 and 9 (49) which resulted in a trisomic state for the additional chromosome 19 material. Further, it was observed that the distribution of chromosome 19 territory shifted to a more peripheral position in the interphase nucleus along with the peripherally located chromosomes 2 and 9. Typically in normal lymphocytes, chromosome 19 is located in the nuclear interior (49). This aberrant spatial positioning alters the surrounding gene density (49), which can misregulate expression of some genes (50). This is true, however, for only specific chromosomes involved in a given translocation and the nuclear positions in which they reside (49).

1.5.3 Chromatin Accessibility during Mitotic Metaphase

Another aspect of maintaining proper chromatin accessibility is the retention of epigenetic information from one cell generation to the next during mitosis. As indicated above, DNA methylation is an epigenetic mark that is stably replicated through cell mitosis. As a consequence of its stability, it is a well suited system to study interactions of genes with their environment (51). For example, changes to the environment, such as exposure to toxins or a methyl deficient diet, show global gene-specific hypomethylation (51). The opposite is true in certain cancers, where many CpG islands undergo hypermethylation, leading to changes in chromatin structure and silencing of tumor suppressor genes (52). Other stable epigenetic marks include selective lineage specific transcription factors such as RUNX, involved in control of mitotic cell cycle, as well as

retention of nuclease hypersensitivity (52). Both are critical for sustained cellular identity in progeny cells. Therefore, the consistency with which these marks are maintained has implications for the heritability of epigenetic states during mitotic metaphase. The error free maintenance of epigenetic marks, especially in certain regions of the genome such as promoters and DNase sensitive hotspots (53), is critical during normal cell division.

Given these implications, surprisingly there are little data on chromatin accessibility within metaphase chromosomes, and how it changes with respect to interphase during normal cell division. Previously, a study digested chromatin fibers from nuclei of lymphoblastoid cells with MNase and then sedimented the fibers through a sucrose gradient (54). Open chromatin with disordered fibers sedimented at a slow rate compared to compact chromatin. These large chromatin fractions from open and compact chromatin were used as DNA probes and localized onto metaphase chromosome spreads using FISH. Chromosomal regions with high gene density (i.e. ranging from ~ 10-20 genes in a 500 kilobase pair [kb] window) contained bright fluorescent signals from fractions of open chromatin fibers. This indicated that these regions showed greater accessibility to the most gene-rich metaphase chromosomes, namely 16, 17, 19 and 22, including gene-rich telomeric sites (55). At a gross level, the brightness of the fluorescence on metaphase chromosomes from the open chromatin fraction was homogenously stained within a chromosome cytoband, but varied in intensity when comparing trans-chromosomal regions (i.e. chromosome 1p36, 11p15.5, 16p13.3). Domains depleted of open chromatin fibers (i.e. compact chromatin) were found within all centromeric, pericentromic (1q12, 9q12), and were unexpectedly enriched in some euchromatic regions corresponding with G-bands (1p31, 3p24, 5q34, 7p21, 12q21) of metaphase chromosomes (54). These regions showed similar levels of compaction to heterochromatin and contained low gene density (< 5 genes/500 kb window) (54). In addition, chromatin fibers that were decondensed cytologically on metaphase chromosomes localized to the periphery of a chromosome territory, typically associated with increase accessibility and gene activity during interphase (54). One conclusion from these findings suggested a link between chromatin fiber accessibility during metaphase and higher order chromatin folding inside the nucleus.

Another study, using immunofluorescence, examined distribution of histone modifications associated with active and inactive chromatin across metaphase chromosomes from normal human lymphoblastoid cells (56). It was discovered that histone modifications associated with open chromatin (e.g. H3K9ac, H3K27ac and H3K4me3) on metaphase chromosomes alternated with regions of inactive chromatin (e.g. H3K27me3). Histone modifications of open chromatin in metaphase also had similar distributions across the equivalent epigenetic profile of interphase chromosomes assembled from ENCODE ChIP-seq data (40). This suggested that the above indicated histone modifications of interphase epigenome may be retained into metaphase. However, the chromatin marks maintaining accessibility within chromosomes in the interphase of one parent cell to the next daughter cell remain to be fully defined.

1.6 Cytological and Molecular Assays of Chromatin Accessibility and Genome Organization

Selection of cytological or molecular assay to investigate chromatin accessibility and its organization depends on the experimental conditions required and the genomic target to be studied. Among cytological methods, FISH is a versatile molecular cytogenetic approach (57) that can reveal chromatin accessibility in context of the cell at specific genomic loci, or the positioning of specific genomic loci in relation to each other (i.e. association of whole chromosomes). By contrast, chromosome conformation capture (3C) and its derivatives (i.e. 4C, 5C, HiC) give a genome wide view of nuclear chromatin organization and association between specific sequences (58). Traditionally molecular methods such as MNase digestion followed by next generation sequencing (seq) or MNase-seq, reveal the total nucleosome population and their positions in the genome. DNase-seq and formaldehyde-assisted isolation of regulatory elements (FAIRE) map open chromatin (59). Ultimately, these assays can be categorized as low throughput (i.e FISH), or high throughput; with advantages and disadvantages to each. FISH, although restricted to only those regions detected by its probe, achieves single cell resolution. Moreover, localization of a given region of interest can be performed without losing chromosome context. Molecular based techniques, for standard accessibility studies of

the human genome, require a large number of cells and over 150-200 million DNA sequence reads (59). Additionally, the results obtained are from all cells averaged over the entire cell cycle. On the contrary, with FISH and 3C heat-induced antigen retrieval (HIAR); the results can be distinguished at different stages of the cell cycle. Further, FISH and 3C have proved instrumental in advancing our understanding of chromatin organization in the human genome (60). Both have been widely used to visualize high order chromatin folding, while maintaining structural integrity of the cellular components they target. An expanded discussion of the two is presented below.

1.6.1 Principles of FISH

FISH allows nucleic acid sequences to be detected directly on metaphase chromosome or in interphase nuclei. FISH is typically performed with DNA or RNA based probes. The probes can target repetitive sequence (e.g. centromeric), locus specific regions (e.g. genic or intergenic), gene transcripts, or entire chromosomes. An essential step in probe preparation is to label the DNA sequence which can be performed by either a direct or indirect method. In the direct method, a reporter molecule is used such as a fluorescent dye incorporated directly into the nucleic acid fragment or recombinant clone (e.g. plasmids, bacteriophage, cosmids). This involves chemically binding a fluorescent tag into a nucleoside triphosphate and then using polymerases and other enzymes (i.e. DNaseI) to replace the probe's nucleosides with labelled ones (61,62). In the indirect method, an intermediary step is required, whereby nick translation (for example) of an amplified nucleic acid with modified biotin or digoxigenin nucleosides can be substituted for pyrimidine nucleotides used to synthesize DNA (62,63). All probes described in this thesis have been indirectly labelled with a nonfluorescent molecule (such as biotin- or digoxigenin- conjugated nucleotide) that can bind fluorophore-labeled avidin or antibody after hybridization. This increases the sensitivity of hybridized probe detection since hybridization is not restricted and multiple fluorophores can be attached to avidin or antibody molecule during detection (62). Detection of probes with fluorophore conjugated directly to the nucleotide can limit probe detection due to steric hindrance.

The basic steps in the FISH procedure are similar to those of Southern blot hybridization, with the main difference being that hybridized DNA probes are visualized on individual cells directly on the chromosome or within the nucleus. As well, with FISH, the cells are usually fixed on microscope slides rather than genomic DNA being transferred to nylon membranes as is common for Southern blots. The fixed specimen is denatured with a combination of formamide, salt, and heat in order to produce single stranded target sequences. Similarly, the DNA probes are also denatured and overlaid on denatured specimen and allowed to hybridize (62). Complementary sequences (i.e. DNA probe in great excess and the genomic target) hybridize to become double stranded. Post-hybridization washes remove non-specific binding of probe with chromosomal target and the hybridization is detected *in situ* (62). The hybridized target is detected using fluorochrome-conjugated protein-based reagents or alternatively with directly labeled fluorochromes and visualized by epifluorescence microscopy (57,62). Visualization of chromosomes or nuclear material following FISH is achieved through the use of DNA counterstains such as 4′,6-diamidino- 2-phenylindole (DAPI) or propidium iodide. DAPI staining produces a distinct banding pattern and permits chromosome identification.

FISH probes can vary in their genomic target length. These include DNA probes cloned into recombinant bacterial or yeast artificial chromosome (BAC, YAC), which detect large genomic targets spanning on the order of ~ 200kb-1 Mb. FISH probes cloned into fosmids or cosmids span ~35-50 kb (57). By comparison, single copy (SC) probes used in the current work typically span 1–5 kb and can be densely designed from within chromosomal targets covered by larger target probes with greater precision (64,65). Relative to recombinant DNA probes, they provide several orders of magnitude higher resolution.

1.6.2 Detecting Chromatin Accessibility with FISH

Apart from the appreciable body of literature that provides evidence for its clinical utility [reviewed in (57)], a broad application of FISH is its ability to analyze genome organization and condensation differences at the single cell level. Using BAC, cosmid or fosmid DNA probes, large chromatin compaction differences have been shown in G_o/G_1

nuclei (66), at key cell differentiation loci (67), and even in mutant cells where defects of core cohesion components cause chromatin decompaction (68). FISH has also defined accessibility in early replicating GC rich chromatin, which appears to condense slower since these sites are less compact, versus AT rich chromatin fiber (69). Moreover, using DNA inserts cloned into bacteriophage (15-20 kb) or cosmid vectors, differences in allele specific replication timing at imprinted loci (70,71) have been observed, suggesting structural allelic differences in chromatin. Much of this work has been performed in interphase with very few studies expanding on how this accessibility mirrors the chromatin state in metaphase.

Using FISH, our group has detected striking probe hybridization fluorescence intensity differences (*or differential accessibility [DA]*) between homologous regions in metaphase chromosomes at a resolution that has not been previously achieved. In this thesis, DA is observed reproducibly with multiple probes and in various samples. My aim is to understand the properties of DA and the mechanism that underlies these differences. In Chapters 3 and 4, this mechanism is elucidated as novel structural differences between homologous regions of normal metaphase chromosomes. At that point, I refer to DA and these structural differences interchangeably.

DA has been observed using a subset of unique single copy (SC) FISH probes, comprised of locus-specific DNA intervals. SC FISH probe technology was developed in our laboratories (64,65) and has demonstrated its utility to detect small chromosomal rearrangements associated with congenital abnormalities, cancer (65), as well as complex genomic architecture responsible for recurrent genomic disorders (72). SC probes have been used in flow cytometry (73) and genomic microarray based platforms (74) to accurately detect pathogenic copy number changes. While SC probes generally contain unique targets, we also developed low copy (LC) DNA probes from within blocks of segmental duplicons (i.e. SDs or low copy repeats) to expedite delineation of DNA breakage interval hotspots (72). SD blocks are organized into large (10kb – 400 kb) near identical paralogs of DNA involved in recurrent genomic disorders (75). LC probes were designed to reflect this genomic organization by detecting distinct paralogs at a copy

level defined by the genomic organization of the SD sequences. This strategy allowed us to delineate chromosomal targets, often associated with pathogenicity, in complex genomic architecture (72). Similar to single copy targets, LC DNA probes also range in size from 1–5 kb. The locations of these probes are obtained directly from the Reference human genome which allows for their genomic coordinates to be known precisely. SC and LC interval locations are determined computationally and verified by BLAST (basic local alignment search tool) (76) to ensure they detect unique sequences or low copy targets. SC and LC probes, unlike BAC, cosmid or fosmids, do not contain any high copy repetitive elements, and therefore the use of human C_ot-1 DNA to suppress these elements is not necessary (64). Our group has discovered that the presence of interspersed single copy intervals within C_ot-1 DNA can cause non-specific hybridization between probes and genomic targets (74,77). We have also automated the process of determining single copy intervals in the human genome, such that prior knowledge of existing repetitive elements is not necessary to identify these intervals genome wide (74). Illustration differentiating SC from LC intervals along with how they are used in FISH is depicted in Figures 1-3 and 1-4, respectively.

1.6.3 Detecting Chromatin Organization with Chromosome Conformation Capture

Using whole chromosome paint probes for FISH, a recurrent observation has been that chromosomes, including domains of homologous chromosomes (78,79), do not intermingle inside the eukaryotic nucleus; but rather are found in individual clusters. 3C was initially described by Dekker et al (80,81) in yeast and a variety of 3C derived methods have been applied since, which extend the analysis genome-wide (82). The basic process entails preserving the chromosome confirmation by crosslinking with formaldehyde, which gives a snapshot of the *in vivo* interaction between DNA and proteins. This is followed by restriction enzyme digestion of the cross-linked chromatin in the region of interest. Next, the digested components undergo intramolecular ligation of their sticky ends. In this manner, genomic regions that co-localize in nuclear space but are far away on a DNA template can be ligated. In order to detect these interactions, the

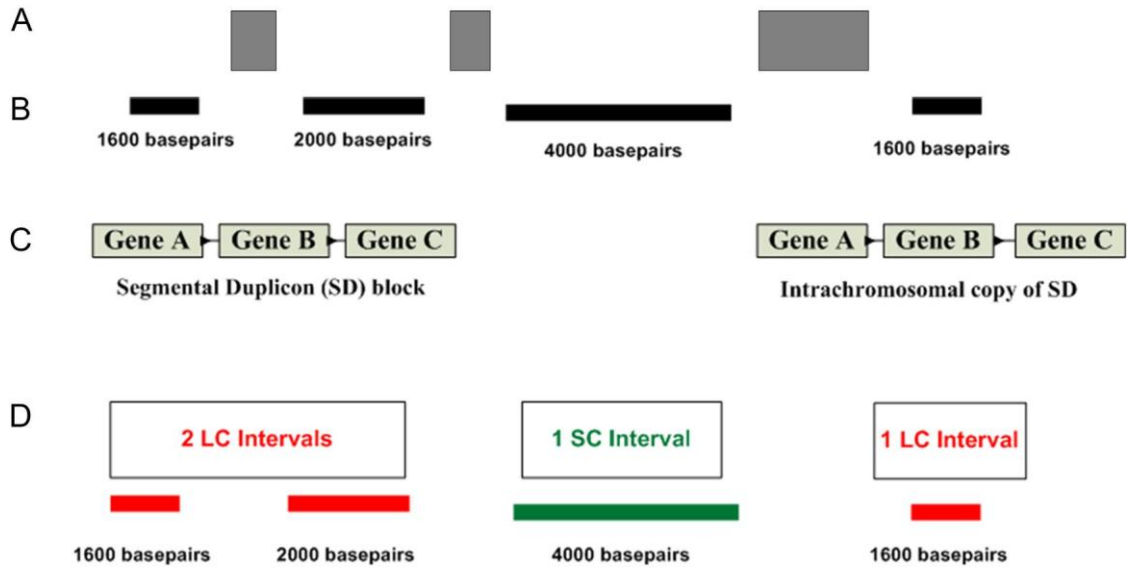

Figure 1-3. Steps involved in deriving locus-specific genomic intervals

(A) Genomic positions of interspersed high copy repeats are obtained from chromosome region of interest (gray boxes). (B) These repeats are examined for non-overlapping genomic intervals ranging in size from 1500-5000 bp (black boxes). (C) Genomic positions of SDs are obtained from the Reference human genome. SDs are paralogous blocks sharing high DNA sequence identity at intra-chromosomal (or trans-chromosomal) locations and often contain genes, as indicated. The specific intervals are aligned against genomic positions of SD blocks. (D) Following alignment with SDs, intervals are binned into low copy (LC) or single copy (SC) sequences. LC sequences occur in multiple copies in the genome whereas SC sequences occur once. In the figure, LC and SC are differentiated by red and green blocks, respectively.

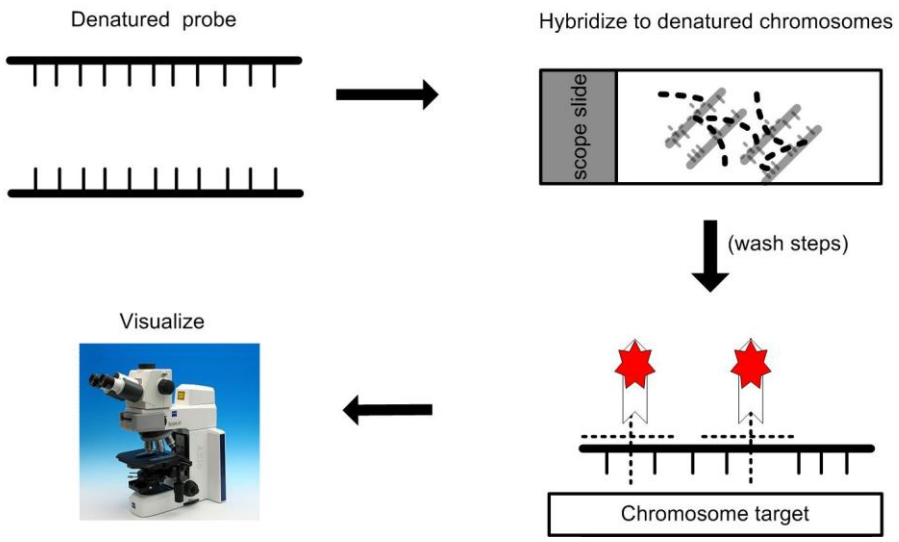

Figure 1-4. Steps involved in FISH.

The order of steps in FISH is shown (clockwise, black arrows). Denatured, labeled DNA probe is hybridized to denatured chromosomes (*in situ*, on microscope slide). Following hybridization, slides are washed to remove nonhybridized probe, hybridized probe is then detected with an antibody conjugated to a fluorophore (red), and visualized by epifluorescence microscopy.

reverse crosslinked DNA is purified, and used as template for quantitative PCR (82). The high-throughput sequencing approach (or HiC) incorporates biotin-labeled nucleotides before the ligation step. Colocalizing fragments can then be isolated with biotin pull down for subsequent analysis of ligation frequencies in the genome (82). 3C experiments show that looping interactions between gene promoters, enhancer, and transcription factor binding sites are common in mammalian cells and tend to occur over an open chromatin region of 100-200 kb (83).

Recently HiC methods have refined these observations by showing that the mammalian genome is organized into cell-type specific globules or domains with an average size of 900 kb (60,84). These domains exhibit frequent interactions with one another and contain chromatin with similar accessibility patterns, reflecting a basic property of genome organization. The average size of these domains, forming the basic building blocks of chromosome territories, is similar to that observed by microscopy using FISH (60). The interactions were also noted to be stable across different cell types and species (84). This is in keeping with the principle that cells express different sets of genes that need to be maintained in open or compact confirmations in different regions of the genome. In mitosis, however, cell type specific domains were not detected (83). Such interactions would not be probable since mitotic chromosomes are transcriptionally silent,

1.7 What is Known about Chromatin Memory?

It remains an open question as to how cells transmit their respective chromatin state through mitosis. It has been postulated that chromatin structures in mitosis are locally dynamic, where individual loci can maintain none, some, or all of their interphase accessibility (53,83). The definitive factors involved in shaping this process are not known, but accumulating experimental evidence (see sections 1.5.2, 1.6.3) has advanced the long-standing hypothesis of Theodor Boveri that chromatin is stably maintained throughout interphase (85). Further, this arrangement is conserved throughout mitosis, resulting in symmetrical arrangements of chromatin in new daughter nuclei (85). In order for chromatin to remain stable through multiple generations, an epigenetic mark can be

qualified based on its retention throughout replication, condensation, and transmission to the daughter cells. A well-known example of this is DNA methylation (sections 1.3.3 and 1.5.3), which by way of DNA methyltransferase I (DNMT1) interacts with the moving replication fork to deposit cytosine methylation post-DNA synthesis (86). Nevertheless, certain model organisms such as *C. elegans* and *Drosophila*, lack substantial cytosine methylation, suggesting that transmission of DNA methylation may not be a universal epigenetic mark of chromatin memory (86,87).

To make a case for histone modifications as marks of chromatin memory poses a far greater challenge. Unlike DNA methylation, there is no direct mechanism to copy histones into nascent DNA. One model proposes that in order for histone marks to be propagated, such as H3K27me3 (88), the particular modification would have to recruit protein complexes with the ability to catalyze the modification and also facilitate its binding activity (89). The best documented histone modification involved in compacting metaphase chromosomes is the phosphorylation of H3 N-terminal tails on serine 10 or serine 28 (16). Phosphorylation of H3 also recruits other marks associated with forming repressive chromatin such as HP1. However, the dramatic compaction into mitotic metaphase chromosomes ejects the majority of HP1 from chromatin. Similarly, chromatin compaction also results in cessation of transcription, in part by inhibiting transcription factor binding to the mitotic chromatin. Despite the loss of transcription factors, DNase I-sensitive regions corresponding to sites of transcription factor binding are surprisingly maintained during mitosis (53). In order to reconcile how this may occur, a body of literature on the concept of ‘mitotic bookmarking’ (90,91) suggests that some chromatin modifiers are retained on mitotic chromosomes even if higher order structures are disrupted, as suggested by HiC data. For example, a mechanism of mitotic bookmarking suggests that certain key transcription factors, FOXA1, GATA1, or chromatin modifiers such as trithorax protein MLL (92) may be sufficient to transmit chromatin memory in order to maintain cellular identity through mitosis. But, the retention of specific chromatin modifiers is often cell-type specific, and do not scale well to control the diverse set of cell regulatory outputs, upon re-entry into G1 (90).

1.8 Chromosome Research by Next Generation Microscopy

There has been criticism over extrapolating data from HiC studies due to the likelihood of false positive interactions that can be captured by indirect formaldehyde crosslinking (60,93). The limitations of 3C and its derivatives in studying mitotic chromosomes are further confounded by their inability to contextualize 3D arrangement of higher order chromatin (83). Overcoming some of these limitations is possible in part with *in situ* based approaches using microscopy, especially super-resolution and non-optical imaging modalities. These tools provide diffraction-unlimited resolution and preserve the native state of chromatin by minimizing preparatory steps. They have also been applied to the study of large-scale chromatin organization and mitotic chromosome structure at ultra-high resolution.

1.8.1 Application of Atomic Force Microscopy to Chromosomes

Earlier studies examining metaphase chromosome using EM were primarily interested with gross morphology (94). These studies complemented historical models of chromosome condensation or provided a means to quantify structural changes at distinct levels of condensation through mitosis (94,95). However, preparation of chromosome spreads for EM is challenging and requires special sample coating and dehydration steps (96). Advances in the field of chromosome nanoscience (67) have allowed more versatile means of investigation of the chromatin fiber at its highest level of compaction (i.e. in metaphase) through to the level of the nucleosome. One of the tools that have enabled these efforts is the atomic force microscope (AFM), which is part of the scanning force microscopy family. AFM scans a sharp silicon nitride tip on the surface of an object (e.g. the chromosome). The tip which is attached to a cantilever spring deflects as it is contoured over the object; generating its surface topography (97). Compared to conventional light microscopy, AFM provides 10-20 fold higher resolution. It does not require additional preparatory steps such as those required with EM (97). AFM applied to the study of metaphase chromosomes shows groove and ridge features along the

chromosomal surface. These features correspond to open and compact chromatin fiber, respectively. This fiber demonstrates a zigzag pattern along the chromatid axis and is arranged into radially coiled loops, favoring the radial-loop model (98). Combination of AFM and scanning near field optical microscopy following FISH can also be used to analyze chromosomal features such as telomeres (99). More recently the use of high speed AFM has been applied to the study of nucleosome dynamics (100), revealing that nucleosomes unwrap spontaneously by moving along the DNA template. This in turn allows accessibility of DNA to regulatory proteins. AFM resolves surface features of the chromatin, while providing precise information about their heights. Beyond the surface, it does not offer information about the internal chromatin structure or its spatial organization.

1.8.2 Application of Super-resolution Microscopy to Chromosomes

Super-resolution microscopy is a powerful diffraction-unlimited technique that has been applied to the study of 3D nuclear architecture and condensed mitotic chromosomes. Depending on the imaging modality, spatial resolution can maximally reach 20 nm in both lateral (x/y axis) and axial (z axis) planes (101). By comparison, conventional wide-field fluorescence microscopy resolves 200 nm in the lateral and 500 nm in the axial plane (101). One of the super-resolution approaches known as photoactivation-localization microscopy (PALM) and its variant stochastic optical reconstruction microscopy has shown how chromatin fibers are organized in mitotic chromosomes with unprecedented detail. PALM on cells from *Drosophila* embryos exhibited condensed mitotic metaphase chromosomes composed of 70 nm filament-like blocks with 35 nm subfilaments (102). These filaments were roughly the same size as the fibers in early G1 interphase. The subfilaments may be 30 nm chromatin fibers commonly observed *in vitro* but as yet not observed *in vivo* (102). The structure of chromatin higher order folding has also been assessed with super-resolution 3D structured illumination microscopy (3D-SIM). 3D-SIM uses patterned illumination with a lateral and axial resolution of 100 nm and 200 nm, respectively (101). It provides rapid acquisition of data, relative to other super-resolution modalities or to AFM. 3D-SIM, if

being combined with FISH, does not require specialized probe preparation steps. In the nucleus, 3D-SIM has confirmed loop-based models of chromatin organization. Among mitotic chromosomes, it has shown that open chromatin tends to occupy the peripheral euchromatic portions of the chromosome arms as the cell progresses into prophase, whereas silent chromatin is more centrally located in the condensed chromosomes (103). This configuration is also maintained in interphase (103). Super-resolution microscopy has resolved many aspects of chromatin imaging that were not previously possible with diffraction-limited methods. For studying chromatin accessibility within cytologically thick samples such as mitotic metaphase chromosomes, 3D-SIM is ideally suited as it provides a high resolution, z-stack projection that can be reconstructed into the structure of the chromosome.

1.9 Thesis Objectives and Contributions

This thesis explores an unrecognized feature of mitotic chromosome condensation between homologous genomic targets. As part of FISH validation of certain short (1.5–5 kb) single copy (SC) DNA probes on human metaphase chromosomes, we observed hybridization fluorescence intensity differences between the target sequences of homologous chromosomes (see Figure 1-5). This was consistently seen in metaphase cells from different individuals for the same probe, even though the cells are normal. Not all SC probes demonstrated these differences; and in fact the majority of SC probes hybridized to both homologs with equivalent intensities. The inter-homolog intensities of large BAC FISH probes (~200-400 kb.) can also vary but is more striking with SC FISH due to the reduced length of the chromosomal target. Such differences in chromatin accessibility and organization have also been recognized in the interphase nucleus (46,60,83), often at homologous domains (78,79). *We hypothesize that there are local or regional epigenetic differences in condensation between metaphase chromosome homologs, leading to differences in accessibility (referred to as differential accessibility [DA]) of the probe to the target sequence, and that these differences are maintained throughout the cell cycle.* To investigate this, our objectives were to:

1. **Develop a correlated *in situ* imaging approach to visualize metaphase chromosome topography at nanoscale resolution (Chapter 2)**

   The study is important, because it allows comparison of the 3D topography of the metaphase chromosome in context of its DNA and protein chromatin nano-structures directly on homologous metaphase chromosomes. It then analyzes whether the context of the chromatin topography is altered at centromeric and non-centromeric locations without DA. Correlated *in situ* imaging further attempts to examine chromatin topography of genomic targets with DA. This study is novel because it contributes to bridging the gap between molecular cytogenetics and nanoscience for examining surface topography of condensed chromatin structures marked by FISH or by immunofluorescence. The approach can be extended to studying abnormal chromosome topography in instances where the chromatin fiber is disrupted, which is known to impair proper chromosome condensation.

2. **Identify whether DA between homologous targets is random or non-random, visualize accessibility of loci with and without DA within metaphase chromatin, and relate these differences to chromatin accessibility in interphase (Chapter 3).**

   The study is important, because it presents evidence that homologous chromosomal regions show non-random differences in condensation during metaphase. It further suggests that an intrinsic difference in underlying chromatin structure causes DA. SC probes act as proxies for detecting chromatin accessibility differences between homologous regions in metaphase. Their use in super resolution microscopy opens new perspectives on sub-diffraction analysis of chromatin accessibility at sequence-specific loci. These intriguing observations led to studies aimed at understanding the mechanistic basis of DA, and may reveal a novel form of epigenetic regulation in the cell.

3. **Target epigenetic modifications involved in chromosome condensation to determine indicators for DA (Chapter 4).**

   The study is important because it demonstrates that altering chromosome unwinding reverses allele-specific differences in metaphase chromosome compaction. This may also have implications in cancer research. The inhibitors of chromosome condensation used for assessing DA may be useful in enhancing chemosensitivity of tumor cells. To the field of molecular cytogenetics, genomic targets in which DA has been equalized expands the array of SC FISH probes that can be used to complement high resolution detection of chromosomal rearrangements.

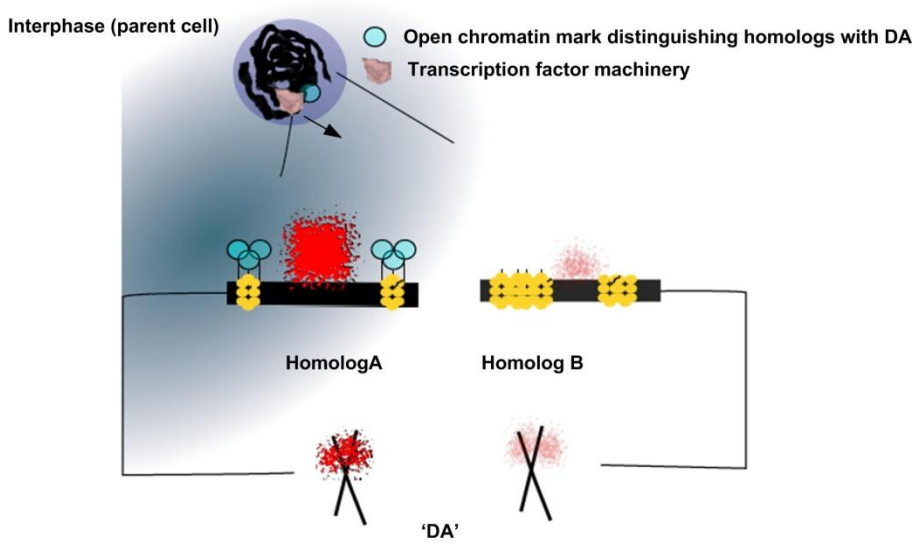

Figure 1-5. Illustration of differential accessibility (DA) between metaphase chromosome homologs.

Interphase chromatin or mitotic metaphase chromosomes (X-shaped) are drawn in black. DNA probe fluorescence is shown as a bright (red) or weak (pink) signal, and yellow demarcates accessible or inaccessible loci. Transcription factors are displaced from interphase chromatin prior to mitosis (arrow). Certain epigenetic marks or nuclease hypersensitivity can be retained on post replicated chromatin. This is illustrated by open chromatin marks (e.g. histone or nonhistone binding proteins) on homolog A (light blue circles) which are absent from homolog B. DA is evident on metaphase chromosomes (X-shaped), i.e. homolog A has a bright fluorescent signal to the accessible target and homolog B has a weak fluorescent signal to the inaccessible target.

1.10 References

1. Crow EW, Crow JF. 100 Years Ago: Walter Sutton and the Chromosome Theory of Heredity. Genetics. 2002 Jan 1;160(1):1–4.

2. Wilson EB. Mendel's Principles of Heredity and the Maturation of the Germ-Cells. Science. 1902 Dec 19;16(416):991–3.

3. Harshman SW, Young NL, Parthun MR, Freitas MA. H1 histones: current perspectives and challenges. Nucleic Acids Res. 2013 Nov;41(21):9593-609.

4. Belmont AS. Mitotic chromosome scaffold structure: New approaches to an old controversy. Proc Natl Acad Sci. 2002 Dec 10;99(25):15855–7.

5. Paulson JR, Laemmli UK. The structure of histone-depleted metaphase chromosomes. Cell. 1977 Jan 11;12(3):817–28.

6. Adolph KW. Organization of chromosomes in mitotic HeLa cells. Exp Cell Res. 1980 Jan;125(1):95–103.

7. Tamayo J. Structure of human chromosomes studied by atomic force microscopy: Part II. Relationship between structure and cytogenetic bands. J Struct Biol. 2003 Mar;141(3):189–97.

8. Sedat J, Manuelidis L. A Direct Approach to the Structure of Eukaryotic Chromosomes. Cold Spring Harb Symp Quant Biol. 1978 Jan 1;42:331–50.

9. Belmont AS. Mitotic chromosome structure and condensation. Curr Opin Cell Biol. 2006 Dec;18(6):632–8.

10. Rattner JB, Lin CC. Radial loops and helical coils coexist in metaphase chromosomes. Cell. 1985 Jan 8;42(1):291–6.

11. Ohta S, Wood L, Bukowski-Wills J-C, Rappsilber J, Earnshaw WC. Building mitotic chromosomes. Curr Opin Cell Biol. 2011 Feb;23(1):114–21.

12. Takata H, Uchiyama S, Nakamura N, Nakashima S, Kobayashi S, Sone T, et al. A comparative proteome analysis of human metaphase chromosomes isolated from two different cell lines reveals a set of conserved chromosome-associated proteins. Genes Cells. 2007 Mar;12(3):269–84.

13. Cooke CA, Bernat RL, Earnshaw WC. CENP-B: a major human centromere protein located beneath the kinetochore. J Cell Biol. 1990 May;110(5):1475–88.

14. Kornberg RD. Chromatin Structure: A Repeating Unit of Histones and DNA. Science. 1974 May 24;184(4139):868–71.

15. Strahl BD, Allis CD. The language of covalent histone modifications. Nature. 2000 Jan 6;403(6765):41–5.

16. Wilkins BJ, Rall NA, Ostwal Y, Kruitwagen T, Hiragami-Hamada K, Winkler M, et al. A cascade of histone modifications induces chromatin condensation in mitosis. Science. 2014 Jan 3;343(6166):77–80.

17. Cosgrove MS. Writers and readers: deconvoluting the harmonic complexity of the histone code. Nat Struct Mol Biol. 2012 Aug;19(8):739–40.

18. Kamakaka RT, Biggins S. Histone variants: deviants? Genes Dev. 2005 Feb 1;19(3):295–316.

19. Fan JY, Gordon F, Luger K, Hansen JC, Tremethick DJ. The essential histone variant H2A.Z regulates the equilibrium between different chromatin conformational states. Nat Struct Biol. 2002 Mar;9(3):172–6.

20. Bönisch C, Hake SB. Histone H2A variants in nucleosomes and chromatin: more or less stable? Nucleic Acids Res. 2012 Nov;40(21):10719-41.

21. Turner BM. Reading signals on the nucleosome with a new nomenclature for modified histones. Nat Struct Mol Biol. 2005 Feb;12(2):110–2.

22. Maeshima K, Laemmli UK. A two-step scaffolding model for mitotic chromosome assembly. Dev Cell. 2003 Apr;4(4):467–80.

23. Samejima K, Samejima I, Vagnarelli P, Ogawa H, Vargiu G, Kelly DA, et al. Mitotic chromosomes are compacted laterally by KIF4 and condensin and axially by topoisomerase IIα. J Cell Biol. 2012 Nov 26;199(5):755–70.

24. Dietzel S, Belmont AS. Reproducible but dynamic positioning of DNA in chromosomes during mitosis. Nat Cell Biol. 2001 Aug;3(8):767–70.

25. Vagnarelli P. Chromatin reorganization through mitosis. Adv Protein Chem Struct Biol. 2013;90:179–224.

26. Vagnarelli P. Mitotic chromosome condensation in vertebrates. Exp Cell Res. 2012 Jul 15;318(12):1435–41.

27. Hudson DF, Vagnarelli P, Gassmann R, Earnshaw WC. Condensin is required for nonhistone protein assembly and structural integrity of vertebrate mitotic chromosomes. Dev Cell. 2003 Aug;5(2):323–36.

28. Vagnarelli P, Hudson DF, Ribeiro SA, Trinkle-Mulcahy L, Spence JM, Lai F, et al. Condensin and Repo-Man-PP1 co-operate in the regulation of chromosome architecture during mitosis. Nat Cell Biol. 2006 Oct;8(10):1133–42.

29. Ishiguro K, Watanabe Y. Chromosome cohesion in mitosis and meiosis. J Cell Sci. 2007 Feb 1;120(3):367–9.

30. Tark-Dame M, Jerabek H, Manders EMM, Heermann DW, van Driel R. Depletion of the chromatin looping proteins CTCF and cohesin causes chromatin compaction: insight into chromatin folding by polymer modelling. PLoS Comput Biol. 2014 Oct;10(10):e1003877.

31. Rybenkov VV, Ullsperger C, Vologodskii AV, Cozzarelli NR. Simplification of DNA Topology Below Equilibrium Values by Type II Topoisomerases. Science. 1997 Aug 1;277(5326):690–3.

32. Wang JC. Cellular roles of DNA topoisomerases: a molecular perspective. Nat Rev Mol Cell Biol. 2002 Jun;3(6):430–40.

33. Bird A. DNA methylation patterns and epigenetic memory. Genes Dev. 2002 Jan 1;16(1):6–21.

34. Pendina AA, Efimova OA, Fedorova ID, Leont'eva OA, Shilnikova EM, Lezhnina JG, et al. DNA methylation patterns of metaphase chromosomes in human preimplantation embryos. Cytogenet Genome Res. 2011;132(1-2):1–7.

35. Episkopou H, Draskovic I, Beneden AV, Tilman G, Mattiussi M, Gobin M, et al. Alternative Lengthening of Telomeres is characterized by reduced compaction of telomeric chromatin. Nucleic Acids Res. 2014 Apr;42(7):4391-405.

36. Wang KC, Yang YW, Liu B, Sanyal A, Corces-Zimmerman R, Chen Y, et al. A long noncoding RNA maintains active chromatin to coordinate homeotic gene expression. Nature. 2011 Apr 7;472(7341):120–4.

37. Dimond A, Fraser P. Long Noncoding RNAs Xist in Three Dimensions. Science. 2013 Aug 16;341(6147):720–1.

38. Heard E. Recent advances in X-chromosome inactivation. Curr Opin Cell Biol. 2004 Jun;16(3):247–55.

39. Chaumeil J, Baccon PL, Wutz A, Heard E. A novel role for Xist RNA in the formation of a repressive nuclear compartment into which genes are recruited when silenced. Genes Dev. 2006 Aug 15;20(16):2223–37.

40. Consortium TEP. An integrated encyclopedia of DNA elements in the human genome. Nature. 2012 Sep 6;489(7414):57–74.

41. Cockerill PN. Structure and function of active chromatin and DNase I hypersensitive sites. FEBS J. 2011 Jul;278(13):2182–210.

42. Thurman RE, Rynes E, Humbert R, Vierstra J, Maurano MT, Haugen E, et al. The accessible chromatin landscape of the human genome. Nature. 2012 Sep 6;489(7414):75–82.

43. Gaffney DJ, McVicker G, Pai AA, Fondufe-Mittendorf YN, Lewellen N, Michelini K, et al. Controls of nucleosome positioning in the human genome. PLoS Genet. 2012;8(11):e1003036.

44. Chen PB, Zhu LJ, Hainer SJ, McCannell KN, Fazzio TG. Unbiased chromatin accessibility profiling by RED-seq uncovers unique features of nucleosome variants in vivo. BMC Genomics. 2014 Dec 15;15(1):1104.

45. Pinkel D, Straume T, Gray JW. Cytogenetic analysis using quantitative, high-sensitivity, fluorescence hybridization. Proc Natl Acad Sci U S A. 1986 May;83(9):2934–8.

46. Cremer T, Cremer C. Rise, fall and resurrection of chromosome territories: a historical perspective. Part I. The rise of chromosome territories. Eur J Histochem. 2006 Sep;50(3):161–76.

47. Müller I, Boyle S, Singer RH, Bickmore WA, Chubb JR. Stable morphology, but dynamic internal reorganisation, of interphase human chromosomes in living cells. PloS One. 2010;5(7):e11560.

48. Dietzel S, Jauch A, Kienle D, Qu G, Holtgreve-Grez H, Eils R, et al. Separate and variably shaped chromosome arm domains are disclosed by chromosome arm painting in human cell nuclei. Chromosome Res Int J Mol Supramol Evol Asp Chromosome Biol. 1998 Jan;6(1):25–33.

49. Meaburn KJ, Misteli T, Soutoglou E. Spatial genome organization in the formation of chromosomal translocations. Semin Cancer Biol. 2007 Feb;17(1):80–90.

50. Finlan LE, Sproul D, Thomson I, Boyle S, Kerr E, Perry P, et al. Recruitment to the nuclear periphery can alter expression of genes in human cells. PLoS Genet. 2008 Mar;4(3):e1000039.

51. Dolinoy DC, Weidman JR, Jirtle RL. Epigenetic gene regulation: linking early developmental environment to adult disease. Reprod Toxicol. 2007 May;23(3):297–307.

52. Zaidi SK, Young DW, Montecino M, Lian JB, Stein JL, van Wijnen AJ, et al. Architectural epigenetics: mitotic retention of mammalian transcriptional regulatory information. Mol Cell Biol. 2010 Oct;30(20):4758–66.

53. Hsiung CC-S, Morrissey CS, Udugama M, Frank CL, Keller CA, Baek S, et al. Genome accessibility is widely preserved and locally modulated during mitosis. Genome Res. 2014 Feb;25(2):213-25.

54. Gilbert N, Boyle S, Fiegler H, Woodfine K, Carter NP, Bickmore WA. Chromatin architecture of the human genome: gene-rich domains are enriched in open chromatin fibers. Cell. 2004 Sep 3;118(5):555–66.

55. Boyle S, Gilchrist S, Bridger JM, Mahy NL, Ellis JA, Bickmore WA. The spatial organization of human chromosomes within the nuclei of normal and emerin-mutant cells. Hum Mol Genet. 2001 Feb 1;10(3):211–9.

56. Terrenoire E, McRonald F, Halsall JA, Page P, Illingworth RS, Taylor AMR, et al. Immunostaining of modified histones defines high-level features of the human metaphase epigenome. Genome Biol. 2010 Nov 15;11(11):R110.

57. Vorsanova SG, Yurov YB, Iourov IY. Human interphase chromosomes: a review of available molecular cytogenetic technologies. Mol Cytogenet. 2010 Jan 11;3(1):1.

58. Ethier SD, Miura H, Dostie J. Discovering genome regulation with 3C and 3C-related technologies. Biochim Biophys Acta. 2012 May;1819(5):401–10.

59. Tsompana M, Buck MJ. Chromatin accessibility: a window into the genome. Epigenetics Chromatin. 2014 Nov 20;7(1):33.

60. Williamson I, Berlivet S, Eskeland R, Boyle S, Illingworth RS, Paquette D, et al. Spatial genome organization: contrasting views from chromosome conformation capture and fluorescence in situ hybridization. Genes Dev. 2014 Dec 15;28(24):2778–91.

61. Cunningham MW, Mundy CR. Labelling nucleic acids for hybridization. Nature. 1987 Apr 16;326(6114):723–4.

62. Knoll JHM, Lichter P. In Situ Hybridization to Metaphase Chromosomes and Interphase Nuclei; in: Haines JL, Korf BR, Morton CC, Seidman CE, Seidman JG, Smith DR (eds): Current Protocols in Human Genetics, pp 4.3.1-4.3.31 (John Wiley & Sons Inc., Malden 2005).

63. Boyle A, Perry-O'Keefe H. Labeling and colorimetric detection of nonisotopic probes; in Ausubel FM (ed): Curr Protoc Mol Biol, pp Unit3.18 (John Wiley & Sons Inc., Malden 2001).

64. Rogan PK, Cazcarro PM, Knoll JHM. Sequence-Based Design of Single-Copy Genomic DNA Probes for Fluorescence In Situ Hybridization. Genome Res. 2001 Jun;11(6):1086–94.

65. Knoll JHM, Rogan PK. Sequence-based, in situ detection of chromosomal abnormalities at high resolution. Am J Med Genet A. 2003 Sep 1;121A(3):245–57.

66. Yokota H, Singer MJ, Engh GJ van den, Trask BJ. Regional differences in the compaction of chromatin in human G0/G1 interphase nuclei. Chromosome Res. 1997 Apr 1;5(3):157–66.

67. Chambeyron S, Bickmore WA. Chromatin decondensation and nuclear reorganization of the HoxB locus upon induction of transcription. Genes Dev. 2004 May 15;18(10):1119–30.

68. Nolen LD, Boyle S, Ansari M, Pritchard E, Bickmore WA. Regional chromatin decompaction in Cornelia de Lange syndrome associated with NIPBL disruption can be uncoupled from cohesin and CTCF. Hum Mol Genet. 2013 Oct 15;22(20):4180–93.

69. Drouin R, Lemieux N, Richer CL. Chromosome condensation from prophase to late metaphase: relationship to chromosome bands and their replication time. Cytogenet Cell Genet. 1991;57(2-3):91–9.

70. Kitsberg D, Selig S, Brandeis M, Simon I, Keshet I, Driscoll DJ, et al. Allele-specific replication timing of imprinted gene regions. Nature. 1993 Jul 29;364(6436):459–63.

71. Knoll JHM, Cheng S-D, Lalande M. Allele specificity of DNA replication timing in the Angelman/Prader–Willi syndrome imprinted chromosomal region. Nat Genet. 1994 Jan;6(1):41–6.

72. Khan WA, Knoll JH, Rogan PK. Context-based FISH localization of genomic rearrangements within chromosome 15q11.2q13 duplicons. Mol Cytogenet. 2011 Aug 8;4(1):15.

73. Newkirk HL, Rogan PK, Miralles M, Knoll JHM. Determination of genomic copy number with quantitative microsphere hybridization. Hum Mutat. 2006 Apr;27(4):376–86.

74. Dorman SN, Shirley BC, Knoll JHM, Rogan PK. Expanding probe repertoire and improving reproducibility in human genomic hybridization. Nucleic Acids Res. 2013 Apr;41(7):e81.

75. Emanuel BS, Shaikh TH. Segmental duplications: an “expanding” role in genomic instability and disease. Nat Rev Genet. 2001 Oct;2(10):791–800.

76. Altschul SF, Gish W, Miller W, Myers EW, Lipman DJ. Basic local alignment search tool. J Mol Biol. 1990 Oct 5;215(3):403–10.

77. Newkirk HL, Knoll JHM, Rogan PK. Distortion of quantitative genomic and expression hybridization by Cot-1 DNA: mitigation of this effect. Nucleic Acids Res. 2005 Jan 1;33(22):e191–e191.

78. Haaf T, Schmid M. Chromosome topology in mammalian interphase nuclei. Exp Cell Res. 1991 Feb;192(2):325–32.

79. Cremer M, Hase J von, Volm T, Brero A, Kreth G, Walter J, et al. Non-random radial higher-order chromatin arrangements in nuclei of diploid human cells. Chromosome Res. 2001 Oct 1;9(7):541–67.

80. Dekker J. Two ways to fold the genome during the cell cycle: insights obtained with chromosome conformation capture. Epigenetics Chromatin. 2014;7(1):25.

81. Dekker J, Rippe K, Dekker M, Kleckner N. Capturing Chromosome Conformation. Science. 2002 Feb 15;295(5558):1306–11.

82. Wit E de, Laat W de. A decade of 3C technologies: insights into nuclear organization. Genes Dev. 2012 Jan 1;26(1):11–24.

83. Dekker J. Two ways to fold the genome during the cell cycle: insights obtained with chromosome conformation capture. Epigenetics Chromatin. 2014 Nov 25;7(1):25.

84. Rao SSP, Huntley MH, Durand NC, Stamenova EK, Bochkov ID, Robinson JT, et al. A 3D Map of the Human Genome at Kilobase Resolution Reveals Principles of Chromatin Looping. Cell. 2014 Dec 18;159(7):1665–80.

85. Cremer T, Cremer M. Chromosome Territories. Cold Spring Harb Perspect Biol. 2010 Mar;2(3):a003889.

86. Ma Y, Kanakousaki K, Buttitta L. How the cell cycle impacts chromatin architecture and influences cell fate. Front Genet. 2015;6:19.

87. Simpson VJ, Johnson TE, Hammen RF. Caenorhabditis elegans DNA does not contain 5-methylcytosine at any time during development or aging. Nucleic Acids Res. 1986 Aug 26;14(16):6711–9.

88. Alabert C, Bukowski-Wills J-C, Lee S-B, Kustatscher G, Nakamura K, de Lima Alves F, et al. Nascent chromatin capture proteomics determines chromatin dynamics during DNA replication and identifies unknown fork components. Nat Cell Biol. 2014 Mar;16(3):281–93.

89. Hansen KH, Bracken AP, Pasini D, Dietrich N, Gehani SS, Monrad A, et al. A model for transmission of the H3K27me3 epigenetic mark. Nat Cell Biol. 2008 Nov;10(11):1291–300.

90. Kadauke S, Blobel GA. Mitotic bookmarking by transcription factors. Epigenetics Chromatin. 2013 Apr 2;6(1):6.

91. Wang F, Higgins JMG. Histone modifications and mitosis: countermarks, landmarks, and bookmarks. Trends Cell Biol. 2013 Jan 4;23(4):175–84.

92. Blobel GA, Kadauke S, Wang E, Lau AW, Zuber J, Chou MM, et al. A reconfigured pattern of MLL occupancy within mitotic chromatin promotes rapid transcriptional reactivation following mitotic exit. Mol Cell. 2009 Dec 25;36(6):970–83.

93. Belmont AS. Large-scale chromatin organization: the good, the surprising, and the still perplexing. Curr Opin Cell Biol. 2014 Feb;26:69–78.

94. Harrison CJ, Allen TD, Britch M, Harris R. High-resolution scanning electron microscopy of human metaphase chromosomes. J Cell Sci. 1982 Aug;56:409–22.

95. Sumner AT. Scanning electron microscopy of mammalian chromosomes from prophase to telophase. Chromosoma. 1991 Jul 1;100(6):410–8.

96. Lučić V, Rigort A, Baumeister W. Cryo-electron tomography: The challenge of doing structural biology in situ. J Cell Biol. 2013 Aug 5;202(3):407–19.

97. Kalle W, Strappe P. Atomic force microscopy on chromosomes, chromatin and DNA: A review. Micron. 2012 Dec;43(12):1224–31.

98. Ushiki T, Hoshi O, Iwai K, Kimura E, Shigeno M. The structure of human metaphase chromosomes: its histological perspective and new horizons by atomic force microscopy. Arch Histol Cytol. 2002 Dec;65(5):377–90.

99. Fukushi D, Shichiri M, Sugiyama S, Yoshino T, Hagiwara S, Ohtani T. Scanning Near-field Optical/Atomic Force Microscopy detection of fluorescence in situ hybridization signals beyond the optical limit. Exp Cell Res. 2003 Oct 1;289(2):237–44.

100. Lyubchenko YL. Nanoscale nucleosome dynamics assessed with time-lapse AFM. Biophys Rev. 2013 May 29;6(2):181–90.

101. Flors C, Earnshaw WC. Super-resolution fluorescence microscopy as a tool to study the nanoscale organization of chromosomes. Curr Opin Chem Biol. 2011 Dec;15(6):838–44.

102. Matsuda A, Shao L, Boulanger J, Kervrann C, Carlton PM, Kner P, et al. Condensed Mitotic Chromosome Structure at Nanometer Resolution Using PALM and EGFP-Histones. PLoS ONE. 2010 Sep 15;5(9):e12768.

103. Strukov YG, Sural TH, Kuroda MI, Sedat JW. Evidence of Activity-Specific, Radial Organization of Mitotic Chromosomes in Drosophila. PLoS Biol. 2011 Jan 11;9(1):e1000574.

Chapter 2

2 Relating Centromeric Topography in Fixed Human Chromosomes to α-Satellite DNA and CENP-B Distribution[1]

[1]This work has been published in the following article: Khan WA, Chisholm R, Tadayyon S, Subasinghe A, Norton P, Samarabandu J, Johnston LJ, Knoll JH, Rogan PK. Relating centromeric topography in fixed human chromosomes to α-satellite DNA and CENP-B distribution. Cytogenet Genome Res. 2013;139(4):234-242. doi: 10.1159/000348744. Permission to use this article in this thesis has been obtained from Karger Publishers, Rights and Permissions Division (see appendix).

2.1 Introduction

The chromatin organization during metaphase distinguishes individual chromosomes by size, centromeric position, and chromosomal banding patterns. Differences in interchromosomal DNA hybridizations between homologous metaphase chromosomes have been observed using single copy (SC) DNA fluorescence in situ hybridization (FISH) probes (1–3). This suggests that homologous chromosomal targets may exhibit differences in compaction detected by SC FISH. We and others (4) have also observed that FISH probes targeting non-centromeric regions do not always occupy the same lateral position on each chromatid. Epigenetic differences between homologous metaphase chromosomes may be investigated by correlating chromosome topography with variability in SC DNA hybridization targets. These differences have not been extensively studied previously; furthermore, our development of a high-resolution method with large DNA targets serves to determine the structural context of chromosomal DNA at specific regions.

In the present study, we investigate the topography of centromeric DNA sequences on metaphase chromosomes prepared with Carnoy's fixative. Although this procedure removes some proteins, the higher-order chromatin structures are largely preserved (5). The distributions of centromeric satellite DNA sequences and associated protein components have been mapped in 2 dimensions by immunofluorescence combined with FISH (immuno-FISH). Their physical distributions have been visualized on extended chromatin fibres, demonstrating distinct localization of CENP immunofluorescence and α-satellite monomers (6). Here, we present the 3-dimensional topography of fixed metaphase chromosomes and determine the context of pericentromeric DNA sequences by combining FISH with atomic force microscopy (AFM) of chromosome 17. Compatible AFM and FISH protocols were developed to simultaneously determine topography and investigate whether α-satellite DNA and a component protein marker co-localize on these structures. AFM generates topographic information at nanometer scale resolution (~ 30 nm), overcoming some limitations of optical microscopy (7,8). The method routinely prepares cytogenetic specimens without additional chromosomal pre-

treatments required for scanning (SEM) or transmission electron microscopy (9). Nevertheless, the distribution of α-satellite DNA could be visualized on metaphase chromosome topography at suboptical resolution.

α-Satellite is the most abundant family of repeats, comprised of 171-bp monomers (10). An important feature of this centromeric DNA family is the presence of a 17-bp repeating sequence identified within α-satellite DNA. This feature, termed the CENP-B-box sequence motif, binds to the CENP-B protein which is a highly conserved component of the centromere (11). CENP-B is distributed within heterochromatin and localizes beneath the kinetochore (12–14). The periodicity of the CENP-B motif within α-satellite DNA varies (13), suggesting that the distributions of interacting CENP-B protein and α-satellite DNA monomers may be inconsistent. However, this notion has not been tested directly on metaphase chromosomes. By correlating high resolution AFM with FISH and immuno-FISH, we investigated whether chromosome 17- specific α-satellite DNA (D17Z1) and CENP-B protein sequences have similar distribution patterns in homologous metaphase chromosomes relative to topographic features.

2.2 Materials & Methods

2.2.1 Chromosome Preparations

Human metaphase chromosomes, prepared from lymphocytes or lymphoblastoid cell lines, were used in this study. Cells were arrested in metaphase and fixed using conventional cytogenetic techniques (15).

2.2.2 Fluorescence *in situ* Hybridization

A DNA probe specific for the chromosome 17 centromeric region (D17Z1 α-satellite) was cloned and hybridized to relate the α-satellite distribution to chromosomal topography in this region. D17Z1 hybridization was confirmed with epifluorescence microscopy (Zeiss Metasystems) prior to AFM.

2.2.3 Immunofluorescence of Centromeric Protein CENP-B and D17Z1 FISH

This immuno-FISH protocol was developed to simultaneously detect the centromere specific protein CENP-B, α-satellite DNA and metaphase chromosome topography. CENP-B was detected on all autosomes using fresh cytogenetic preparations suspended in Carnoy's fixative (methanol:acetic acid 3: 1) for less than 1 week. CENP-A was also tested but could not be detected due to loss of this epitope, confirming a previous report (16). Chromosomal FISH using formamide denaturation (70% formamide/2x SSC for 2 min at 70°C) reduced CENP-B immunofluorescence, which was also consistent with earlier observations (17). Therefore, to maximize probe hybridization efficiency and CENP-B labelling, we denatured freshly fixed chromosomes with a heat-induced antigen retrieval (HIAR) process that avoided formamide. Details of HIAR are provided below (section 2.2.6) and also appear in the online Supplemental material of this paper (for all online Supplemental material, see www.karger.com/doi/10.1159/000348744). For immunofluorescence CENP-B detection without FISH, cells on microscope coverslips were denatured with HIAR buffer, immersed in blocking buffer, incubated with CENP-B antibody, detected with fluorescein-conjugated IgG secondary antibody, DAPI (4′ ,6-diamidino- 2-phenylindole) stained and mounted in McIlvaine buffer (0.1 M citric acid, 0.2 M disodium phosphate; pH 7.2). CENP-B was also localized on chromosomes 1 and 2 and imaged with AFM, as these two chromosomes can be readily identified in the absence of centromere specific FISH probes.

2.2.4 Correlated FISH and AFM Imaging

The high viscosity of the antifade solution (90–95% glycerol) used in FISH (18,19) was incompatible with AFM, and attempts to remove it by rinsing in PBS or McIlvaine buffer were unsuccessful due to residual glycerol that interfered with imaging. Therefore, all correlated imaging was performed in the absence of glycerol-based antifade solution. Instead, coverslips taken through the FISH procedure were mounted in McIlvaine buffer, prior to transport to the AFM facility. Correlated FISH and AFM images were captured either on a JPK Nanowizard II BioAFM integrated with an Olympus IX81 inverted

optical microscope or a BioScope Catalyst integrated with a Zeiss LSM 510 inverted confocal microscope. Metaphase cells with well spread chromosomes were located by raster scanning the coverslip, while simultaneously monitoring the DAPI image. AFM imaging was performed in tapping mode and topography and fluorescent images were correlated using either the GNU Image Manipulation Program (GIMP; http://www.gimp.org/) or with the Veeco Microscope Image Registration and Overlay software. The DAPI and Cy3 images were scaled to ensure registration with the AFM scanned image.

Probe binding patterns were visualized by superimposing cross-sections of hybridized D17Z1 with chromosome 17 topography. Although we recognize that the centromere comprises a larger block of constitutive heterochromatin, measurements are taken at the narrowest cross-section, hereafter referred to as the primary constriction. Cross-sections were drawn across the primary constriction, as assessed from the boundaries of the chromosome 17 AFM profile. This profile often coincided with the most prominent features (ridges) of each chromatid at the centromere. Lateral peak-to-peak distances along the x-axis (i.e. difference between peak 1 and peak 2 in nm) and interpeak heights along the z-axis were calculated (in nm) from the AFM topography. Lateral differences in chromosome topography at the primary constriction were obtained by subtracting axial groove from peak ridge heights. Following AFM, D17Z1 Cy3-fluorescence cross-sections were determined at the same coordinates after image registration.

2.2.5 Quantitative Analysis of Correlated Images

To compute the ratio of D17Z1 fluorescence intensities between homologs, we implemented a gradient vector flow (GVF) algorithm (20) to simultaneously determine background intensity and the FISH signal boundaries. This was performed on images captured on different microscope systems at independent AFM imaging facilities. Solving the GVF snake model iteratively, based on the initial binary contour, provided a smooth and connected object boundary for the FISH probe signal. Following GVF image processing (Supplemental Figure 2-6), the absolute area (in pixels) occupied by the

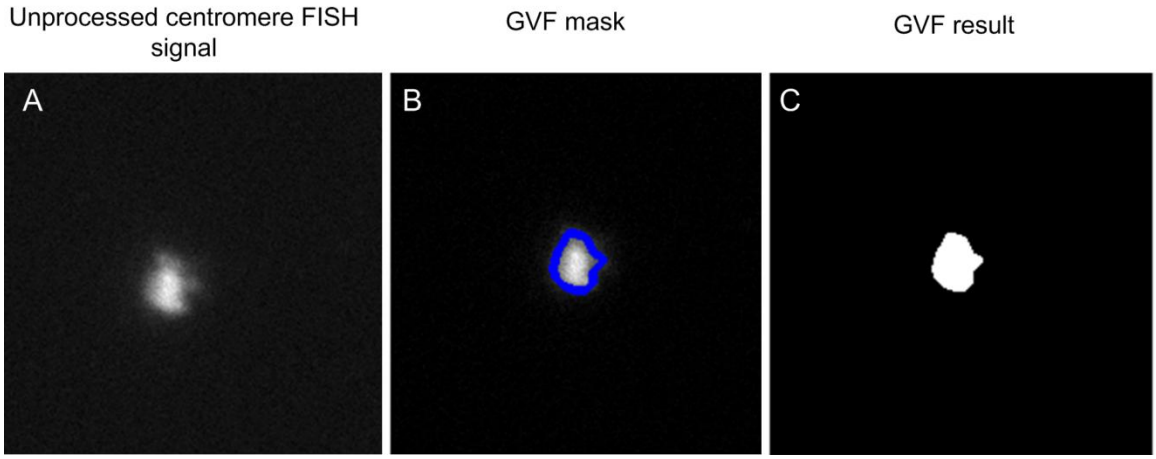

Supplemental Figure 2-6. Example of a GVF mask using a D17Z1 FISH signal.

The boundary of the unprocessed DNA probe signal (A) was determined using GVF (B). The final result (C) produced the values for integrated and average intensities needed to calculate intensity ratios among chromosome 17 homologs (see Table 2-2). Above images were processed in MATLAB graphical user interface. The GVF process from one homolog is shown. However, for chromosome homolog pairs in this metaphase, integrated intensity and fluorescence area ratios were 1.85 and 1.03, respectively.

region hybridized with chromosome 17 α-satellite probe was computed, given the integrated and average intensity values. Integrated intensity values were also used to determine FISH signal heterogeneity between homologs in the same cells in which centromere topography had been measured.

2.2.6 Supplemental Methods

Chromosomal preparations were stored in Carnoy's fixative (3:1 methanol:acetic acid) until they were used for FISH and/or immunofluorescence studies with CENP-B. Cells were deposited onto pre-cleaned glass coverslips (22 mm square, No. 1 ½ thickness for FISH and 25 mm circular, No. 1 thickness for immuno-FISH [VWR]) and dried under ambient temperature and humidity. For FISH, cells on coverslips were aged overnight at room temperature (RT). For immuno-FISH, cells were aged for 15 min at 40°C on a slide-warmer prior to chromosomal denaturation. D17Z1 (CEN-17) is a 2.7-kb sequence probe that we cloned into a modified ZeroBlunt vector. It consists of 16 alphoid monomers (21) targeting the pericentromeric region of chromosome 17. D17Z1 was indirectly labeled with digoxigenin-11-dUTP (Roche Applied Sciences) by nick translation, denatured and hybridized to denatured chromosome preparations (70% formamide in 2× sodium chloride/sodium citrate buffer [SSC], pH 7.0) as previously described (19). Subsequently, 3 post hybridization washes were performed (30 min each in 50% formamide/2× SSC at 37°C; 2× SSC at 37°C; 1× SSC at room temperature [RT]), and the hybridized probe was detected with Cy3-conjugated IgG fraction monoclonal mouse anti-digoxin antibody (Jackson ImmunoResearch Laboratories, Inc; diluted 1:200 [1.7 mg/ml] in 4× SSC with 1% bovine serum albumin at 37°C for 1 hour in the dark). Coverslips were rinsed 3 times for 15 min each in 1× SSC at RT, counterstained with DAPI (0.1 μg/ml) (19), and mounted in McIlvaine buffer (0.1 M citric acid, 0.2 M disodium phosphate, pH 7.0).

Fresh chromosome preparations for immunofluorescence with CENP-B or immuno-FISH were obtained from a human lymphoblastoid cell line cultured in RPMI-1640 medium supplemented with 10% fetal bovine serum at 37°C with 5% CO_2. Actively dividing cells were arrested in metaphase and fixed using routine cytogenetic methods (15). Fixed cell

preparations on round coverslips were denatured (97°C for 10 min) on the same day in a HIAR buffer solution (10 mM Tris pH 7.2, 1 mM EDTA, 0.05% Tween-20) (22), rinsed in cold 100% ethanol (1 min), and hybridized with the D17Z1 DNA probe (37°C, 16 h). Following hybridization, the coverslips were washed according to our post-hybridization procedure (see above). Subsequently, the coverslips were immersed in blocking buffer (1× PBS with 3% BSA and 0.25% Triton-X at RT, 20 min), incubated with CENP-B primary antibody (1/100 [0.5 mg/ml, Abcam®] in 1× PBS at 4°C for 16–18 h), and washed 3 times in 1× PBS (5 min each at RT). The hybridized DNA probe and CENP-B protein were then detected in series. D17Z1 was detected with Cy3 conjugated digoxin antibody (60 min incubation at RT in darkness), followed by 3 washes (1× SSC, 1× SSC with 0.1% Triton-X 100 and 1× SSC; 15 min each at RT). The CENP-B antibody was subsequently detected with a Dylight-488-conjugated IgG secondary antibody (1/50 [0.5 mg/ml, Abcam®] in 1× PBS) for 60 min at 37°C, followed by 3 washes (1× PBS for 5 min each at RT). The cytogenetic preparations were stained with DAPI (0.1 µg/ml, 20 min), and rinsed in McIlvaine buffer (pH 7.0) supplemented with 9 mM p-phenylenediamine. Detection of CENP-B and D17Z1 on metaphase cells was confirmed by epifluorescence microscopy (Zeiss Metasystems) prior to AFM imaging. For AFM, chromosomes on a 25 mm circular coverslip were secured in an O-ring with a disc shaped cross-section and imaged in supplemented McIlvaine buffer. The specific time and reagent parameters for hybridization, detection and imaging of CENP-B alone were the same as those for simultaneous CENP-B and D17Z1 visualization.

AFMs were equipped with a high resolution CCD camera (CoolSNAP, Photometrics, Olympus; AxioCam HRm, Zeiss). Epifluorescent images of chromosomes 17 were collected for DAPI and D17Z1 signals, using a 100× (Olympus, NA = 1.42, Oil), or a 63× objective (Zeiss, NA = 1.4, Oil) with DAPI-5060B and Cy3-4040B filter sets (Semrock, Inc). The optical resolution was estimated by imaging 20-nm diameter dye-labeled polymer beads using the Cy3 filter set, giving values of 286 ± 36 nm and 320 ± 30 nm (full width at half maximum intensity, n = 10 beads) for the Olympus and Zeiss microscopes, respectively. MikroMasch Ultrasharp (NSC15/AIBS) or Nanosensors (NCH-W) cantilevers, operated at resonant frequencies with a scan rate of 1 Hz, were

used for tapping mode AFM. Independent overlays of chromosome topography and fluorescent images verified that image correlation was not dependent upon differences in software or procedures between the two laboratories. The X,Y offset and rotation angle of the AFM topography image were adjusted to track the overlay of topography of chromosomes to fluorescent signal obtained from the inverted DAPI image. The Cy3 fluorescence signal transparency was adjusted for visualization of D17Z1 probe localization and distribution with respect to the chromosome 17 centromere topography. The image overlay procedure was checked using samples of dye labeled polymer spheres (20 nm and 200 nm diameter).This procedure resulted in shifts of <1 pixel (1 pixel = 64.5 nm) between the maxima for AFM topography and fluorescence intensity for individual features. Registration of region hybridized with D17Z1 probe to centromere topography was performed using Image J processing software and the resulting data plotted.

In order to yield a consistent method for determining background noise and quantifying FISH probe signals, a gradient vector flow (GVF) active contour approach was used. Given the edge map *(edge(I))*, such that, $edge(I) = E_{external}(x, y)$, we can define a static vector field, $v(x, y) = [u(x, y), v(x, y)]$, which minimizes the energy function:

$$\varepsilon = \iint_{x,y} \mu(u_x^2 + u_y^2 + v_x^2 + v_y^2) + |\nabla edge|^2 |v - \nabla edge|^2 \, dxdy$$

where $\nabla edge$ is the gradient of the edge map and u_x is the partial derivative of component u (x, y) with respect to x ($u_x = \partial u(x,y) / \partial x$). An extracted window from the main image was first subjected to global thresholding based on Otsu's method (23).We empirically set a scaling factor of 1.5 times higher than the normal Otsu calculation to obtain consistent segmentation, while limiting the effects from intensity fading around the probe signal. A gray scale image of D17Z1 fluorescence contained a diffuse signal targeting a centromere 17 homolog while the majority of the image consisted of dark (low intensity) pixels. However, there were also slightly higher levels of intensities throughout parts of the gray-scale image (Supplemental Figure 2-6A). As a prerequisite for reducing background intensities, a histogram based approach was taken to effectively

select the peak of the intensities of the background prior to running the GVF analysis. The background pixel intensities were textured throughout these images. A different background intensity value was assigned for each digital image, while limiting its maximum range to the intensity value of 20. The 20 value limit was based on heuristics and was empirically set. The window of the histogram that fell within the range of background intensities [0, 20] was extracted and its peak value used as the background intensity level for a given metaphase and the process repeated for the next image in our data set.

2.3 Results

2.3.1 AFM Topography Resolves Structural Features at Centromeres

At the nanoscale resolution of correlated AFM, details of the metaphase chromosome and in particular the centromeric structure are evident which cannot be appreciated by epifluorescence microscopy alone (Figure 2-7). At higher resolution, and as indicated by the cross-sections (Figure 2-7D-G), the surface of individual chromatids exhibited a granular structure (Figure 2-7G; Supplemental Figure 2-8) consisting of raised topographic features. These features have been classified previously as ridges and grooves along the length of human chromosomes, consisting of ~50-nm-thick strongly twisted chromatin fibres (24,25). Distinctions between ridges at the centromere in the current study were based on their relationships to adjacent ridge features and computing a background threshold from the surrounding granular structure on the chromatids covering the rest of the chromosome surface. Prominent ridge features (~50-150 nm in height) extending across the lateral axis of the primary constriction were significantly higher (cross-section of chromosome 17 in Figure 2-7E, ~10-15 nm above background) than non-centromeric chromatin (Figure 2-7D-E), and were consistently observed in all metaphase cells. Similar to denatured chromosomes, ridge structures within the chromosome arms were also observed in an undenatured control chromosome (Supplemental Figure 2-9). Chromosome height was reduced by ~30 nm in denatured air-dried metaphase chromosomes, without any loss of ridge morphology (Supplemental Figure 2-9).

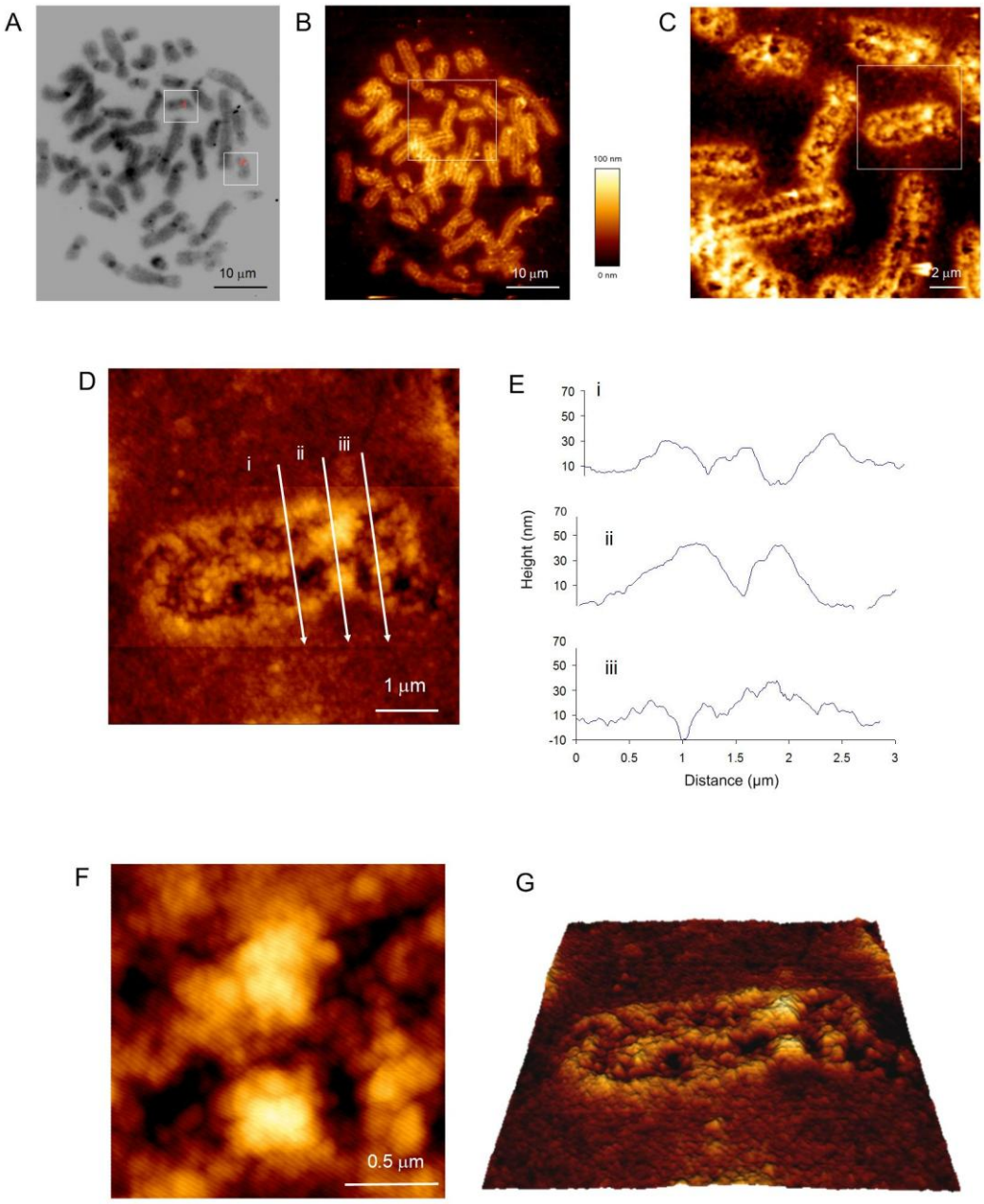
A
10 μm
B
10 μm
100 nm
0 nm
C
2 μm
D
i
ii
iii
1 μm
E
i
ii
iii
70
50
30
10
-10
Height (nm)
0
0.5
1
1.5
2
2.5
3
Distance (μm)
F
0.5 μm
G

Figure 2-7. FISH and AFM images of human metaphase chromosomes.

(A) Cell hybridized with an α-satellite DNA probe (D17Z1, red), stained with DAPI, viewed with epifluorescence and imaged in inverted grey scale. Hybridized chromosomes 17 are framed. (B) Topographic AFM image of the same cell with the height color scale. (C) Increased resolution of the framed region in B shows the ridge structure on individual chromosomes. (D) Higher-resolution AFM image of one chromosome 17 framed in (C), and (E) cross-sectional chromosomal height tracings at the centromere (ii) and in adjacent arms (i, iii) demonstrating centromeric peaks. Line traces across the lateral axis of the primary constriction of chromosome 17 topography measured the ridge peak to be μ= 60 nm at its highest point (n = 11 metaphase cells, ranging from ∼50-150 nm). The centromeric ridge peak was nearly 2 fold higher and did not overlap ridged regions in chromosome arm, which are ~30 nm in height. Line trace data were obtained for denatured chromosomes using measurements from 2 independent atomic force microscopes. (F) A high-resolution AFM image of the centromere region. (G) 3D image for the same chromosome as shown in D. All topographic height information should be interpreted in context of denatured chromosomes (see Results) and is displayed as color gradations in heat map.

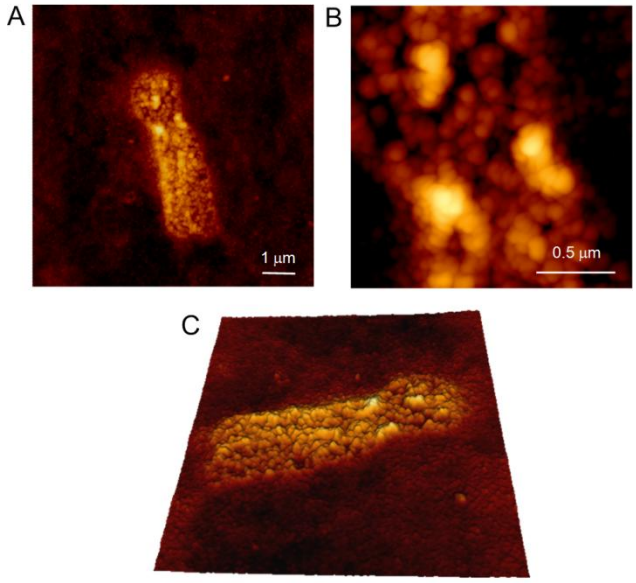

Supplemental Figure 2-8. Reproducibility of high-resolution AFM imaging of chromosomes 17.

The chromosome in these panels was imaged from a sample processed independently of that shown in Figure 2-7. Similar chromosomal features are observed (A, B higher magnification of centromeric region). Two intense features at lateral edges of the centromere constriction constitute the specific centromere ridge structures (B). A 3D image for the chromosome is shown in panel C.

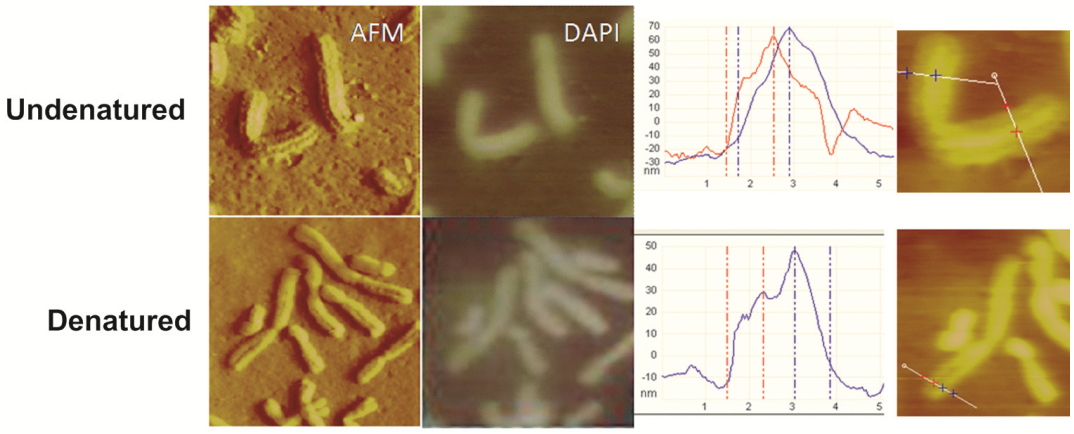

Supplemental Figure 2-9. Effects of FISH treatment on metaphase chromosomes imaged simultaneously by AFM and fluorescence microscopy.

Top panels show images of undenatured chromosomes without FISH; lower panels have been exposed to conditions which denature chromosomes. Left to right: Deflective AFM images, epifluorescence showing DAPI staining, cross-sectional height (Y) × width (X), location of slice and positions of measurements for chromosome 3.

Linear cross-sections of height along the width in the centromeric region of high-resolution AFM images revealed different ridge patterns (Figure 2-10). In most chromosomes (14 of 22), the centromere ridge showed a bimodal pattern consisting of 2 distinct maxima coincident with the sister chromatids (Figure 2-10B, N and/or D, P). The remaining chromosomes displayed a single broad, continuous ridge (8 of 22 chromosomes, Figure 2-10A, M and/or C, O) extending across the region hybridized to D17Z1. Comparing the centromere regions of homologous chromosomes 17, half of the cells (n = 8) showed the same ridge structure for both homologs, and the remaining cells showed differences in topography between homologs. The average ridge width at the primary constriction for all chromosomes, 740 nm (ranging from 720-770), was similar to the width of chromosomes with bimodal patterns (730 nm).

2.3.2 Correlation of Centromere 17 Topography with α-Satellite DNA Hybridization Patterns

α-Satellite DNA displayed 4 different distributions along the lateral axis of the chromosome 17 centromere in the context of the prominent topographic features (Figure 2-10). The observed patterns were interpeak (Figure 2-10E, M, Q), skewed (Figure 2-10F, N, R), diffuse (Figure 2-10G, O, S), and doublet (Figure 2-10H, P, T). DNA distribution patterns could be assigned in different chromosomes, based on cross-sectional analysis at the primary constriction. The interpeak α-satellite DNA distribution showed a fluorescence profile that was concentrated within the centre of the metaphase centromere (Figure 2-10E, M). The diffuse pattern was characterized by a broad elliptical shape (Figure 2-10G, O), consistent with redistribution of the DNA towards the lateral edges of the centromere. Two distinct α-satellite doublets centered on individual chromatids are shown in Figure 2-H, L and P. A skewed-doublet pattern (Figure 2-10F, J, N) was evident when the α-satellite DNA was localized on a single sister chromatid. When patterns between homologous chromosomes within a cell were compared, α-satellite DNA was organized according to 1 of 8 different combinations (Table 2-1), with homologs in most cells (70%) adopting distinct distributions relative to organization of ridge structure at the primary constriction.

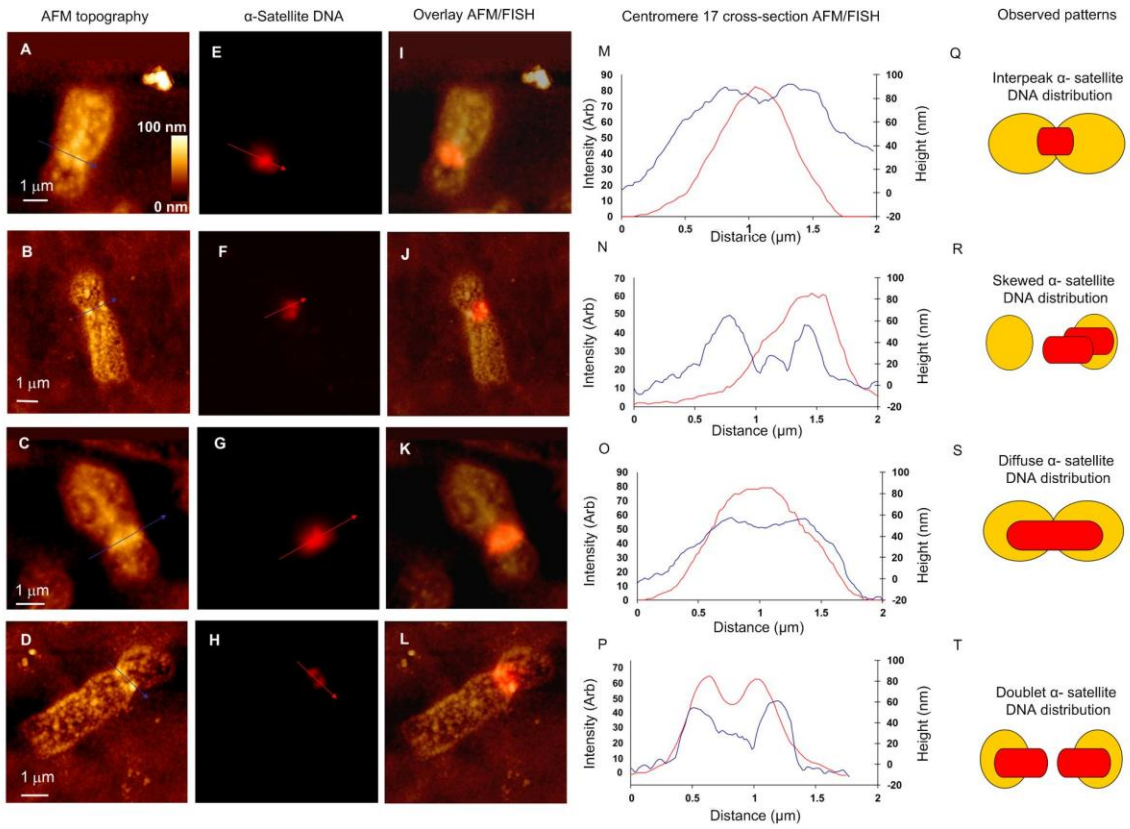

Figure 2-10. α-Satellite DNA distribution observed by AFM.

(A-D) Topographic images of chromosomes 17 from different cells. (E-H) Corresponding D17Z1 FISH probe hybridizations. (I-L) Overlays of topography and FISH images. (M-P) Line cross-section analysis through centromere topography (blue lines) and D17Z1 hybridization probe (red lines). (Q-T) Schematics of the 4 α-satellite DNA D17Z1 FISH probe hybridization patterns (red bars) relative to centromere ridge structures (yellow circles). The observed patterns include interpeak, skewed, diffuse and doublet α-satellite DNA distribution.

Table 2-1. D17Z1 fluorescence patterns on chromosome 17 homologs relative to centromere topography.

α-Satellite fluorescence profile for homologous chromosomes 17[a]	No. of metaphases	No. of individual chromosomes	
Doublet/skewed	3	diffuse = 14	predominant pattern
Diffuse/diffuse	2		
Interpeak/skewed	1	interpeak = 14	
Interpeak/diffuse	7		
Interpeak/interpeak	3	doublet = 6	
Diffuse/skewed	2		
Diffuse/doublet	1	skewed = 6	minor pattern
Doublet/doublet	1		

Diffuse and interpeak DNA fluorescence patterns are predominant relative to cetromere topography. [a] Individual homologs are separated by a slash (/).

Comparison of AFM topography and fluorescence cross-sections indicated that interpeak and diffuse patterns of D17Z1 DNA were equiprobable for chromosomes with either bimodal or continuous ridge structures. Doublet D17Z1 fluorescence signal patterns were only observed for chromosomes with a bimodal ridge, indicating co-localization of α-satellite DNA with the lateral edge of the centromere. The skewed α-satellite DNA distribution pattern predominantly co-localized with one of the bimodal peaks or a part of the continuous centromere ridge structure.

2.3.3 Quantification of D17Z1 Chromosome Targets

The ratios of D17Z1 integrated intensities between homologs on fixed metaphase chromosomes from 4 different individuals varied, on average, by 1.4-fold (Table 2-2). Factors contributing to differences in these integrated intensities following FISH could include variation in: (a) hybridization target length resulting from polymorphisms of 171-bp α-satellite D17Z1 arrays among different individuals (26–28), and/or (b) structural preservation of chromosomal regions due to the degree of DNA compaction (29), affecting probe accessibility. Generally, chromosomes with a diffuse DNA distribution and a larger area of fluorescence (μm^2) did not correlate with the inter-ridge width along the centromere cross-section. All chromosomes with the wider centromere topography taken across the primary constriction, relative to their homologs, are asterisked (Table 2-2, *).

2.3.4 Centromere 17 α-Satellite DNA Distribution Relative to Immunolocalization of CENP-B

Dual-color detection of D17Z1 DNA and CENP-B revealed that in about half of the cells (8 of 15), CENP-B and D17Z1 are distributed differently on one or both homologous chromosomes (Figure 2-11: compare panels B vs. C and D vs. E). In the remaining cells, CENP-B and D17Z1 were coincident on individual chromosomes 17, but the co-localization patterns were not consistent on different homologs. The highest structures seen by AFM at the primary constriction corresponded to the maximum CENP-B fluorescence (Figure 2-11F). It is also notable that CENP-B localized to the bimodal and

Table 2-2. Quantification of fluorescence intensity and area occupied by D17Z1 FISH probe.

Integrated intensities of homologs A/B[a]	Intensity ratio[b]	Fluorescence area (μm^2) homologs A/B[c]	Area ratios	D17Z1 FISH patterns on centromere topography of homologs
Set 1[d]				
69,770/37,535	1.85	1.046/1.011*	1.03	skewed/interpeak
31,778/26,844	1.18	2.063*/2.279	0.91	doublet/skewed
74,809/64,192	1.16	0.985/0.955*	1.03	diffuse/interpeak
59,452/39,530	1.50	0.989*/1.005	0.98	interpeak /interpeak
75,665/37,159	2.03	0.987*/1.018	0.97	doublet /doublet
77,229/42,800	1.80	1.018*/0.944	1.08	doublet/skewed
Set 2[d]				
86,572/49,994	1.73	0.577*/0.520	1.11	diffuse /diffuse
272,281/78,749	3.45	0.383*/0.224	1.71	diffuse/interpeak
232,951/59,203	2.72	0.360*/0.355	1.01	diffuse/interpeak
86,996/59,203	1.47	0.514/0.686*	0.74	diffuse/doublet
11,382/6,208	1.83	2.400*/1.900	1.26	diffuse/interpeak

[a] Integrated intensities for D17Z1 were measured on each homolog using their gradient vector flow (GVF) boundaries. Homologs were denoted as 'A' and 'B'. The homolog with greatest probe fluorescence intensity was assigned as 'A' and served as the numerator for calculating intensity ratios.

[b] Signal intensity ratios between homologs from 4 different individuals varied 1.4-fold on average (set 1: $\mu = 1.59 \pm 0.37$; set 2: $\mu = 2.24 \pm 0.82$).

[c] Probe fluorescence area was calculated by dividing the integrated intensity value by the average intensity value and then converting to μm^2 by multiplying with the pixel size. The area occupied by probe fluorescence (set 1: $\mu = 1.00 \pm 0.06$; set 2: $\mu = 1.17 \pm 0.36$) demonstrated that a higher integrated intensity value, in a subset of metaphase cells, did not correlate with a larger florescence area. * = Homolog with wider centromere topography measured by AFM.

[d] Set 1 and set 2 represent analyses of data collected on different AFM microscopes and demonstrate reproducibility.

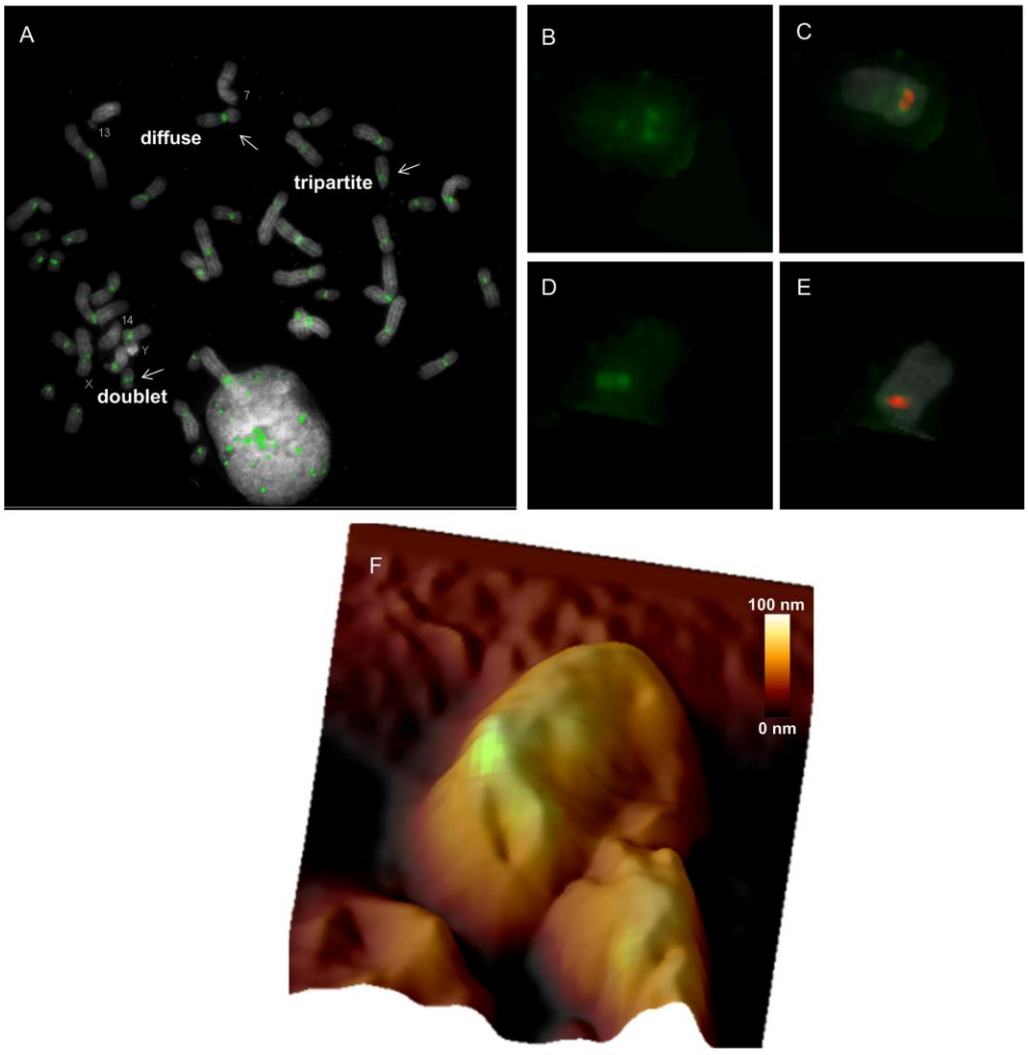
A
B
C
D
E
F
diffuse
tripartite
doublet
7
13
14
Y
X
100 nm
0 nm

Figure 2-11. CENP-B appearance on metaphase chromosomes and localization relative to D17Z1.

(A) Doublet, diffuse and tripartite CENP-B detection in a representative metaphase cell with immunofluorescence staining. (B-E) Chromosome 17 homologs from another cell. Simultaneous immuno-FISH with CENP-B (green) and D17Z1 (red) demonstrated similar fluorescent signal patterns in one homolog (B, C with doublets for both CENP-B and D17Z1), and dissimilar patterns in the other homolog (D, E with doublet for CENP-B and a singlet pattern for D17Z1 located centrally between CENP-B). (F) 3D view of a chromosome 17 with CENP-B (green) peak intensities in the same region as the centromeric ridge. Images were captured using an epifluorescence microscope equipped with single-band pass filter for green (B, D) and a triple-band pass filter for red, green and blue (A, C, E). All correlated AFM with immuno-FISH samples were imaged wet in McIlvaine buffer to slow rapid quenching of the Dylight-488 secondary antibody.

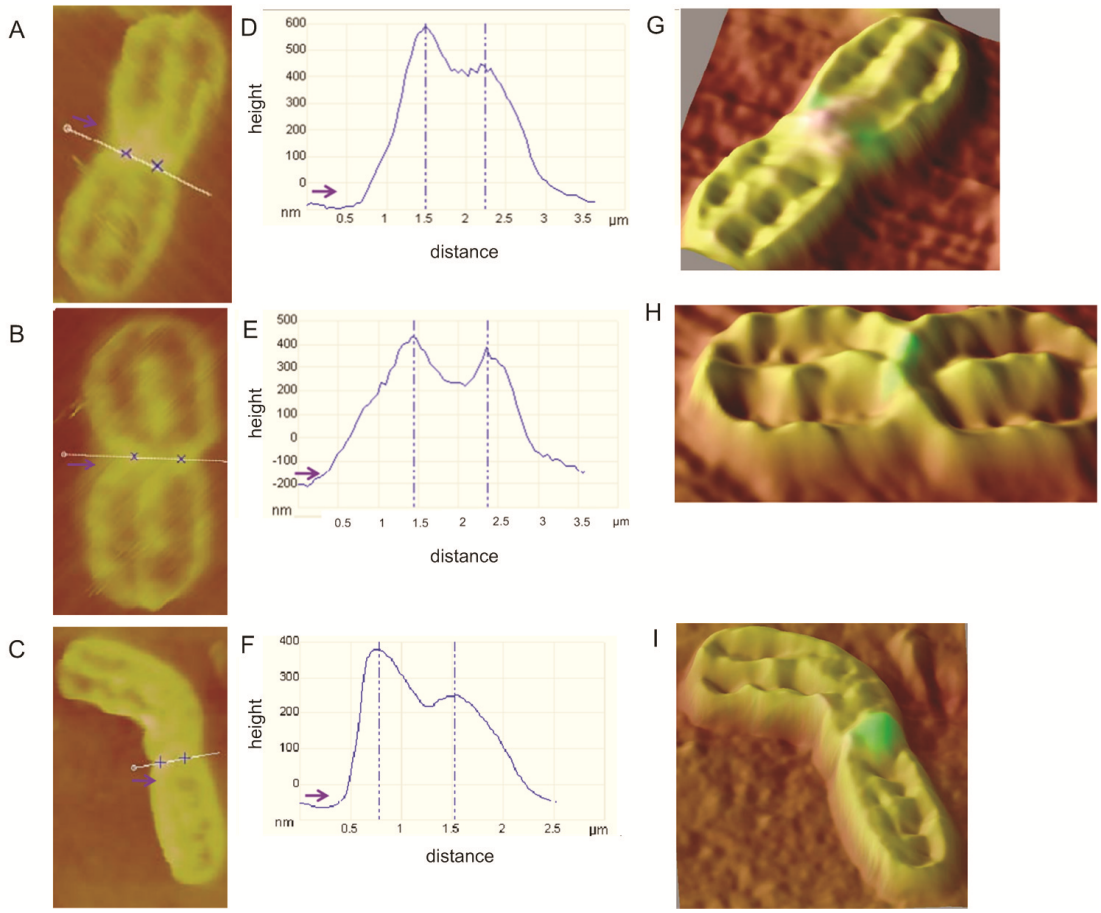

Supplemental Figure 2-12. CENP-B co-localization with ridge peaks on chromosomes 1 and 2.

AFM of human chromosomes 1 (A, B) and 2 (C) with bound CENP-B (green) localized to the centromere ridge (G, H, I). Topography profiles (D, E, F) at the centromeres show a bimodal ridge distribution as observed for chromosome 17. Arrows (A-F) indicate direction of the centromere topography line trace and crosses (A, B, C) represent centromere ridge height maxima.

continuous ridges at the primary constriction on chromosomes 1 and 2 (Supplemental Figure 2-12).

2.4 Discussion

The configurations of α-satellite DNA and CENP-B during metaphase are variable, but nevertheless co-localize with prominent structures apparent in centromeric regions. A novel method was used to correlate imaging of these markers with topographical information, which demonstrated bimodal or continuous ridges at the primary constriction of metaphase centromeres (Figure 2-10). In a subset of chromosomes (5 of 22) imaged by correlated AFM and FISH, we observed a small interstitial feature between the major bimodal structures (Figure 2-10N). Previously, this has been noted in early metaphase chromosomes (30) and could represent the remnants of a transitional intermediate in the formation of a bimodal ridge. α-Satellite DNA did not always co-localize with CENP-B or with prominent ridge structures present in this region of the metaphase chromosomes. Other centromeric proteins present in the centromere are not likely localized solely by DNA sequence recognition (31–35). Since CENP-B is a stably associated centromere marker (11,12,36), it is conceivable that partitioning of this protein could occur prior to α-satellite DNA reorganization during mitosis.

Previously, in stretched metaphase chromatin, large α-satellite DNA arrays were not always coincident with CENP-B (6). This is consistent with our suggestion that α-satellite DNA and CENP-B distributions can be discordant (Figure 2-10D, E). The skewed FISH probe signals we observed could either be related to differences in condensation of individual chromatids affecting DNA probe accessibility, random rotation of the chromatids during condensation, or isolation of metaphase chromosomes, resulting in superimposition of sister chromatids (4).

On metaphase chromosomes, ridge and groove structures along the length of chromosome arms have been previously described (8). These fibrillar structures have been observed on chromosomes treated with trypsin/protease K (7,30,37) or imaged in the native state by AFM (25,38). Enzymatic or heat-based denaturation affects

chromosome structure (39). For example, after trypsinization, the height of chromosome 2 was reduced by 260 nm (37). We also see a reduction in chromosome height to a lesser degree by heat denaturation (Supplemental Figure 2-9). The highest chromosome features were observed (400-800 nm) by AFM on native chromosome preparations (8,38). Our focus was to investigate the topography on chromosomes routinely prepared for molecular cytogenetic analysis, and heat or enzymatic treatment is unavoidable. Preservation of chromosome structure by formaldehyde crosslinking prior to denaturation was not an option because such crosslinking creates DNA adducts, compromising the efficiency of metaphase FISH (39).

The presence of ridge and groove structures in the centromeric region is less well understood. Centromeric ridges may be formed at highly compacted chromatin fibres and appear as 50 nm thick, globular structures (8), which is consistent with our own observations of denatured chromosomes. Such prominent rounded projections at the centromere (40) and the pericentromeric region of C-banded chromosomes have been observed by SEM (40,41) and AFM (42). Interestingly, compaction in the pericentromeric region was affected to a lesser degree than along the chromosome arms (40). However, prominent ridges and grooves that constitute the chromatin fibre along the chromosome or at the primary constriction have not been previously reported by SEM (37).

The integration of high-resolution, topographic analysis of centromeric chromatin on fixed metaphase chromosomes will contribute to our understanding of the organization of these components prior to sister chromatid separation. This would also require studies addressing the dynamic relationship between centromeric DNA segregation and the surrounding chromatin structure in vivo. Our study indicates the relationship between centromeric topography, centromeric DNA, and CENP-B distributions, albeit limited by the number of metaphase cells that could be imaged. This was primarily due to the slow scan speed of conventional tapping mode AFM, affecting our ability to obtain a large number of chromosome images (3-4 h of scan time per homolog). Correlated AFM/immuno-FISH adversely affected retention of CENP-B fluorescence, which also

limited the number of images obtained. To circumvent this, we processed all immuno-FISH coverslips in buffer which only resulted in a minor loss of detail in chromatin topography. Nevertheless, raised topographic features were still apparent in the centromeric region. These findings are consistent with a previous report of human chromosomes imaged in fluid (43). To further minimize imaging artefacts, the silicon-nitride tip for AFM was replaced with each new scan during correlative scanning of metaphase chromosome topography.

The approach we have taken for studying the structure of highly condensed metaphase chromosomes is one of many applications of AFM. AFM also has broad usage in the field of nanobiosciences that merge biology-, chemistry- and physics-based applications (44). Generally AFM does not require special treatments of the specimen prior to imaging as often required for other specialized microscopy techniques. To this end, we did not change any crucial steps that are common to molecular cytogenetic studies of metaphase chromosomes. Additionally, we were able to image fixed chromosome samples in liquid or air-dried state without requiring any vacuum or desiccation. Therefore, AFM is a powerful technique that can provide 3-dimensional information and surface profile of a given specimen. By adding to it a fluorescence imaging component, specific cellular components can be localized accurately at nanoscale resolution.

To summarize, we have introduced an approach that allows for the simultaneous visualization of a centromeric protein along with α-satellite DNA directly on chromosome topography. It should be feasible to extend our approach to additional genomic regions, where precise DNA sequences can be localized onto chromosome topography for mapping differences in chromatin nanostructures on homologous loci.

2.5 References

1. Rogan PK, Cazcarro PM, Knoll JHM. Sequence-Based Design of Single-Copy Genomic DNA Probes for Fluorescence In Situ Hybridization. Genome Res. 2001 Jun;11(6):1086–94.

2. Knoll JHM, Rogan PK. Sequence-based, in situ detection of chromosomal abnormalities at high resolution. Am J Med Genet A. 2003 Sep 1;121A(3):245–57.

3. Khan WA, Knoll JH, Rogan PK. Context-based FISH localization of genomic rearrangements within chromosome 15q11.2q13 duplicons. Mol Cytogenet. 2011 Aug 8;4(1):15.

4. Strukov YG, Belmont AS. Mitotic chromosome structure: reproducibility of folding and symmetry between sister chromatids. Biophys J. 2009 Feb 18;96(4):1617–28.

5. Hepperger C, Otten S, von Hase J, Dietzel S. Preservation of large-scale chromatin structure in FISH experiments. Chromosoma. 2007 Apr;116(2):117–33.

6. Haaf T, Ward DC. Structural analysis of alpha-satellite DNA and centromere proteins using extended chromatin and chromosomes. Hum Mol Genet. 1994 May;3(5):697–709.

7. Thalhammer S, Gobbi P, Falconi M, Mazzotti G, Heckl WM. High-resolution analysis of the 3D organization of human metaphase chromosomes. Methods Mol Biol Clifton NJ. 2004;242:245–54.

8. Ushiki T, Hoshi O. Atomic force microscopy for imaging human metaphase chromosomes. Chromosome. 2008;16(3):383–96.

9. Liu X, Sugiyama S, Xu Q, Kobori T, Hagiwara S, Ohtani T. Atomic force microscopy study of chromosome surface structure changed by protein extraction. Ultramicroscopy. 2003 Apr;94(3-4):217–23.

10. Schueler MG, Sullivan BA. Structural and functional dynamics of human centromeric chromatin. Annu Rev Genomics Hum Genet. 2006;7:301–13.

11. Muro Y, Masumoto H, Yoda K, Nozaki N, Ohashi M, Okazaki T. Centromere protein B assembles human centromeric alpha-satellite DNA at the 17-bp sequence, CENP-B box. J Cell Biol. 1992 Feb;116(3):585–96.

12. Cooke CA, Bernat RL, Earnshaw WC. CENP-B: a major human centromere protein located beneath the kinetochore. J Cell Biol. 1990 May;110(5):1475–88.

13. Pluta AF, Saitoh N, Goldberg I, Earnshaw WC. Identification of a subdomain of CENP-B that is necessary and sufficient for localization to the human centromere. J Cell Biol. 1992 Mar;116(5):1081–93.

14. Yoda K, Kitagawa K, Masumoto H, Muro Y, Okazaki T. A human centromere protein, CENP-B, has a DNA binding domain containing four potential alpha helices at the NH2 terminus, which is separable from dimerizing activity. J Cell Biol. 1992 Dec;119(6):1413–27.

15. Bangs CD, Donlon TA. Metaphase chromosome preparation from cultured peripheral blood cells; in Haines JL, Korf BR, Morton CC (eds): Curr Protoc Hum Genet, pp 4.1.1-4.1.19 (John Wiley & Sons Inc., Malden 2005).

16. Jeppesen P. Immunofluorescence techniques applied to mitotic chromosome preparations. Methods Mol Biol Clifton NJ. 1994;29:253–85.

17. Masumoto H, Sugimoto K, Okazaki T. Alphoid satellite DNA is tightly associated with centromere antigens in human chromosomes throughout the cell cycle. Exp Cell Res. 1989 Mar;181(1):181–96.

18. Platt JL, Michael AF. Retardation of fading and enhancement of intensity of immunofluorescence by p-phenylenediamine. J Histochem Cytochem Off J Histochem Soc. 1983 Jun;31(6):840–2.

19. Knoll JHM, Lichter P. In Situ Hybridization to Metaphase Chromosomes and Interphase Nuclei; in Haines JL, Korf BR, Morton CC, Seidman CE, Seidman JG, Smith DR (eds): Current Protocols in Human Genetics, pp 4.3.1-4.3.31 (John Wiley & Sons Inc., Malden 2005).

20. Arachchige AS, Samarabandu J, Knoll J, Khan W, Rogan P. An image processing algorithm for accurate extraction of the centerline from human metaphase chromosomes. 2010 17th IEEE International Conference on Image Processing (ICIP). 2010. p. 3613–6.

21. Waye JS, Willard HF. Structure, organization, and sequence of alpha satellite DNA from human chromosome 17: evidence for evolution by unequal crossing-over and an ancestral pentamer repeat shared with the human X chromosome. Mol Cell Biol. 1986 Sep;6(9):3156–65.

22. Stoll VS, Blanchard JS. Buffers: principles and practice. Methods Enzymol. 2009;463:43–56.

23. Otsu N. A Threshold Selection Method from Gray-Level Histograms. Syst Man Cybern IEEE Trans On. 1979;9:62–6.

24. Ushiki T, Hoshi O, Iwai K, Kimura E, Shigeno M. The structure of human metaphase chromosomes: its histological perspective and new horizons by atomic force microscopy. Arch Histol Cytol. 2002 Dec;65(5):377–90.

25. Hoshi O, Shigeno M, Ushiki T. Atomic force microscopy of native human metaphase chromosomes in a liquid. Arch Histol Cytol. 2006 Mar;69(1):73–8.

26. Jabs EW, Goble CA, Cutting GR. Macromolecular organization of human centromeric regions reveals high-frequency, polymorphic macro DNA repeats. Proc Natl Acad Sci U S A. 1989 Jan;86(1):202–6.

27. Johnson MD, Fresco JR. Third-strand in situ hybridization (TISH) to non-denatured metaphase spreads and interphase nuclei. Chromosoma. 1999 Jul;108(3):181–9.

28. Rudd MK, Wray GA, Willard HF. The evolutionary dynamics of alpha-satellite. Genome Res. 2006 Jan;16(1):88–96.

29. Gilbert N, Boyle S, Fiegler H, Woodfine K, Carter NP, Bickmore WA. Chromatin architecture of the human genome: gene-rich domains are enriched in open chromatin fibers. Cell. 2004 Sep 3;118(5):555–66.

30. Argüello-Miranda O, Sáenz-Arce G. Interchromatidal central ridge and transversal symmetry in early metaphasic human chromosome one. J Mol Recognit. 2008 Jun;21(3):184–9.

31. Earnshaw WC, Ratrie H, Stetten G. Visualization of centromere proteins CENP-B and CENP-C on a stable dicentric chromosome in cytological spreads. Chromosoma. 1989 Jun;98(1):1–12.

32. Murphy TD, Karpen GH. Localization of centromere function in a Drosophila minichromosome. Cell. 1995 Aug 25;82(4):599–609.

33. Vafa O, Sullivan KF. Chromatin containing CENP-A and alpha-satellite DNA is a major component of the inner kinetochore plate. Curr Biol. 1997 Nov 1;7(11):897–900.

34. Warburton PE, Cooke CA, Bourassa S, Vafa O, Sullivan BA, Stetten G, et al. Immunolocalization of CENP-A suggests a distinct nucleosome structure at the inner kinetochore plate of active centromeres. Curr Biol. 1997 Nov 1;7(11):901–4.

35. Cheeseman IM, Desai A. Molecular architecture of the kinetochore-microtubule interface. Nat Rev Mol Cell Biol. 2008 Jan;9(1):33–46.

36. Prendergast L, van Vuuren C, Kaczmarczyk A, Doering V, Hellwig D, Quinn N, et al. Premitotic assembly of human CENPs -T and -W switches centromeric chromatin to a mitotic state. PLoS Biol. 2011 Jun;9(6):e1001082.

37. Hoshi O, Owen R, Miles M, Ushiki T. Imaging of human metaphase chromosomes by atomic force microscopy in liquid. Cytogenet Genome Res. 2004;107(1-2):28–31.

38. Hoshi O, Fukushi D, Ushiki T. Atomic Force Microscopy of Human Chromosomes in Relation to Their Higher-Order Structure; in Fukui K, Tatsuo U (eds): Chromosome Nanoscience and Technology, pp 105-118 (Taylor & Francis, Boca Raton 2008).

39. Shichiri M, Yoshino T, Fukushi D, Hagiwara S, Akazawa K, et al: Scanning near-field optical/ atomic force microscopy as a tool for simultaneous specification of chromosome topography and particular gene location on the nanometer scale; in Fukui K, Ushiki T (eds): Chromosome Nanoscience and Technology, pp 137–154 (Taylor & Francis, Boca Raton 2008).

40. Jack EM, Harrison CJ, Allen TD, Harris R. The structural basis for C-banding. A scanning electron microscopy study. Chromosoma. 1985;91(5):363–8.

41. Schroeder-Reiter E, Wanner G. Chromosome centromeres: structural and analytical investigations with high resolution scanning electron microscopy in combination with focused ion beam milling. Cytogenet Genome Res. 2009;124(3-4):239–50.

42. Tan E, Sahin FI, Ergün MA, Ercan I, Menevşe A. C-banding visualized by atomic force microscopy. Scanning. 2001 Feb;23(1):32–5.

43. Picco LM, Dunton PG, Ulcinas A, Engledew DJ, Hoshi O, Ushiki T, et al. High-speed AFM of human chromosomes in liquid. Nanotechnology. 2008 Sep 24;19(38):384018.

44. de Asis ED, You L, Austin AJ, Leung J, Nguyen CV: Carbon nanotube atomic force microscopy with applications to biology and electronics; in Bhushan B (ed): Scanning Probe Microscopy in Nanoscience and Nanotechnology, pp 129–168 (Springer-Verlag, Berlin 2010).

Chapter 3

3 Localized, Non-random Differences in Chromatin Accessibility between Homologous Metaphase Chromosomes[1]

[1] This work has been published in the following article: Khan WA, Rogan PK, Knoll JH. Localized, non-random differences in chromatin accessibility between homologous metaphase chromosomes. Mol Cytogenet. 2014; 7(1):70. Highly Accessed, doi: 10.1186/s13039-014-0070-y.

3.1 Introduction

Homologous metaphase chromosome structures are heterogeneous at optical, sub-optical and atomic resolution (1–5). This heterogeneity is manifest as distinctive chromosomal banding patterns superimposed on a highly conserved banding framework (6,7). Within the same cell, each chromosome of a homologous pair may be laterally and longitudinally asymmetric (8,9) or display differences in DNA methylation (10), and replication timing (11–14). Differences in chromosome band resolution and histone modifications are distributed along the length of the mitotic metaphase chromosomes (15). In fact, phosphorylation of core histones-H3 and H4 at specific residues is retained in metaphase chromosomes, as an intermediate step in chromosome condensation (16). By contrast, lysine methylation and acetylation of histones are transient chromosome marks, with the loss of acetylation observed on all core histones in G_2/M-arrested cells (17,18). High fidelity mitotic metaphase chromosome condensation is essential for accurate transmission and differentiation of the genome into daughter cells, however this process tolerates some degree of structural heterogeneity between chromosome homologs (1). Despite advances in modeling higher order chromosome condensation, the locus-specific accessibility of chromatin within highly condensed metaphase chromosomes is not well understood. Some progress, however, has been made through investigations of histone and nonhistone proteins that reorganize chromatin into its condensed state (19).

We have noted reproducible differences in chromatin accessibility between homologous metaphase chromosomes in specific genomic regions using locus-specific short (1.5-5 kb), fluorescence in situ hybridization (FISH) probes (20,21). These differences manifest as variation in hybridization intensities between homologs at single cell resolution. This phenomenon has been observed for ~10% of the 305 genomic probes that we have reported (20–25), however the reasons for such variation were not understood. The remaining genomic regions show no significant differences in hybridization intensities between allelic loci on metaphase chromosomes.

In this study, we investigated locus-specific targets in metaphase chromosome regions that show consistent differences in DNA probe fluorescence intensity between homologs. Evidence is presented that these differences in hybridization of DNA probes result from their differential accessibility (DA) to their respective genomic targets. Using optical, and super-resolution microscopy with short target, unique sequence single copy FISH probes; these allelic chromosome regions exhibit consistent, non-random differences between their respective chromosome structures. Further, sequence analyses of interphase epigenetic marks at these loci suggest the possibility that such differences may be related to the presence of specific chromatin modifications.

3.2 Materials & Methods

3.2.1 Probe Selection and Scoring of Differential Accessibility (DA) on Hybridized Metaphase Chromosomes

Single copy genome-coordinate defined DNA probes were previously developed and used with FISH to precisely localize breakpoints in rearranged metaphase chromosomes for many different diseases and disorders (20–25). All single copy probes are devoid of repetitive elements and their nucleotide composition and genomic coordinates are precisely known. They map to a single location and can be developed from any unique region in the genome (e.g. exons, introns, intergenic, regulatory). As part of the development and validation of these single copy probes for FISH, they were hybridized to normal human chromosomes from the lymphocytes of at least one male and one female to confirm mapping of the probes to the expected genomic location (20–25). Genomic locations of single copy probes were also compared to locations of common CNVs (≥1% of general population) from blood derived DNA in two independent sample sets from healthy individuals. Common CNVs on both sample sets were identified on Affymetrix CytoScan HD array using ChAS (Chromosome Analysis Suite) software. These population CNV data were obtained from Ontario Population Genomics Platform (873 individuals of European ancestry with minimum of 25 probes per CNV; Database of Genomic Variants) and Healthy sample track (~400 individuals with minimum of 35 probes per CNV; obtained from Affymetrix). During our validation studies, it was

observed that while most single probes hybridized with similar affinity to both homologs within a cell, there were some probes in the validation samples with consistent, striking probe hybridization fluorescence intensity differences (or differential accessibility [DA]) between homologs. These probes were not pursued for clinical applications. In this study, we revisited some of these probes to begin to characterize the disparate fluorescence intensity differences between homologs. In order to determine if the hybridization intensity patterns were non-random, we selected DA probes based on availability of patient samples with cytogenetically distinguishable homologs (one normal, one rearranged) and the specific chromosomes involved in the rearrangements. Table 3-1 lists the FISH probes, their chromosomal location and the karyotypic findings of the 10 cell lines used to assess chromatin accessibility. These DA FISH probes were euploid and did not overlap the rearranged chromosomal regions. Parental origin of the chromosome rearrangement was known for 4 cell lines. Three cell lines (II-1 [mother], III-1 and III-2 [children]) were from a family carrying a microdeletion within the chromosome 15q12 imprinted region (13,26). The remaining cells lines were from unrelated individuals.

3.2.2 Chromosomes Preparations and Fluorescence in situ Hybridization

Peripheral blood lymphocytes or lymphoblastoid cell lines were cultured and chromosomes harvested using routine cytogenetic methods that included 0.075 M KCl hypotonic solution and 3:1 methanol:acetic acid fixation (Carnoy's fixative) (also see Supplemental Methods section 3.3) (27). With the exception of single copy FISH probe designed from within *CCNB1* (2.47 kb) on chromosome 5q13.2 (genomic coordinates, Table 3-2), all probes were previously developed (20–25). The *CCNB1* probe was specifically designed from a genomic region with hallmarks of open chromatin (28–33). Single copy FISH probes used in this study ranged from 1.78 kb to 3.55 kb in length. Details of probe amplification, purification, labeling, hybridization, and detection are provided in Supplemental material and have been previously described (34). To identify the chromosome 15q12 submicroscopic deletion (II2, III-1 and III-2), different biotin-

Table 3-1. Cell lines and single copy FISH probes used to assess chromatin accessibility.

Sample ID: Cytogenetics	Probes for tracking homologs	
	Cytoband, Gene: Interval	**Status**
GM10958: 46,XX, t(1;11)(q31.2;q25) pat	1q43.3, *RGS7*:IVS4-IVS5	DA
	1p36.3, intergenic	Equivalent
GM10273: 46,XX, t(11;22)(p13;q12.2) pat	22q13.3, *ACR*:Ex1-IVS3	DA
GM01921: 47,XY, t(8;14)(q13;q13), inv(9)(p11q13) mat, +21	9q34.3, *CACNA1B*:Ex29-IVS31	DA
	9p24.3, *C9orf66*:Ex1	Equivalent
GM06326: 46, X, t(Y;17)(q11.21;q21) pat	17p12, *PMP22*:IVS3 & *ADORA2B*:IVS1	DA
	17p12, *PMP22*:IVS4-Ex5 & *ADORA2B*:Promoter-Ex1	Equivalent
GM10958: 46,XX, t(1;11)(q31.2;q25) pat	11q25, *OPCML*:IVS1	DA
GM10273: 46,XX, t(11;22)(p13;q12.2) pat	11q25, *OPCML*:IVS1	DA
II-2: 46,XX.ish del (15)(q11.2q13)(D15S10-,*UBE3A*-) pat	15q12, *SNRPN:*Promoter:IVS1 & *GABRA5*:IVS3	DA
	15q13.1, *HERC2*:IVS12-IVS13	DA
III-1: 46,XY.ish del(15)(q11.2q13)(D15S10-,*UBE3A*-) mat	Same as II-2	DA
III-2: 46,XX.ish del(15)(q11.2q13)(D15S10-,*UBE3A*-) mat	Same as II-2	DA
L12-1980: 46,XX, t(1;17)(p10;q10)	1q43.3, *RGS7*:IVS4-IVS5	DA
	17p12, *PMP22*:IVS3 & *ADORA2B*:IVS1	DA
L13-72: 46,XX,9qh+	9q34.3, *CACNA1B*:Ex29-IVS31	DA
L11-729: 46,XY, t(7;22)(q32;q13.33)	22q13.3, *ACR*:Ex1-IVS3	DA

Cytogenetic nomenclature for each of the samples is indicated. Parental origins of the rearrangements are indicated when known (mat = maternal, pat = paternal). Cells are from human lymphocytes (L12-1980, L13-72, L11-729) or lymphoblastoid cell lines [GM10958, GM10273, GM01921, GM06326, and family II-1 (mother), III-1 (child), III-2 (child)].

Table 3-2. Comparison of open chromatin features to single copy genomic regions with and without DA.

		Open Chromatin Features					
SC Probe Location [GrCh37]	**Gene interval or cytoband**	**DNase-OS**	**FAIR-OS**	**H3K4me**	**H3K9Ac**	**H3K27Ac**	**H3K4me2**
chr1:1171789-1175143*	1p36.3, intergenic	11592	8710	544.0	168.4	115.6	120.6
chr1:1181574-1185503	*FAM132A*:Ex1-IVS1	7394	9695	596.5	143.0	102.8	160.9
chr1:1628792-1633615	*CDK11B*:IVS6	10378	14274	326.3	222.1	121.8	177.6
chr1:1632683-1637407	*CDK11B*:IVS6	12139	12829	290.7	125.8	51.8	51.8
chr1:240965538-240967390	*RGS7*: IVS13-IVS14	1420	9976	200.6	74.0	12.1	29.6
chr1:240988582-240990678*	*RGS7*:IVS4-IVS5	2840	8999	125.3	55.3	7.4	59.2
chr4:3242502-3246008	*HTT*:Ex67	9225	15222	248.0	142.8	81.4	51.8
chr5:1421588-1425427	*SLC6A3*:IVS4-IVS5	4702	8574	172.0	80.3	66.6	14.8
chr5:9355970-9358454	*SEMA5A*:IVS3	2827	16953	235.4	103.6	36.5	29.6
chr5:9361501-9365307	*SEMA5A*:IVS3	12398	40009	3017.6	597.4	1993.0	1530.2
chr5:9371425-9374496	*SEMA5A*:IVS3	1397	18058	531.5	48.5	81.4	59.2
chr5:11042187-11044508	*CTNND2*:IVS16	2221	15462	253.7	80.3	32.6	44.4
chr5:11071700-11076039	*CTNND2*:IVS16	4422	19382	344.8	158.4	118.5	77.8
chr5:11084988-11089067	*CTNND2*:IVS15	2942	16403	297.3	81.4	81.4	22.2
chr5:68462247-68464721*	*CCNB1*:Ex1-IVS3	31707	29162	1400.2	2378.9	1953.4	2076.3
chr7:73506616-73509661	*L1MK1*:IVS14	32349	30750	3473.0	4213.1	5870.8	4186.7
chr7:73534615-73536880	*L1MK1*:Ex1-IVS3	3639	9068	237.2	47.3	0	22.2
chr8:116658428-116661455	*TRPS1*:IVS1	3738	15369	650.0	224.2	78.6	396.1
chr8:116661938-116665132	*TRPS1*:IVS1	2031	15754	316.0	112.2	59.2	57.9
chr9:213762-215844*	*C9orf66*:Ex1	10945	15191	868.4	1550.5	503.2	1667.6
chr9:133587757-133589963	*ABL1*:Ex1b-IVS1b	32515	25514	616.8	3043.7	2278.6	1563.2
chr9:133616347-133618188	*ABL1*:IVS1b	1917	10733	341.9	83.6	42.0	71.1
chr9:133733132-133735051	*ABL1*:IVS3	2859	8103	188.8	50.9	74.2	37.0
chr9:133735369-133737639	*ABL1*:IVS3	2211	11425	259.7	62.8	56.1	95.6
chr9:133745513-133749828	*ABL1*:IVS4-IVS6	18884	37627	4959.4	477.6	982.4	998.7
chr9:133759487-133764440	*ABL1*:Ex11	7053	15356	322.9	174.4	142.9	74.0
chr9:140952206-140954439*	*CACNA1B*:Ex29-IVS31	4956	8277	302.2	88.8	33.8	51.8
chr9:140969092-140971796	*CACNA1B*:IVS33-IVS34	4127	7686	151.2	69.2	44.4	37.0
chr11:133180187-133182699*	*OPCML*:IVS1	2306	11280	202.1	77.4	37.0	133.8
chr12:11958559-11960434	*ETV6*:IVS2	2403	19900	2947.6	327.2	751.8	757.8
chr12:11992883-11994726	*ETV6*:IVS2	2257	16709	786.4	134.8	384.3	62.9
chr12:11992883-11995741	*ETV6*:IVS3	2988	23954	887.0	206.0	453.6	232.7

chr13:100626271-100630715	13q32.3, intergenic	11678	18628	216.6	76.2	65.8	23.2
chr13:100643221-100648153	13q32.3, intergenic	7452	25389	687.8	115.4	83.2	221.4
chr15:22690247-22693115	15q11.2, intergenic	1705	4996	347.0	85.2	47.4	29.6
chr15:22853681-22855541	*TUBGCP5*:IVS11-IVS13	1049	21106	132.0	75.4	96.9	22.2
chr15:23864038-23868139	15q11.2, intergenic	4260	17789	272.4	74.0	38.6	79.6
chr15:23883747-23886037	15q11.2, intergenic	1969	6908	84.0	76.3	10.5	29.6
chr15:23886989-23890525	*MAGEL2*:Promoter- 3′UTR	7602	12049	198.2	88.8	51.8	50.9
chr15:25016909-25018586	15q11.2, intergenic	1670	5764	216.6	38.2	48.1	111.5
chr15:25052358-25054037	15q11.2, intergenic	671	6051	83.8	51.9	7.4	0
chr15:25068481-25070727*	*SNRPN:*Promoter:IVS1	1524	7291	149.1	74.4	19.3	22.2
chr15:25199392-25201602	*SNRPN*:IVS4	6799	10253	258.1	1391.0	937.3	486.3
chr15:25613407-25617676	*UBE3A*:IVS7-IVS8	2728	26796	3025.0	81.4	182.8	96.0
chr15:27117096-27119866*	*GABRA5*:IVS3	5815	8082	140.0	40.8	37.0	29.6
chr15:28509526-28511337*	*HERC2*:IVS12-IVS13	4580	10908	854.2	313.8	728.2	465.3
chr15:102388168-102389774	*OR4F13P*:IVS3-Ex5	950	8872	64.0	47.6	37.0	29.6
chr16:15013674-15017156	16p13.11, intergenic	814	984	248.3	51.8	62.2	53.0
chr16:16412325-16415807	*PKD1P1*:IVS2-IVS7	473	268	168.0	76.8	71.4	51.8
chr16:16452359-16455837	16p13.11, intergenic	418	670	98.7	54.1	65.2	44.4
chr16:16234893-16236784	*ABCC1*:IVS30-Ex31	4867	11513	451.2	103.6	89.3	45.6
chr16:18440574-18444056	16p12.3, intergenic	110	0	181.5	74.0	73.4	31.2
chr16:18484058-18487536	16p12.3, intergenic	616	907	167.7	89.9	51.8	19.1
chr17:905599-910582	*ABR*:IVS21-3′UTR	10824	19481	304.9	174.9	132.8	2.9
chr17:941273-943865	*ABR*:IVS16	3508	6315	170.9	89.1	74.0	71.8
chr17:2591614-2594572	*CLUH*:IVS25-3′UTR	10756	11515	576.5	96.2	384.9	163.2
chr17:2596810-2599164	*CLUH*:IVS13-IVS19	5323	6551	301.9	112.5	63.3	37.0
chr17:2603297-2606091	*CLUH*:IVS3-IVS9	7600	7093	222.1	57.0	51.8	123.2
chr17:18128679-18133300	*LLGL1*:Promoter-Ex2	36213	27618	1016.0	647.8	219.2	743.9
chr17:18143933-18146387	*LLGL1*:Ex17-IVS22	7467	8690	136.8	114.2	37.0	16.8
chr17:15133018-15136902*	*PMP22*:IVS4-Ex5	5482	14180	207.3	113.3	60.8	34.6
chr17:15150757-15153084*	*PMP22*:IVS3	4694	12616	321.0	77.7	28.7	44.4
chr17:15174803-15176657	17p12, intergenic	2574	11	163.0	89.3	37.0	31.4
chr17:15847751-15849832*	*ADORA2B*:Promoter-Ex1	10751	9889	763.1	241.5	79.0	980.8
chr17:15868752-15870532*	*ADORA2B*:IVS1	2859	17457	711.4	95.0	78.8	84.7
chr17:18150509-18152632	*FLII*:IVS15-Ex21	23767	14999	2289.9	74.7	439.4	75.6
chr17:18153505-18154823	*FLII*:IVS12-IVS14	3547	3937	47.1	36.7	36.8	0
chr17:19286892-19288934	*MFAP4*:IVS3-Ex6	3415	5897	286.5	139.3	95.8	54.8

chr17:37861465-37863632	*ERBB2*:IVS5-IVS6	5144	6170	296.6	90.6	78.3	84.4
chr17:37882684-37886219	*ERBB2*:IVS27-Ex31	9666	16440	1561.2	617.8	331.8	836.4
chr17:38500482-38504359	*RARA*:IVS2	17458	19211	3584.2	597.6	650.9	813.2
chr17:38512106-38514271	*RARA:*IVS8-Ex9	5468	6830	177.2	130.6	125.8	88.3
chr17:38608442-38610468	*IGFBP4*:IVS1-IVS3	4526	10512	230.8	39.5	29.6	62.7
chr17:38613433-38617530	*IGFBP4*:Ex4	8748	18085	557.1	155.4	88.8	74.0
chr17:80290070-80293112	*SECTM1*:Ex1-IVS1	13714	13008	2005.4	294.1	202.4	1002.5
chr20:10642756-10644909	*JAG1*:IVS2-IVS3	2943	15006	1104.1	118.6	49.2	225.7
chr21:36259933-36264124	*RUNX1*:IVS2	26119	30777	1920.4	2050.4	1478.7	2915.8
chr21:39454065-39456057	*DSCR4*:IVS2	2440	7032	155.4	65.3	24.6	65.9
chr21:39463783-39466136	*DSCR4*:IVS2	2017	10359	126.5	63.2	51.8	25.6
chr21:39473031-39475467	*DSCR4*:IVS2	2256	10103	137.4	86.9	37.0	0.2
chr22:19338598-19342289	*HIRA*:IVS21-IVS24	3429	12123	325.1	150.0	59.2	37.0
chr22:23578368-23581572	*BCR*:IVS1	6792	19899	2489.1	283.0	240.2	284.8
chr22:23604414-23607814	*BCR*:IVS4	11921	14381	1989.6	425.4	621.7	362.3
chr22:23623055-23625566	*BCR*:IVS8	21132	16241	2543.9	311.6	501.8	451.4
chr22:51175125-51178674*	*ACR*:Ex1-IVS3	11986	12916	175.2	85.1	37.0	58.9
chrX:592626-595515	*SHOX*:IVS2-Ex3	7316	7254	125.9	55.3	29.6	37.0
chrX:597816-600430	*SHOX*:IVS3	6234	7821	64.0	74.0	41.5	44.4
chrX:602538-605057	*SHOX*:IVS5	4319	4191	147.9	29.6	7.0	14.8
chrX:7891853-7895877	*PNPLA4*:Ex1-IVS2	19932	42372	1854.3	2340.4	2553.7	1715.7
chrX:8440844-8443508	Xp22.31	1639	12112	151.2	59.2	30.0	45.5
chrX:8505855-8509075	*KAL1*:IVS9-IVS10	4319	14875	147.9	106.6	14.8	44.4
chrX:9613498-9617784	*TBL1X*:IVS4	4522	20294	429.2	164.6	115.6	133.7
chrX:9685383-9689409	*TBL1X*:Ex18	3938	43044	336.8	101.4	65.5	90.3

Probes from 93 genomic regions exhibiting DA (bold) or equivalent accessibility by metaphase FISH listed by chromosome number and GRCh37 genomic coordinates. Single copy intervals marked with * were characterized by FISH in this study; the other intervals were previously reported (20–25). Single copy probes that overlapped genes are specified relative to their exonic (Ex), intronic (IVS) or untranslated (UTR) positions. Single copy probes from intergenic regions were specified by cytogenetic location. Integrated signal intensities of the open chromatin features from ENCODE (35) are shown. As appropriate, values are shown with one significant digit after the decimal.

labeled and digoxigenin-labeled single copy probes (one probe from within the deletion and one adjacent to the deletion), were hybridized simultaneously and detected in different colors to distinguish the deleted homolog from the normal one. For the other cell lines, the normal and rearranged homologs were distinguishable by DAPI staining and single copy probe hybridizations were performed. DA was scored as differences in FISH probe hybridization intensities between homologous loci by direct examination using epifluorescence microscopy, and subsequently by quantification of hybridized probe epifluorescence images. At the microscope, hybridized probe fluorescence signals for each homolog were scored as bright, intermediate, dim, or nil. For a cell to be scored as DA, one homolog was required to exhibit an intermediate or bright probe signal and the other homolog a different intensity signal (e.g. bright/intermediate, bright/dim, bright/nil, intermediate/dim or intermediate/nil on homologs in a cell). For a cell to be scored as having equivalent accessibility, both homologs were required to exhibit probe hybridization of similar intensities (e.g. bright/bright, intermediate/intermediate). Microscope slides with metaphase cells were coded, hybridized and scored by 2 certified cytogeneticists. Twenty-five to 50 hybridized cells were scored for each sample. To exclude bias resulting from inefficient hybridizations, cells with dim hybridizations on both homologs or in which one homolog had a dim hybridization and the other had no hybridization were not scored. A two proportion Z-test was used to determine whether the fraction of cells showing DA or equivalent accessibility was statistically significant at $\alpha = 5.0E\text{-}02$. Variance in the frequency of cells reported to have DA among different samples was assessed for significance ($\alpha = 5.0E\text{-}02$) using Bartlett's test for equality of variances.

For DA probes, a two proportion Z-test was also used to determine whether there was non-random preference for one parental homolog to have brighter probe fluorescence intensity (i.e. more accessible hybridization). From the Z-test score, a *p*-value was obtained to determine whether the proportion of the brighter hybridizations showed a significant bias ($\alpha = 5.0E\text{-}02$) to one homolog. Additionally, probe fluorescence intensities in each cell were quantified by integrated gradient vector flow (GVF) analysis (next section).

3.2.3 Gradient Vector Flow (GVF) Analysis to Quantify Differences in Probe Intensity between Homologs

We previously developed a GVF-based algorithm that determined probe hybridization boundaries and quantified probe fluorescence (5,36). The GVF algorithm generated an active binary contour of the gray scale image of the probe fluorescence on each homolog. From the active contour, the integrated intensity values (in pixels) were calculated. The intensity values were normalized for each cell by taking the difference in integrated intensities between homologs, and dividing this difference by the sum of the intensities of both homologs. This converted raw total intensity values into a set of normalized intensity ratios (0 to 1). Values close to 0 confirmed that the probe intensities between the homologs appeared equivalent and ratios close to 1 indicated DA. A bias in hybridization intensities between homologous regions was reported as statistically significant (α = 5.0E-02) using a two-tailed *t*-test.

3.2.4 Nanoscale Analysis of Short Target Hybridized Probe Features using Atomic Force Microscopy

Nanoscale analysis of short target low copy FISH probes required correlating atomic force microscopy (AFM) with epifluorescence imaging. Correlated AFM with FISH, using a large centromere target, was used to develop the approach for subsequent examination of metaphase chromosome topography at non centromeric sites. The details of this process and our findings are described in detail in Chapter 2. At non centromeric sites, we used FISH probes to detect low copy genomic targets on chromosome 16p that did not exhibit differences in hybridization between homologs (i.e. equivalent accessibility).These probes also retain fluorescence in the absence of *p*-phenylenediamine antifade mounting medium which could not be used in AFM (5). The genomic locations of the PCR amplified product for the low copy target, *NOMO1*, are provided below (section 3.2.5). Chromatin accessibility following AFM was determined by whether probe fluorescence coincided with either ridge or groove topography of the metaphase chromosome.

Correlated AFM with FISH could not be pursued using single copy probes with DA for several reasons. First, the slow scan speed with which AFM generated metaphase chromosome topography limited the amount of data that could be collected. This tended to vary depending on the size of the chromosomes. Typically, imaging time was on the order of about ~4 hours per one chromosome 17 and even longer for other chromosomes with greater genetic content. Second, as a result of the extended imaging time for correlated AFM, single copy FISH probes which exhibit lower intrinsic levels of fluorescence were more susceptible to quenching of fluorescent emissions. This prevented the ability to extract correlated measurements. Third, there was limited access to the AFM equipment to optimize our approach once the centromeric and low-copy probe data had been obtained. Finally, and perhaps, most important, AFM only localized FISH probes on the chromosome surface, without providing any insight into internal metaphase chromatin structure of these sequences. These factors, in combination with the diffraction-limited resolution of epifluorescence, motivated the pursuit of a higher resolution optical approach that was not constrained by the Rayleigh limit, in order to visualize the internal 3D structure of metaphase chromosomes at genomic targets that exhibited DA or were equally accessible by scFISH probes.

3.2.5 Examination of Short Target Hybridized Probe Features using High Resolution 3-D Structured Illumination Super-resolution Microscopy

3D-SIM (Nikon Corporation) was used to examine and quantify volume and depth of single and low copy DNA probe fluorescence embedded in metaphase chromatin. Low copy (LC) probes recognize multi-target DNA sequences that occur within segmental duplications (24). 3D-SIM image reconstruction algorithms, for generating high resolution chromosome images, were optimized using a low copy probe from within *NOMO1* hybridized to normal metaphase chromosomes. This probe yielded bright fluorescence signals on both homologs as it hybridized to multiple genomic targets on chromosome 16 duplicons, ([GRCh37] genomic coordinates: 16452359–16455837,

15013674–15017156, 16412325–16415807, 18440574–18444056, and 18484058–18487536).

Chromosome image acquisition was performed on a motorized inverted Ti-E microscope equipped with a CFI Apo TIRF 100X oil (NA 1.49) objective (Nikon USA) and SIM illuminator (Nikon Corporation) in stack 3D-SIM mode. The epifluorescence image was captured using total internal reflection fluorescence mode followed by 3D-SIM on the same cell to gain resolution in the X/Y/Z dimensions. Compatible lasers with wavelengths of 457 nm and 561 nm were used to excite DAPI (chromosome counterstain) and Cy3 (probe fluorescence), respectively. Using moiré superimposed pattern formation (37), high frequency signal components were captured and deduced from the image reconstruction algorithms. Fast Fourier transforms were generated to validate that previously irresolvable high frequency signals from the epifluorescence metaphase image had been properly acquired by 3D-SIM (Supplemental Figure 3-13). The NIS-Elements AR software (version 4.13.00, Nikon Canada Inc.) reconstructed 3D-SIM images of hybridized sequence-defined probes demonstrating DA (*HERC2*, *PMP22*:IVS3, *ACR*) or equivalent accessibility (*NOMO1*) to metaphase chromosome homologs. The lateral fluorescence depth of each probe was calculated from a maximum of 20 reconstructed optical sections. Each section was collected in 0.1 μm steps from a total of 20 metaphase cells for *NOMO1*, 10 cells each for *HERC2* and *PMP22*:IVS3, and 2 cells for ACR. A threshold on the gray scale image of the DNA probe signal was performed in NIS-elements software using image segmentation, which converted the gray scale image into a binary image contour. Following probe fluorescence thresholding, the volume of bound probe fluorescence was calculated over all reconstructed optical sections. From these data, differences in probe volume and depth between homologs were quantified (NIS-Elements AR software) and analyzed for significance (α = 5.0E-02, two-tailed t test). Movie montages of DNA probe volume and depth were generated as AVI files, using the Movie Maker option (NIS-Elements AR software). Key frames depicting DA between homologs from all angles were added to the movie in order to emphasize the volume view, which built and rotated the metaphase chromosome 360° around the X/Y/Z axis.

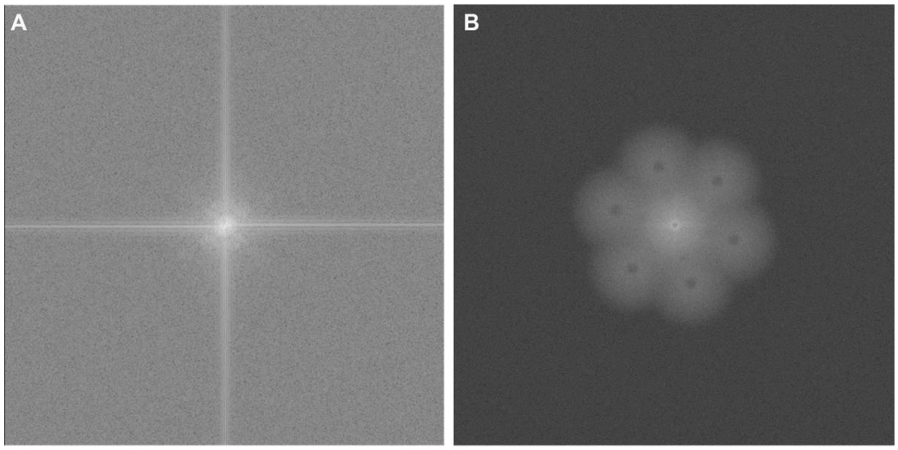

Supplemental Figure 3-13. Validation of super-resolution imaging of metaphase chromosomes before and after 3D-structured illumination microscopy.

(A) Fast Fourier transform (FFT) shows the point spread function from a wide field epifluorescence metaphase with a hybridized single copy probe with DA (*HERC2*, 1812 bp). (B) FFT on the same cell following 3D-SIM. This verified that the point spread function of super-resolution 3D-SIM was an order of magnitude higher than the wavelengths of wide field epifluorescence, as it captured high frequency measurements of fluorescent objects. This was used as a quality control metric to validate resolution of the 3D-SIM data on the Nikon Ti-E SIM illuminating system.

3.2.6 Sequence Analysis of Epigenetic Chromatin Marks for Single Copy Probes Detecting DA or Equivalent Accessibility

The genomic sequence of the single copy probes, which displayed DA or equivalent hybridization accessibility (asterisks, Table 3-2) in metaphase were compared with epigenomic DNA features that characterize open chromatin and active regulatory elements during interphase in multiple cell types (35,38). The epigenomic features from ENCODE (35) that we examined include DNase1 HS, Formaldehyde-Assisted Isolation of Regulatory Elements (FAIRE), and histone marks (H3K4me1, H3K9ac, H3K27ac, H3K4me2). The cell line used for ENCODE interphase comparisons, (GM12878, Coriell Cell Repository), was of the same B-cell lineage that we used to characterize DA and equivalent chromatin accessibility on metaphase homologs (Table 3-1). Furthermore, the cells were grown under the same culture conditions (37°C/5% CO_2 in RPMI-1640 complete medium with 15% fetal bovine serum). ENCODE chromatin immunoprecipitation sequencing (ChIP-seq) data generated high resolution, multidimensional view of chromatin accessibility from the above-mentioned epigenomic DNA features (39). ChIP-seq signal intensities of each open chromatin feature were visualized along the full length of a given single copy interval using the UCSC (University of California Santa Cruz) genome browser. Individual data points of the ChIP-seq signal intensities overlapping the genomic length of each single copy interval (Table 3-2) were retrieved from the UCSC table browser using the Duke DNase1 HS, University of North Carolina FAIRE seq, and Broad Institute histone modification custom tracks. The data point intensities were summed for each single copy interval (Table 3-2) and mean integrated single intensity values with standard deviations at 95% confidence were computed and plotted for all open chromatin features within each category (DA or equivalent accessibility). We then determined whether the differences in these values were significant by the analysis of variance test (ANOVA) for DA probes versus those with equivalent accessibility. Significance was determined from the *p* value of the F ratio following ANOVA.

3.3 Supplemental Methods

3.3.1 Chromosome Preparation

Lymphoblastoid/lymphocyte cells were cultured in T25 tissue culture flasks in RPMI-1640 medium (Gibco, Life Technologies Inc. ON, Canada) supplemented with L-glutamine, 15% fetal bovine serum (Gibco) and1% penicillin/streptomycin (Gibco). Cells were grown at 37^{o}C/5% CO_2 in a humidified incubator; and harvested in logarithmic growth phase at a concentration of 1x10^{6} cells/ml by arresting cells in metaphase [30µl of 10µg/ml Colcemid, Gibco) in a final volume of 10ml culture medium for 30 minutes. Subsequently, cells were pelleted by centrifugation, resuspended in hypotonic solution (0.075M KCl) for 20 minutes and fixed with 3 parts methanol (ACP Chemicals Inc. ON, Canada) to 1 part acetic acid (Caledon laboratory chemicals, ON, Canada).

3.3.2 Single copy DNA Probe Preparation

All genomic intervals were amplified using long PCR from genomic DNA using a high fidelity hot start DNA polymerase (KapaBiosystems, MA, USA) on a gradient PCR thermocycler (Eppendorf vapo.protect^{TM}). PCR primers for single copy amplicons were designed using Primer3 (http://primer3.ut.ee/ V. 4.0.0) and custom synthesized by Integrated DNA Technologies. Cycling parameters used an initial denaturation of 94^{o}C for 4 minutes, followed by 20 second denaturation at 98^{o}C for each cycle. The annealing temperature and time (1min/kilobase pair) were optimized for each amplicon. A final extension step at 72^{o}C was performed for 10 minutes. These parameters were repeated for 30-35 cycles. Each amplicon were purified using the gel/PCR DNA fragment extraction kit (Geneaid Biotech Ltd., Taiwan) and the amplicon DNA was labeled by nick translation with biotin-dUTP (Roche Diagnostics, ON, Canada) or digoxigenin-dUTP (Roche Diagnostics, ON, Canada). Nick translation reactions were performed at 15^{o}C using DNA polymerase I (Roche Diagnostics, ON, Canada), DNase I (Worthington Biochemicals, NJ, USA), 1µg of purified PCR product, and above-mentioned modified dUTPs. To this reaction, a 10µl solution comprised of 100mM dNTPs, 1M Tris-HCl, 1M $MgCl_2$, 12.5M 2-Mercaptoethanol (Sigma-Aldrich, ON, Canada), and 20µg/ml bovine

serum albumin (Roche Diagnostics, #10711454001) was added. Each nick translation reaction was brought to a final volume of 100ul with nanopure water. Incubation time of the reaction was optimized to obtain nick translated products in a size range of 250-700 base pairs. Biotin or digoxigenin labeled single copy DNA probes were ethanol precipitated and resuspended in 10µl of nanopure water.

3.3.3 In situ Hybridization, Detection and Imaging

Cytogenetic preparations on microscope slides were dehydrated in standard saline solution (2X SSC) for 10 minutes in a 37^{o}C water bath, and dehydrated in 80, 90, and 100% ethanol washes (1 minute per wash). Chromosomes were then denatured using ultrapure deionized formamide (70% in 2X SSC) (BioBasic Canada) for 2 minutes, dehydrated in 70 (on ice), 80, 90, and 100% ethanol washes (2 minutes each). An aliquot of labeled probe DNA (150-250ng) was mixed with 10ul of deionized formamide, denatured (10 minutes at 70^{o}C) and then mixed with equal volume (10ul) hybridization buffer solution (comprised of 2mg/ml bovine serum albumin, 0.2% SSC, 50% w/v dextran sulfate). The probe mixture was then hybridized to denatured metaphase chromosomes overnight at 37^{o}C. Labeled probes were detected with Cy3 conjugated to IgG fraction monoclonal mouse anti-digoxin (Jackson ImmunoResearch, PA, USA) (diluted 1:200 [1.7mg/ml]) or Alexa Fluor® 488 conjugated to streptavidin (Jackson ImmunoResearch, PA, USA) (diluted 1:500 [1.5mg/ml]) depending on the modified nucleotide incorporated. Post-detection washes were performed in 1X SSC, 1X SSC/0.1% triton-X 100, and 1X SSC, 15 minutes each at room temperature. Cells were stained with 4'-6-Diamidino-2-phenylindole (DAPI; 0.1ug/ml phosphate buffered saline) (EMD, #CA85001-386) for 20 minutes, rinsed in McIlvaine buffer (0.1M citric acid, 0.2M disodium phosphate; pH 7.2) for 2 minutes. Microscope slide preparations were mounted in *p*- phenylenediamine antifade. Cells were viewed, analyzed and/or imaged using epifluorescence microscopy or 3-dimensional structured illumination microscopy.

3.4 Results

3.4.1 Differential Hybridization Patterns Detected on Normal Metaphase Chromosomes

Our previous studies demonstrated consistent differences in hybridization intensities for single copy probes in at least two-thirds of the metaphase cells. DA was probe and genomic interval specific and not related to either probe labeling or the individual samples hybridized. To illustrate different hybridization behaviours between homologs with short-target, single copy FISH probes, we compare examples of normal metaphase chromosomes hybridized with probes that show differences in accessibility to probes with equivalent accessibility. Single copy probes with differences in fluorescence intensities (i.e. differential accessibility or DA) between homologs (*CACNA1B*, *HERC2*, and *PMP22*:IVS3 genes) are shown in Figure 3-14A, Table 3-2 and are contrasted with hybridized probes that show similar fluorescence intensities (i.e. equivalent accessibility) to each homolog (*CCNB1*,*C9orf66*, *BCR*, Figure 3-14B and Table 3-2).

A potential alternative explanation is that differences in probe fluorescence might be related to polymorphic copy number differences in the genome. The genomic intervals covering each of the probes were examined for common copy number variants (CCNV) in the normal population. Two probes within the same genomic interval (*CDK11B*:IVS6; Table 3-2) overlapped a ~55 kb CCNV (chr1:1,616,989-1,672,591[GRCh37]), but neither exhibited DA. The remaining single copy probes (Table 3-2) either did not overlap any CCNVs or were known to overlap pathogenic CNV intervals. Population CCNVs cannot account for hybridization intensity differences between homologous chromosomes.

3.4.2 Chromatin Accessibility to Homologous Metaphase Chromosomes is Non-random for most Differentially Accessible Targets

FISH probes from chromosomes 1, 5, 9, 11, 15, 17 and 22 showing DA were hybridized to patient samples, in which specific homologs could be distinguished by the presence of

a chromosome rearrangement (e.g. a translocation, inversion or heteromorphism) (Table 3-1). We investigated whether the same homolog in a sample was more likely to have a brighter probe hybridization signal than its counterpart (e.g. non-random), or whether hybridization intensity differences were random (e.g. the brighter signal occurred with equal frequency between homologs).

Single copy probes from within genomic regions overlapping *RGS7, CACNA1B, PMP22:*IVS3, *ADORA2B:*IVS1, and *ACR* showed preferential hybridization (based on probe fluorescence intensity) to the same homologous chromosome in different cells (non-random, p <5.0E-02, two proportion z-test; average of 80% metaphase cells [range 68-86%], n = 30–50 cells, Figures 3-15 and 3-16A). Interestingly, non-random DA was noted within *PMP22*:IVS3 and *ADORA2B*:IVS1, while adjacent single copy probes targeting different portions of these same genes (*ADORA2B*:Promoter-Ex1,*PMP22*:IVS4-Ex5) showed similar hybridization intensities (e.g. equivalent accessibility) between homologs. Control single copy probes from within *CCNB1* (Figure 3-14B, left panel), *C9orf66* (Figure 3-14B, middle panel), and an intergenic region within 1p36.3 also exhibited equivalent accessibility between homologs. DA is not exclusive to chromosomes originating from one parent-of-origin. For example, single copy probes from within *CACNA1B* and *ACR* exhibited greater accessibility (i.e. brighter fluorescent intensities) to the maternally-derived chromosomal target, whereas *RGS7, ADORA2B:*IVS1, and *PMP22*:IVS3 exhibited increased accessibility to the paternally-derived homolog (Figures 2 and 3A). The non-random nature of DA confirmed in a set of independent samples (L12-1980, L13-72, L11-729, Table 3-1) with distinguishable homologs (Supplemental Figure 3-17), of which parental origins were not known. Non-random DA was observed for probes from within *RGS7, CACNA1B, PMP22:*IVS3, *ADORA2B:IVS1* and *ACR*, in which the accessible homolog exhibited significantly brighter probe hybridizations (p <5.0E-02; average of 74% metaphase cells [range 69-85%], n =25-50 metaphases per cell line, Figure 3-16B). Single copy probes from within *PMP22*:IVS3 (in cell line, GM06326) and *RGS7* (GM10958) showed the brighter probe signal hybridized to the abnormal (i.e. derivative) chromosome homolog in the majority of cells analyzed (Figure 3-16A). By contrast, the same probes when mapped to

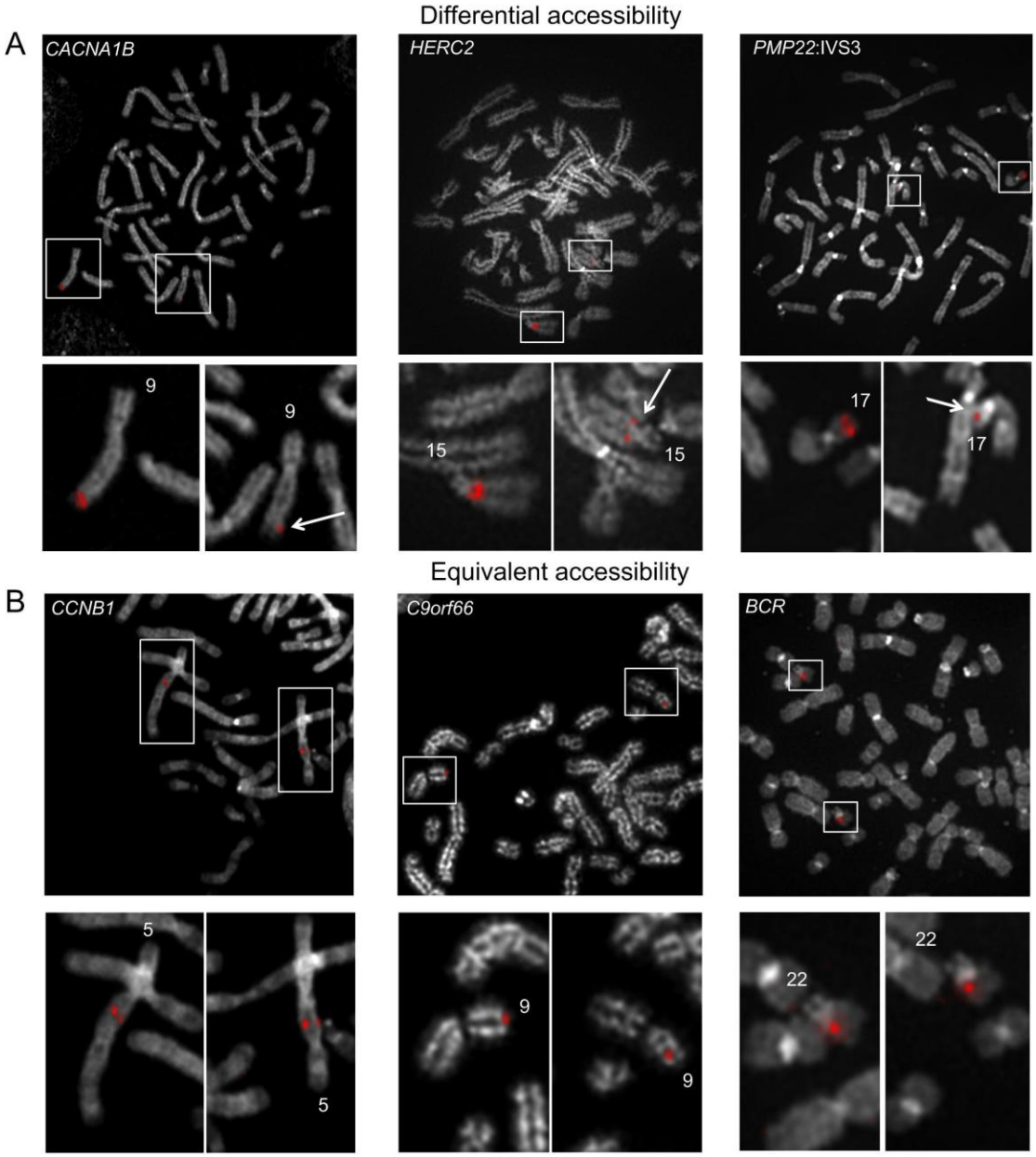
Differential accessibility
A
CACNA1B
HERC2
PMP22:IVS3
9
9
15
15
17
17
Equivalent accessibility
B
CCNB1
C9orf66
BCR
5
5
9
9
22
22

Figure 3-14. Differential accessibility (DA) and equivalent accessibility patterns between metaphase chromosome homologs detected by single copy probes.

(A) Human chromosomes hybridized with single copy FISH probes developed from *CACNA1B* (2.23 kb), *HERC2* (1.81 kb), and *PMP22*:IVS3 (2.32 kb) (left to right) show differential hybridization between homologs. Arrows indicate the homolog with less fluorescence (or less accessibility). (B) Examples of human cells with single copy FISH probes developed from within *CCNB1* (2.47 kb), *C9orf66* (2.08 kb), and *BCR* (3.4 kb) (left to right) that show similar fluorescence intensities (or equivalent accessibility) between homologous regions. Chromosomes were counterstained with DAPI (converted to gray scale in image) and probes were labelled with digoxigenin d-UTP and detected with Cy3 digoxin antibody.

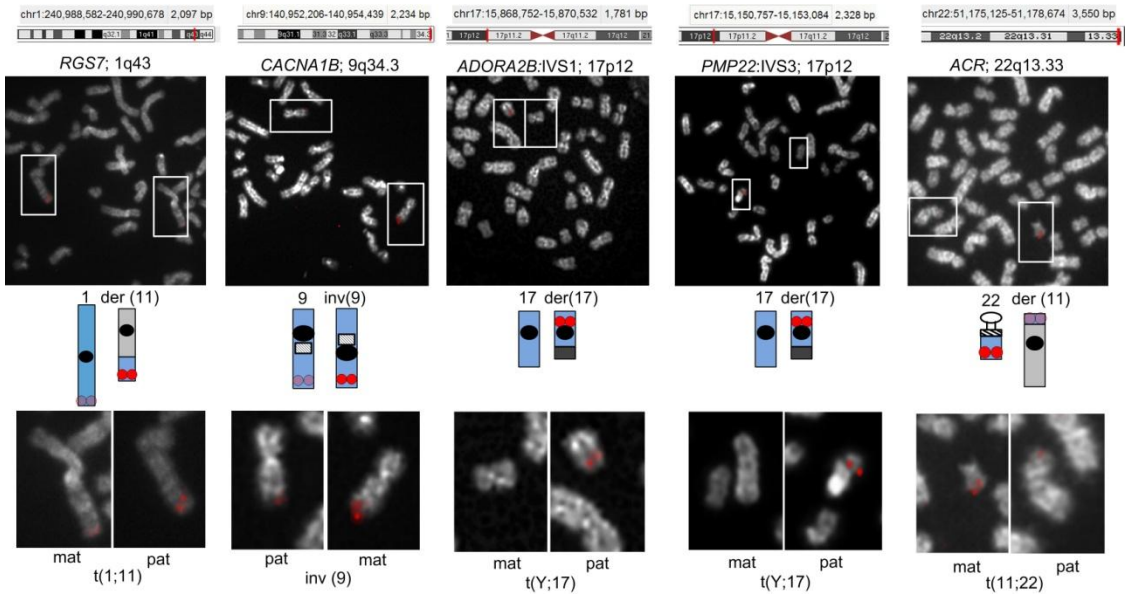

Figure 3-15. **Detection of DA within cytogenetically-distinguishable homologous regions of known parental origin.**

Genomic coordinates of single copy probes detecting DA within 5 different chromosomal regions are indicated. Schematic of the normal and derivative (der) or inverted (inv) chromosome with homologous target are shown. Specific chromosomes are highlighted (white rectangles), 'mat' and 'pat' refer to the maternal or paternal origin of the altered homolog, respectively. Brighter probe intensity was recurrently observed on the same homolog for a probe for each cell line. *RGS7* probe had greater target accessibility on the der chromosome 11 (paternal, GM10958). *CACNA1B* had greater target accessibility on the inv chromosome 9; (maternal, GM01921). *ADORA2B*:IVS1 and *PMP22*:IVS3 hybridizations were brighter on the derivative chromosome 17 (paternal, GM06326) and *ACR*:Ex1-IVS3 hybridizations were brighter on the normal chromosome 22 (maternal, GM10273).

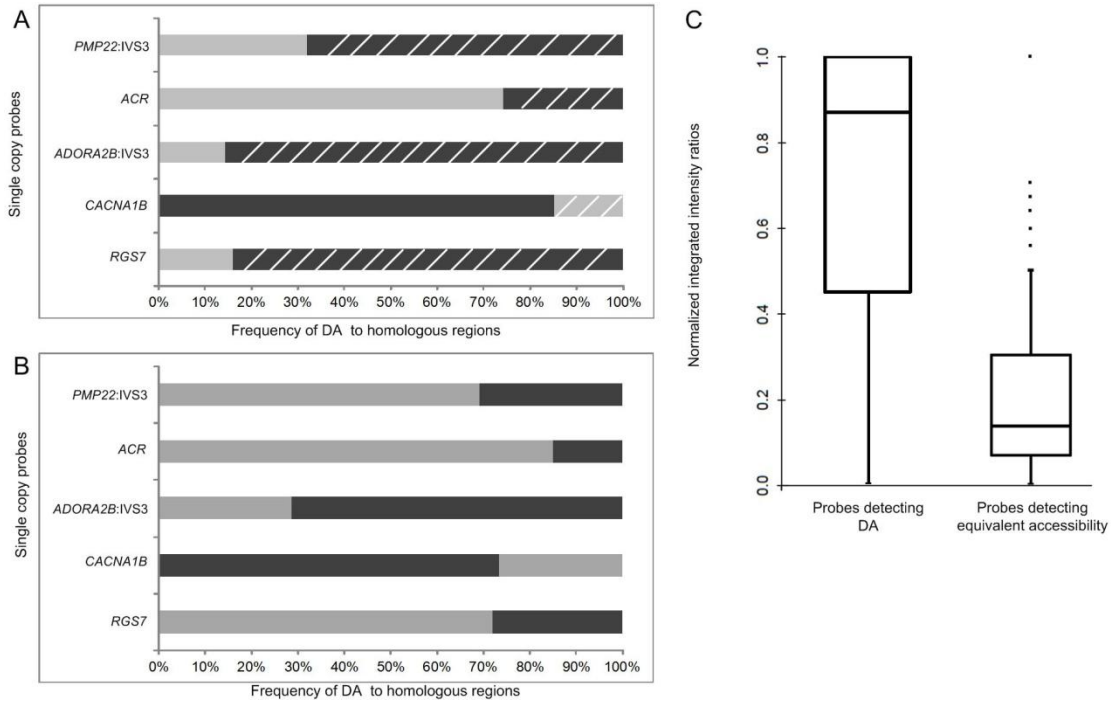
A
Single copy probes
PMP22:IVS3
ACR
ADORA2B:IVS3
CACNA1B
RGS7
0%
10%
20%
30%
40%
50%
60%
70%
80%
90%
100%
Frequency of DA to homologous regions
B
Single copy probes
PMP22:IVS3
ACR
ADORA2B:IVS3
CACNA1B
RGS7
0%
10%
20%
30%
40%
50%
60%
70%
80%
90%
100%
Frequency of DA to homologous regions
C
Normalized integrated intensity ratios
0.0
0.2
0.4
0.6
0.8
1.0
Probes detecting DA
Probes detecting equivalent accessibility

Figure 3-16. **DA is non-random and reproducible between individuals.**

(A**)** The light gray and black shading represents the brighter hybridization to either the normal or abnormal homolog, respectively (hatched marks indicate the *paternal* homolog). Bars depicting higher percentages correspond to the more accessible, brighter homolog in a given cell. This was the abnormal paternal homolog for *RGS7* (sample ID: GM10958), abnormal maternal for *CACNA1B* (GM01921), abnormal paternal for *ADORA2B*:IVS1, and *PMP22*:IVS3 (GM06326), and normal maternal homolog for *ACR* (GM10273). (B) Non-random DA was confirmed using cells from individuals in which the parental origin of the specific chromosomal rearrangement was unknown. The light gray and black shading represents the brighter hybridization to either the normal or abnormal homolog, respectively. Bars depicting higher percentages correspond to the more accessible, brighter homolog in a given cell. *RGS7* probe had greater probe target accessibility on the normal chromosome 1 (sample ID: L12-1980). *CACNA1B* had greater accessibility on chromosome 9 with heteromorphic variant (L13-72). *ADORA2B*:IVS1 and *PMP22*:IVS3 probes were brighter on the abnormal and normal chromosome 17s, respectively (L12-1980) while *ACR* showed greater accessibility to the normal chromosome 22 (L11-729). (C) Quantification of probe signal fluorescence between homologs are shown by box plots of normalized integrated fluorescence intensity ratios. Single copy probes detecting DA (*RGS7, CACNA1B, PMP22*:IVS3, *ADORA2B*:IVS1, *ACR*) exhibited large differences in hybridization intensities between homologs. This is indicated by the broad inter-quartile range of normalized intensity ratios from 0.55-1 (median intensity ratio, 0.87). By contrast, normalized intensity ratios for single copy FISH probes (*CCNB1*, *Corf66*,*PMP22:*IVS4-Ex 5, *ADORA2B*:Promoter-Ex1 and 1p36.3 intergenic region) with equal accessibility ranged from 0.07-0.31 (median intensity ratio, 0.14). Intensity differences between homologs were quantified by GVF from 125 metaphase cells for each probe category.

an additional cell line with a structural alteration (L12-1980), showed that the normal chromosome homolog (Figure 3-16B) had a more intense hybridization signal. This indicates that DA is not influenced by the presence of particular chromosome rearrangements. Although chromatin accessibility for most DA targets exhibited a non-random preference for one homolog, one DA probe (*OPCML*; 2.53 kb) had a random pattern. This finding was confirmed on two different cell lines with cytogenetically distinguishable chromosome 11s (Table 3-1 and Supplemental Figure 3-17).

We also examined if DA was heritable in 3 members of an Angelman Syndrome (AS) family with a chromosome 15q12 microdeletion (Table 3-1) at loci adjacent to the rearrangement (13,26). In this family, the unaffected mother (II-1, Figure 3-18) inherited the microdeletion from her father (not available for study); and passed on the deleted chromosome to her AS children (III-1, III-2, Figure 3-18). A dual probe-dual labeling and color detection FISH strategy (Figure 3-18A) was utilized to distinguish the chromosome 15 homologs based on the presence or absence of the microdeletion. A 4.9 kb single copy FISH probe within the deletion interval (*UBE3A*:IVS7-IVS8, Table 3-1) served as a control (green circle in Figure 3-17A) to track the abnormal chromosome 15. Single copy probes detecting DA (dark and light red circles in Figure 3-18A) targeted intact sequences outside the deletion interval that occurred both within the AS imprinted domain (*GABRA5* [2.77 kb], *SNRPN* [2.09 kb]) and adjacent to the imprinted domain (*HERC2* [1.81 kb]). Irrespective of their imprinted status, probes within *GABRA5*, *SNRPN*, and *HERC2* all showed a bias in non-random hybridization. The paternally inherited chromosome 15, which was deleted in II-1 and intact in III-1 and III-2, consistently exhibited greater probe accessibility (Figure 3-17B). Previously, we have reported biased early-replication during S phase at the same loci on the paternally-derived chromosome (13). The variance in the fraction of cells reported to have DA among different samples (Table 3-1) for all single copy probes described above (*RGS7*, *CACNA1B*, *OPCML*, *GABRA5*, *SNRPN*, *HERC2*, *ADORA2B*:IVS1, *PMP22*:IVS3, and *ACR*) was not significant ($\sigma 2 = 9.72$, $p = 8.65E\text{-}01$, $\mu = 35$ cells analyzed per sample, Bartlett's test for homogeneity of variance).

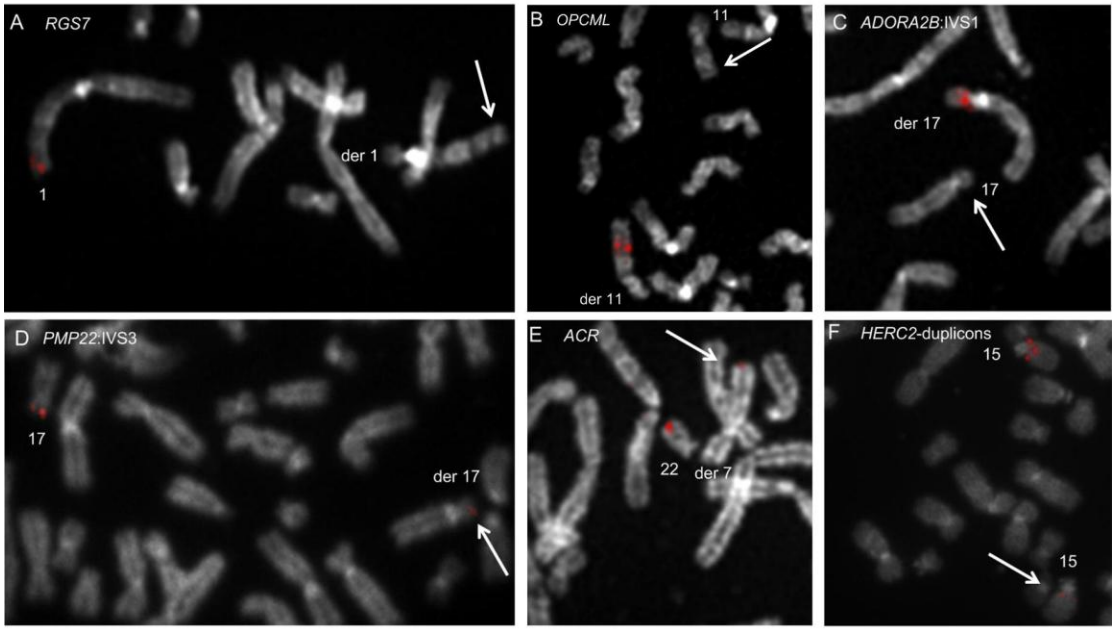

Supplemental Figure 3-17. **Examples of probes with DA by FISH.**

Arrows indicate the less accessible homolog (i.e. the weaker hybridization signal). (A-E) Single Copy Probes: Dim or no hybridization is on the derivative chromosome 1 for *RGS7* (cell line L12-1980), the normal chromosome 11 for *OPCML* (cell line GM10958), the normal chromosome 17 for *ADORA2B*:IVS1 (cell lines L12-1980), the derivative chromosome 17 for *PMP22*:IVS3 (cell line L12-1980), and the derivative chromosome 7 for *ACR* (cell line L12-1989), respectively. The other homolog in each panel has brighter hybridization signals. (F) Low Copy Probe: *HERC2* duplicon probe detects three distinct paralogous targets spanning 8.5 kb on chromosome 15s from a normal cell.

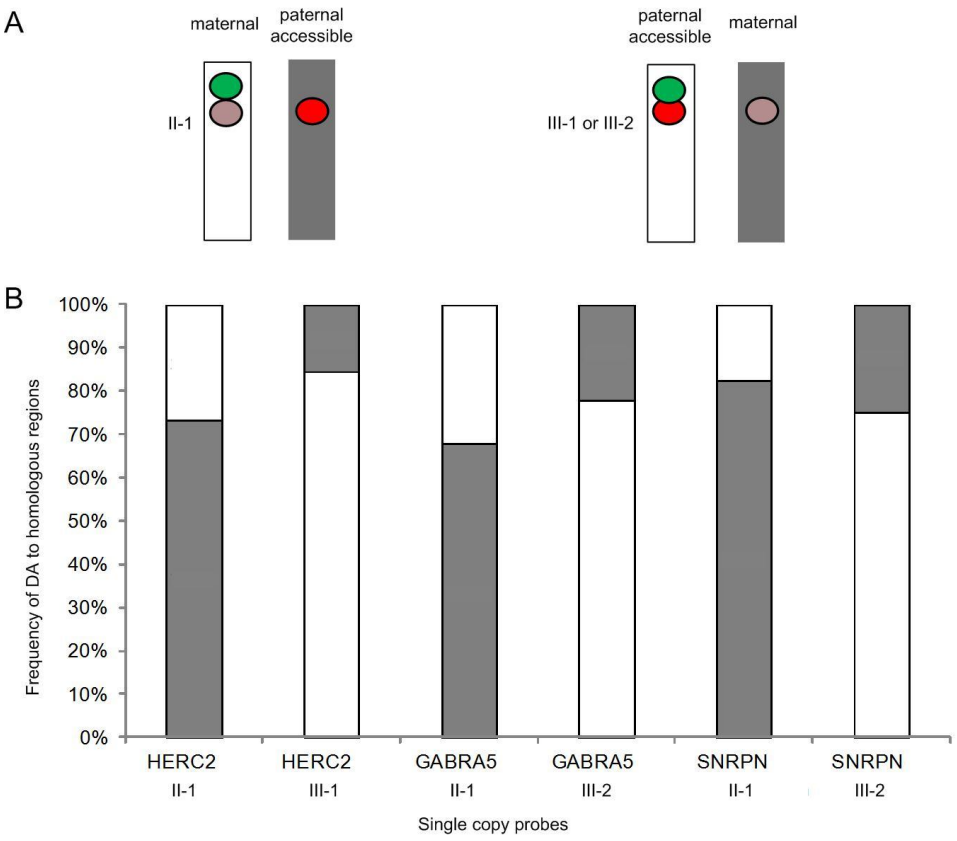
A
maternal
paternal accessible
II-1
paternal accessible
maternal
III-1 or III-2
B
Frequency of DA to homologous regions
100%
90%
80%
70%
60%
50%
40%
30%
20%
10%
0%
HERC2
II-1
HERC2
III-1
GABRA5
II-1
GABRA5
III-2
SNRPN
II-1
SNRPN
III-2
Single copy probes

Figure 3-18. DA is non-random among related individuals.

(A) Schematic of a two probe two color single copy FISH strategy to distinguish chromosome 15 homologs is shown. The hemizygous deletion on proximal chromosome 15q is identified by the loss of probe *UBE3A*(green) on one homolog and the presence of *HERC2, GABRA5, SNPRN* (red, pink). The deletion occurs on the paternal homolog in individual II-1 (mother) and on the maternal homolog in the children (III-1 and III-2). DA for probes outside of the deletion is represented by a bright hybridization on one homolog (red circle) and weak fluorescence hybridization on the other one (pink circle). The deleted chromosome is gray and the normal chromosome is white. (B) DA detected by *HERC2, GABRA5, SNPRN* showed that the paternal chromosome in the three individuals (deletion in II-1; normal in III-1 and III-2) contained the brighter fluorescence intensities (*HERC2* II-1, 73.3% of metaphase cells III-1, 84.6%; *GABRA5* II-1, 68% III-2, 77.8%; *SNRPN* II-1, 82.6% III-2, 75.0%) and was more accessible.

3.4.3 Quantification of Hybridizations Confirm Variation in Fluorescence Intensities between Homologs for Probes Detecting DA versus Equivalent Accessibility

The extent of variation in DNA probe hybridization intensity between homologs was quantified by gradient vector flow (GVF) analysis for both DA probes (*RGS7*, *CACNA1B*, *PMP22*:IVS3, *ADORA2B*:IVS1, *ACR*), and control probes with equivalent accessibility (*CCNB1*, *C9orf66*, *ADORA2B*:Promoter-Ex1, *PMP22*:IVS4-Ex 5, and 1p36.3 intergenic region). Significant differences in integrated fluorescence intensities between homologs with DA were found relative to probes detecting equivalent hybridization ($p < 5.0E-02$; n = 250 total metaphases, Figure 3-16C). The normalized intensity ratios between homologs in metaphase cells with DA were more variable ($\sigma 2 = 0.111$, $\mu = 0.716$) than control probes with equivalent accessibility to homologous targets ($\sigma 2 = 0.049$, $\mu = 0.221$).

3.4.4 AFM of Short Target FISH Probes

Low copy probe from within *NOMO1* (3.4 kb) was mapped onto metaphase chromosome topography by correlated AFM and FISH. Topography and hybridization of both homologs could be analyzed in 19 metaphase cells. Figure 3-19A is an example of correlated AFM/FISH with *NOMO1*. These genomic targets with equivalent accessibility mapped to groove-like chromatin cavities or invaginations (Figure 3-19B-D) more often (88% within grooves or at groove-ridge interfaces for both *NOMO1* and *NOMO3*) than to ridge structures (Figure 3-19E-G). Although the topographic distribution of target sequences on the chromosome surface can be visualized with correlated AFM/FISH (5), their volume and depth cannot be resolved by this technique. These properties were assessed at super-optical resolution by 3D-SIM.

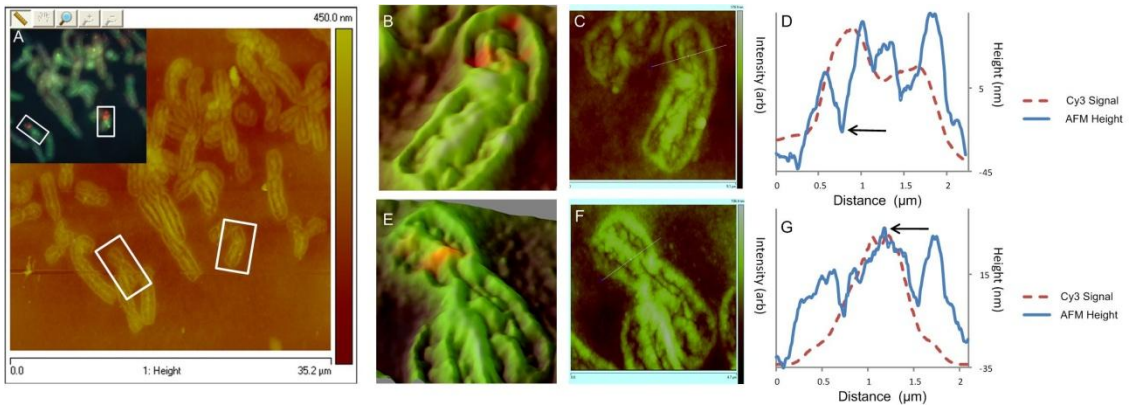

Figure 3-19. Correlated AFM/FISH groove-ridge topography with a chromosome 16p specific low copy probe.

(A) AFM image of a metaphase cell. Boxes indicate the chromosome 16 homologs and their height is indicated by the scale bar on right. The epifluorescence image (inset) shows the same cell with chromosome 16s hybridized with a 3.4 kb low copy probe for *NOMO1* (red). A control 16q heterochromatin probe (green) was included as a marker for quick identification (due to quenching in the absence of antifade). The chromosome 16 homologs in panel A are presented individually in the subsequent panels. (B) Registration of probe epifluorescence image onto chromosome topography for one homolog. (C) Location of cross-section measurement of hybridized target on chromosome topography. (D) Graphical representation shows preference for fluorescence groove localization (arrow) for this homolog and was the predominant localization for 88% of homologs. The probe fluorescence (red line) is coincident with the height of the groove by AFM (blue line). (E, F, G) Registration of probe fluorescence onto chromosome topography for the other homolog, showing corresponding cross-sectional profile of probe intensity superimposed on chromosome topography. For this homolog, the probe was localized to the ridge (arrow, panel G). This pattern was observed in very few homologs (12%).[§§]

[§§] The correlated AFM/FISH data presented here does not appear in the online version of this paper.

3.4.5 DA is Related to Differences in Internal Chromatin Accessibility of Homologous Targets

Using 3D-SIM, we demonstrated reproducible and significant differences in probe volume (p = 3.72E-07, n = 22 metaphase cells**)** and depth (p = 1.41E-07, n = 22) between homologous regions of three DA probes (*PMP22*:IVS3, *HERC2, ACR*). The distribution of probe volume and depth was broad in regions with DA (Supplemental Figure 3-20A) relative to those with equivalent accessibility (Supplemental Figure 3-20B). For example, a 1.81 kb single copy probe detecting DA within *HERC2* (Figure 3-21A) exhibited a large difference between homologs (Figure 3-21B, 0.22 μm^3 left panel and 0.001 μm^3 right panel). Notably, the axial distributions (i.e. depth) of the probe fluorescence from the accessible (Figure 3-21C**,** left panel) and less accessible (Figure 3-21C, right panel) homologs were 1.70 μm and 0.80 μm, respectively. These differences in volume and depth projections can also be viewed by traversing through cross-sections of the hybridized chromosomes (Supplemental Movie 3-22, probe *PMP22*:IVS3). The hybridization signals of accessible and DA probes were contained within different focal planes of metaphase chromatin, and there was large variation in the number of reconstructed optical sections hybridized to the same target on different homologs (Figure 3-21C). By contrast, a probe detecting 5 distinct targets on chromosome 16 (*NOMO1*, Figure 3-23A) with equivalent accessibility to both homologs showed similar probe volumes (Figure 3-23B, 0.60 μm^3, left panel and 0.89 μm^3, right panel) and depths (Figure 3-23C, 1.4 μm both panels) (also see Supplemental Movie 3-24). Hybridization to each of these low copy targets were assessed for volume and depth differences as a single fluorescent target due to their close genomic proximity (~1 Mb apart). Among all cells, differences in *NOMO1* probe volume (p = 1.30E-01, n = 20 metaphase cells analyzed) and depth (p = 8.90E-01, n = 20 metaphase cells) between homologs were not significant (Supplemental Figure 3-20B). These findings provide direct evidence that DA is due to the genomic target sequence being less accessible on one of the chromosome homologs.

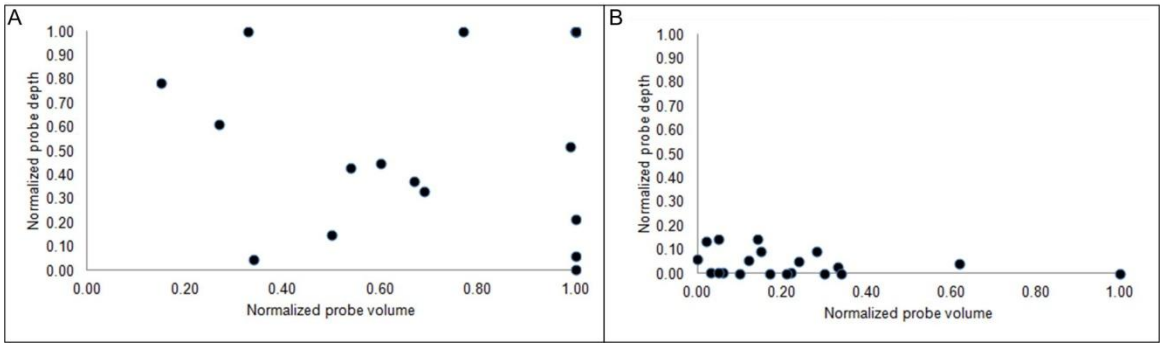

Supplemental Figure 3-20. Quantification of differences in DNA probe volume and depth between probe regions for DA and equivalent accessibility following 3D-SIM.

(A) Genomic targets within *HERC2*, *PMP22*:IVS3, and *ACR* had 3.3-fold greater volumetric, normalized integrated probe intensities (μ =0.72 μm3, range: 0.15-1.0 μm3, n =22 cells) compared to a genomic target with equivalent accessibility within *NOMO1* (panel B, μ = 0.22 μm3, range: 0–0.34 μm3, n = 20 cells). Genomic targets within *HERC2*, *PMP22*:IVS3, and *ACR* (panel A) also had broad distributions of probe depth (range: 0.005-1.0 μm) confirming DA versus genomic targets within *NOMO1* (panel B) which showed smaller differences in probe depth (range: 0–0.14 μm), confirming equivalent accessibility between homologous regions. Probe volume and depth were not correlated for genomic regions with DA (r =0.163) and equivalent accessibility (r = − 0.281). Following quantification, normalization for probe volume was performed by subtracting the volumes between homologous targets and dividing by the total probe volume for each cell. Similar normalization was done for probe depth.

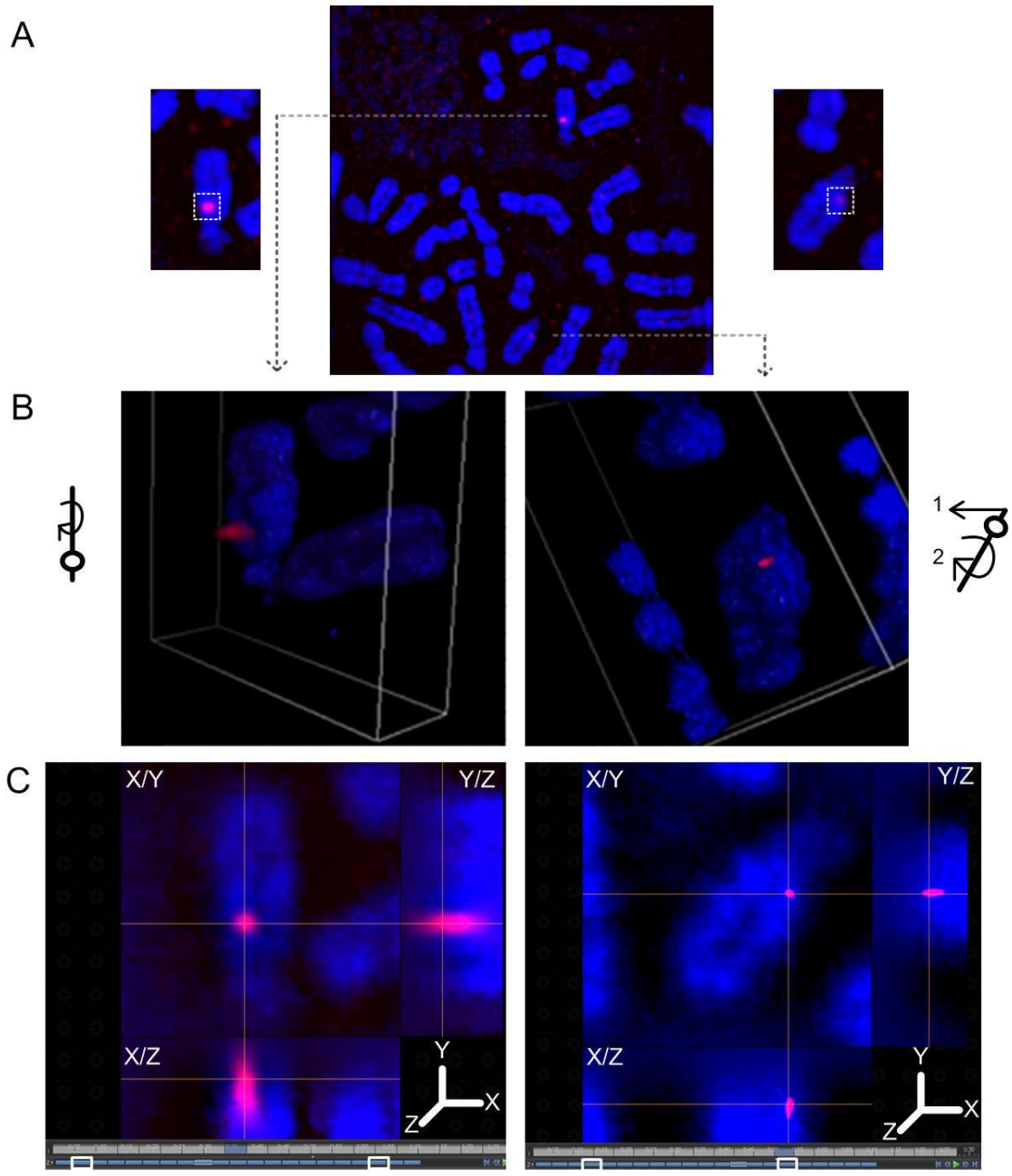
A
B
1
2
C
X/Y
Y/Z
X/Z
Y
X
Z
X/Y
Y/Z
X/Z
Y
X
Z

Figure 3-21. Visualization of metaphase chromosome differential accessibility in 2- and 3-dimensions.

(A) Epifluorescence image of metaphase cell hybridized with *HERC2* single copy probe (1.81 kb) shows a DA pattern. Chromosome 15 homologs are magnified. 3D structured illumination microscopy of hybridized probe volume (panel B) and probe depth (panel C) for the magnified homologs in panel A are presented. (B) The left homolog with greater accessibility contains fluorescence embedded within the chromosome and protrudes above the surface. In contrast, the right homolog with less accessibility has a much smaller volume of hybridized probe fluorescence and is mainly embedded within the chromosome. Reconstructed volume view in the left homolog was generated by rotating it clockwise about the z-axis (see orientation schematic). Volume view in the right homolog was generated by up-righting it (arrow 1) and turning it clockwise (arrow 2) (see schematic). (C) Crosshairs are centered over the maximal fluorescent intensity projection along the XY, XZ and YZ axes for each chromosome 15 homolog, and highlight differences in chromatin accessibility. The axial projection (depth) of the probe fluorescence spans 18 of 21 0.1 μm reconstructed optical sections (white rectangles delineate boundaries along the z axis) in the left more accessible homolog; and only 12 of 21 reconstructed optical sections in the right homolog (white rectangles).

Supplemental Movie 3-22. 3D anaglyph view of single copy FISH probe targets with DA (PMP22:IVS3) between chromosome homologs.

Movie in upper left panel shows differences in probe fluorescence depth, dynamically visualized through 0.1 μm optical cross-sections of the hybridized chromosome 17 homologs. Upper right panel is a 3D projection of the DNA probe fluorescence, from which probe volume was obtained. The lower panel shows the same homologs, as in upper left, with occupancy of probe volume in the context of the reconstructed chromosomes, rotated 360° in the X/Y/Z axes and depicting inter-homolog DA from all angles. Reconstructed optical sections were taken over 20 z-stacks, at 0.1 μm per stack with 3D-Structured Illumination Microscopy.[***]

[***] Direct link to download this movie can be accessed through the journal's website http://www.molecularcytogenetics.org/content/7/1/70/suppl/S3 (open source MP4 file, Khan et al. *Mol Cytogen* 2014 7:70).

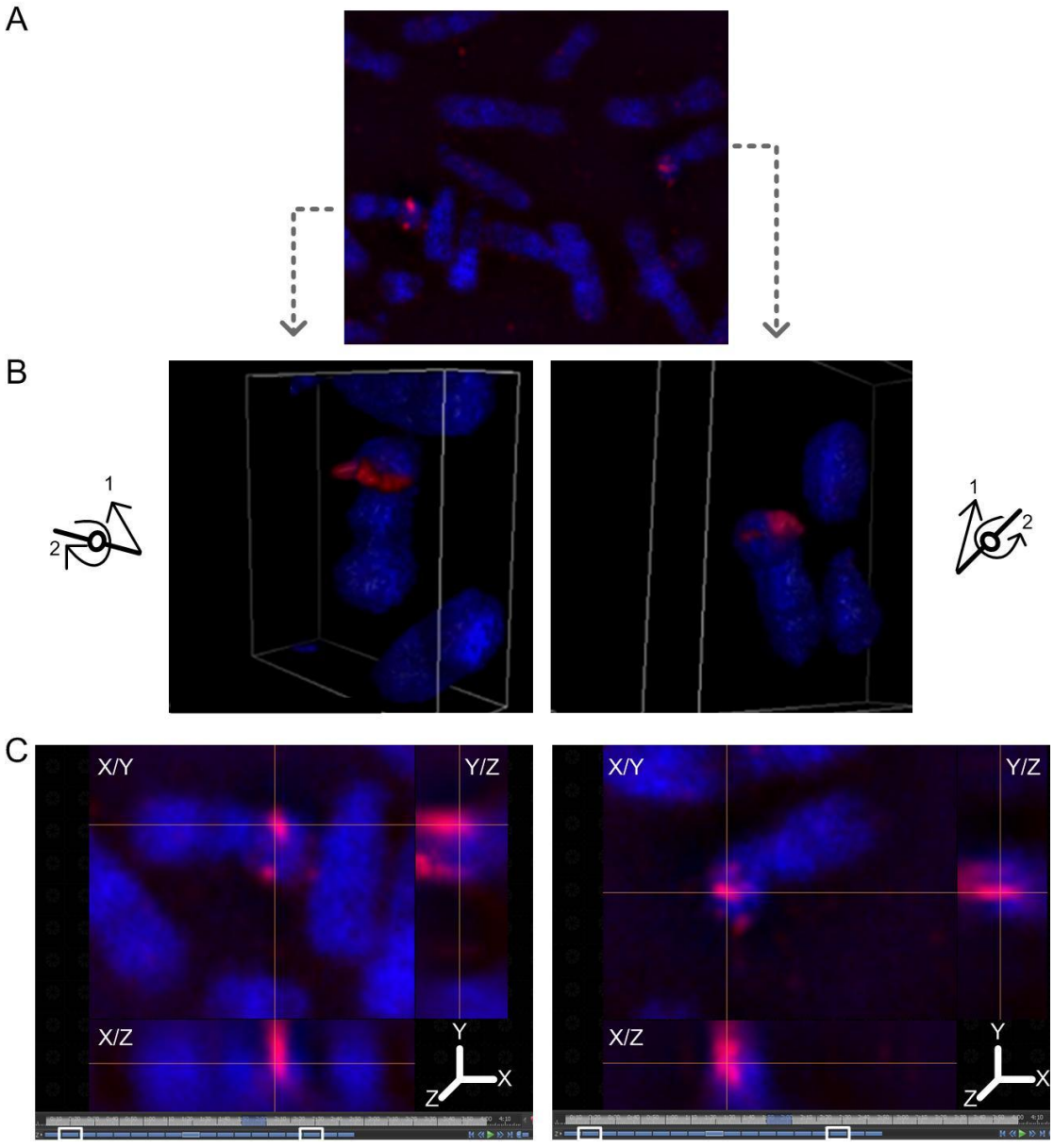
A
B
1
2
1
2
C
X/Y
Y/Z
X/Z
Y
X
Z
X/Y
Y/Z
X/Z
Y
X
Z

Figure 3-23. Visualization of metaphase chromosome equivalent accessibility in 2- and 3-dimensions.

(A) Epifluorescence image of metaphase cell hybridized with a low copy probe (3.4 kb) within *NOMO1*. 3D structured illumination microscopy of hybridized probe volume (panel B) and probe depth (panel C) for the homologs in panel A are presented. (B) Both homologs show equivalent hybridization accessibility, where the fluorescence is embedded within the chromosome and protrudes above the surface. Reconstructed volume view in the left homolog was generated by up-righting it (arrow 1) and turning it clockwise about the z-axis (arrow 2) (see orientation schematic). Volume view in the right homolog was generated by up-righting it (arrow 1) and turning it counter-clockwise (arrow 2) (see schematic). (C) Crosshairs are centered over the maximal fluorescent intensity projection along the XY, XZ and YZ axes for each chromosome 16 homolog. The axial projection (depth) of the probe fluorescence spans 15 of 18 0.1 μm reconstructed optical sections for both homologs, depicting equivalent chromatin accessibility (white rectangles delineate boundaries along the Z axis).

Supplemental Movie 3-24. 3D anaglyph view of low copy FISH probe targets (*NOMO1*) with equivalent accessibility between homologs.

The upper panels show probe volumes in the reconstructed chromosomes, rotated 360° around the X/Y/Z axes. Lower left panel is a 3D projection of the DNA probe fluorescence from which probe volume was obtained. In lower right panel, *NOMO1* probe fluorescence is shown embedded within the accessible invaginations of metaphase chromatin topography. Chromosome topography was generated by tapping mode raster scanning using atomic force microscopy. Topography and fluorescent probe signals were correlated using overlay procedures previously described [see reference (5)]. Reconstructed optical sections were taken over 18 z-stacks, at 0.1 μm per stack. Chromosome 16 homologs shown are from a different metaphase cell than Figure 3-23. †††

††† Direct link to download this movie can be accessed through the journal's website http://www.molecularcytogenetics.org/content/7/1/70/suppl/S4 (open source MP4 file, Khan et al. *Mol Cytogen* 2014 7:70).

3.4.6 Epigenetic Features of Open Chromatin are Enriched in Genomic Regions Exhibiting Equivalent Accessibility versus those with DA

The source of the differences in single copy FISH probe accessibility between metaphase homologs is not known, however other markers of localized, sequence specific chromosome accessibility during interphase are well established (35). We compared common epigenetic chromosomal modifications diagnostic for open chromatin during interphase to the same genomic intervals that show DA or equivalent accessibility in metaphase (n = 93 genomic regions**,** Table 3-2). Interphase epigenetic patterns for single copy intervals detecting equivalent probe accessibility to both homologs showed higher integrated signal intensities. In particular, Deoxyribonuclease I hypersensitivity (DNase I HS), and open chromatin features marked by modifications such as Histone 3 lysine 4 mono-methylation (H3K4me1) and Histone 3 lysine 27 acetylation (H3K27ac) (Figure 3-25A). These targets exhibited higher integrated signal intensities for DNase HS and histone marks of open chromatin than other marks associated with transcriptionally active chromatin (i.e. H3K36me3, H4K20me1). By contrast, homologous chromosomal intervals exhibiting DA generally had lower integrated signal intensities for the same open chromatin features (Figure 3-25B), which would be consistent with diminished levels of open chromatin marks at less accessible metaphase loci. Collectively, the average integrated signal intensities of all open chromatin marks (DNase I HS, FAIRE, H3K4me1, H3K9ac, H3K27ac, H3K4me2) in the DA genomic intervals was significantly lower ($\mu = 2830$, $\sigma = 1900$) relative to intervals with equivalent accessibility ($\mu = 4330$, $\sigma = 3650$) ($F = 62.28$, $p = 1.0E\text{-}04$;Figure 3-25C and Table 3-2).

3.4.7 Analysis of DA in a Cell line of Mesodermal Origin

Presently the analysis of DA has been restricted to normal lymphocytes or lymphoblasts, as these are the tissue types in which it was initially documented. However in a separate set of experiments, we examined two genomic targets, (*RGS7* [1q43] and *PMP22*:IVS3 [17p12]) by single copy FISH on chromosomes from human fibroblast cells (mesodermal

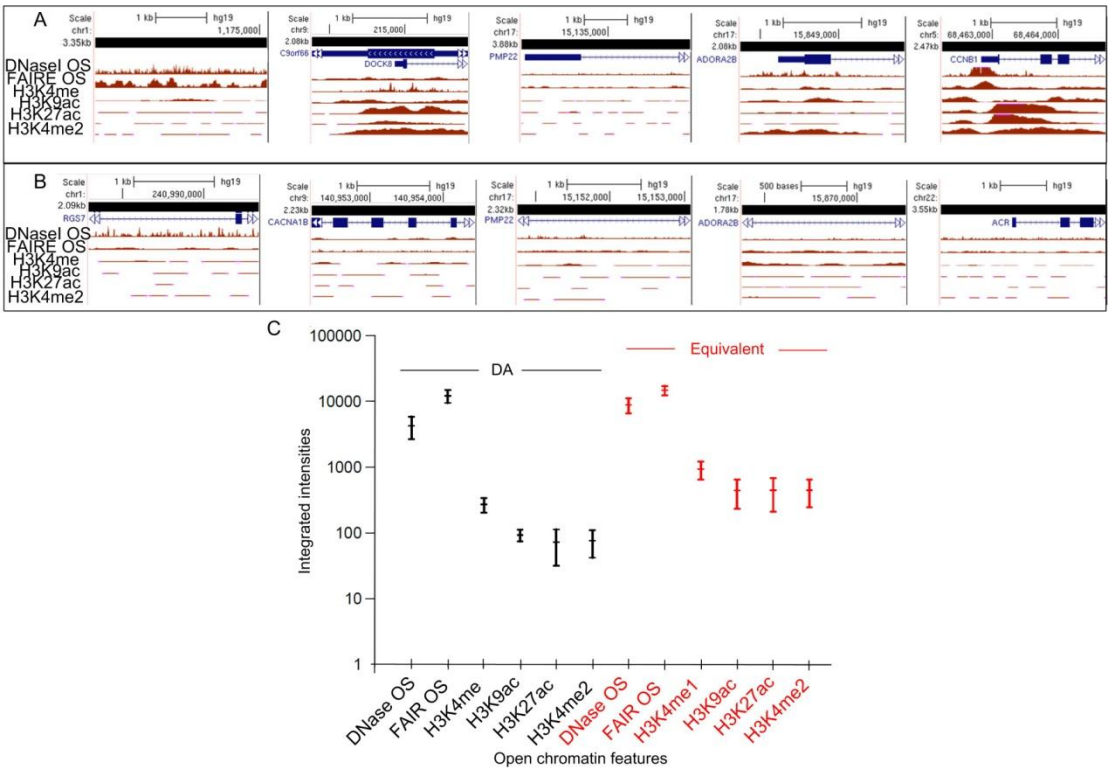

Figure 3-25. Correspondence of metaphase chromosome accessibility with epigenetic marks associated with open chromatin in interphase.

Genome browser tracks show integrated ChIP-seq signal intensities of open chromatin features (y-axis) determined by ENCODE. Genomic locations for a set of representative single copy probe intervals is provided (GRCh37) along x-axis, probe size in kilobase pairs is represented by black bar, and genes are shown in blue. (A) Genomic regions with equivalent accessibility show a higher density of open chromatin epigenetic features than regions with DA (panel B). (C) The distributions of integrated intensities for each open chromatin feature were plotted around the 95% confidence interval for all probe intervals provided in Table 1, and grouped according to whether the probes showed DA (black bars) or equivalent accessibility (red bars). Group means of the integrated intensity values are shown on the y-axis (y = log 10) and individual features of open chromatin are indicated on the x-axis. The mean integrated ChIP-seq intensities of open chromatin features were significantly different by ANOVA (p =1.0E-04), in particular for all histone marks and DNase I HS, between DA and sequences with equivalent accessibility.

origin, results not shown). Originally, *RGS7* and *PMP22*:IVS3 have shown DA in lymphocytes or lymphoblastoid cells (ectodermal origin) (Figures 3-15, 3-16). Both probes were mapped in fibroblast chromosomes from two individuals, coded FB01 (postnatal sample) and FB02 (prenatal sample).

Following hybridization with a single copy probe to within *RGS7*, differences in fluorescence intensities between homologs were observed in 33 of the 40 cells, in FB01, indicating DA in cells of fibroblast origin (p = 6.0E-04, z-score = 3.447, two-proportion z test). These findings were confirmed using the same single copy probe (*RGS7*) hybridized to fibroblast cells from a second individual, FB02, in which 22 of the 26 cells showed differences in fluorescence intensities between homologs (p = 3.7E-03, z-score = 2.900, two-proportion z test).

For single copy genomic target hybridized to within *PMP22*:IVS3, 62 of the 84 cells analyzed showed DA in FB01 and 21 of 30 cells showed DA in FB02 (p =1.0E-04, z-score = 3.939, two proportion z test). A different single copy probe within *PMP22*:IVS4-Ex5 on chromosome 17p12, which detects equivalent accessibility (i.e. no DA previously observed in ~75% of cells analyzed from lymphoblastoid), did not maintain equivalent accessibility in fibroblasts. Here DA was observed in ~50% of cells (n = 20 out of 41 analyzed, p = 8.73E-01, z-score = -0.16, two proportion z test) in FB01. In FB02, due to limited number of analyzable cells (i.e. low mitotic index and poor chromosome morphology), a comprehensive analysis could not be performed for *PMP22*:IVS4-Ex5. Although DA is apparent in an additional cell type of mesodermal origin, the extent to which it occurs for additional genomic regions is not known and a more comprehensive analysis is necessary.[‡‡‡]

[‡‡‡] Evaluation of DA in fibroblast cells, described above, did not appear in the original publication corresponding to this Chapter, as it was a response to one reviewer's comment. This finding is discussed further in Chapter 5.

3.5 Discussion

We have demonstrated differences in accessibility of allelic genomic targets in homologous metaphase chromosomes using independent and complementary approaches. First, we have detected and characterized DA with short, single copy FISH probes in genomic regions representative of telomeric, pericentromeric and chromosome arms (*RGS7*, *CACNA1B*, *PMP22*:IVS3, *ADORA2B*:IVS1, *ACR*, *HERC2*,*GABRA5*, and *SNRPN*) on cytogenetically distinguishable homologs. Differences in probe accessibility between homologs were non-random, and these findings were unrelated to the presence of chromosomal rearrangements that were used as markers to distinguish the homologs. With the one exception (*OPCML*), the brighter signal for each of the probes exhibiting non-random DA was biased to the same homolog in the cells from an individual. At the *OPCML* locus, DA occurred randomly, with either homolog exhibiting greater accessibility. Aside from non-random hybridization patterns, DA was also found to be heritable. The proximal 15q region showed greater accessibility on the paternally-derived homolog, irrespective of the presence of a small molecular deletion adjacent to these probes. This pattern was stable and preserved across two generations in a family carrying the deletion. While our results do not inform on the degree to which parent-of-origin effects contribute to DA, future studies of additional familial rearrangements of known parental origin (e.g. chromosome 11;22 translocation carriers) for the probes in this study, as well as others, will be useful in demonstrating this.

The three dimensional distribution of probes displaying DA was visualized by 3D-SIM. This technique improves optical resolution by two-fold over conventional imaging, and more precisely delineates probe signals. Imaging at sub-optical diffraction scale occurs at a much higher frame rate, which enabled us to quantify differences in chromatin structure between homologous regions for single copy FISH probes more efficiently relative to other super-resolution techniques (5,37,40). The spatial distributions of fluorescent hybridization to chromosome targets, emitted by single copy probes with DA, varied between homologous metaphase regions. The homolog with a lower hybridization intensity signal exhibited restricted probe occupancy in both the lateral and axial dimensions. The depth of the target sequences on the less accessible chromosome was

also found to be an order of magnitude less than its corresponding homolog in the same cell. Finally, the target sequence in the homolog with lower intensity hybridization occupied a smaller volume of metaphase chromatin based on the spatial distribution of its probe fluorescence. The radial chromosome structure hypothesis, suggests that accessibility should be related to the proximity of the target sequence to the chromosome surface (41). Our results suggest rather, that the differences in the volume and depth of the hybridized target sequence are more likely related to the degree of compaction of corresponding DNA in each of the homologous chromosomes.

Based on our ENCODE analysis of genomic regions with DA or equivalent accessibility (Figure 3-25 and Table 3-2), we envision that the differential condensation of homologous chromosomes represents a transition between parental and daughter cell epigenetic states. Histone marks and chromatin binding proteins may potentiate some genomic loci to maintain a less condensed configuration of one or both alleles during metaphase, which might then poise them to restructure open chromatin regions during the subsequent interphase in daughter cells (28–33). This transition state may be akin to a type of chromatin memory that recalls epigenetic marks derived from the preceding interphase so that they can be transmitted and re-established in subsequent daughter cells. To assess DA as a means of storing chromatin memory will be technically challenging. Chromatin modifications catalyze dynamic structural changes that arise over the course of interphase. It would be necessary to score DA at different cell cycle stages (e.g. G1, S, G2) to place these results in context. This would require enriched, synchronized cell populations at the end of G2 still possessing markers of interphase chromatin at the inception of chromosome condensation. Only a small fraction of unsynchronized cells are in G2. Interphase analysis was beyond the scope of the present study which was to demonstrate and characterize DA on mitotic metaphase chromosomes.

Reduced DNA accessibility may affect chromatin structure and histone modification (the most extreme instance being X chromosome inactivation), enabling the cell to maintain control over epigenetic variation in regulatory regions (42,43). This mechanism could exclude co-regulation of both allelic regions at a DA locus (44). Differences in chromatin accessibility may be a way to distinguish and spatially organize homologous loci so that

the less accessible locus is separated from its accessible counterpart. To this end, homologous chromosomes are known to be in repulsion, e.g. significantly more distant from one another in the interphase nucleus relative to heterologous pairs (45). Alternatively, DA could be envisioned as a stepwise process of chromosome condensation that packages DNA into highly condensed polymers in a tightly confined space (46), producing heterogeneous levels of compaction, as we have observed at discrete allelic loci.

Specific epigenetic marks such as histone modifications or topological constraints on chromatin that characterize each allele at the same locus may be a mechanism that underlies DA. Epigenetic marks can be propagated to ensure stability of chromatin memory and cellular identity in daughter cells, following mitosis (47). Our findings can be interpreted in this context. Previous studies have demonstrated retention of nuclease hypersensitivity, transcription factor occupancy, and selective histone marks on mitotic chromatin (28–33). Tri-methylation of histone H3 on lysine 9 and 27 is stably transmitted through interphase including mature post-replicative chromatin (48). Differential condensation of homologous chromosomal regions could encode these features in a structural form that effectively memorizes the state of chromatin preceding metaphase. Maintenance of chromatin memory would be important for normal development and disease avoidance (48).

Previous work has demonstrated differences in intrachromosomal compaction using large FISH probes (e.g. cosmids or bacterial artificial chromosome [BAC] based probes) hybridized to a complex mix of chromatin fibers (49). Reproducible differential hybridization patterns between metaphase homologs over short genomic distances (Table 3-2) have not been previously reported. The probes used to demonstrate DA are distinct from short single copy oligonucleotide (25–50 basepairs) DNA probes (50), densely tiled along a particular genomic region of ≥25 kb in length, that produce fluorescence signal intensities equivalent to a cosmid or a BAC. The differences in hybridization intensities to homologous chromosome regions of tiled oligonucleotides or large recombinant DNA probes are much less pronounced than the contiguous single copy probes used in the present study. BAC-based FISH probes, therefore, are not as

sensitive for detection of DA, as these probes likely contain both genomic intervals with equivalent accessible and DA targets, and their longer target length increases their overall fluorescence intensity.

We have combined single or low copy probes for FISH, which together are on average 10 kb or more in genomic length, to assess boundaries of chromosomal rearrangements in complex genomic architecture (20,21,24). The total length of these genomic targets does not solely dictate signal intensity. Probes of similar length and composition can vary in fluorescence intensity when hybridized to different regions in the human genome (20,21). In the present study, a 3.5 kb probe detects DA on chromosome 22 within *ACR* (Figure 3-15), whereas a smaller 2.08 kb single copy probe within *C9orf66* (Figure 3-14B) shows equivalent accessibility and bright signals to both homologs. In addition, a low copy probe with 3 distinct genomic targets spanning 8.5 kb within *HERC2* segmental duplicons exhibits DA (Supplemental Figure 3-17F). Finally, we did not find any remarkable differences in the GC content of individual single copy probes exhibiting DA relative to those showing equivalent accessibility (Supplemental Table 3-3). Our findings instead suggest that the context of the chromosomal regions themselves and their respective degrees of condensation primarily determine the differences in hybridization signal intensities that we observe.

3.6 Conclusions

We have previously designed and tested (20,21) novel single copy DNA probes to precisely ascertain small pathogenic chromosome copy number changes and complex genomic architecture in the human genome (24). In this study, we have expanded the utility of single copy DNA sequences to investigate chromatin accessibility differences between metaphase chromosome homologs. We demonstrate that chromatin accessibility differences are non-random with respect to specific homologous loci, they occur within exons, introns and intergenic regions, and these regions are not enriched for epigenetic marks of accessible interphase chromatin. Examination of allelic regions with DA, by super-resolution 3D-SIM, further showed that the internal chromatin structure of the accessible locus is less condensed relative to its inaccessible counterpart. Expanding the

analysis of DA on a genomic scale to larger chromosomal domains containing allelic regions can help generate a high resolution map of chromatin accessibility during metaphase. Relating this information to epigenetic modifications during interphase may provide possible insight into how higher order chromatin structure is remodeled during mitosis.

Supplemental Table 3-3. DA probe intervals with chromosome location (column 1), genomic coordinates (columns 2 and 3) and fractional GC content (column 4).

Chromosome (chr)	Start genomic coordinate [GrCh37]	End genomic coordinate [GrCh37]	% GC
chr1	240965538	240967390	0.34
chr1	240988582	240990678	* 0.41
chr5	1421588	1425427	0.62
chr5	9355970	9358454	0.42
chr5	9371425	9374496	0.42
chr8	116658428	116661455	0.38
chr8	116661938	116665132	0.39
chr9	140952206	140954439	*0.56
chr9	140969092	140971796	0.54
chr11	133180187	133182699	*0.41
chr13	100626271	100630715	0.47
chr13	100643221	100648153	0.42
chr15	22690247	22693115	0.49
chr15	22853681	22855541	0.38
chr15	25016909	25018586	0.44
chr15	25052358	25054037	0.36
chr15	25068481	25070727	*0.38
chr15	27117096	27119866	*0.40
chr15	28509526	28511337	*0.48

chr15	102388168	102389774	0.39
chr17	905599	910582	0.58
chr17	15150757	15153084	*0.46
chr17	15174803	15176657	0.48
chr17	15868752	15870532	*0.52
chr17	18153505	18154823	0.59
chr17	37861465	37863632	0.59
chr17	38512106	38514271	0.62
chr22	51175125	51178674	*0.54
chrX	592626	595515	0.57
chrX	597816	600430	0.51
chrX	602538	605057	0.65
chrX	8505855	8509075	0.38
chrX	9613498	9617784	0.42
chrX	9685383	9689409	0.48

GC content was calculated for an interval by obtaining the genomic sequence in FASTA format using the Galaxy Metaserver (url: https://usegalaxy.org/ website) and then inputting the sequence into Galaxy EMBOSS tool (‘geecee’) to calculate GC percentage. Average GC content for the 34 genomic regions with DA was 47.3% with a low standard deviation ($\mu = 0.473$, $\sigma = 0.08$). ‘*’ indicates probes hybridized on cells with distinguishable chromosome homologs in this study to examine random vs nonrandom features of chromatin accessibility. Refer to Table 1 for specific genic regions within each interval.

3.7 References

1. Londoño-Vallejo JA, DerSarkissian H, Cazes L, Thomas G. Differences in telomere length between homologous chromosomes in humans. Nucleic Acids Res. 2001 Aug 1;29(15):3164–71.

2. Ghosh PK, Rani R, Nand R. Lateral asymmetry of constitutive heterochromatin in human chromosomes. Hum Genet. 1979 Nov 1;52(1):79–84.

3. Wang Y, Maharana S, Wang MD, Shivashankar GV. Super-resolution microscopy reveals decondensed chromatin structure at transcription sites. Sci Rep. 2014;4:4477.

4. Ushiki T, Hoshi O. Atomic force microscopy for imaging human metaphase chromosomes. Chromosome Res. 2008;16(3):383–96.

5. Khan WA, Chisholm R, Tadayyon S, Subasinghe A, Norton P, Samarabandu J, et al. Relating centromeric topography in fixed human chromosomes to α-satellite DNA and CENP-B distribution. Cytogenet Genome Res. 2013;139(4):234–42.

6. Craig JM, Bickmore WA. Chromosome bands--flavours to savour. BioEssays. 1993 May;15(5):349–54.

7. Watanabe Y, Maekawa M. R/G-band boundaries: genomic instability and human disease. Clin Chim Acta. 2013 Apr 18;419:108–12.

8. Goradia RY, Davis BK. Asymmetry in sister chromatids of human chromosomes. J Hered. 1978 Dec;69(6):369–72.

9. Brito-Babapulle V. Lateral asymmetry in human chromosomes 1, 3, 4, 15, and 16. Cytogenet Cell Genet. 1981;29(4):198–202.

10. Schmid M, Haaf T, Grunert D. 5-Azacytidine-induced undercondensations in human chromosomes. Hum Genet. 1984;67(3):257–63.

11. Chambers EV, Bickmore WA, Semple CA. Divergence of mammalian higher order chromatin structure is associated with developmental loci. PLoS Comput Biol. 2013 Apr;9(4):e1003017.

12. Izumikawa Y, Naritomi K, Hirayama K. Replication asynchrony between homologs 15q11.2: cytogenetic evidence for genomic imprinting. Hum Genet. 1991 May;87(1):1–5.

13. Knoll JHM, Cheng S-D, Lalande M. Allele specificity of DNA replication timing in the Angelman/Prader–Willi syndrome imprinted chromosomal region. Nat Genet. 1994 Jan;6(1):41–6.

14. Dutrillaux B, Couturier J, Richer CL, Viegas-Péquignot E. Sequence of DNA replication in 277 R- and Q-bands of human chromosomes using a BrdU treatment. Chromosoma. 1976 Oct 12;58(1):51–61.

15. Terrenoire E, McRonald F, Halsall JA, Page P, Illingworth RS, Taylor AMR, et al. Immunostaining of modified histones defines high-level features of the human metaphase epigenome. Genome Biol. 2010 Nov 15;11(11):R110.

16. Banerjee T, Chakravarti D. A peek into the complex realm of histone phosphorylation. Mol Cell Biol. 2011 Dec;31(24):4858–73.

17. Jenuwein T, Allis CD. Translating the histone code. Science. 2001 Aug 10;293(5532):1074–80.

18. Bonenfant D, Towbin H, Coulot M, Schindler P, Mueller DR, van Oostrum J. Analysis of dynamic changes in post-translational modifications of human histones during cell cycle by mass spectrometry. Mol Cell Proteomics. 2007 Nov;6(11):1917–32.

19. Vagnarelli P. Chromatin reorganization through mitosis. Adv Protein Chem Struct Biol. 2013;90:179–224.

20. Rogan PK, Cazcarro PM, Knoll JHM. Sequence-Based Design of Single-Copy Genomic DNA Probes for Fluorescence In Situ Hybridization. Genome Res. 2001 Jun;11(6):1086–94.

21. Knoll JHM, Rogan PK. Sequence-based, in situ detection of chromosomal abnormalities at high resolution. Am J Med Genet A. 2003 Sep 1;121A(3):245–57.

22. Knoll J, Rogan P, inventors; Knoll J, Rogan P, original assignee: Single copy genomic hybridization probes and method of generating same. United States patent US 20030224356 A1. 2003 Dec 4

23. Knoll J, Rogan PK, inventors; Children's Mercy Hospital, Knoll J, Rogan P, assignee: Subtelomeric DNA probes and method of producing the same. International Patent WO2004029283 A2. 2004 Apr 8

24. Khan WA, Knoll JH, Rogan PK. Context-based FISH localization of genomic rearrangements within chromosome 15q11.2q13 duplicons. Mol Cytogenet. 2011 Aug 8;4(1):15.

25. Dorman SN, Shirley BC, Knoll JHM, Rogan PK. Expanding probe repertoire and improving reproducibility in human genomic hybridization. Nucleic Acids Res. 2013 Apr;41(7):e81.

26. Hamabe J, Kuroki Y, Imaizumi K, Sugimoto T, Fukushima Y, Yamaguchi A, et al. DNA deletion and its parental origin in Angelman syndrome patients. Am J Med Genet. 1991 Oct 1;41(1):64–8.

27. Bangs CD, Donlon TA. Metaphase chromosome preparation from cultured peripheral blood cells; in Haines JL, Korf BR, Morton CC (eds): Curr Protoc Hum Genet, pp 4.1.1-4.1.19 (John Wiley & Sons Inc., Malden 2005).

28. John S, Workman JL. Bookmarking genes for activation in condensed mitotic chromosomes. BioEssays. 1998 Apr;20(4):275–9.

29. Xing H, Wilkerson DC, Mayhew CN, Lubert EJ, Skaggs HS, Goodson ML, et al. Mechanism of hsp70i gene bookmarking. Science. 2005 Jan 21;307(5708):421–3.

30. Xing H, Vanderford NL, Sarge KD. The TBP-PP2A mitotic complex bookmarks genes by preventing condensin action. Nat Cell Biol. 2008 Nov;10(11):1318–23.

31. Zhao R, Nakamura T, Fu Y, Lazar Z, Spector DL. Gene bookmarking accelerates the kinetics of post-mitotic transcriptional re-activation. Nat Cell Biol. 2011 Nov;13(11):1295–304.

32. Yan J, Enge M, Whitington T, Dave K, Liu J, Sur I, et al. Transcription factor binding in human cells occurs in dense clusters formed around cohesin anchor sites. Cell. 2013 Aug 15;154(4):801–13.

33. Zaidi SK, Young DW, Montecino M, Lian JB, Stein JL, van Wijnen AJ, et al. Architectural epigenetics: mitotic retention of mammalian transcriptional regulatory information. Mol Cell Biol. 2010 Oct;30(20):4758–66.

34. Knoll JHM, Lichter P. In Situ Hybridization to Metaphase Chromosomes and Interphase Nuclei; in Haines JL, Korf BR, Morton CC, Seidman CE, Seidman JG, Smith DR (eds): Current Protocols in Human Genetics, pp 4.3.1-4.3.31 (John Wiley & Sons Inc., Malden 2005).

35. ENCODE Project Consortium. An integrated encyclopedia of DNA elements in the human genome. Nature. 2012 Sep 6;489(7414):57–74.

36. Arachchige AS, Samarabandu J, Knoll J, Khan W, Rogan P. An image processing algorithm for accurate extraction of the centerline from human metaphase chromosomes. 2010 17th IEEE International Conference on Image Processing (ICIP). 2010. p. 3613–6.

37. Flors C, Earnshaw WC. Super-resolution fluorescence microscopy as a tool to study the nanoscale organization of chromosomes. Curr Opin Chem Biol. 2011 Dec;15(6):838–44.

38. Barski A, Cuddapah S, Cui K, Roh T-Y, Schones DE, Wang Z, et al. High-resolution profiling of histone methylations in the human genome. Cell. 2007 May 18;129(4):823–37.

39. Thurman RE, Rynes E, Humbert R, Vierstra J, Maurano MT, Haugen E, et al. The accessible chromatin landscape of the human genome. Nature. 2012 Sep 6;489(7414):75–82.

40. Kner P, Chhun BB, Griffis ER, Winoto L, Gustafsson MGL. Super-resolution video microscopy of live cells by structured illumination. Nat Methods. 2009 May;6(5):339–42.

41. Strukov YG, Sural TH, Kuroda MI, Sedat JW. Evidence of Activity-Specific, Radial Organization of Mitotic Chromosomes in Drosophila. PLoS Biol. 2011 Jan 11;9(1):e1000574.

42. Gimelbrant A, Hutchinson JN, Thompson BR, Chess A. Widespread monoallelic expression on human autosomes. Science. 2007 Nov 16;318(5853):1136–40.

43. Wagner JR, Ge B, Pokholok D, Gunderson KL, Pastinen T, Blanchette M. Computational analysis of whole-genome differential allelic expression data in human. PLoS Comput Biol. 2010;6(7):e1000849.

44. Koeman JM, Russell RC, Tan M-H, Petillo D, Westphal M, Koelzer K, et al. Somatic pairing of chromosome 19 in renal oncocytoma is associated with deregulated EGLN2-mediated [corrected] oxygen-sensing response. PLoS Genet. 2008;4(9):e1000176.

45. Heride C, Ricoul M, Kiêu K, von Hase J, Guillemot V, Cremer C, et al. Distance between homologous chromosomes results from chromosome positioning constraints. J Cell Sci. 2010 Dec 1;123(Pt 23):4063–75.

46. Berndsen ZT, Keller N, Grimes S, Jardine PJ, Smith DE. Nonequilibrium dynamics and ultraslow relaxation of confined DNA during viral packaging. Proc Natl Acad Sci U S A. 2014 Jun 10;111(23):8345–50.

47. Margueron R, Reinberg D. Chromatin structure and the inheritance of epigenetic information. Nat Rev Genet. 2010 Apr;11(4):285–96.

48. Alabert C, Bukowski-Wills J-C, Lee S-B, Kustatscher G, Nakamura K, de Lima Alves F, et al. Nascent chromatin capture proteomics determines chromatin dynamics during DNA replication and identifies unknown fork components. Nat Cell Biol. 2014 Mar;16(3):281–93.

49. Gilbert N, Boyle S, Fiegler H, Woodfine K, Carter NP, Bickmore WA. Chromatin architecture of the human genome: gene-rich domains are enriched in open chromatin fibers. Cell. 2004 Sep 3;118(5):555–66.

50. Yamada NA, Rector LS, Tsang P, Carr E, Scheffer A, Sederberg MC, et al. Visualization of fine-scale genomic structure by oligonucleotide-based high-resolution FISH. Cytogenet Genome Res. 2011;132(4):248–54.

Chapter 4

4 Reversing Chromatin Accessibility Differences that Distinguish Homologous Mitotic Metaphase Chromosomes[1]

[1] Khan WA, Rogan PK, Knoll JH. Submitted

4.1 Introduction

Large-scale chromatin reorganization from interphase to metaphase is driven by mitotic-specific condensation factors (1,2). Broadly speaking, this is thought to include histone proteins undergoing post translational modifications and interaction of histone tails with neighboring nucleosomes (1). This is complemented with a network of non-histone proteins such as DNA methyltransferases involved in chromatin remodeling (3). At later stages of the cell cycle, solenoidal supercoiling by topoisomerase concomitant with structural maintenance of chromosomal (SMC) proteins (4) further influences the condensation process.

Previous studies have used chromatin-modifying reagents to study chromosome biology and investigate the large scale folding of the chromatin fiber. This has been performed, for instance, using chemical inhibitors which disrupt canonical chromatin-associating proteins (5–9) or enzymes which map chromatin accessibility in the human genome (10). Our interest in chromatin accessibility arose out of an observation that short, locus-specific, single copy DNA probes detect differences in DNA compaction between homologs at ~10% of allelic loci on mitotic metaphase chromosomes (11–13). This is referred to as differential accessibility (or DA) to specific, condensed chromosomal targets. In human lymphoblastoid cells, DA was non-random, heritable, and not unique to imprinted regions (13). This led to the suggestion that DA represents an intergenerational mechanism of storing epigenetic memory in mitotic metaphase chromosomes between parent and daughter cells (13).

The underlying basis for DA is unknown. Here, we assess the contributions of different epigenetic factors towards these allelic differences in chromatin accessibility during metaphase. Cells are treated with chromatin-modifying reagents that are known to alter chromosome condensation, with the objective of providing insight into the basis of DA during mitotic metaphase.

4.2 Materials & Methods

4.2.1 Cell Line and Single Copy DNA Probe Selection

Human lymphoblastoid cell lines were obtained from NIGMS Human Genetic Cell Repository [Coriell Institute, Camden, New Jersey]. Characterization of DA on cell lines used in the present study (GM06326, GM10958) has been previously determined by single copy DNA FISH probes (13). The homologous targets detected by these FISH probes are chromosomally normal. Additional cell lines with mutations of core cohesin components (Coriell Institute; GM20000, GM20466; Supplemental Table 4-1), causing chromatin decompaction (14), were also tested as potential indicators for DA. Single copy FISH probes detecting no DA (i.e. equivalent accessibility) (*C9orf66, PMP22*:IVS–Ex4) (13) were used as control hybridizations in cells with cohesin mutations alongside DA probes (*CACNA1B*, *PMP22*:IVS3). All cells were cultured, harvested for metaphase chromosomes, and processed for single copy FISH as described previously (15,16). Single copy probes detecting DA were tested among different concentrations of decondensation treatments in each cell line (Supplemental Table 4-1). Probes were selected from within chromosomal regions representative of telomeric, pericentromeric and loci adjacent to these sites. Details of the process by which single copy probes are designed and used to score for differences in chromatin accessibility has been described elsewhere (11–13).

4.2.2 Chromatin Decondensation Treatments

Chromatin-modifying reagents were incorporated *in vitro* into rapidly dividing, nonsynchronized, lymphoblastoid cell cultures. The reagents targeting non-histone proteins included ICRF-193 (a bisdioxopiperazine derivative inhibitor of mammalian DNA topoisomerase IIα; Sigma-Aldrich) and 5-AZC (inhibits DNA methyltransferase; Sigma-Aldrich). Targets of histone proteins included OA (inhibitor of protein phosphatase I; Sigma-Aldrich), TSA (inhibitor of histone deacetylase; Sigma-Aldrich), and UNC1999 (small molecule inhibitor of histone lysine methyltransferases EZH2 and EZH1 catalyzing H3K27me3; Sigma-Aldrich). Each treatment dose (Supplemental Table

4-1) was optimized to our experimental design using baseline concentrations previously reported from pharmacokinetic, biochemical, and cytological studies on lymphocyte, HeLa or MCF-7 cells (5–9). This was important, as it permitted the concentration to be optimized in order to minimize cell toxicity and preserve chromosome morphology and banding for homolog identification following FISH. Specifically, final concentrations in cell culture ranged from 0.05–3 µM (ICRF-193), 0.1–0.5 µM (OA), 0.2–15 µM (TSA), 5–45 µM (UNC1999), and 3.5–35 µM (5-AZC). Using published time points as a baseline (5–9), duration in cell culture was 0.5, 1, 20, 72, and 7 hours for ICRF-193, OA, TSA, UNC1999, and 5-AZC, respectively. Changes to higher order chromatin structure were visualized by DAPI-staining and epifluorescence microscopy before performing metaphase FISH. Cell cultures with no decondensation treatment were included as controls and taken through the chromosome harvest and FISH procedures in parallel with the treated cell cultures.

4.2.3 Immunofluorescence

Immunofluorescence staining of nuclear histone protein H3K27me3 was achieved with a rabbit IgG monoclonal antibody to H3K27me3 according to the manufacturer's protocol (Cell Signaling Technologies). This was performed to determine whether UNC1999 has an effect in reducing H3K27me3. Briefly, human lymphoblast cells were fixed in methanol/water (50:50 vol/vol), immediately spun onto microscope slides using a cytospin microcytocentrifuge (Statspin®), immersed in blocking buffer (0.3% triton X-100 with 3% BSA in 1X PBS) for 1 hour, and incubated with a primary rabbit monoclonal antibody against H3K27me3 overnight at 4^{o} C (antibody diluted in same diluent as blocking buffer except with 1% BSA). Cells were washed in 1X PBS and detected with goat anti-rabbit IgG conjugated to Dylight® 488 fluorochrome (Abcam®) for 1 hour at 37^{o}C, followed by three 5 minute washes in 1X PBS, and counterstained with DAPI. Nuclei were examined for presence of punctuate granular fluorescent signals. All UNC1999-treated cell cultures were set-up in duplicate. One set was harvested for metaphase chromosomes to evaluate the level of DA and corresponding culture set was processed for immunofluorescence staining of nuclei, as described above.

4.2.4 Quantification of DA following Metaphase Chromosome Decondensation

Single copy FISH probe epifluorescence was performed on Zeiss AxioImager.Z2 microscope and cells imaged with a CoolCube 1 camera using Metafer software (Metasystems). With background corrected, integrated probe signal intensities were determined using our previously described gradient vector flow algorithm (13,17). Probe signal intensities were normalized by taking the difference in integrated intensities between homologs, and dividing by the sum of the intensities of both homologs in a given cell.

Using 3D-SIM (Nikon Corporation), inter-homolog probe volume and depth were also quantified in treated cells relative to untreated controls. 3D-SIM images were reconstructed with NIS-Elements AR software (version 4.13.00, Nikon Canada Inc.) as previously described (13). The lateral fluorescence depth of a probe's signal on a given homolog was calculated from reconstructed optical sections, and volume of probe fluorescence was calculated following image segmentation and thresholding. All parameters quantified were analyzed for significance ($\alpha = 0.05$, two-tailed *t* test).

4.3 Results

4.3.1 Effects of Chromatin-Modifying Reagents on Metaphase Chromatin

Chromosome condensation was altered in two lymphoblastoid cell lines (GM06326, GM10958 obtained from NIGMS Cell Repository [Camden])) by separately treating them with several reagents known to modify chromatin. Treatments were directed at essential DNA modifications, proteins altering DNA structure, and histone proteins with established roles in chromatin compaction and remodeling (1,2,8). We assessed chromosome decatenation by inhibition of topoisomerase IIα with ICRF-193, histone dephosphorylation with okadaic acid (OA), deacetylation with trichostatin A (TSA), histone H3K27me3 demethylation with UNC1999, and DNA hypomethylation by

incorporation of 5-azacytidine (5-AZC). We also analyzed metaphase chromosomes from cell lines of patients with cohesin mutations (Supplemental Table 4-1, GM20000 and GM20466).

Chromatin-modifying inhibitor concentrations were first optimized to establish cytogenetic or immunofluorescence phenotypes in which their effects were clearly detectable, without significantly compromising mitotic indices or chromosome identification. Compared to untreated controls (Figure 4-26A), chromosome decatenation was decreased with 0.10–0.50 μM ICRF-193, which resulted in longer entangled metaphase chromosomes (Figure 4-26B-D). Incubation with only 0.25 μM and 0.50 μM OA caused premature chromosome condensation (PCC) (Figure 4-26E, F), as previously documented (5). Inhibition of histone deacetylation and K27 trimethylation by TSA (at 0.40 μM and 15.0 μM) and UNC1999 (5.0 μM and 15.0 μM), respectively, produced treated metaphase chromosomes that were similar in morphology to untreated control metaphase chromosomes. The TSA conditions used were based on a previous report of TSA-induced spreading of euchromatin, resulting in increased nuclear volume in HeLa cells (6). Relative to untreated cells (~5-6% of cells in metaphase), a decrease in mitotic cells (~1%) and occasional polyploid cells were also observed with 0.40 μM and 15.0 μM of TSA. Effects from UNC1999 treatment were confirmed by demonstrating substantially lower H3K27me3 immunofluorescence of interphase nuclei (Supplemental Figure 4-27). At the highest dose of UNC1999 [45 μM], absence of metaphase cells precluded further analysis. Incubation with 17.5 μM and 35.0 μM of 5-AZC showed decondensed heterochromatic regions (Figure 4-26G), as previously reported (8). At lower concentrations of 5-AZC (i.e. 3.5 μM and 7.0 μM), decondensation was not evident. As expected (18), immortalized cells from an individual with SC phocomelia showed absence of primary constrictions (Figure 4-26H) or heterochromatic repulsion (Figure 4-26F) in chromosomes due to cohesin mutation in *ESCO2* (Supplemental Table 4-1). Chromosomes of a Cornelia de Lange Syndrome individual with a mutation in *NIPBL*, another cohesion gene, exhibited apparently normal morphology.

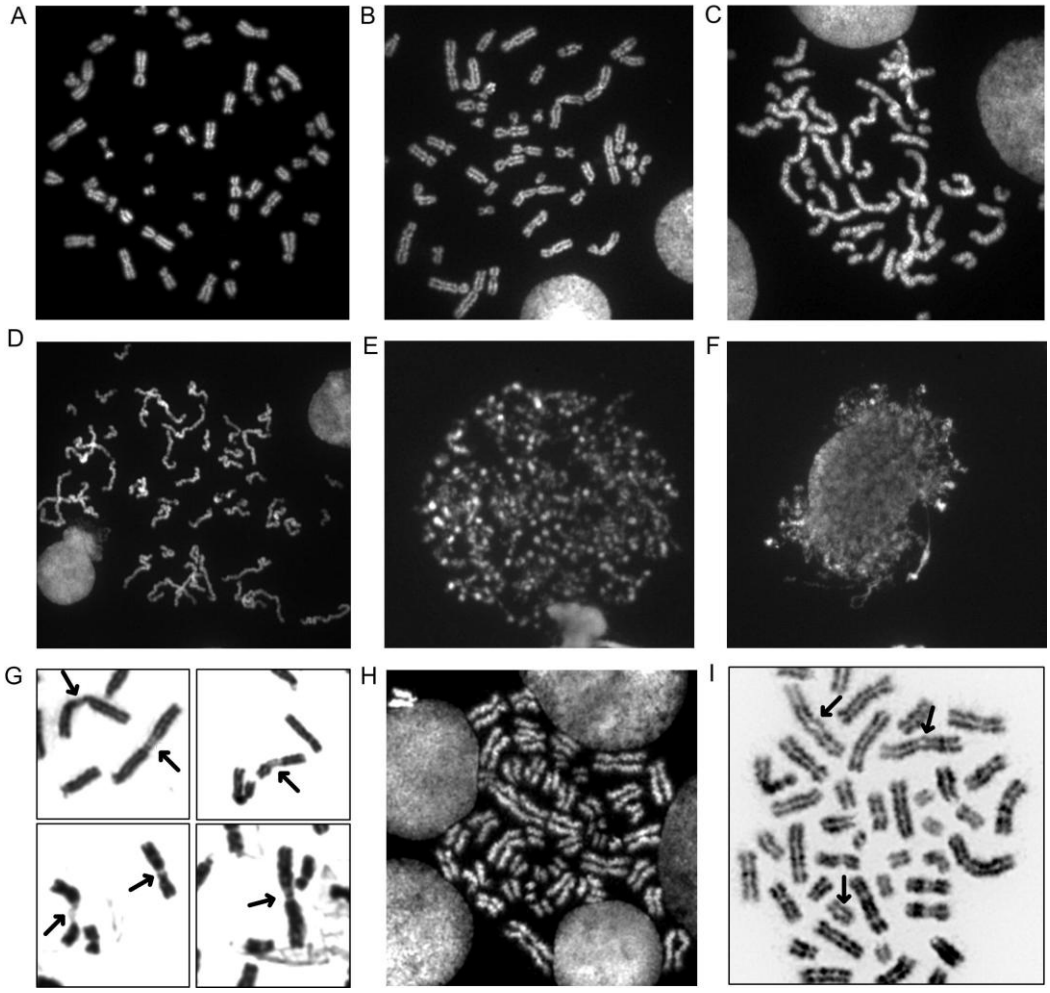

Figure 4-26. Decondensation treatments with visible effects on metaphase chromosome morphology.

(A) Normal metaphase cell with no treatment. (B–D) ICRF-193 treated cells at increasing drug concentrations (0.10, 0.25 and 0.50 μM; left to right) show increasingly elongated chromosomes. OA treated cells with (E) early condensation at S and (F) later S phase of cell cycle. G) 5-AZC treated metaphase chromosomes showing heterochromatin regions that did not condense (arrows). (H) Cell from individual with SC phocomelia (mutation in *ESCO2* c.604C>T, c.752delA, exon 3) showing premature sister chromatid separation primarily at heterochromatic regions near centromeres and I) heterochromatic repulsion (arrows) in most pericentromic regions resulting in a railroad track appearance to the chromosomes. Metaphase chromosomes from Cornelia de Lange individual (*NIPBL* c.5721del5, exon 31) appeared similar to untreated normal cells (panel A).

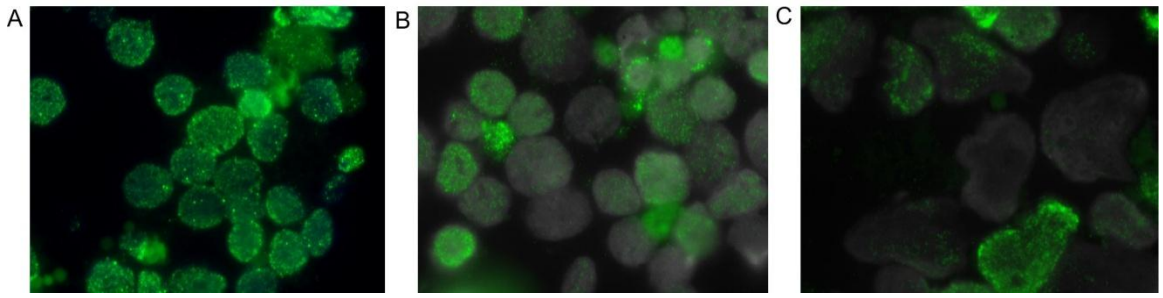

Supplemental Figure 4-27. Immunofluorescence staining of lymphoblastoid nuclei following selective inhibition of H3K27me3 associated with inactive chromatin.

(A) H3K27me3 staining shows bright punctate nuclear signals in untreated cells, but diminished fluorescence and reduced signals post-treatment with (B) 5μM and (C) 15μM UNC1999.

4.3.2 Targeting Topoisomerase IIα Eliminates Inter-homolog Chromatin Accessibility Differences in Metaphase at Distinct Loci with DA

In prior studies where we documented DA at ~ 10 % of the 305 genomic loci (11–13), ≥ 66% of metaphase cells (two-proportion Z-test, $p < 0.05$) consistently exhibited non-random differences in DNA probe fluorescence intensity between homologous regions (13). A set of single copy (sc) DNA probes for fluorescence *in situ* hybridization (scFISH), from imprinted and non-imprinted loci (*RGS7;* 2.09 kb, *CACNA1B*; 2.23 kb, *HERC2*; 1.82kb, *SNRPN*; 2.08kb, *ADORA2B*; 1.78kb, *PMP22*:IVS3; 2.32kb, *ACR*; 3.5kb, see Supplemental Table 4-1 for genomic coordinates), were hybridized to metaphase chromosomes and scored for DA according to these criteria (13).

We examined the effects of modifiers of chromatin accessibility that alter DNA compaction (topoisomerase IIα) on DA (Figure 4-28A). Inhibition of chromosome decatenation with the topoisomerase IIα inhibitor, ICRF-193, eliminated DA at multiple single copy loci, equalizing probe intensities on both homologs. This loss of DA was noted at multiple genomic targets in ICRF-193 treated cells (Figure 4-28B, C), including *RGS7*, *CACNA1B*, *ADORA2B*, *PMP22*:IVS3, and *ACR*. The effects of ICRF-193 on DA varied for certain genomic targets (e.g. *PMP22*:IVS3, *ACR*), between the cell lines (Figure 4-28B, C). *HERC2* was the only exception of a locus that maintained differences in accessibility (DA) across a range of ICRF-193 concentrations (Figure 4-28B, C, Supplemental Table 4-1). We suggest that the genomic context of this gene may explain the lack of response (see Discussion).

4.3.3 Quantification of Chromatin Accessibility following Topoisomerase IIα Inhibition

We quantified differences in probe hybridization between homologous loci using gradient vector flow (GVF) image analysis after ICRF-193 treatment, and compared results to untreated cells (13,17) (Figure 4-29, Supplemental Figure 4-30). Intensity differences in mean normalized probe fluorescence after ICRF-193 treatment were reduced by 2-fold

($\Delta\mu = 0.352$) relative to untreated control cells ($\Delta\mu = 0.725$) for *RGS7, CACNA1B, ADORA2B, PMP22*:IVS3, and *ACR* (Figure 4-29, Supplemental Figure 4-30), indicating that the drug equalizes accessibility of the probe to both homologous targets. In contrast, the intensities of a probe detecting DA within *HERC2* were similar in treated ($\Delta\mu = 0.662$) and untreated cells ($\Delta\mu = 0.713$) (Figure 4-29C, Supplemental Figure 4-30C).

Super-resolution 3-dimensional structured illumination microscopy (3D-SIM) provided direct evidence of the effects of ICRF-193 on equalization of chromosome target accessibility. 3D-SIM increases the spatial resolution with which metaphase chromatin accessibility can be visualized and quantified. Larger volumes and greater depths of probe hybridization are consistent with decreased condensation and lower DNA superhelicity. Quantification of the volumes occupied by the hybridized probe showed large differences in the distributions of probe depth between both homologs in untreated cells with DA (for example, *PMP22*:IVS3; Figure 4-31A). By contrast, Figure 4-31B shows the effects of ICRF-193 treatment, notably that both chromosomes are hybridized to similar depths and occupy equivalent volumes with the same single copy FISH probe, consistent with abrogation of DA. Overall, probe volume and depth were consistently different between untreated and treated categories (Figure 4-31C). The differences in probe hybridization volume are also visualized with 3D-anaglyph displays of untreated (Supplemental Movie 4-32) and ICRF-193-treated (Supplemental Movie 4-33) chromosome homologs from the same metaphase cells.

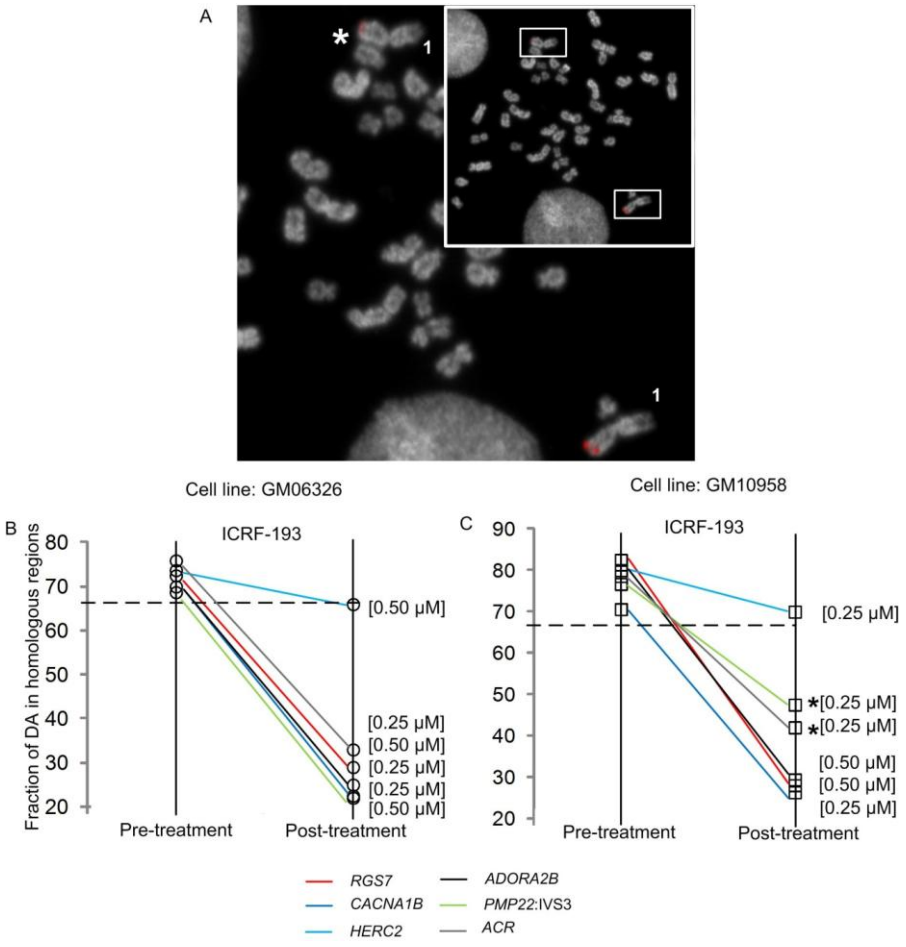
A
*
1
1
Cell line: GM06326
Cell line: GM10958
B
ICRF-193
Fraction of DA in homologous regions
80
70
60
50
40
30
20
[0.50 µM]
[0.25 µM]
[0.50 µM]
[0.25 µM]
[0.25 µM]
[0.50 µM]
Pre-treatment
Post-treatment
C
ICRF-193
90
80
70
60
50
40
30
20
[0.25 µM]
*[0.25 µM]
*[0.25 µM]
[0.50 µM]
[0.50 µM]
[0.25 µM]
Pre-treatment
Post-treatment
RGS7
CACNA1B
HERC2
ADORA2B
PMP22:IVS3
ACR

Figure 4-28. Representative example of differential accessibility (DA) and its reduction with topoisomerase IIα inhibitor ICRF-193.

(A) Metaphase cell showing chromosome 1 homologs hybridized with single copy DNA FISH probe from within *RGS7* (2.09 kb). Relative to its homolog, * marks the chromosome with the weaker probe hybridization signal; indicating DA. Inset shows metaphase cell with homologs of interest (boxed). (B-C) Ladder plots compare effect of topoisomerase IIα inhibitor, ICRF-193, on DA at various concentrations and genomic loci in two lymphoblastoid cell lines. Colored lines connecting two points, pre and post-treatment (x axis), represent different genomic targets indicated in the key. Frequency of DA to homologous regions is expressed as a percentage (y axis). Greater than two-thirds (dotted line) of the cells analyzed (n = 20-100 cells, μ = 43 cells/per target) in pre-treatment control showed DA. (B) In cell line GM06326, with the exception of *HERC2*, DA was significantly reduced post-treatment (z-score < -2.0, $p < 0.05$, two-proportion z test) at distinct genomic targets. (C) These findings were reproduced in a second cell line, GM10958, however in this case, reduction in DA was marginally significant at *PMP22*:IVS3 and *ACR* (indicated by *).

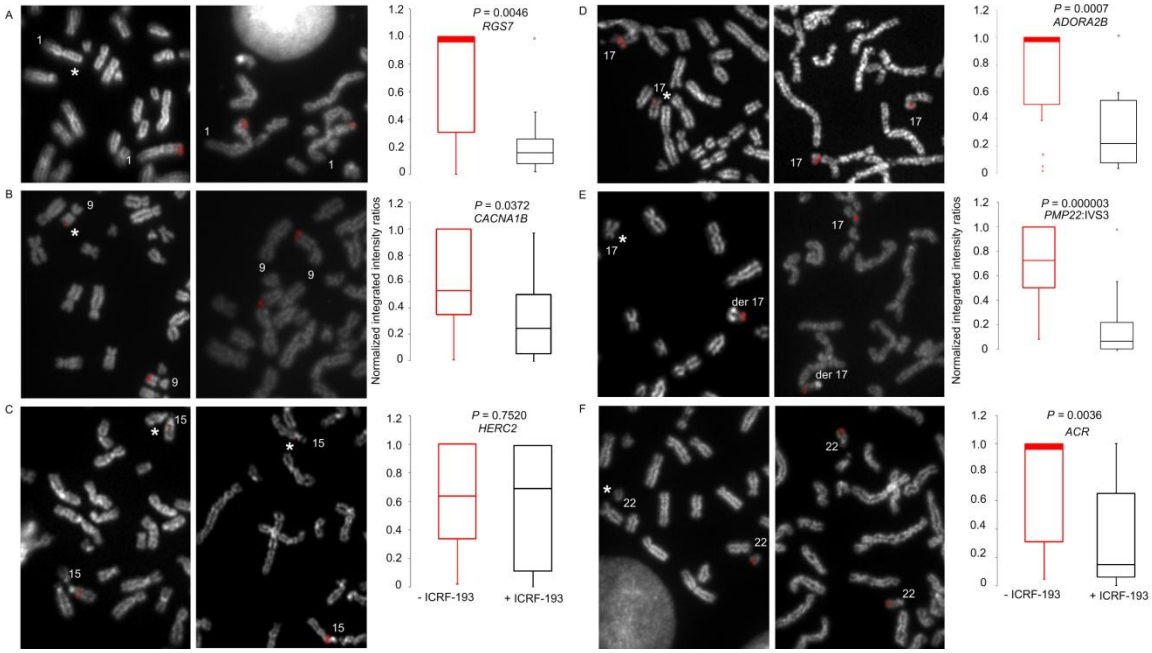
A
B
C
D
E
F
P = 0.0046
RGS7
P = 0.0372
CACNA1B
P = 0.7520
HERC2
P = 0.0007
ADORA2B
P = 0.000003
PMP22:IVS3
P = 0.0036
ACR
Normalized integrated intensity ratios
- ICRF-193
+ ICRF-193
der 17

Figure 4-29. Quantification of inter-homolog fluorescence intensities following chromosome decondensation with ICRF-193– part 1

(A-F) FISH with single copy probes targeting six distinct genomic regions within chromosomes 1q43 (*RGS7*), 9q34.3 (*CACNA1B*), 15q13.1 (*HERC2*), 17p12 (*ADORA2B*, *PMP22*:IVS3), and 22q13.33 (*ACR*) are indicated. For untreated chromosomes (left column, panels A-F respectively), probe signal is bright on one homolog and appears dim or not visible on corresponding target (*). For chromosomes treated with ICRF-193, (middle column, panels A-F respectively) probe signal is bright on both homologs. Probes detecting DA exhibited larger differences in inter-homolog DNA probe fluorescence (red box plots in right column: median intensity ratios: from 0.53 to 1, n = 125 cells). ICRF-193-treated chromosomes exhibited smaller differences in DNA probe fluorescence (black box plots in right column: median intensity ratios from 0.08-0.27, n = 121 cells) ($p < 0.05$; two tail t-test), suggesting that both chromosomal homologs were equally accessible, except at the *HERC2* locus, where DA was not completely reversed. In instances where median is coincident with upper quartile, it is emphasized by a thick line to show distinction with median in corresponding category. The notation ‘der 17’ refers to a derivative chromosome 17 homolog resulting from a translocation between chromosome Y and 17.

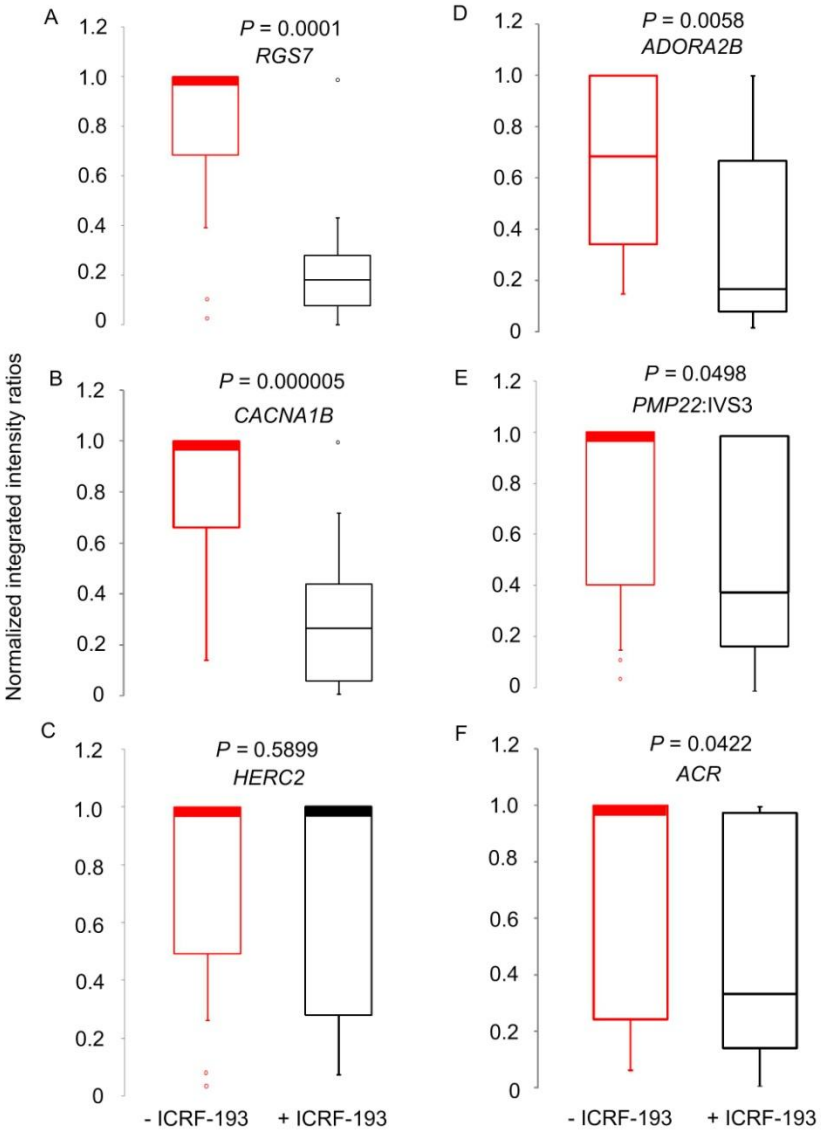
A
P = 0.0001
RGS7
D
P = 0.0058
ADORA2B
B
P = 0.000005
CACNA1B
E
P = 0.0498
PMP22:IVS3
C
P = 0.5899
HERC2
F
P = 0.0422
ACR
Normalized integrated intensity ratios
1.2
1.0
0.8
0.6
0.4
0.2
0
- ICRF-193
+ ICRF-193

Supplemental Figure 4-30. Quantification of inter-homolog fluorescence intensities following chromosome decondensation with ICRF-193 in independent cell lines – part 2

(A–F) Box plots show normalized integrated intensity ratios (y axis) following scFISH for six distinct genomic regions within chromosomes 1q43 (*RGS7*), 9q34.3 (*CACNA1B*), 15q13.1 (*HERC2*), 17p12 (*ADORA2B*, *PMP22*:IVS3), and 22q13.33 (*ACR*) in untreated and treated cells (x axis). GVF measurements in cells hybridized with single copy probes detecting DA from within *RGS7*, *HERC2*, *PMP22:*IVS3, and *ACR* are indicated from cell line GM10958. Measurements of normalized inter-homolog intensities for *CACNA1B*, and *ADORA2B* are indicated from cell line GM06326. The same genomic regions were hybridized in opposite cell lines and inter-homolog differences quantified, as shown in Figure 4-29. Probes detecting DA exhibited larger differences in inter-homolog DNA probe fluorescence (red box plots: median intensity ratios: from 0.68 to 1, n = 125 cells). ICRF-193 treated chromosomes exhibited smaller differences in DNA probe fluorescence (black box plots: median intensity ratios from 0.15-0.39 , n = 118 cells) ($p < 0.05$; two tail t-test,), suggesting retrieval of the less accessible chromosome target, except in the case *HERC2*, in which DA was not completely reversed. In instances where median is coincident with upper quartile, it is emphasized by a thick line to show distinction with median in corresponding category.

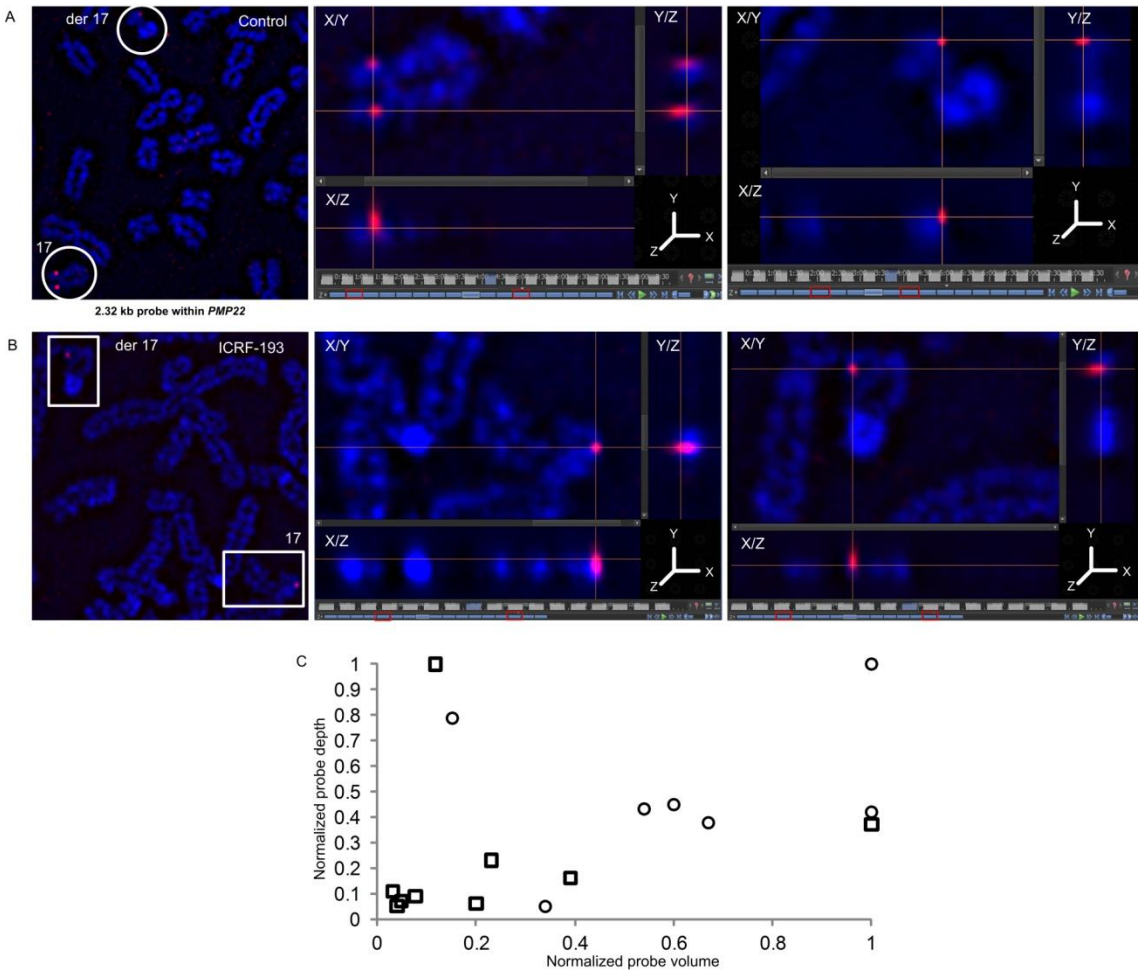
A
der 17
Control
17
2.32 kb probe within PMP22
X/Y
Y/Z
X/Z
B
der 17
ICRF-193
17
C
Normalized probe depth
Normalized probe volume
0
0.1
0.2
0.3
0.4
0.5
0.6
0.7
0.8
0.9
1

Figure 4-31. Visualization of internal chromosome accessibility with super resolution 3D-SIM.

(A) Untreated metaphase cell showing DA between chromosome 17 homologs (left panel, circled) hybridized with single copy FISH probe within *PMP22*:IVS3 (2.32 kb). Probe depth spans 1.30 μm or 10 of 17 (middle panel, red boxes) and 0.65 μm or 5 of 17 (right panel, red boxes) optical sections within accessible and less accessible homologs, respectively. (B) Decondensed metaphase chromosomes (left panel, boxed) hybridized with same *PMP22*:IVS3 (2.32kb) single copy probe exhibits equal accessibility to both homologs. Probe depth (10 of 17 and 11 of 17 sections) for each homolog spans 1.30 μm (middle panel) and 1.43 μm (right panel), respectively. Same cell line (GM06326) is used in A and B. Crosshairs are over maximal fluorescence. Der 17 refers to derivative chromosome 17. This was used as a cytogenetic marker to distinguish parental homologs. (C) Scatterplot of individual cells showing differences in hybridized probe volume and depth for untreated and treated cells. Normalized mean differences in hybridized probe volume ($\Delta\mu = 0.730\ \mu m^3$, circles) and depth ($\Delta\mu = 0.651\ \mu m$, squares) for different untreated cells (n = 10 cells) for genomic target (*PMP22*:IVS3) with DA. These were significantly greater (volume: p = 0.003, depth: p = 0.013; two-tailed t test) compared to the same genomic target post-treatment (indicated with squares) in which both alleles were accessible (volume: $\Delta\mu = 0.237\mu m^3$, depth: $\Delta\mu = 0.238\ \mu m$, n = 9 cells). Single cell outliers (y_{max} or x_{max}) with ICRF-193 treatment did not affect p-value cut off ($\alpha = 0.05$). Normalized probe volume and depth were not strongly correlated pre (r = 0.559) and post-treatment (r = 0.164).

Supplemental Movie 4-32. 3D anaglyph view of single copy FISH target (*PMP22*:IVS3) between chromosome homologs.

Chromosome 17 homologs appear in object space rotated 360^{o} around the z-axis at 15 frames per second to emphasize DNA probe volume in context of reconstructed chromosomes. Probe volume inside the metaphase chromosome in left panel (corresponding to normal chr 17 in Figure 4-31A) exhibits greater occupancy compared to its less accessible target (right panel, corresponding to der 17 in Figure 4-31B), depicting inter-homolog DA from all perspectives. Reconstructed optical sections were taken over 17 z-stacks, at 0.13 μm per stack, with 3D-Structured Illumination Microscopy. (Link to movie S1) ‡‡‡‡

‡‡‡‡ Movie uploaded to Thesis repository at University of Western Ontario (Scholarship@Western) and can also be linked through http://www.cytognomix.com/wp-content/uploads/2015/03/Movie-S1-PMP22-without-ICRF-193.mp4

Supplemental Movie 4-33. 3D anaglyph view of single copy FISH target (*PMP22:*IVS3) between chromosome homologs following topoisomerase IIα inhibition.

Chromosome 17 homologs appear in object space rotated 360° around the z-axis at 15 frames per second to emphasize DNA probe volume in context of reconstructed chromosomes. Probe volume inside the metaphase chromosome in left panel (corresponds to normal chr 17 in Fig 4-31B) is similar compared to the other homologous target (right panel, corresponds to der 17 in Fig 4-31B) depicting equalization of DA from all angles. Bottom panels show still image of equalized probe fluorescence without chromosome context. Reconstructed optical sections were taken over 17 z-stacks, at 0.13 µm per stack, with 3D-Structured Illumination Microscopy. (Link to Movie S2)[§§§§]

[§§§§] Movie uploaded to Thesis Repository at University of Western Ontario (Scholarship@Western) and can also be linked through http://www.cytognomix.com/wp-content/uploads/2015/03/Movie-S2-PMP22-with-ICRF-193.mp4

4.3.4 Inhibitors of Histone Modifications, Cytosine Methylation, and Mutations in Cohesin, a Non-histone Protein, do not alter DA

We also examined the effects of histone modifications that typically influence interphase chromatin accessibility on DA in metaphase. Differences in probe hybridization intensity were evaluated by scFISH following treatment with OA, which inhibits protein phosphatase I and IIα (5), leading to PCC (Figure 4-26E,F). We observed that the range of cell numbers (n = 20–66) with DA following OA treatment were not significantly different ($p > 0.05$, two proportion z test) with respect to untreated cells (n = 32–51) (Supplemental Table 4-1). This was observed among single copy probes detecting distinct genomic targets within *RGS7*, *CACNA1B*, and *ADORA2B* at both concentrations (0.25 μM and 0.50 μM) in duplicate cell lines (Supplemental Figure 4-34A). OA treatment also produced a population of rare tetraploid-like cells (Supplemental Figure 4-35) [possibly due to unscheduled DNA replication (19)]. In terms of morphology, they look similar to G1-PCC cells as observed in human lymphocytes (20). Among tetraploid-like cells, it was observed that the extra pair of homologs did not hybridize using probes from within distinct genomic targets (*ADORA2B* with DA or *PMP22*:IVS-Ex5 no DA, Supplemental Figure 4-35). This result suggests that in order to re-establish their respective allelic accessibility patterns for newly synthesized genomic templates, progression through a complete mitotic cycle may be a prerequisite. Relative to diploid cells in which brighter hybridizations occurred predominantly to the derivative chromosome 17, tetraploid-like cells did not show a bias in bright hybridizations to the derivative chromosome for probes detecting DA (*ADORA2B*) or equivalent accessibility (*PMP22*:IVS-Ex5) (Supplemental Figure 4-36). Moreover, the majority of the cells showed hybridizations to fewer than 4 chromosomes (Supplemental Figure 4-36), suggesting DA or equivalent accessibility was unperturbed between homologous targets.

Metaphase chromosomes from cells treated with TSA, an agent with well characterized properties in producing hyperacetylated chromatin during mitosis (6), were hybridized with two single copy probe targets from within *RGS7* and *CACNA1B*. The range of cells exhibiting DA (n = 25–37) were not significantly different ($p > 0.05$, two proportion z

test) with respect to untreated cells (n = 28–34) (Supplemental Table 4-1). This was observed at both concentrations (0.40 μM and 15.0 μM) in duplicate cell lines (Supplemental Figure 4-34B), evaluated from these homologous targets. The deacetylase inhibitor, therefore, did not change differential chromatin accessibility at locus specific sites. TSA produces hyperacetylated, highly distorted chromatin that is incompatible with proper mitotic chromosome condensation (21). Although we did not observe distorted chromatin structures in our analyses, it is likely that the decrease in the number of analyzable mitoses (~1% observed in metaphase), relative to untreated cells (5–6%) is a consequence of this effect of the deacetylase inhibitor.

Certain marks of histone methylation such as lysine 27 tri-methylation on histone H3 are stable through interphase and are found on post-replicative chromatin (22). H3K27me3 is associated with formation of silent chromatin (7). It was targeted in order to evaluate whether it can eliminate DA in mitotic metaphase. Selective inhibition of H3K27me3 by UNC1999 was monitored using immunofluorescence and was found to be reduced relative to untreated cells (Supplemental Figure 4-27). UNC1999 blocks histone methyltransferase EZH2, a component of the polycomb repressive complex which catalyzes H3K27me3 (7). We found that following UNC1999 inhibition of H3K27me3, the range of cells (n = 20–40) exhibiting DA post-treatment were similar ($p > 0.05$, two proportion z test) compared to untreated cells (n = 27–36) (Supplemental Table 4-1). DA was observed among single copy probes detecting distinct genomic targets within *RGS7*, *ADORA2B*, and *SNRPN* at multiple concentrations (5μM and 15 μM) of UNC1999 in duplicate cell lines (Supplemental Figure 4-34C). Only cells treated with 5μM of UNC1999 from GM10958 cell line were included in the statistical analysis of DA for *SNRPN* and *ADORA2B*, due to insufficient numbers of mitoses at 15μM (Supplemental Table 4-1). While the persistence of K27 methylation on post-replicative chromatin has been documented (22), the polycomb group of proteins which catalyze its effect are lost from mitotic chromosomes during the condensation process (23). Therefore, targeting proteins which catalyze such modifications, especially where mitotic chromatin organization interferes with their stability (24), may not be sufficient to eliminate inter-homolog differences in chromatin accessibility.

In addition to inhibition of histone methylation, we tested loss of DNA methylation with 5-AZC as a potential basis for DA. 5-AZC incorporates into replicating DNA and induces its demethylation by blocking DNA methyltransferase activity (8). Following scFISH of 5-AZC treated metaphase chromosomes, we observed that the range of cells (n = 23–80 μ = 40 cells) in which DA was observed were not significantly different ($p > 0.05$, two proportion z test) with respect to untreated cells (n = 26–45, μ = 34) (Supplemental Table 4-1). This was true for single copy probes detecting distinct genomic targets within *RGS7*, *PMP22*:IVS3 as well as *HERC2*, which is in proximity to a heterochromatic region of chromosome 15.The latter contains highly methylated DNA and is sensitive to effects of 5-AZC induced decondensation (8). Since high dose of 5-AZC concentrations are also suggested to cause multiple decondensations at Giemsa-band positive regions along chromosomes (8), we tested 5–10 fold higher concentrations in our study (Supplemental Table 4-1) relative to previous reports (8). Despite this, the fraction of DA was not altered by loss of DNA methylation with 5-AZC at all tested concentrations in duplicate cell lines (Supplemental Figure 4-34D). It has been suggested that cytidine analogs which block DNA methylation do not affect all loci uniformly (25) or to the same degree, as we observed for ICRF-193 treated metaphase chromosomes.

SC phocomelia and Cornelia de Lange cell lines with regulatory mutations in cohesin (Supplemental Table 4-1) were used to evaluate DA since they have been reported to cause global chromatin decompaction in interphase (14). Relative to control single copy probes detecting no DA within genomic targets corresponding to *C9orf66* and *PMP22*:IVS4–Ex5 (Supplemental Figure 4-34E), single copy probes with DA (*CACNA1B*, and *PMP22*:IVS3) retained differences in fluorescence intensities for each probe (Supplemental Figure 4-34E) in at least 66% of metaphase cells examined. Unlike the effect of topoisomerase IIα on DA, cohesin likely does not have a role in shaping DNA accessibility differences between metaphase chromosomes.

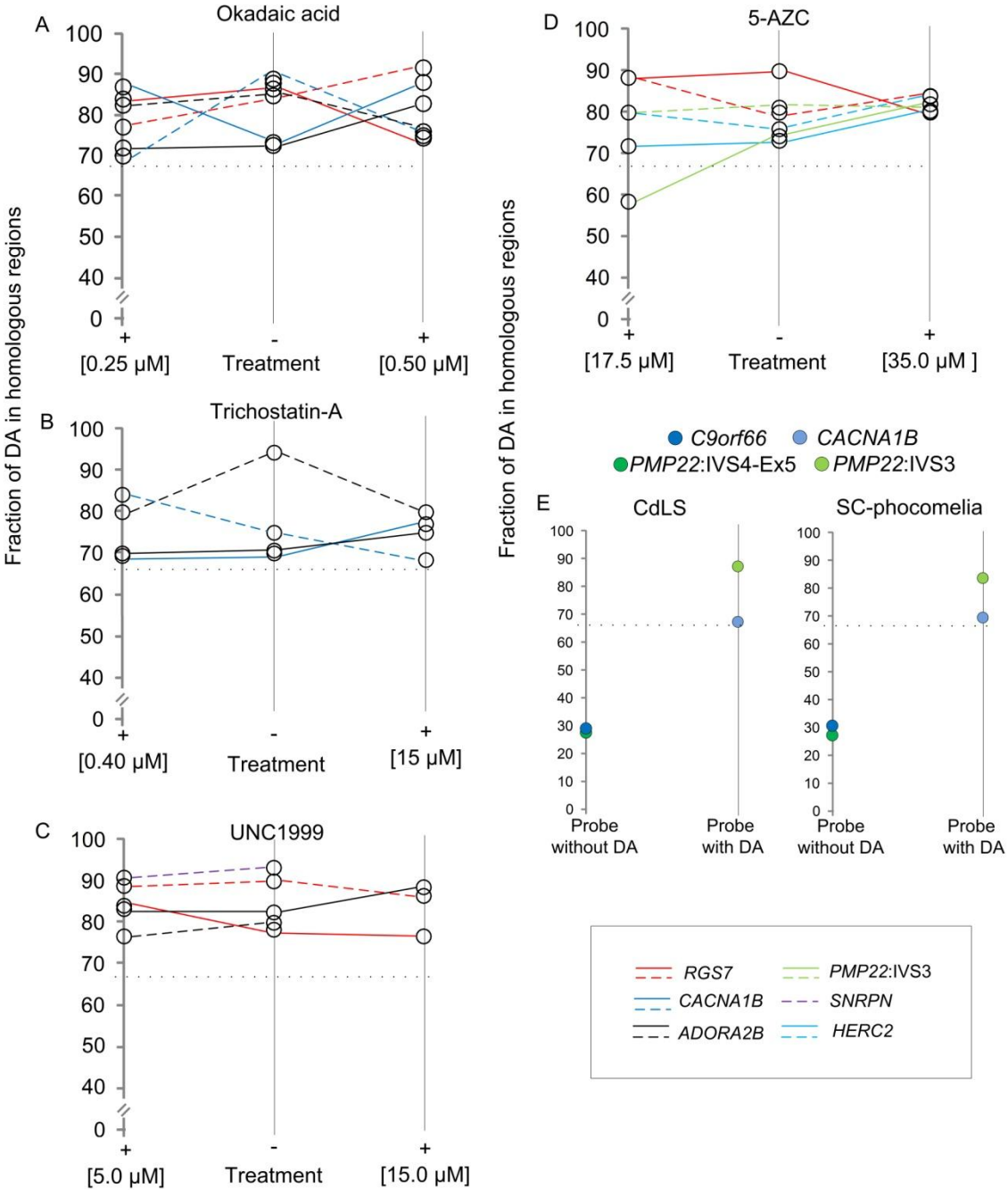
A
Okadaic acid
Fraction of DA in homologous regions
[0.25 µM]
Treatment
[0.50 µM]
B
Trichostatin-A
[0.40 µM]
Treatment
[15 µM]
C
UNC1999
[5.0 µM]
Treatment
[15.0 µM]
D
5-AZC
[17.5 µM]
Treatment
[35.0 µM]
C9orf66
CACNA1B
PMP22:IVS4-Ex5
PMP22:IVS3
E
CdLS
SC-phocomelia
Probe without DA
Probe with DA
RGS7
CACNA1B
ADORA2B
PMP22:IVS3
SNRPN
HERC2

Supplemental Figure 4-34. Pre- and post-treatment effects of chromatin-modifying reagents and cells with cohesin mutations on DA.

(A–E). Ladder plots compare fraction of DA (i.e. expressed as a percentage along y axis) with (+) and without (-) chromatin-modifying reagents at various concentrations (x axis). Fraction of DA is illustrated with solid and dashed lines for GM06326 and GM10958 cells, respectively. Each line color corresponds to a different probe (indicated in key; *RGS7*, *CACNA1B*, *ADORA2B*, *PMP22*:IVS3, *SNRPN*, *HERC2)* or control probes exhibiting equal accessibility (*C9orf66*, *PMP22*:IVS4-Ex5). (A-C) In all cases, greater than two-thirds of the cells analyzed (n = 20–100, μ = 43 cells/per target) maintained DA pre- and post- reagent treatment in both cell lines at all concentrations tested. Black dotted line indicates threshold for DA. This suggests allelic chromatin accessibility differences were not reversed with chromatin-modifying reagents targeting histone proteins. This was also true for chromatin-modifying reagents that prevent (D) cytosine methylation (single outlier in panel D is *PMP22*:IVS3) or cohesin mutations (E) in cells from individuals with Cornelia de Lange Syndrome (CdLS) and SC-phocomelia Syndrome. Probes that do not detect DA, *C9orf66* and *PMP22*:IVS4-Ex5, were hybridized to cell lines with cohesin mutations, as controls. Outlier in panel D (*PMP22*:IVS3) refers to ~ 60% of the cells (n = 41 cells total) with DA in cell line GM06326 following 5-AZC [17.5 μM].

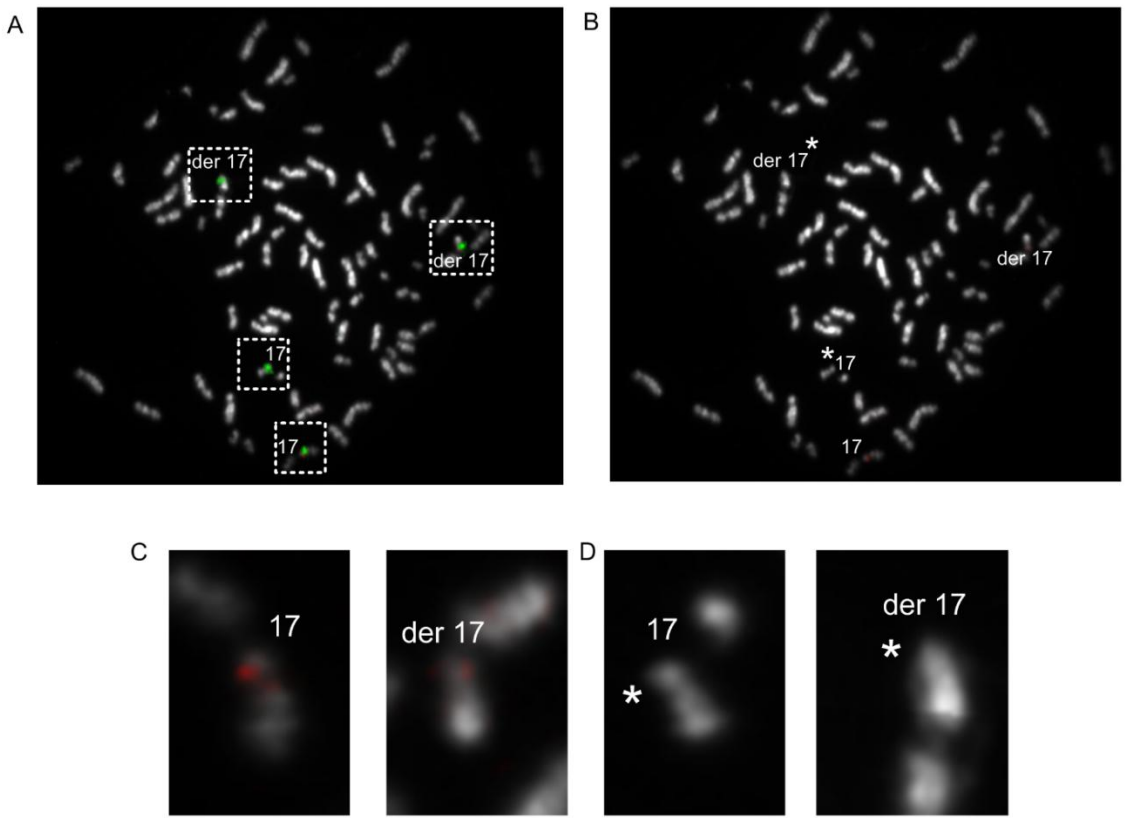
A
der 17
der 17
17
17
B
der 17
*
der 17
*17
17
C
17
der 17
D
17
*
der 17
*

Supplemental Figure 4-35. Examples of DA in tetraploid-like cells after okadaic acid treatment.

(A) Chromosome 17s are marked with centromeric probe (D17Z1, green) to identify the four copies in the tetraploid-like cell (boxed). The parental homologs were distinguishable based on a Y;17 chromosome translocation in cell line GM06326, resulting in a normal chromosome 17 and a derivative (der) 17. (B) Tetraploid-like cell shows two of the four homologs hybridized with a 1.78 kb scFISH probe (red) within *ADORA2B* on chromosome 17p12, indicating DA. (C) Zoom in view of the same cell from panel B shows a bright hybridization to the normal chromosome 17 and a weaker hybridization to its corresponding homolog (observed in n = 16/25 cells). (D) The other pairs of normal chromosome 17 and der 17 (asterisk) showed absence of hybridization to their respective allelic targets (n = 12/28 cells). The same outcome shown in panel D was predominantly observed in a region with no DA (*PMP22*: IVS-Ex5) in which two of the four homolog pairs did not hybridize (n = 13/17 cells).

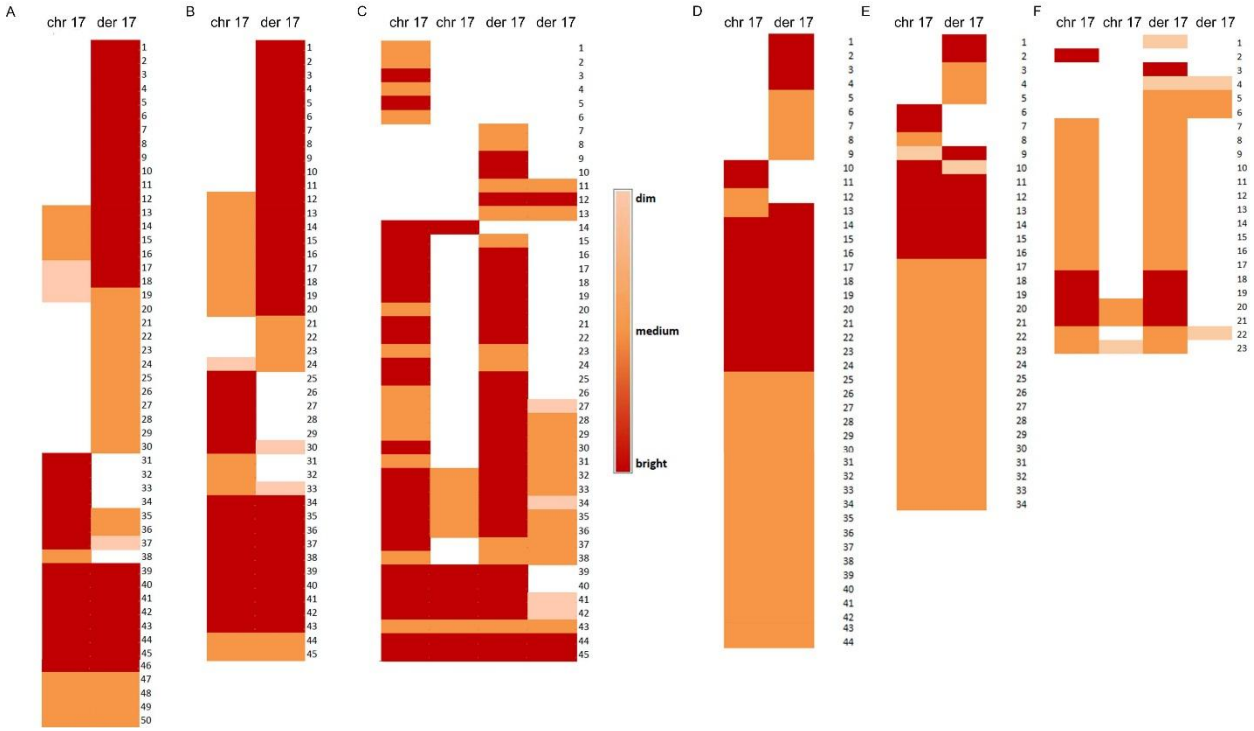
A
chr 17
der 17
B
chr 17
der 17
C
chr 17
chr 17
der 17
der 17
dim
medium
bright
D
chr 17
der 17
E
chr 17
der 17
F
chr 17
chr 17
der 17
der 17

Supplemental Figure 4-36. Map of hybridization patterns with and without premature chromosome condensation

Metaphase cells are numbered consecutively along right margin of each panel. Chromosome 17 homologs are labeled at the top of each panel as the normal 'chr 17' or derivative chromosome 17 (der 17). The der 17 homolog in GM06326 cell line is involved in a (Y;17) reciprocal translocation. The hybridization intensities of 1.78 kb (with DA, panels A-C) and 3.8 kb (without DA, panels D-F) single copy probes within *ADORA2B* (17p12) and *PMP22*:IVS4-Ex5 respectively are divided into dim (light pink), medium (orange), bright (red) or none (white box). (A) Hybridization map of diploid metaphase cells with no OA treatment shows DA in 38 out of 50 cells (cells 1-38), with bright hybridization predominantly on the der 17 (cells 1-30). (B) Diploid metaphase cells treated with OA with similar hybridization patterns to those observed in panel A. (C) Hybridization map of tetraploid-like cells indicate 2 normal and 2 der 17 homologs per cell. The majority of the cells show hybridizations to fewer than 4 chromosomes, with the more intense fluorescence common to either one copy of a normal or a copy of der chromosome 17. (D) Hybridization map of diploid metaphase cells with no OA treatment predominantly show equivalent accessibility in 31 out of 44 cells (cell numbers 14-44). (E) Diploid metaphase cells treated with OA with similar hybridization patterns to those observed in panel D. (F) Hybridization map of tetraploid-like cells indicate equivalent accessibility between 1 normal and 1 der 17 (cells 7-23). Similar to panel C, hybridizations to the second pair of normal 17 or der 17 are either absent (white box) or appear dim. Tetraploid-like cells with single chromosome hybridizations, hybridizations to only two normal chromosome 17s or two der 17s were excluded, as they could not be analyzed for DA which is assessed between homologs.

Supplemental Table 4-1. Summary of cells with and without DA following chromosome decondensation treatments.

Cell line	sc probe location (GRCh37); Overlapping Gene	Decondensation treatment [concn.]	No of cells	
			w/ DA	w/o
DNA modifying inhibitors				
GM06326	chr1:240988582-240990678; *RGS7*	ICRF-193 [0.50 µM]	11	27
" "	" "	ICRF-193 [0.25 µM]	25	5
" "	" "	No ICRF-193 control	29	11
GM10958	chr1:240988582-240990678; *RGS7*	ICRF-193 [0.50 µM]	18	46
" "	" "	ICRF-193 [0.25 µM]	25	27
" "	" "	No ICRF-193 control	33	7
GM06326	chr9:140952206-140954439; *CACNA1B*	ICRF-193 [0.50 µM]	9	31
" "	" "	ICRF-193 [0.25 µM]	14	16
" "	" "	No ICRF-193 control	21	9
GM10958	chr9:140952206-140954439; *CACNA1B*	ICRF-193 [0.50 µM]	10	28
" "	" "	ICRF-193 [0.25 µM]	18	14
" "	" "	No ICRF-193 control	24	10
GM06326	chr15:28509526-28511337; *HERC2*	ICRF-193 [0.50 µM]	33	17
" "	" "	ICRF-193 [0.25 µM]	22	9
" "	" "	No ICRF-193 control	27	10
GM10958	chr15:28509526-28511337; *HERC2*	ICRF-193 [0.50 µM]	40	8
" "	" "	ICRF-193 [0.25 µM]	56	24
" "	" "	No ICRF-193 control	32	8

GM06326	chr17:15868752-15870532; *ADORA2B*	ICRF-193 [0.50 µM]	10	25
" "	" "	ICRF-193 [0.25 µM]	10	30
" "	" "	No ICRF-193 control	37	16
GM10958	chr17:15868752-15870532; *ADORA2B*	ICRF-193 [0.50 µM]	10	24
" "	" "	ICRF-193 [0.25 µM]	23	18
" "	" "	No ICRF-193 control	47	13
GM06326	chr17:15150757-15153084; *PMP22*:IVS3	ICRF-193 [0.50 µM]	11	39
" "	" "	ICRF-193 [0.25 µM]	14	16
" "	" "	No ICRF-193 control	35	16
GM10958	chr17:15150757-15153084; *PMP22*:IVS3	ICRF-193 [0.50 µM]	23	22
" "	" "	ICRF-193 [0.25 µM]	19	21
" "	" "	No ICRF-193 control	23	7
GM06326	chr22:51175125-51178674; *ACR*	ICRF-193 [0.50 µM]	14	28
" "	" "	ICRF-193 [0.25 µM]	14	16
" "	" "	No ICRF-193 control	41	13
GM10958	chr22:51175125-51178674; *ACR*	ICRF-193 [0.50 µM]	13	18
" "	" "	ICRF-193 [0.25 µM]	21	23
" "	" "	No ICRF-193 control	22	13
GM06326	chr1:240988582-240990678; *RGS7*	5-AZC [35.0 µM]	40	10
" "	" "	5-AZC [17.5 µM]	38	5
" "	" "	no 5-AZC control	45	5

GM10958	chr1:240988582-240990678; *RGS7*	5-AZC [35.0 µM]	42	8
" "	" "	5-AZC [17.5 µM]	38	5
" "	" "	no 5-AZC control	40	10
GM06326	chr15:28509526-28511337; *HERC2*	5-AZC [35.0 µM]	37	9
" "	" "	5-AZC [17.5 µM]	23	9
" "	" "	no 5-AZC control	30	11
GM10958	chr15:28509526-28511337; *HERC2*	5-AZC [35.0 µM]	73	14
" "	" "	5-AZC [17.5 µM]	80	20
" "	" "	no 5-AZC control	38	12
GM06326	chr17:15150757-15153084; *PMP22*:IVS3	5-AZC [35.0 µM]	41	9
" "	" "	5-AZC [17.5 µM]	24	17
" "	" "	no 5-AZC control	26	9
GM10958	chr17:15150757-15153084; *PMP22*:IVS3	5-AZC [35.0 µM]	24	6
" "	" "	5-AZC [17.5 µM]	27	11
" "	" "	no 5-AZC control	26	6
Inhibitors of histone modification				
GM06326	chr1:240988582-240990678; *RGS7*	Okadaic acid [0.50 µM]	32	11
" "	" "	Okadaic acid [0.25 µM]	42	8
" "	" "	No Okadaic acid control	51	7
GM10958	chr1:240988582-240990678; *RGS7*	Okadaic acid [0.50 µM]	66	6
" "	" "	Okadaic acid [0.25 µM]	27	8
" "	" "	No Okadaic acid control	39	7

GM06326	chr9:140952206-140954439; *CACNA1B*	Okadaic acid [0.50 µM]	37	5
" "	" "	Okadaic acid [0.25 µM]	20	3
" "	" "	No Okadaic acid control	33	12
GM10958	chr9:140952206-140954439; *CACNA1B*	Okadaic acid [0.50 µM]	27	9
	" "	Okadaic acid [0.25 µM]	28	12
	" "	No Okadaic acid control	32	4
GM06326	chr17:15868752-15870532; *ADORA2B*	Okadaic acid [0.50 µM]	34	7
" "	" "	Okadaic acid [0.25 µM]	36	14
" "	" "	No Okadaic acid control	45	17
GM10958	chr17:15868752-15870532; *ADORA2B*	Okadaic acid [0.50 µM]	38	12
" "	" "	Okadaic acid [0.25 µM]	33	7
" "	" "	No Okadaic acid control	32	5
GM06326	chr9:140952206-140954439; *CACNA1B*	Trichostatin A [15.0 µM]	37	11
" "	" "	Trichostatin A [0.40 µM]	25	11
" "	" "	No Trichostain A control	28	12
GM10958	chr9:140952206-140954439; *CACNA1B*	Trichostatin A [15.0 µM]	26	12
" "	" "	Trichostatin A [0.40 µM]	32	6
" "	" "	No Trichostatin A control	30	10
GM06326	chr17:15868752-15870532; *ADORA2B*	Trichostatin A [15.0 µM]	30	10
" "	" "	Trichostatin A [0.40 µM]	28	12
" "	" "	No Trichostain A control	29	12

GM10958	chr17:15868752-15870532; *ADORA2B*	Trichostatin A [15.0 µM]	28	7
" "	" "	Trichostatin A [0.40 µM]	32	8
" "	" "	No Trichostatin A control	34	2
GM06326	chr1:240988582-240990678; *RGS7*	UNC1999 [15.0 µM]	23	7
" "	" "	UNC1999 [5.0 µM]	37	7
" "	" "	No UNC1999 control	36	10
GM10958	chr1:240988582-240990678; *RGS7*	UNC1999 [15.0 µM]	32	5
" "	" "	UNC1999 [5.0 µM]	40	5
" "	" "	No UNC1999 control	27	3
GM06326	chr17:15868752-15870532; *ADORA2B*	UNC1999 [15.0 µM]	39	6
" "	" "	UNC1999 [5.0 µM]	25	5
" "	" "	No UNC1999 control	33	7
GM10958	chr17:15868752-15870532; *ADORA2B*	UNC1999 [15.0 µM]	8	1
" "	" "	UNC1999 [5.0 µM]	33	9
" "	" "	No UNC1999 control	36	9
GM10958	chr15:25068481-25070727; *SNRPN*	UNC1999 [15.0 µM]	8	0
" "	" "	UNC1999 [5.0 µM]	20	2
" "	" "	No UNC1999 control	28	2
Cell lines with cohesin mutations				
GM20000	chr9:140952206-140954439; *CACNA1B*	c.5721del5	27	13
" "	chr9:213762-215844; *C9orf66*	" "	10	24

GM20466	chr9:140952206-140954439; *CACNA1B*	c.604C>T, c.752delA	37	13
" "	chr9:213762-215844; *C9orf66*	" "	11	25
GM20000	chr17:15150757-15153084; *PMP22*:IVS3	c.5721del5	74	11
" "	chr17:15133018-15136902; *PMP22*:IVS4-Ex5	" "	12	30
GM20466	chr17:15150757-15153084; *PMP22*:IVS3	c.604C>T, c.752delA	34	6
" "	chr17:15133018-15136902; *PMP22*:IVS4-Ex5	" "	12	31

Human lymphoblastoid cell lines harvested for metaphase chromosomes were hybridized with single copy (sc) probes from indicated GRCh37 genomic coordinates. Concentrations of each treatment, optimized for *in situ* hybridization are indicated. The numbers of metaphase cells with and without (w/o) DA is indicated for each treatment dose along with a no treatment control prepared at the same time. Cell lines with cohesin mutations c.5721del5 and c.604C>T, c.752delA are present in exon 31 and exon 3 of *NIPBL* and *ESCO2* respectively.

4.4 Discussion

In this study, we investigated epigenetic modifications responsible for allelic differences in chromatin accessibility reported between homologous mitotic metaphase chromosome (13). Our results demonstrate that metaphase chromatin accessibility differences between allelic loci are more susceptible to inhibition of topoisomerase IIα, which controls levels of DNA superhelicity, and are not a reflection of underlying histone modifications, cohesion of sister chromosomes, or effects of cytosine methylation.

ICRF-193 attenuates variation in fluorescent signal intensities from specific loci that exhibited DA (Figures 4-28, 4-29, and Supplemental Figure 4-30); which were further confirmed by super-resolution 3D-SIM (Figure 4-31). ICRF-193 is a bisdioxopiperazine compound that disrupts the catalytic activity of ATP-bound DNA topoisomerase IIα, rendering it an inactive clamp that is prevented from unwinding DNA (26,27). This bisdioxopiperazine compound was selected as there was evidence for its ability to effect chromatin condensation in mitotic metaphase (9). Further biochemical studies suggest that it is not as cytotoxic as fluoroquinolones and other exogenous poisons of intracellular topoisomerase II that lead to cell death by inducing the formation of reactive oxygen species or apoptosis (27). The latter system would not be useful for analysis of DA which requires actively dividing cells in mitotic metaphase. We recognize, however, that since the catalytic activity of ATP-bound topoisomerase IIα is required at different steps, such as DNA binding, cleavage or strand passage; it is not certain where in the topoisomerase reaction cycle (27) DA is attenuated.

Inhibiting the catalytic activity of topoisomerase IIα changes the overall morphology of mitotic chromosomes (Figure 4-26, panels B-D). Our findings are consistent with the possibility that by changing DNA topology, less accessible DNA targets on one of the homologs become more exposed. Distinct levels of DNA catenation of each homolog could be established, for example, through differences in either the local concentration of the enzyme on the chromosome, which is bound to chromosomes in metaphase (28) or structural differences between homologs at the target chromosome locus that impact substrate accessibility.

Changes in chromatin accessibility are known to be associated with post-translational modifications to histones (29). Inhibitors of histone modifying enzymes (e.g. protein phosphatase, histone deacetylase, histone lysine methyl transferase) or of DNA modification (DNA methyltransferase) did not affect DA (Supplemental Figure 4-34A–D). In particular, by inhibition of protein phosphatase I and IIα, we observed two pairs of each of the homologous chromosomes in a given tetraploid-like cell. These are likely due to the treatment effects of OA which induces an unusual M phase, where chromosomes undergo unscheduled replication with concomitant segregation defects (i.e. abnormal spindle formation, failure to develop kinetochore) (19). We observed that DNA probe hybridization patterns (Supplemental Figure 4-36) following treatment with OA did not equalize allelic chromatin accessibility differences, even among tetraploid-like cells. These histone modifications tend to be dynamic, are active at earlier points in the cell cycle, and often have simultaneously antagonizing effects on chromatin structure (29). At certain imprinted loci, however, restoration of expression of the inactive allele (30) coincides with the loss of lysine trimethylated histones (31,32). Multiple histone modifications may need to be targeted to trigger an effect in DNA accessibility at higher levels of chromatin organization (29), but there is little evidence that these modifications are relevant to chromatin accessibility or are even present on mitotic chromosomes (33).

Reversal of DA by inhibiting or disrupting metaphase chromosome compaction most likely depends on the stage of chromosome condensation at which the drug or mutated protein acts. Regulatory mutations in cohesin, which affect tethering of sister chromatids by the onset of prophase, leading to regional decompaction (14,34) , also had no effect on DA (Supplemental Figure 4-34E). The loss of chromosome structural integrity precluded our evaluation of condensin mutations which result in mislocalization of topoisomerase IIα (35). ICRF-193 targets the early stages (prophase, pre-metaphase) of mitotic chromosome condensation by preventing compaction of 300 nm chromatin fibers to 600 nm diameter chromatids (36). DA, therefore, seems most likely to become established in early metaphase.

Topoisomerase IIα is rapidly degraded as the cell enters G1. This is followed by a rise in its expression at G2/M, which is greatest among proliferating cells (37). An increase in

log phase growth or expression of topoisomerase IIα lowers sensitivity to topoisomerase inhibitors (38). Thus, the degree to which endogenous topoisomerase IIα is inhibited by ICRF-193 in culture is likely to vary. This is relevant since loss of DA, while evident in both cell lines (e.g. GM06326, GM10958), did not occur to the same degree at the *PMP22*:IVS3 and *ACR* loci (Figure 4-28B, C). The genomic target within *HERC2* notably showed similar percentages of DA in ICRF-193 treated and untreated cells (Figure 4-28B, C). One possible explanation for this is presence of extremely long palindromes (~210 kb), adjacent to and including *HERC2* segmental duplications (39), that might result in structural configurations that are simply recalcitrant to hybridization (40), or experimentally-induced chromosome decompaction.

ICRF-193 has been used as a general method to produce axially decondensed metaphase chromosomes for high resolution chromosome analysis (9). In this study, we demonstrate the use of a topoisomerase IIα inhibitor to normalize the effects of DA and to alter overall mitotic chromosome accessibility. It is recognized that different inhibitors of topoisomerase IIα disrupt its function at various points of association with the DNA duplex (27). Compounds have been identified that prevent actual binding of topoisomerase IIα to DNA; by competing with ATP (simocyclinone d8), blocking ATPase activity (novo- and cholorobiocins) or have irreversible effects on the enzyme (e.g. etoposides) (27). In considering any anti-topoisomerase compound, it will be important to avoid those with high cytotoxic and genotoxic effects, such as etoposides, that cause excessive DNA damage. If different agents impact DA to varying extents, this could further elucidate the mechanism by which DA is established or maintained.

The feasibility of our approach to reduce ATP-driven condensation of mitotic chromosomes in order to increase DNA accessibility or alter gene expression has been substantiated by other studies (28,41,42). We show that DA is a stable structural mark of metaphase chromosomes that cannot be influenced by inhibitors of histone-modification, cytosine methylation or cohesin mutations, which alter chromosome accessibility during interphase. Nevertheless, inhibition of topoisomerase IIα can reverse DA. We suggest that targeting catalytic activity of ATP-bound DNA topoisomerase IIα, equalizes superhelical densities between metaphase chromosome homologs in locus-specific

regions of DA. This raises the possibility that in normal untreated cells, the winding number of topoisomerase-induced supercoils can vary between homologous sequences within these regions (Figure 4-37). Combined with our previous study (13), this suggests that DA is the result of variable catenation levels at specific loci which are distinguishable and heritable between homologous chromosomes.

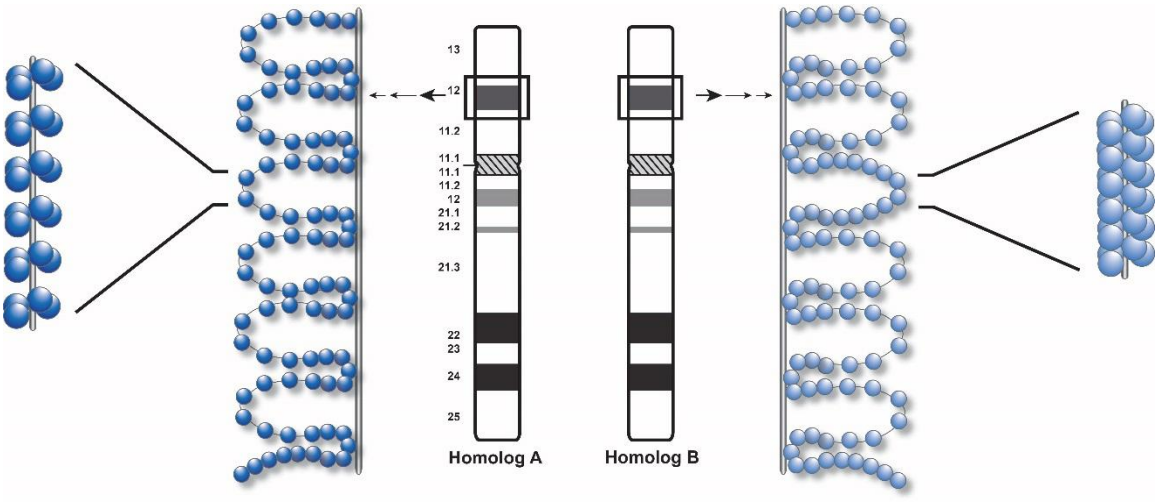

Figure 4-37. Working model hypothesis of solenoidal supercoiling between homologous regions with differential accessibility (DA)

The model illustrates localized differences in chromatin accessibility at specific homologous loci in untreated cells (i.e. with DA, default state). Example of a homologous chromosomal region within 17p12 (black rectangle) ideogram is shown in the middle of the illustration. Immediately flanking each ideogram, chromatin loop size, its frequency, and distance between each helical turn (i.e. helical pitch) is kept the same for both homologs but inter-homolog accessibility within a localized loop is depicted to be variable. For homologous region A, this is illustrated as low-level compaction with widely spaced circles (dark blue) in contrast with high-level compaction in homologous region B (closely spaced circles, light blue). The outer most images show a partial cross section of each loop. In homolog A, the solenoid structure with greater accessibility has low longitudinal supercoiling vs. homolog B. For simplicity, additional levels of packing beyond the 300 nm loop fiber (indicated by black arrows) are not shown. Chromatin loops are drawn in two-dimensions of a 3-D configuration found *in vivo*.

4.5 References

1. Wilkins BJ, Rall NA, Ostwal Y, Kruitwagen T, Hiragami-Hamada K, Winkler M, et al. A cascade of histone modifications induces chromatin condensation in mitosis. Science. 2014 Jan 3;343(6166):77–80.

2. Vagnarelli P. Mitotic chromosome condensation in vertebrates. Exp Cell Res. 2012 Jul 15;318(12):1435–41.

3. Burgers WA, Fuks F, Kouzarides T. DNA methyltransferases get connected to chromatin. Trends Genet. 2002 Jun;18(6):275–7.

4. Baxter J, Aragón L. A model for chromosome condensation based on the interplay between condensin and topoisomerase II. Trends Genet. 2012 Mar;28(3):110–7.

5. Prasanna PG, Escalada ND, Blakely WF. Induction of premature chromosome condensation by a phosphatase inhibitor and a protein kinase in unstimulated human peripheral blood lymphocytes: a simple and rapid technique to study chromosome aberrations using specific whole-chromosome DNA hybridization probes for biological dosimetry. Mutat Res. 2000 Mar 23;466(2):131–41.

6. Rao J, Bhattacharya D, Banerjee B, Sarin A, Shivashankar GV. Trichostatin-A induces differential changes in histone protein dynamics and expression in HeLa cells. Biochem Biophys Res Commun. 2007 Nov 16;363(2):263–8.

7. Konze KD, Ma A, Li F, Barsyte-Lovejoy D, Parton T, MacNevin° CJ, et al. An Orally Bioavailable Chemical Probe of the Lysine Methyltransferases EZH2 and EZH1. ACS Chem Biol. 2013 Jun 21;8(6):1324–34.

8. Schmid M, Haaf T, Grunert D. 5-Azacytidine-induced undercondensations in human chromosomes. Hum Genet. 1984;67(3):257–63.

9. Kohda A, Taguchi H, Okumura K. Preparation of extended metaphase chromosomes from human cultured cells using a topoisomerase II inhibitor, ICRF-193. Biosci Biotechnol Biochem. 2001 May;65(5):1248–51.

10. Weil MR, Widlak P, Minna JD, Garner HR. Global survey of chromatin accessibility using DNA microarrays. Genome Res. 2004 Jul;14(7):1374–81.

11. Rogan PK, Cazcarro PM, Knoll JHM. Sequence-Based Design of Single-Copy Genomic DNA Probes for Fluorescence In Situ Hybridization. Genome Res. 2001 Jun;11(6):1086–94.

12. Knoll JHM, Rogan PK. Sequence-based, in situ detection of chromosomal abnormalities at high resolution. Am J Med Genet A. 2003 Sep 1;121A(3):245–57.

13. Khan WA, Rogan PK, Knoll JH. Localized, non-random differences in chromatin accessibility between homologous metaphase chromosomes. Mol Cytogenet. 2014;7(1):70.

14. Nolen LD, Boyle S, Ansari M, Pritchard E, Bickmore WA. Regional chromatin decompaction in Cornelia de Lange syndrome associated with NIPBL disruption can be uncoupled from cohesin and CTCF. Hum Mol Genet. 2013 Oct 15;22(20):4180–93.

15. Bangs CD, Donlon TA. Metaphase chromosome preparation from cultured peripheral blood cells; in Haines JL, Korf BR, Morton CC (eds): Curr Protoc Hum Genet, pp 4.1.1-4.1.19 (John Wiley & Sons Inc., Malden 2005).

16. Knoll JHM, Lichter P. In Situ Hybridization to Metaphase Chromosomes and Interphase Nuclei; in: Haines JL, Korf BR, Morton CC, Seidman CE, Seidman JG, Smith DR (eds): Current Protocols in Human Genetics, pp 4.3.1-4.3.31 (John Wiley & Sons Inc., Malden 2005).

17. Khan WA, Chisholm R, Tadayyon S, Subasinghe A, Norton P, Samarabandu J, et al. Relating centromeric topography in fixed human chromosomes to α-satellite DNA and CENP-B distribution. Cytogenet Genome Res. 2013;139(4):234–42.

18. Gerkes EH, van der Kevie-Kersemaekers A-MF, Yakin M, Smeets DFCM, van Ravenswaaij-Arts CMA. The importance of chromosome studies in Roberts syndrome/SC phocomelia and other cohesinopathies. Eur J Med Genet. 2010 Feb;53(1):40–4.

19. Ghosh S, Schroeter D, Paweletz N. Okadaic acid overrides the S-phase check point and accelerates progression of G2-phase to induce premature mitosis in HeLa cells. Exp Cell Res. 1996 Aug 25;227(1):165–9.

20. Hatzi VI, Terzoudi GI, Paraskevopoulou C, Makropoulos V, Matthopoulos DP, Pantelias GE. The use of premature chromosome condensation to study in interphase cells the influence of environmental factors on human genetic material. Scientific World Journal. 2006;6:1174–90.

21. Cimini D, Mattiuzzo M, Torosantucci L, Degrassi F. Histone Hyperacetylation in Mitosis Prevents Sister Chromatid Separation and Produces Chromosome Segregation Defects. Mol Biol Cell. 2003 Sep;14(9):3821–33.

22. Alabert C, Bukowski-Wills J-C, Lee S-B, Kustatscher G, Nakamura K, de Lima Alves F, et al. Nascent chromatin capture proteomics determines chromatin dynamics during DNA replication and identifies unknown fork components. Nat Cell Biol. 2014 Mar;16(3):281–93.

23. Aoto T, Saitoh N, Sakamoto Y, Watanabe S, Nakao M. Polycomb group protein-associated chromatin is reproduced in post-mitotic G1 phase and is required for S phase progression. J Biol Chem. 2008 Jul 4;283(27):18905–15.

24. Doenecke D. Chromatin dynamics from S-phase to mitosis: contributions of histone modifications. Cell Tissue Res. 2014 Jun;356(3):467–75.

25. Ito Y, Nativio R, Murrell A. Induced DNA demethylation can reshape chromatin topology at the IGF2-H19 locus. Nucleic Acids Res. 2013 May 1;41(10):5290–302.

26. Classen S, Olland S, Berger JM. Structure of the topoisomerase II ATPase region and its mechanism of inhibition by the chemotherapeutic agent ICRF-187. Proc Natl Acad Sci. 2003 Sep 16;100(19):10629–34.

27. Vos SM, Tretter EM, Schmidt BH, Berger JM. All tangled up: how cells direct, manage and exploit topoisomerase function. Nat Rev Mol Cell Biol. 2011 Dec;12(12):827–41.

28. Kawamura R, Pope LH, Christensen MO, Sun M, Terekhova K, Boege F, et al. Mitotic chromosomes are constrained by topoisomerase II–sensitive DNA entanglements. J Cell Biol. 2010 Mar 8;188(5):653–63.

29. Bannister AJ, Kouzarides T. Regulation of chromatin by histone modifications. Cell Res. 2011 Mar;21(3):381–95.

30. Rogan PK, Seip JR, White LM, Wenger SL, Steele MW, Sperling MA, et al. Relaxation of imprinting in Prader-Willi syndrome. Hum Genet. 1998 Dec;103(6):694–701.

31. Li T, Chen H, Li W, Cui J, Wang G, Hu X, et al. Promoter histone H3K27 methylation in the control of IGF2 imprinting in human tumor cell lines. Hum Mol Genet. 2014 Jan 1;23(1):117–28.

32. Cruvinel E, Budinetz T, Germain N, Chamberlain S, Lalande M, Martins-Taylor K. Reactivation of Maternal SNORD116 Cluster via SETDB1 knockdown in Prader-Willi Syndrome iPSCs. Hum Mol Genet. 2014 Apr 23;ddu187.

33. Naumova N, Imakaev M, Fudenberg G, Zhan Y, Lajoie BR, Mirny LA, et al. Organization of the mitotic chromosome. Science. 2013 Nov 22;342(6161):948–53.

34. Onn I, Heidinger-Pauli JM, Guacci V, Unal E, Koshland DE. Sister chromatid cohesion: a simple concept with a complex reality. Annu Rev Cell Dev Biol. 2008;24:105–29.

35. Hudson DF, Vagnarelli P, Gassmann R, Earnshaw WC. Condensin is required for nonhistone protein assembly and structural integrity of vertebrate mitotic chromosomes. Dev Cell. 2003 Aug;5(2):323–36.

36. Ishida R, Sato M, Narita T, Utsumi KR, Nishimoto T, Morita T, et al. Inhibition of DNA topoisomerase II by ICRF-193 induces polyploidization by uncoupling chromosome dynamics from other cell cycle events. J Cell Biol. 1994 Sep;126(6):1341–51.

37. Heck MM, Hittelman WN, Earnshaw WC. Differential expression of DNA topoisomerases I and II during the eukaryotic cell cycle. Proc Natl Acad Sci U S A. 1988 Feb;85(4):1086–90.

38. Sullivan DM, Glisson BS, Hodges PK, Smallwood-Kentro S, Ross WE. Proliferation dependence of topoisomerase II mediated drug action. Biochemistry. 1986 Apr 22;25(8):2248–56.

39. Antonacci F, Dennis MY, Huddleston J, Sudmant PH, Steinberg KM, Rosenfeld JA, et al. Palindromic GOLGA8 core duplicons promote chromosome 15q13.3 microdeletion and evolutionary instability. Nat Genet. 2014 Dec;46(12):1293–302.

40. Dorman SN, Shirley BC, Knoll JHM, Rogan PK. Expanding probe repertoire and improving reproducibility in human genomic hybridization. Nucleic Acids Res. 2013 Apr;41(7):e81.

41. Powell WT, Coulson RL, Gonzales ML, Crary FK, Wong SS, Adams S, et al. R-loop formation at Snord116 mediates topotecan inhibition of Ube3a-antisense and allele-specific chromatin decondensation. Proc Natl Acad Sci. 2013 Aug 20;110(34):13938–43.

42. Thakurela S, Garding A, Jung J, Schübeler D, Burger L, Tiwari VK. Gene regulation and priming by topoisomerase IIα in embryonic stem cells. Nat Commun. 2013;4:2478.

Chapter 5

5 General Discussion

5.1 Summary of Findings and Implications

Major discoveries in chromosome biology, from classical cytogenetics and biochemical studies (1,2) to advances in molecular approaches (3,4), have contributed to our understanding of mitotic chromosome condensation. The inherent process of condensation leads to a heterogeneous organization of chromosomes that are visible at optical and sub-optical resolutions (5,6). At the structural level, this heterogeneity manifests as differences in the spatial organization of chromosomes in interphase (7,8) or the presence of accessible and compact chromatin within metaphase chromosomes (9). At the protein level, differences in metaphase chromosome condensation have been suggested to be shaped by a diverse set of histone modifications (10) or preferential binding of major scaffold associating proteins (11). These condensation differences along the lengths of mitotic metaphase chromosomes are well known, but between homologous regions they have not been recognized.

In this thesis, I have investigated localized allelic and centromeric differences in chromatin structure between homologous metaphase chromosomes. The motivation for this work arose out of a set of observations, in which short single copy (SC) DNA probes (1500-5000 nucleotides) showed differences in their probe fluorescence intensities between homologous chromosomal sequences from normal individuals. These differences involve the same homologs among the majority of cells analyzed from a given sample at ~10% of an approximate 305 genomic probe targets mapped in the human genome (12–14). A possibility as to why only a subset of genomic probes (i.e. ~10%) show localized differences in chromatin structure may be a property of the natural state of the cell. There is a growing appreciation that many (~5%) autosomal regions exhibit gene regulatory differences whereby one of the two homologous alleles remain active (15,16). Further, our analysis of open chromatin marks from interphase of the same regions marked by differential accessibility in metaphase (i.e. ~10% of the probes), exhibited a 2 fold difference in marks of accessible chromatin in certain genic as well as non-genic sites. At the remaining loci, no differences in probe hybridization intensities were detected, presumably because the metaphase chromatin structures of homologous

chromosomes are consistent. Therefore, genomic targets need not exclusively show DA or equivalent chromatin structure at all genomic targets, and would be one way by which a cell maintains diversity in its regulatory output.

The thesis presents evidence that the variation in hybridization of a subset of SC DNA probes results from their differential accessibility (DA) to distinct genomic targets. The differences in these hybridization patterns are reproducible and do not result from sources of experimental variability in the hybridization technique or preparation of chromosome material for hybridization. SC probes that cover genomic targets with DA are processed in parallel using the same labelling and hybridization parameters as probes detecting accessible chromatin structural features or equivalent accessibility (i.e. no DA). Moreover, by combining proximate SC FISH probes to increase their overall genomic length, intensities increase; however DA remains present between homologous targets in the same cell. The occurrence of DA or equivalent accessibility is evident from within different portions of the same gene, and cannot be attributed to common copy number variants or chromosome structural rearrangements. Further, the evidence for DA from FISH studies relies on quantification of signals and distinguishable homologous chromosomes. This is backed up by ultra-high super-resolution microscopy to resolve variation in chromatin structures within the condensed metaphase chromosome at sub-optical wavelengths. These findings, among others, are supported by three independent studies presented in Chapters 2-3.

In Chapter 2, I developed a novel correlated *in situ* imaging approach that combined atomic force microscopy (AFM) with FISH. These experiments provided a means for nanometer scale mapping of specific chromosomal components among individual metaphase chromosomes and between homologs. Initially, to perform correlated optical and topographic imaging of short FISH probes, I used a large centromeric target for a cloned α-satellite DNA sequence of chromosome 17. It was demonstrated that α-satellite DNA was distributed distinctly, represented by any of 8 different pattern combinations between homologs, relative to the centromeric ridge topography (see Table 2-1). We suggest this represents variability in α-satellite DNA distribution relative to centromere ridge topography and provides a snapshot of different transition points of centromeric

DNA segregation within metaphase chromatin. For example, in early metaphase chromosomes, the transverse height measurements of cross-sections at the centromere and along the length of the chromosome do not contain bimodal ridge structures (17). Instead, a continuous ridge morphology, similar to what we observed, is present in each homolog. This is also consistent with interaction between sister chromatids prior to disjunction. This inter-chromatid interaction is expected to disappear as the chromosome progresses from early to late metaphase (17). Bimodal (observed in the majority of chromosomes, see section 2.3.1) or continuous ridges were consistently found in all metaphase centromeres, irrespective of the segregation pattern of α-satellite DNA among parental homologs. We also observed a small interstitial feature, ~ 10-15 nm above the surrounding chromatin, between the major bimodal structures. This feature may represent a transitional intermediate in the formation of a bimodal ridge. In theory, the α-satellite DNA distribution should undergo changes consistent with chromosome segregation. However, we found that in the majority of chromosomes examined by AFM (Table 2-1), an interpeak, diffuse, doublet, or skewed α-satellite DNA distribution occurred with equal frequency in chromosomes having either a continuous or biomodal ridge structure at the centromere. Moreover, immuno-FISH demonstrated that α-satellite DNA segregation maintained this spatial discordance with respect to CENP-B motifs, a stably associated centromere marker, within α-satellite DNA monomers. In particular, CENP-B was found predominantly localized to the centromere ridge topography between homologs, prior to α-satellite DNA segregation.

Despite extensive biochemical analyses on centromeric proteins (CENPs), detailed studies of centromere structure have provided limited information about its topography (18). Our findings are novel because the relationship between centromeric ridge structure and DNA organization has not been previously described, because compatible AFM and FISH protocols that simultaneously determine topography and locate specific DNA sequences have not been available. This is important because the distributions of α-satellite DNA, CENP-B, and accompanying ridge structures suggest that segregation of centromeric DNA and hemisomal proteins comprising the kinetochore (19) are not tightly coordinated. This observation is contrary to the notion that these sequences reside within

the same restricted domains as centromere antigens on metaphase chromosomes (20). We have observed these differences between individual chromosomes as well as chromosomal homologs. Since CENP-B is a stably associated centromere marker (21,22), partitioning of this and other associated proteins along with the concurrent establishment of the kinetochore attachment site may occur prior to α-satellite DNA segregation.

The significance of our findings suggests that the underlying centromeric proteins dictate in part the spatial geometry of the centromere, rather than the arrangement of DNA within the centromere. This spatial organization of chromatin at centromeric sites may be important to maintain proper chromosome segregation dynamics (23), and is an underappreciated area of centromere research (23). I next utilized correlated AFM/FISH to examine topographic features at non-centromeric sites marked by locus specific short DNA probe targets. As presented in Chapter 3, examination of non-centromeric locations, in instances where probe hybridizations detected no DA, showed a bias towards the groove chromatin topography associated with accessible chromatin as oppose to compact ridge structures. Indeed, previous studies have shown that chromosomal DNA is thought to be accessible within groove-like structures on metaphase chromatin (5). This further suggested that the underlying epigenetic structures determine the chromatin compaction state, as detected by the hybridization patterns of short DNA probes using AFM/FISH. Analogous to the study of centromeric chromatin, as demonstrated, AFM/FISH has potential for nanoscale analysis of multiple chromatin components at non-centromeric sites, comprising higher-order chromosome structures. However, with correlated AFM/FISH, it was difficult to resolve the physical volume and depth occupied by the hybridizing target to homologous sequences. This is in part due to the diffraction limited resolution of conventional epifluorescence microscopy.

In Chapter 3, I employed super-resolution 3D-structured illumination microscopy (3D-SIM), as an alternative. Importantly, 3D-SIM demonstrated that the internal chromatin structure of the accessible homolog was less condensed relative to its inaccessible counterpart. It was important to determine whether this accessibility was intrinsic to the chromosome structure or formed at random. To address this, I systematically investigated

whether chromatin accessibility was biased to specific parental homologous chromosomes which were distinguishable cytogenetically. The individuals from which the specific homologs were analyzed harbored either a chromosome translocation, submicroscopic deletion, or a heteromorphism. This was used to mark one of the homologs in a metaphase cell. Parental information from previous studies on how the translocation or heteromorphism was inherited (either maternally or paternally) was also available for 7 of the 10 cell lines analyzed (Table 3-2). Locus-specific differences in chromatin accessibility were found to be non-random and reproducible within an individual; but were not unique to known imprinted regions.

To investigate the source of these differences, genomic regions exhibiting DA or equivalent accessibility during metaphase were compared to epigenetic features of open chromatin in interphase mapped by the ENCODE project Consortium (24). Mining ENCODE data from chromatin immunoprecipitation-sequencing experiments showed that genomic regions with equivalent accessibility between metaphase homologs were enriched in epigenetic features of accessible interphase chromatin relative to those regions with DA. This also suggested that the latter are found in a compact chromatin environment. These findings support the hypothesis that epigenetic marks established in interphase might be programmed as structural differences distinguishing homologous regions during metaphase. With respect to the ENCODE data (24), we examined marks of interphase open chromatin obtained by deoxyribonuclease I hypersensitivity (DNase HS) as well as formaldehyde-assisted isolation of regulatory elements (FAIRE). The difference between the two is that the DNase HS assay measures all accessible chromatin located preferentially adjacent to nucleosome-bound genomic regions (25). Conversely, FAIRE assay exploits crosslinking efficiency between nucleosomes and sequence-specific regulatory factors depleted of nucleosomes to differentiate the two fractions. It then uses phenol-chloroform extraction in downstream processing, and only provides a footprint of accessibility from within open chromatin sites associated with regulatory regions (25). As expected, we found that interphase marks of open chromatin mapped by DNase HS or FAIRE coincided with allelic targets with equivalent accessibility and were absent from regions with DA. But in rare instances (i.e. *ADORA2B*:IVS1 DA region vs.

ADORA2B:Promoter-Ex1, equivalent accessible region, Table 3-2 shows the raw data for each mark of open chromatin that was computed), FAIRE-seq showed increase open chromatin in regions with DA vs. equivalent accessible targets. This may be related to how the two data sets are generated. Unlike DNase I HS, FAIRE experiments depend on fixation efficiency with the use of formaldehyde that can alter accessibility depending on cell permeability and a variety of other physiological factors (25). Moreover, the FAIRE assay can identify additional distal regulatory elements not recovered by DNase HS footprinting of accessible targets (25). These differences between the two assays may account for the discrepancy observed when looking at these marks of open chromatin individually. Therefore, when mining the ENCODE data, the normalized chromatin immunoprecipitation intensities for each mark of open chromatin were integrated across all 93 genomic targets with and without DA. This was to avoid singling out one feature for one probe, as it did not provide an accurate measure of chromatin accessibility.

Following the characterization of DA, in Chapter 4, I explored key epigenetic modifications of histone and non-histone proteins (26) that may be responsible for these differences. To achieve this, I performed *in vitro* chromosome decondensation within human lymphoblastoid cells using histone or DNA modifying treatments implicated in forming compact chromosome structures. Inhibitors of histone modifying enzymes such as protein phosphatase I and IIα, histone deacetylase; including the K27 trimethylation mark of mature post-replicative chromatin, did not affect DA. Allelic chromatin accessibility differences were also unaltered by loss of cytosine methylation or in cell lines with two different cohesin mutations.

However by targeting DNA superhelicity through inhibition of topoisomerase IIα, the axial condensation of metaphase chromosomes was experimentally decreased. This, in turn, exposed previously less accessible chromosomal DNA for hybridization and equalized SC FISH probe intensities between homologs. The implications of this raised the possibility that levels of DNA superhelicity between homologous regions of metaphase chromosomes were variable across untreated cells exhibiting default levels of DA (see model in Chapter 4, section 4.4). Further, the reproducibility of DA initially described in Chapter 3 implies that under these ordinary conditions, (i.e. chromosomes

without decondensation treatment), topoisomerase IIα acts on a specific set of sequences (or structures) on the metaphase chromosomes. Its locations at these sites are non-random and interrupted by the presence of other structural proteins that define the chromosome scaffold (27).

It is proposed that DA results from topoisomerase IIα unwinding each homolog to different degrees. The inhibition of the enzyme prevents this differential unwinding, which is observed as entangled metaphase homologs with equivalent locus specific hybridization patterns. Therefore, one of the markers of DA could be the distribution of topoisomerase IIα and another could be the accessibility of specific loci on each homolog to topoisomerase IIα along the chromosome axis. Although these findings are an important advance to the current paradigm which views histone modifications or other DNA bound proteins as prevailing determinants of chromatin memory (28,29), topoisomerase IIα itself may not be the only mark responsible for DA.

While we did not observe an effect from histone modifying enzymes, DNA modifications (DNMT1) or cohesin mutations on reversing DA, it does not exclude the possibility these do not somehow contribute to the observed allelic structural differences. First, the dose of histone modifying proteins inhibitors, for example, was carefully titrated (Supplemental Table 4-1) so as to avoid complete loss of chromosome structure or apoptosis. Therefore, we may not have substantially reversed their effect on chromosome compaction in order to disrupt DA. Second, it should be considered that histone modification are transient and have a diverse range of effects (30). For example one of the inhibitors of histone deacetylase, trichostatin-A – used in the work presented in Chapter 4, is known to trigger concomitant and differential changes in phosphorylation of linker histone proteins (31), along with the expected increase in chromatin accessibility. Okadaic acid, apart from inhibiting protein phosphatase, is known to modulate the activity of a tyrosine kinase that overrides the S phase checkpoint (32). Since histone modifying proteins involved in regulating chromatin structure and function antagonize similar pathways, chemical inhibitors that alter their mode of action need to be carefully selected, as described in the experiments from Chapter 4. We could not simply inhibit, for example, phosphorylation of histone H3 serine 10 (H3 S10), thought to be a signature event in initiation of mitosis,

because targeting these canonical pathways in chromosome condensation would invariably impact the ability to form chromosomes in metaphase (33) for subsequent DA analysis. In keeping with the diverse effect of these modifications, H3S10 phosphorylation also acts upon histone deacetylation (33). Specifically, it triggers the removal of an acetyl group from histone H4 lysine 16 freeing the H4 tail to interact with the surface of neighboring nucleosomes and promoting chromatin fiber hyper-condensation (33). Taken together, modifications of histones are complex and a lack of response from these reagents is possibly due to their transient and often antagonistic nature. They also are active at earlier points in the cell cycle (30) and might not have a sustained effect on higher order chromatin folding. On the other hand ICRF-193, by inhibiting catalytic activity of topoisomerase IIα, specifically hinders compaction of 300-nm chromatin fibers to form into chromatids with prometaphase-level compaction (34). Besides targeting ATP-hydrolysis activity that is common to different points in the topoisomerase II reaction cycle (35), it has not been implicated in off target effects that may antagonize this decompaction. Therefore, it is possible that with this approach, we were able to elicit a specific and sustained effect on metaphase chromosome decompaction which is sufficient to attenuate DA.

5.2 Potential Biological Functions of Differential Accessibility

Assessing biological function differences between genomic regions with versus without DA (i.e. equivalent accessibility) would ultimately involve examination of their epigenetic status (i.e. open/compact chromatin features, possible transcriptional status) at allelic sites in interphase. In this thesis, we have compared marks of interphase open chromatin (see Chapter 3) in regions with versus without DA using chromatin immunoprecipitation-sequencing data from the same unsynchronized lymphoblastoid cell lines used in our metaphase analysis. Direct comparisons of metaphase and interphase chromatin states is challenging, especially since most studies that provide chromatin organization or accessibility information during interphase contain a mixture of maternally and paternally derived DNA. In other words, the published interphase studies

essentially ignore the phase of the DNA or the unique nucleotide content of the two homologous chromosomes from a given individual (36). This is a pre-requisite for assessment of loci for DA. Nonetheless, in the context of our findings, we can speculate on the biological significance of DA (also see Chapter 3 discussion).

First, the occurrence of DA between allelic loci is not uniform among all cells in a culture. The majority of cells show quantifiable non-random differences in accessibility between homologous regions at a certain level of significance, typically expressed as a fraction of cells (i.e. percentage) in a given individual. One possible mechanism to explain this might be that the regions where DA is observed in a fraction of cells, are not as highly structurally regulated as loci displaying equivalent accessibility to both homologs. The near absence of marks of open chromatin (see section 3.4.6) from DA regions may confer differences in the chromatin state at the end of interphase that affect the density, binding, or activity of topoisomerase IIα to each allele. By contrast, this hypothesis suggests that the structural state of equivalently accessible regions maintains strict degree of regulation dictated in part by an array of open chromatin marks established during the prior interphase. Our results imply that inhibition of topoisomerase IIα reverses DA and restores equivalent accessibility by preventing disparities in superhelicity between homologs. Otherwise, lax structural regulation by topoisomerase IIα in DA regions would enable differences in superhelicity. In the latter instance, some cells would show preference of accessibility from the maternal locus and others show a paternal accessibility preference in the same individual.

An alternative explanations is that equivalent accessibility may represent an intrinsic, essential structural feature for proper chromosome condensation. It would be expected that this process would be stringently controlled and it is not surprising that it comprises the vast majority of loci (90% of probes tested). As discussed in Chapter 3, cellular dynamics packaging DNA into highly condensed polymers tends to produce rather heterogeneous levels of compaction, especially in the tightly confined space of the nucleus (37). This may explain why we observe a mixture of both DA and equivalent accessible genomic regions at discrete allelic loci. Assuming the interphase marks of open chromatin loci correspond to their accessibility state in metaphase, genomic targets

need not exclusively show DA or equivalent chromatin structure. Many (~5%) autosomal regions exhibit gene regulatory differences, where one of the two homologous alleles remain transcriptionally active (15,16). This heterogeneity in chromatin accessibility may simply be a reflection of the natural epigenetic program in the nucleus.

Given the above considerations on formation of DA or equivalent accessible loci through separate topological constraints on chromatin, it still remains to be determined what benefit, if any, would such differences have? The presence or absence of DA itself does not induce a state of chromatin memory in the cell, since our view is that it is a structural feature that distinguishes homologous regions. However, the observed allelic differences in chromatin accessibility could be a way to not only distinguish but also to spatially organize homologous regions so that the less accessible locus remains separated from its accessible counterpart. This may in turn ensure stability of chromatin structures in daughter cells. Based on multi-color 3D FISH and 3D image analysis, a given chromosome is generally more proximate in the nucleus to a heterologous chromosome than to its homolog (38). FISH and recent chromosome conformation studies have shown that physical interactions between homologous loci influence gene regulatory output (39), at times with pathogenic outcome (40). On the other hand, monoallelic expression of numerous human genes (15) is consistent with the hypothesis that dispersion of homologous chromosomes may prevent transcriptional co-regulation of both alleles. Yet, another view proposes that maintaining distance between homologs in differentially compacted chromosome territories could suppress damaging both copies of a gene through environmental or intrinsic stressors such as radiation or reactive oxygen species (38).

Since homologous chromosomes are known to be in repulsion in the interphase nucleus relative to heterologous pairs (38), it is feasible that such a mechanism could exclude transcriptional co-regulation of both allelic regions at a DA locus (15,38) and allow for their transient spatial clustering at equivalent accessible loci (39,41). However, in our work, allelic regions with and without DA did not show an obvious link with transcriptional activity. For example, we did not find a role for histone modifications associated with transcriptionally active chromatin at sites of DA (section 3.4.6). Further

the specific genic regions in which single copy probes were analyzed for DA or equivalent accessibility (Table 3-1) were under-expressed in lymphocytes or lymphoblastoid cells. Therefore, given the current analysis, DA or regions with equivalent accessibility cannot be envisioned as determinants of transcriptional output. Rather, the degree of repulsion of homologs as they condense under different topological constraints in the cell, in part mediated by topoisomerase IIα, could have secondary effects on transcriptional output.

5.3 Alternate Hypothesis of Chromatin Memory

To assess whether regions exhibiting DA or equivalent accessibility direct the differential binding of chromosomal proteins that are able to transfer between cell generations will be technically challenging. However, if such a mechanism could be delineated, it would further our understanding as to how chromatin memory is stably maintained in descendant cells during mitosis (42). Previous studies have demonstrated post-translational modifications, such as trimethylation of histone H3 at lysine 27, are stably retained through interphase including in mature post-replicative chromatin (43), and some transcription factors continue to occupy sites in mitotic chromatin (44) (also see section 1.7).

Apart from the large body of literature which suggests a transfer of epigenetic information between cell generations (28,29,44–48), we consider the alternate hypothesis that the cell reassembles its complex nucleoprotein structure completely *de novo* in each cell generation. Previous studies have demonstrated that the *PGK1* transcription complex, known to interact with the active X chromosome, forms *de novo* at each cell generation (49). Recent chromosome conformation capture data have further shown that following mitosis, chromatin structures form *de novo* in early G1, and do not themselves carry epigenetic memory (50).

Whether or not mitotic chromosomes preserve the structural features that define interphase chromosomes, the fact that metaphase chromosomes acquire a similar organization, even in different cell types, raises the important question as to how

epigenetic information is inherited through mitosis. This could be addressed in future studies, employing higher resolution 3D microscopy coupled with locus-specific FISH, and, for example, deep sequencing at these loci at multiple stages of the cell cycle using synchronized cell lines. Integrated studies that tract the same loci over time may provide insight into the complex folding pathways that connect interphase and mitotic chromosome structures.

5.4 Limitations

FISH has proven to be versatile in the analysis of eukaryotic chromosome structure. There is a large body of literature that describes inference of biological insights by application of FISH with epifluorescence or high resolution microscopy to the study of chromosome differences in condensation. Chromatin condensation differences using FISH have been identified during metaphase (9), interphase (7,51), at different stages of cell differentiation *in vitro* (52), *in vivo* (53), or even between wild type and mutant cells (54). In this thesis, I have used FISH in combination with specialized microcopy to examine locus specific chromatin accessibility at single cell resolution. However, certain caveats for studying chromatin accessibility and its organization using *in situ* based approaches are important to consider. First, our approach is low-throughput and given that chromosome accessibility is dynamic across the genome, it would be useful to complement FISH with other emerging technologies such as chromosome confirmation capture and high throughput sequencing of many loci simultaneously (3). Chromosome conformation capture provides genome wide perspective on chromatin organization (3). However these methods restrict study of cells in metaphase, which would have to be addressed in order for them to be used for the analysis of metaphase epigenetic marks. Further, FISH visualizes only chromosomal targets corresponding to the regions detected by the probes, at limited spatial resolution. By contrast, super-resolution microscopy is improving diffraction-limited resolution of FISH; especially with respect to analyzing the high packing density of mitotic chromosomes (6). Apart from the broad limitations discussed here, specific limitations to each of the studies are outlined below.

In Chapter 2, a challenge to studying chromosomes by correlated AFM/FISH was preserving chromosome structure and probe fluorescence in the absence of antifade reagent (which had to be eliminated because it was incompatible with AFM, due to its viscosity). Retention of fluorescence was especially difficult in instances when immuno-FISH was used to simultaneously detect CENP-B and α-satellite DNA on chromosome topography. A key improvement to this approach will be to use AFM with sufficient speed to overcome loss of fluorescence that is inherent to scanning probe imaging modalities. This may now be feasible with recent advances in high speed AFM (55). At the time of our study, however, we found that rapid quenching of CENP-B fluorescence could be partly circumvented by imaging the chromosomes in a low salt aqueous medium. The fact that we were able to perform AFM on hydrated chromosomes is an advantage, as it has been suggested that this is closer to its native state (56). Second, we recognize that steps common to chromosome cell culture, which were performed prior to AFM/FISH, involve the use of Carnoy's fixation (e.g. methanol:acetic acid), which can impact chromosome structure because it extracts weakly bound chromosomal proteins. To preserve chromosome structure, investigators in the past have used various chromosome isolation technique (e.g. from organic solvents to hexylene glycol methods) as well as performed chromosome hardening by acidic and dehydration treatments (e.g. ethanol baths) (57). In spite of these efforts, modifications to *in vitro* procedures which deal with chromosome isolation and preparation will not preserve the chromosome structure found inside the cell. In addition, the AFM technology has not advanced enough to allow chromosome topography to be acquired on *in vivo* samples. Given the additional means to preserve structure that has been recognized in the literature, we did not want to go beyond the Carnoy's fixation procedure. This also ensured minimal modifications to the conventional procedure, since our objective was to validate results obtained by FISH using the higher resolution imaging modality. Moreover, isolating chromosomes using Carnoy's fixative removed the bulk of the major cytosol contaminants prior to AFM and provided sufficient quality and numbers of metaphase spreads for our study. The topography generated was clear and could be easily processed for further measurements.

In Chapter 3, a systematic analysis of DA in interphase is not presented since the focus of this study was characterization of these differences in metaphase. Interphase chromatin is dispersed and highly decondensed, lacking the context and easy recognition that metaphase chromosomes provide. This would make accurate assessment of chromatin accessibility with short (1.5–5 kb) SC probes challenging. The presence of a mixture of nuclei at different stages of condensation in the interphase stage of the cell cycle can further confound the analysis. Therefore, to accurately determine if DA is present in interphase would require a technically challenging approach, where the cells at different stages of interphase are separated by flow sorting. The synchronized cell populations are then followed by hybridization and comparison of probes with DA versus equally accessible controls. It is also anticipated that chromosomes of interest would need to be identified by co-hybridization with nearby probes to ensure accurate location of the short SC FISH signal in the interphase nuclei.

A challenge to the studies performed in Chapter 4 was the ability to readily identify chromosome homologs of interest by DAPI chromosome banding, following *in vitro* de condensation treatments. In instances where this occurred (e.g. for ICRF-193 treated chromosomes), we co-hybridized large chromosome specific BAC DNA probes (400 kb-1Mb in genomic length) with short SC probes. These DNA probes marked part of a different chromosome band or centromeric region in order to identify chromosome homologs of interest. While decondensation of chromosomes in cell culture was optimized to limit disruption of higher order chromosome structure, toxicity of the drug sometimes decreased the mitotic index (e.g. UNC1999 treatment). Fewer analyzable cells limited a complete analysis of DA. Additionally, during the quantification of probe fluorescence intensities using gradient vector flow (GVF) analysis, some cells had to be excluded as GVF did not accurately determine the true intensity of the hybridizations between homologs from the original image during microscope analysis. This was apparent in instances where auto-fluorescence around the hybridizing region was excessive, which was included in the final pixel calculation by the GVF algorithm, thus inflating the total intensity of a given probe signal.

5.5 Future considerations

In this thesis, DA was characterized at locus specific sites, a natural question this raises is how commonly it is observed on a genomic scale, and whether it is found in other cell types? Additionally, experiments to determine the DNA decatenation levels at differentially accessible loci can further our insight into its mechanism.

An exhaustive analysis of probes detecting locus-specific DA on chromosomes obtained from fibroblasts or other cell types should provide insight into variation in allelic chromatin structure in various tissues. Our preliminary findings show that differences in DNA accessibility between certain homologous regions (*RGS7*, *PMP22*:IVS3) is not altered in cells obtained from tissues of distinct cellular origin (i.e. mesodermal vs. ectodermal, see Chapter 3 on analysis of DA in fibroblasts). In fact, locus-specific DA was maintained among lymphocytes and lymphoblastoid cells of B-cell origin at different stages of differentiation, since lymphoblasts are considered to be precursors to the development of the mature lymphocyte (58). To build on these findings, genomic loci with and without DA can be evaluated in pluripotent stem cells to determine if observed chromatin accessibility signatures change as the cell lines become terminally differentiated. Possible outcomes would include either that a genomic region exhibiting DA in terminally differentiated cells maintains DA or it shows the opposite outcome, where no DA is observed in stem cells. Moreover, DA can be evaluated at different stages of development (e.g. amniocytes) or in paternal and maternal alleles of imprinted genes during development. In the latter, it is well known that methylation patterns are maintained in somatic tissues of imprinted genes throughout embryonic development, but are erased in primordial germ cells (59). Such findings would have implications for determining whether or not an allelic difference in chromatin accessibility is set and maintained early in cell differentiation and development. For these studies, one should also consider whether single nucleotide polymorphisms or common copy number variants affect chromatin accessibility. In our previous work, we did not find evidence for such variation. However, a discordance in chromatin accessibility in monozygotic twins (60) or allele-specific chromatin accessibility differences have been reported in different tissue types due to underlying genetic polymorphisms (61,62).

Although we have seen consistent localized non-random differences in compaction at homologous targets, it is not known whether these differences are localized to discrete SC regions that occasionally have different DA designation within the same gene (e.g. *PMP22*:IVS3 vs. *PMP22*:IVS4-Ex5, see Chapter 3) or are part of a larger chromosomal domain. Future work that builds on our findings in Chapter 3 can potentially quantify DA on a genomic-scale using high throughput DNA sequencing. One of the requirements is that cells in mitotic metaphase have to be enriched in order to ensure any differences in accessibility detected emanate from metaphase chromosomes. Second, since the evidence for DA must be sequence based, any strategy would have to use known heterozygous loci in the sample. Lastly, careful consideration should be given to determining sequence coverage required to distinguish DA from equally accessible chromatin with adequate statistical significance.

It should also be noted that single copy probes detecting DA have application primarily in research and should not be used in a clinical setting, due to the possibility that they could result in false positive molecular cytogenetic diagnostic results. As a recommendation, chromosome segregation of genomic regions with DA (i.e. non-random vs. random) should be performed in cells with cytogenetically distinguishable homologs. The trans-generational aspect of DA described in Chapter 3 is particularly worthy of further studies using larger pedigrees at a greater number of loci. It is probably unnecessary to require further super-resolution 3D-SIM microscopic analyses on subsequent DA loci, as it is now well established in this thesis that the quantifiable differences in probe intensities result from structural differences in internal chromatin accessibility between allelic targets.

Future studies related to results described in Chapter 4 could investigate the precise role that topoisomerase IIα plays in establishing and/or maintaining differences in chromatin accessibility. Conceptually, one way to determine how topoisomerase IIα is decatenating DNA at differentially accessible loci would be to utilize an approach from previous studies that have assessed helical tension in chromosomal DNA (63). Many of these studies have relied on psoralens, a compound that intercalates and photobinds to DNA and crosslinks its complementary strands. As previously demonstrated, accessibility of

intercalating psoralen is higher in chromosomal DNA with less superhelicity compared with bulky chromatin in which the DNA is more compact (63,64). Using intercalating psoralen as a biochemical probe, therefore, may be one possible way to determine the absolute DNA decatenation levels at differentially accessible loci. The challenge with these experiments would be to calculate the relative differences of psoralen crosslinks at allelic loci and to be able to detect psoralen activity at specific chromosomal regions. Despite these limitations, efforts have been directed at assessing the helical state of chromosomal DNA on a genome scale using this approach (63).

5.6 References

1. Paulson JR, Laemmli UK. The structure of histone-depleted metaphase chromosomes. Cell. 1977 Jan 11;12(3):817–28.

2. Manuelidis L. A view of interphase chromosomes. Science. 1990 Dec 14;250(4987):1533–40.

3. Dekker J. Two ways to fold the genome during the cell cycle: insights obtained with chromosome conformation capture. Epigenetics Chromatin. 2014 Nov 25;7(1):25.

4. Williamson I, Berlivet S, Eskeland R, Boyle S, Illingworth RS, Paquette D, et al. Spatial genome organization: contrasting views from chromosome conformation capture and fluorescence in situ hybridization. Genes Dev. 2014 Dec 15;28(24):2778–91.

5. Ushiki T, Hoshi O. Atomic force microscopy for imaging human metaphase chromosomes. Chromosome Res Int J Mol Supramol Evol Asp Chromosome Biol. 2008;16(3):383–96.

6. Flors C, Earnshaw WC. Super-resolution fluorescence microscopy as a tool to study the nanoscale organization of chromosomes. Curr Opin Chem Biol. 2011 Dec;15(6):838–44.

7. Cremer M, Hase J von, Volm T, Brero A, Kreth G, Walter J, et al. Non-random radial higher-order chromatin arrangements in nuclei of diploid human cells. Chromosome Res. 2001 Oct 1;9(7):541–67.

8. Bickmore WA, van Steensel B. Genome architecture: domain organization of interphase chromosomes. Cell. 2013 Mar 14;152(6):1270–84.

9. Gilbert N, Boyle S, Fiegler H, Woodfine K, Carter NP, Bickmore WA. Chromatin architecture of the human genome: gene-rich domains are enriched in open chromatin fibers. Cell. 2004 Sep 3;118(5):555–66.

10. Terrenoire E, McRonald F, Halsall JA, Page P, Illingworth RS, Taylor AMR, et al. Immunostaining of modified histones defines high-level features of the human metaphase epigenome. Genome Biol. 2010 Nov 15;11(11):R110.

11. Adachi Y, Käs E, Laemmli UK. Preferential, cooperative binding of DNA topoisomerase II to scaffold-associated regions. EMBO J. 1989 Dec 20;8(13):3997–4006.

12. Rogan PK, Cazcarro PM, Knoll JHM. Sequence-Based Design of Single-Copy Genomic DNA Probes for Fluorescence In Situ Hybridization. Genome Res. 2001 Jun;11(6):1086–94.

13. Knoll JHM, Rogan PK. Sequence-based, in situ detection of chromosomal abnormalities at high resolution. Am J Med Genet A. 2003 Sep 1;121A(3):245–57.

14. Khan WA, Knoll JH, Rogan PK. Context-based FISH localization of genomic rearrangements within chromosome 15q11.2q13 duplicons. Mol Cytogenet. 2011 Aug 8;4(1):15.

15. Gimelbrant A, Hutchinson JN, Thompson BR, Chess A. Widespread monoallelic expression on human autosomes. Science. 2007 Nov 16;318(5853):1136–40.

16. Eckersley-Maslin MA, Thybert D, Bergmann JH, Marioni JC, Flicek P, Spector DL. Random monoallelic gene expression increases upon embryonic stem cell differentiation. Dev Cell. 2014 Feb 24;28(4):351–65.

17. Argüello-Miranda O, Sáenz-Arce G. Interchromatidal central ridge and transversal symmetry in early metaphasic human chromosome one. J Mol Recognit. 2008 Jun;21(3):184–9.

18. Ushiki T, Hoshi O, Iwai K, Kimura E, Shigeno M. The structure of human metaphase chromosomes: its histological perspective and new horizons by atomic force microscopy. Arch Histol Cytol. 2002 Dec;65(5):377–90.

19. Ribeiro SA, Vagnarelli P, Dong Y, Hori T, McEwen BF, Fukagawa T, et al. A super-resolution map of the vertebrate kinetochore. Proc Natl Acad Sci U S A. 2010 Jun 8;107(23):10484–9.

20. Masumoto H, Sugimoto K, Okazaki T. Alphoid satellite DNA is tightly associated with centromere antigens in human chromosomes throughout the cell cycle. Exp Cell Res. 1989 Mar;181(1):181–96.

21. Muro Y, Masumoto H, Yoda K, Nozaki N, Ohashi M, Okazaki T. Centromere protein B assembles human centromeric alpha-satellite DNA at the 17-bp sequence, CENP-B box. J Cell Biol. 1992 Feb;116(3):585–96.

22. Cooke CA, Bernat RL, Earnshaw WC. CENP-B: a major human centromere protein located beneath the kinetochore. J Cell Biol. 1990 May;110(5):1475–88.

23. Verdaasdonk JS, Bloom K. Centromeres: unique chromatin structures that drive chromosome segregation. Nat Rev Mol Cell Biol. 2011 May;12(5):320–32.

24. Consortium TEP. An integrated encyclopedia of DNA elements in the human genome. Nature. 2012 Sep 6;489(7414):57–74.

25. Tsompana M, Buck MJ. Chromatin accessibility: a window into the genome. Epigenetics Chromatin. 2014 Nov 20;7(1):33.

26. Vagnarelli P. Mitotic chromosome condensation in vertebrates. Exp Cell Res. 2012 Jul 15;318(12):1435–41.

27. Maeshima K, Laemmli UK. A two-step scaffolding model for mitotic chromosome assembly. Dev Cell. 2003 Apr;4(4):467–80.

28. John S, Workman JL. Bookmarking genes for activation in condensed mitotic chromosomes. BioEssays. 1998 Apr;20(4):275–9.

29. Zaidi SK, Young DW, Montecino M, Lian JB, Stein JL, van Wijnen AJ, et al. Architectural epigenetics: mitotic retention of mammalian transcriptional regulatory information. Mol Cell Biol. 2010 Oct;30(20):4758–66.

30. Bannister AJ, Kouzarides T. Regulation of chromatin by histone modifications. Cell Res. 2011 Mar;21(3):381–95.

31. Rao J, Bhattacharya D, Banerjee B, Sarin A, Shivashankar GV. Trichostatin-A induces differential changes in histone protein dynamics and expression in HeLa cells. Biochem Biophys Res Commun. 2007 Nov 16;363(2):263–8.

32. Ghosh S, Schroeter D, Paweletz N. Okadaic acid overrides the S-phase check point and accelerates progression of G2-phase to induce premature mitosis in HeLa cells. Exp Cell Res. 1996 Aug 25;227(1):165–9.

33. Wilkins BJ, Rall NA, Ostwal Y, Kruitwagen T, Hiragami-Hamada K, Winkler M, et al. A cascade of histone modifications induces chromatin condensation in mitosis. Science. 2014 Jan 3;343(6166):77–80.

34. Ishida R, Sato M, Narita T, Utsumi KR, Nishimoto T, Morita T, et al. Inhibition of DNA topoisomerase II by ICRF-193 induces polyploidization by uncoupling chromosome dynamics from other cell cycle events. J Cell Biol. 1994 Sep;126(6):1341–51.

35. Vos SM, Tretter EM, Schmidt BH, Berger JM. All tangled up: how cells direct, manage and exploit topoisomerase function. Nat Rev Mol Cell Biol. 2011 Dec;12(12):827–41.

36. Tewhey R, Bansal V, Torkamani A, Topol EJ, Schork NJ. The importance of phase information for human genomics. Nat Rev Genet. 2011 Mar;12(3):215–23.

37. Berndsen ZT, Keller N, Grimes S, Jardine PJ, Smith DE. Nonequilibrium dynamics and ultraslow relaxation of confined DNA during viral packaging. Proc Natl Acad Sci U S A. 2014 Jun 10;111(23):8345–50.

38. Heride C, Ricoul M, Kiêu K, von Hase J, Guillemot V, Cremer C, et al. Distance between homologous chromosomes results from chromosome positioning constraints. J Cell Sci. 2010 Dec 1;123(Pt 23):4063–75.

39. Brown JM, Leach J, Reittie JE, Atzberger A, Lee-Prudhoe J, Wood WG, et al. Coregulated human globin genes are frequently in spatial proximity when active. J Cell Biol. 2006 Jan 16;172(2):177–87.

40. Koeman JM, Russell RC, Tan M-H, Petillo D, Westphal M, Koelzer K, et al. Somatic pairing of chromosome 19 in renal oncocytoma is associated with deregulated EGLN2-mediated [corrected] oxygen-sensing response. PLoS Genet. 2008;4(9):e1000176.

41. Hewitt SL, Yin B, Ji Y, Chaumeil J, Marszalek K, Tenthorey J, et al. RAG-1 and ATM coordinate monoallelic recombination and nuclear positioning of immunoglobulin loci. Nat Immunol. 2009 Jun;10(6):655–64.

42. Margueron R, Reinberg D. Chromatin structure and the inheritance of epigenetic information. Nat Rev Genet. 2010 Apr;11(4):285–96.

43. Alabert C, Bukowski-Wills J-C, Lee S-B, Kustatscher G, Nakamura K, de Lima Alves F, et al. Nascent chromatin capture proteomics determines chromatin dynamics during DNA replication and identifies unknown fork components. Nat Cell Biol. 2014 Mar;16(3):281–93.

44. Xing H, Vanderford NL, Sarge KD. The TBP-PP2A mitotic complex bookmarks genes by preventing condensin action. Nat Cell Biol. 2008 Nov;10(11):1318–23.

45. Wang F, Higgins JMG. Histone modifications and mitosis: countermarks, landmarks, and bookmarks. Trends Cell Biol. 2013 Jan 4;23(4):175–84.

46. Xing H, Wilkerson DC, Mayhew CN, Lubert EJ, Skaggs HS, Goodson ML, et al. Mechanism of hsp70i gene bookmarking. Science. 2005 Jan 21;307(5708):421–3.

47. Zhao R, Nakamura T, Fu Y, Lazar Z, Spector DL. Gene bookmarking accelerates the kinetics of post-mitotic transcriptional re-activation. Nat Cell Biol. 2011 Nov;13(11):1295–304.

48. Yan J, Enge M, Whitington T, Dave K, Liu J, Sur I, et al. Transcription factor binding in human cells occurs in dense clusters formed around cohesin anchor sites. Cell. 2013 Aug 15;154(4):801–13.

49. Hershkovitz M, Riggs AD. Metaphase chromosome analysis by ligation-mediated PCR: heritable chromatin structure and a comparison of active and inactive X chromosomes. Proc Natl Acad Sci U S A. 1995 Mar 14;92(6):2379–83.

50. Naumova N, Imakaev M, Fudenberg G, Zhan Y, Lajoie BR, Mirny LA, et al. Organization of the mitotic chromosome. Science. 2013 Nov 22;342(6161):948–53.

51. Yokota H, Singer MJ, Engh GJ van den, Trask BJ. Regional differences in the compaction of chromatin in human G0/G1 interphase nuclei. Chromosome Res. 1997 Apr 1;5(3):157–66.

52. Morey C, Da Silva NR, Perry P, Bickmore WA. Nuclear reorganisation and chromatin decondensation are conserved, but distinct, mechanisms linked to Hox gene activation. Development. 2007 Mar;134(5):909–19.

53. Eskeland R, Leeb M, Grimes GR, Kress C, Boyle S, Sproul D, et al. Ring1B compacts chromatin structure and represses gene expression independent of histone ubiquitination. Mol Cell. 2010 May 14;38(3):452–64.

54. Nolen LD, Boyle S, Ansari M, Pritchard E, Bickmore WA. Regional chromatin decompaction in Cornelia de Lange syndrome associated with NIPBL disruption can be uncoupled from cohesin and CTCF. Hum Mol Genet. 2013 Oct 15;22(20):4180–93.

55. Ando T, Uchihashi T, Kodera N. High-speed AFM and applications to biomolecular systems. Annu Rev Biophys. 2013;42:393–414.

56. Hoshi O, Shigeno M, Ushiki T. Atomic force microscopy of native human metaphase chromosomes in a liquid. Arch Histol Cytol. 2006 Mar;69(1):73–8.

57. Chromosome Nanoscience and Technology [Internet]. [cited 2015 Feb 23]. Available from: http://www.crcpress.com/product/isbn/9781420044911

58. PubMed Health [Internet]. Bethesda. US National Library of Medicine; 2015 [cited 2015 Mar 12]. Available from: http://www.ncbi.nlm.nih.gov/pubmedhealth/PMHT0022047/

59. Li E. Chromatin modification and epigenetic reprogramming in mammalian development. Nat Rev Genet. 2002 Sep;3(9):662–73.

60. Kim K, Ban H-J, Seo J, Lee K, Yavartanoo M, Kim SC, et al. Genetic factors underlying discordance in chromatin accessibility between monozygotic twins. Genome Biol. 2014 May 29;15(5):R72.

61. McDaniell R, Lee B-K, Song L, Liu Z, Boyle AP, Erdos MR, et al. Heritable Individual-Specific and Allele-Specific Chromatin Signatures in Humans. Science. 2010 Apr 9;328(5975):235–9.

62. Zhang K, Li JB, Gao Y, Egli D, Xie B, Deng J, et al. Digital RNA allelotyping reveals tissue-specific and allele-specific gene expression in human. Nat Methods. 2009 Aug;6(8):613–8.

63. Bermúdez I, García-Martínez J, Pérez-Ortín JE, Roca J. A method for genome-wide analysis of DNA helical tension by means of psoralen–DNA photobinding. Nucleic Acids Res. 2010 Oct 1;38(19):e182–e182.

64. Matsumoto K, Hirose S. Visualization of unconstrained negative supercoils of DNA on polytene chromosomes of Drosophila. J Cell Sci. 2004 Aug 1;117(Pt 17):3797–805.

Appendices

Appendix 1. Copyright release licenses

SPRINGER LICENSE
TERMS AND CONDITIONS

Feb 17, 2015

This is a License Agreement between Wahab A Khan ("You") and Springer ("Springer") provided by Copyright Clearance Center ("CCC"). The license consists of your order details, the terms and conditions provided by Springer, and the payment terms and conditions.

All payments must be made in full to CCC. For payment instructions, please see information listed at the bottom of this form.

License Number	3571630427596
License date	Feb 17, 2015
Licensed content publisher	Springer
Licensed content publication	Chromosome Research
Licensed content title	Atomic force microscopy for imaging human metaphase chromosomes
Licensed content author	Tatsuo Ushiki
Licensed content date	Jan 1, 2008
Volume number	16
Issue number	3
Type of Use	Thesis/Dissertation
Portion	Figures
Author of this Springer article	No
Order reference number	None
Original figure numbers	Figure 10
Title of your thesis / dissertation	(for chapter 1 - General Introduction of thesis)
Expected completion date	Apr 2015
Estimated size(pages)	150
Total	0.00 CAD

ELSEVIER LICENSE
TERMS AND CONDITIONS

Feb 11, 2015

This is a License Agreement between Wahab A Khan ("You") and Elsevier ("Elsevier") provided by Copyright Clearance Center ("CCC"). The license consists of your order details, the terms and conditions provided by Elsevier, and the payment terms and conditions.

All payments must be made in full to CCC. For payment instructions, please see information listed at the bottom of this form.

Supplier	Elsevier Limited The Boulevard,Langford Lane Kidlington,Oxford,OX5 1GB,UK
Registered Company Number	1982084
Customer name	Wahab A Khan
Customer address	
License number	3565940445274
License date	Feb 11, 2015
Licensed content publisher	Elsevier
Licensed content publication	Journal of Structural Biology
Licensed content title	Structure of human chromosomes studied by atomic force microscopy Part II. Relationship between structure and cytogenetic bands
Licensed content author	Javier Tamayo
Licensed content date	March 2003
Licensed content volume number	141
Licensed content issue number	3
Number of pages	9
Start Page	189
End Page	197
Type of Use	reuse in a thesis/dissertation
Portion	figures/tables/illustrations
Number of figures/tables/illustrations	1
Format	both print and electronic
Are you the author of this Elsevier article?	No
Will you be translating?	No
Original figure numbers	Figure 10
Title of your thesis/dissertation	(for chapter 1 - General Introduction of thesis)
Expected completion date	Apr 2015
Estimated size (number of pages)	150
Elsevier VAT number	GB 494 6272 12
Permissions price	0.00 CAD
VAT/Local Sales Tax	0.00 CAD / 0.00 GBP

Cytogenetic and genome research

Order detail ID: 66163751
Order License Id: 3571510697214

ISSN: 1424-859X
Publication Type: e-Journal
Volume:
Issue:
Start page:
Publisher: S. KARGER AG

Permission Status: Granted

Permission type: Republish or display content
Type of use: Thesis/Dissertation

Hide details

Requestor type	Author of requested content
Format	Print, Electronic
Portion	chapter/article
Title or numeric reference of the portion(s)	complete article , including supplemental material
Title of the article or chapter the portion is from	Relating Centromeric Topography in Fixed Human Chromosomes to ÃÂ±-Satellite DNA and CENP-B Distribution
Editor of portion(s)	N/A
Author of portion(s)	N/A
Volume of serial or monograph	N/A
Page range of portion	
Publication date of portion	2013
Rights for	Main product and any product related to main product
Duration of use	Life of current edition
Creation of copies for the disabled	no
With minor editing privileges	yes
For distribution to	Worldwide
In the following language(s)	Original language of publication
With incidental promotional use	no
Lifetime unit quantity of new product	Up to 499
Made available in the following markets	university, academic
The requesting person/organization	Wahab A. Khan / University of Western Ontario
Order reference number	
Author/Editor	Wahab A. Khan
The standard identifier	thesis
Title	Ch 2 of Wahab Khan's PhD thesis
Publisher	University of Western Ontario
Expected publication date	Mar 2017
Estimated size (pages)	150

Note: This item will be invoiced or charged separately through CCC's **RightsLink** service. More info **$ 0.00**

Appendix 2. Ethics approval for use of human participants

Research Western

Use of Human Participants - Ethics Approval Notice

Principal Investigator: Dr. Joan Knoll
Review Number: 15345E
Review Level: Delegated
Approved Local Adult Participants: 500
Approved Local Minor Participants: 0
Protocol Title: Validation of Single Copy DNA Probes
Department & Institution: Schulich School of Medicine and Dentistry\Pathology, University of Western Ontario
Sponsor:
Ethics Approval Date: March 15, 2012 **Expiry Date:** July 31, 2015
Documents Reviewed & Approved & Documents Received for Information:

Document Name	Comments	Version Date
Revised Study End Date	The study end date has been extended to July 31, 2015 to allow for continued data collection.	

This is to notify you that The University of Western Ontario Research Ethics Board for Health Sciences Research Involving Human Subjects (HSREB) which is organized and operates according to the Tri-Council Policy Statement: Ethical Conduct of Research Involving Humans and the Health Canada/ICH Good Clinical Practice Practices: Consolidated Guidelines; and the applicable laws and regulations of Ontario has reviewed and granted approval to the above referenced revision(s) or amendment(s) on the approval date noted above. The membership of this REB also complies with the *membership requirements for REB's as defined in Division 5 of the Food and Drug Regulations.*

The ethics approval for this study shall remain valid until the expiry date noted above assuming timely and acceptable responses to the HSREB's periodic requests for surveillance and monitoring information. If you require an updated approval notice prior to that time you must request it using the UWO Updated Approval Request Form.

Members of the HSREB who are named as investigators in research studies, or declare a conflict of interest, do not participate in discussion related to, nor vote on, such studies when they are presented to the HSREB.

The Chair of the HSREB is Dr. Joseph Gilbert. The UWO HSREB is registered with the U.S. Department of Health & Human Services under the IRB registration number IRB 00000940.

Ethics Officer to Contact for Further Information

Janice Sutherland (jsutherl@uwo.ca)	✓ Grace Kelly (grace.kelly@uwo.ca)	Shantel Walcott (swalcot@uwo.ca)

This is an official document. Please retain the original in your files.

Appendix 3. Biosafety permit

University of Western Ontario
Permit Summary

Permit Holder	Knoll, Joan H		
Permit #	BIO-UWO-0215	**Classification**	2
Department	Pathology		
Phone		**Ext.**	86407
Email			
Approval Date	Oct 20, 2014	**Expiration Date**	Oct 19, 2017
BioSafety Officer's Signature			

Organism	E.coli DH5 alpha
Cell	Human (primary), lymphocyte, fibroblast, Human (established), lymphoblastoid, fibroblast, tumour cell lines: BT-474, MCF-7, SKBR3, Hs-578T [AppB]
Human	blood (whole), tissue (unpreserved), fibroblast, tissues (preserved), lymphocytes
Gene Therapy	
GMO	pcR2.1T0P0, pcR Blunt AppC
Animals	
Toxin	
Plant/Insect	

Building	Room	Room Area	Lab Phone	Ext.	Level
Dental Sciences Building	5002	5002			2
Dental Sciences Building	5002A	5002A			2
Dental Sciences Building	5003 LEVEL 2	5003 Level 2			2

University of Western Ontario
Permit Summary

Permit Holder	Knoll, Joan H		
Permit #	BIO-UWO-0215	**Classification**	2
Department	Pathology		
Phone		**Ext.**	86407
Email			
Approval Date	Oct 20, 2014	**Expiration Date**	Oct 19, 2017
BioSafety Officer's Signature			

Permit Conditions

1 INTERNAL PERMIT HOLDER RESPONSIBILITIES

Comply with UWO BioSafety Safety Policies and Standard Operating Procedures. Ensure that the Health Canada Biosafety Guidelines, relevant regulations and safe laboratory practices are followed.

1.1 Receive adequate biosafety training from the institution. Permit Holders are responsible for the provision of specific training and instruction in biohazard agent handling that is necessary for the safe use of this material in their own laboratories. Supervisors must ensure that workers understand the health and safety hazards of the work or task (due diligence).

1.2 Ensure that the UWO Biosafety Manual is available to all lab personnel under the permit.

1.3 Report incidents of loss or theft of any biohazardous material immediately to the Biosafety Coordinator;

2 WORKER RESPONSIBILITIES
Be familiar with the UWO Biosafety Manual, attend all required safety training sessions and obey all safety regulations required by the UWO Biosafety Committee.

2.1 Report to the Permit Holder any incident involving known or suspected exposure, personal contamination or a spill involving a biohazardous agent.

I accept the above responsibilities as a Internal Permit Holder and I am accountable for following UWO BioSafety Guidelines and Procedures Manual for Containment Level 1 and 2 Laboratories.

Permit Holder Name _____ Signed _____ Date _____

Appendix 4 Assurance form for use of Biomaterial – NHGRI Repository for Human Genetics Research

NHGRI SAMPLE REPOSITORY FOR HUMAN GENETIC RESEARCH

ASSURANCE FORM FOR BIOMATERIALS

To ensure compliance with the Office for Human Research Protections (OHRP), Department of Health and Human Services (DHHS), regulations for the protection of human subjects (45 CFR Part 46), before human cell lines, DNA samples, BAC or Fosmid clones (biomaterials) can be shipped from the NHGRI Sample Repository for Human Genetic Research, the principal investigator must provide the Repository with a written description of the purpose of the research project to be conducted using these biomaterials. Both the principal investigator and the institutional official who is authorized to make legally binding agreements for the institution must sign this statement agreeing to adhere to the following conditions.

The Statement of Research Intent must be submitted electronically with the online order and the signed Assurance forms must be returned to the Coriell Cell Repositories.

WARRANTY AND LIABILITY

The recipient acknowledges that the conditions for use of the biomaterials are governed by the Institutional Review Board (IRB) of the Coriell Cell Repositories, in accordance with DHHS regulations (45 CFR Part 46). The recipient agrees to comply fully with all such conditions and to report promptly to the Institutional Review Board (IRB) of the Coriell Cell Repositories any proposed changes to the research project and any unanticipated events involving risks to subjects or others. A new Statement of Research Intent Form must be submitted if any major changes to the research project are proposed. The recipient remains subject to all applicable state and local laws and regulations and institutional policies that provide additional protections for human subjects.

Repository staff will under no circumstances provide information that will allow investigators to identify subjects; the repository does not have identifying information for subjects who contributed samples to the HapMap Project or to the 1000 Genomes Project.

CONDITIONS OF USE

1) The signatories agree to report to the Coriell Cell Repositories any proposed changes to the research project that differ from the description provided in the Statement of Research Intent.
2) The signatories agree not to try to identity or contact the donor subjects from whom these biomaterials were derived.
3) The signatories agree that the biomaterials are provided without warranty of merchantability or fitness.
4) The signatories agree not to use biomaterials for human experimentation without the approval of the Coriell Cell Repositories' IRB and of an IRB at the recipient site.
5) The signatories agree not to sell biomaterials from the Repository to a third party.
6) The signatories agree not to distribute biomaterials from the Repository to a third party except after pre-approval by the Coriell Cell Repositories for specific circumstances, which include: (a) single purpose collaborations; or (b) the distribution of aliquots or derivatives of biomaterials for use as biological standards. Approval will be contingent upon the requestor submitting to the Coriell Cell Repositories a Statement of Research Intent describing such secondary use.

7) The signatories acknowledge that cultured cells have the potential to carry viruses and other infectious agents and that appropriate precautions will be taken. These cells should always be handled carefully by trained persons under laboratory conditions that afford adequate biohazard containment following minimum safety guidelines recommended for working with human cell cultures.
8) The signatories acknowledge that if it is found that the biomaterials are used for purposes other than those explicitly stated in the Statement of Research Intent they will be asked to return the biomaterials to the Coriell Cell Repositories immediately and will not receive financial compensation for the unused portion.
9) The signatories acknowledge their understanding that each donor community has set up a Community Advisory Group (CAG) to serve as a liaison between the community and the Coriell Cell Repositories. The signatories acknowledge their understanding that the CAG will be informed that their research group has received the biomaterials and their statement of the purpose of the research. In addition, the Coriell Cell Repositories provide a link from the biomaterials to any papers which have published results based on the use of the samples.
10) The signatories acknowledge their understanding that as part of an ongoing process of community consultation with the donor communities through the CAGs, a community could decide, after careful discussion and consultation with the Coriell Cell Repositories and with researchers, to withdraw its biomaterials from the Coriell Cell Repositories. This might occur based on the use of the biomaterials in a way that the community found unacceptable or stigmatizing. In the unlikely event that this happens, the signatories will be asked to return the biomaterials to the Coriell Cell Repositories and will receive financial compensation in the amount they initially paid to the Coriell Cell Repositories for the biomaterials if they had not yet used any of the samples, and a prorated amount for any biomaterials not used.

WARRANTIES:

1. THE REPOSITORY MAKES NO REPRESENTATIONS AND EXTENDS NO WARRANTIES OF ANY KIND, EITHER EXPRESSED OR IMPLIED. THERE ARE NO EXPRESS OR IMPLIED WARRANTIES OF MERCHANTABILITY OR FITNESS FOR A PARTICULAR PURPOSE, OR THAT THE USE OF THE MATERIAL WILL NOT INFRINGE ANY PATENT, COPYRIGHT, TRADEMARK, OR OTHER PROPRIETARY RIGHTS.

2. The biomaterials are provided as a service to the research community. They are provided without warranty of merchantability or fitness for a particular purpose and without any other warranty, expressed or implied.

   For State Institutions: The recipient institution agrees to be responsible for any claims, costs, damages, or expenses resulting from any injury (including death), damage, or loss that may arise solely from the use of these biomaterials to the extent permitted under the laws of this state. This provision shall also apply to any byproducts or derivatives of these biomaterials
   For U.S. Government Laboratories: The United States assumes the liability for any claims, damages, injury, or expenses arising from the use of material or any byproduct or derivative, but only to the extent provided under the Federal Tort Claims Act (28 U.S.C. Chapter 171).
   For All Other Institutions: To the extent permitted under the Laws of the recipient State. The recipient institution agrees to indemnify and hold harmless the United

States Government, Coriell Institute for Medical Research, and the contributor from any claims, costs, damages, or expenses resulting from any injury (including death), damage, or loss that may arise from its use of these biomaterials. This provision shall also apply to any byproducts or derivatives of these biomaterials.

RESEARCH USE, COMMERCIAL USE, AND USE AS STANDARDS IN GENETICS LABORATORIES

The Coriell Cell Repositories provide biomaterials as a service to the research community. The purpose of the NHGRI Sample Repository for Human Genetic Research is to stimulate and facilitate research in genetics, genomics, and related fields, leading to a better understanding of normal genetic and cellular processes, to the identification and function of disease-related genes, and to the diagnosis and treatment of genetic disorders. It is expressly understood that the biomaterials delivered pursuant to this Agreement are experimental and are for use in research, in teaching and as standards in clinical genetics laboratories. Recipients employing biomaterials for use as research standards or controls are responsible for complying with all laws and regulations applicable to the intended use of the materials, including any requirements for FDA approval.

I, the undersigned, have read and understand this document:

Name of Institution: Schulich Sch. Med/Univers. of Western Ontario

Principal Investigator (typed or printed)

Signature of Principal Investigator:

Date: 10/24/2012

I, the undersigned, have read and understand this document and agree to adhere to the restrictions and warnings stated therein. Must be signed by the Institutional Official who can make legal commitments on behalf of the institution. Please see the document regarding the Institutional Official.

Institutional Official (typed or printed): Dan Sinai

Full Title of Institutional Official: Acting AVP (Research)

Department or Area of Responsibility: Research Development & Services | Ethics

Signature of Institutional Official:

Date: October 26, 2012

To contact the CORIELL CELL REPOSITORIES:
Write: 403 Haddon Avenue; Camden, New Jersey 08103 USA
Call: 800-752-3805 in the United States; 856-757-4848 from other countries
Fax: 856-757-9737
E-mail: ccr@coriell.org

Reviewed By
DM

Form 1401-18:NHGRI Assurance Form Rev: B-031709

Joseph L. Mintzer
Executive Vice President
Chief Operating Officer
11/06/2012

Curriculum Vitae

Name: Wahab Altaf Khan

Post-secondary Education and Degrees:

University of Connecticut
Storrs, CT, USA
1999-2003 B.Sc. (Diagnostic Genetics)

The University of Western Ontario
London, Ontario, Canada
2008-2010 M.Sc. (Biochemistry)

The University of Western Ontario
London, Ontario, Canada
2010-2015 Ph.D. (Pathology)

Honors and Awards:

10/2011 Dutkevitch Memorial Foundation travel award, University of Western Ontario, to present at the 12th International Congress of Human Genetics in Montreal, Quebec

05/2012 Dr. Cameron Wallace Graduate Student Award for excellence in research and coursework, University of Western Ontario

10/2013 Society of Graduate Studies travel award, University of Western Ontario, to present at the annual ASHG conference in Boston, MA

02/2014 Dutkevitch Memorial Foundation award for academic excellence, University of Western Ontario

03/2014 Dr. M. Daria Haust Award for best basic science presentation, Annual Pathology Research Day, University of Western Ontario

06/2014 Nellie L. Farthing Memorial Fellowship in the Medical Science, Schulich School of Medicine University of Western Ontario

08/2014 Institute of Cancer Research - Canadian Institutes of Health Research travel award, to present at the annual ASHG conference in San Diego, CA

Related Work Experience:

Position:	Research Scientist
Institution:	Cytognomix Inc. London, Ontario and Ontario Centers of Excellence
Dates:	2010-2011

Position:	Licensed Clinical Cytogenetic Technologist
Institution:	The Hospital for Sick Children, Pathology and Laboratory Medicine, Toronto,
Dates:	2004-2008

Research Support:

1. Ontario Graduate Scholarship, University of Western Ontario, provincial scholarship (Ph.D.), 09/2013/-09/2014

2. Graduate Research Award, University of Western Ontario, institutional award from Schulich School of Medicine and Dentistry (Ph.D.), 01/2013-08/2013

3. Ontario Graduate Scholarship, University of Western Ontario, provincial scholarship (Ph.D.), 09/2012-09/2013

4. Graduate Research Award, University of Western Ontario, institutional award from Schulich School of Medicine and Dentistry (Ph.D.), 01/2012-08/2012

5. Ontario Graduate Scholarship, University of Western Ontario, provincial scholarship (PhD), 09/2011-09/2012

6. Queen Elizabeth II Graduate Scholarship in Science & Technology, University of Western Ontario, provincial scholarship (M.Sc.), 09/2009-09/2010

Publications:

Peer Reviewed Articles

1. Arachchige AS, Samarabandu J, Knoll J, **Khan W**, Rogan PK. An accurate image processing algorithm for detecting FISH probe locations relative to chromosome landmarks on DAPI stained metaphase chromosome images. Computer & Robot Vision – IEEE 2010; 223-230, DOI: 10.1109/CRV.2010.36.

2. Arachchige AS, Samarabandu J, Knoll J, **Khan W**, Rogan PK. An image processing algorithm for accurate extraction of the centerline from human metaphase chromosomes. Proceeding of the IEEE ICIP 2010; 4108:3613-3616.

3. **Khan WA**, Knoll JH, Rogan PK. Context-based FISH localization of genomic rearrangements within chromosome 15q11.2q13 duplicons. Molecular Cytogenetics 2011; 4:15 (highly accessed).

4. **Khan WA**, Chisholm RA, Tadayyon SM, Subasinghe A, Samarabandu J, Johnston LJ, Norton PR, Knoll, JHM, Rogan PK. Relating centromeric topography in fixed human chromosomes to alpha-satellite DNA and CENP-B distribution. Cytogenetics and Genome Research 2013; 139:234-242.

5. Rogan PK, Li Y, Wickramasinghe A, Subasinghe A, Caminsky N, **Khan W**, Samarabandu J, Wilkins R, Flegal F, Knoll JH. Automating dicentric chromosome detection from cytogenetic biodosimetry data. Radiation Protection Dosimetry 2014; 159:95-104.

6. **Khan WA**, Rogan PK, Knoll JH. Localized, non-random differences in chromatin accessibility between homologous metaphase chromosomes. Molecular Cytogenetics 2014 7:70 (highly accessed)

7. **Khan WA,** Rogan PK, Knoll JHM. Reversing chromatin accessibility differences that distinguish homologous mitotic metaphase chromosomes. 2015, in preparation.

Book Chapters

1. **Khan WA.** "Online Genetic Resources & References." The AGT Cytogenetics Laboratory Manual 4th Ed; Marilyn Arsham, Margaret Barch, Helen Lawce (editors), Humana Press 2015, in print.

International & National Conference Presentations

1. **Khan WA**, Voralia M, van den Berghe JA. Static cytometry identifies development of hyperdiploid clones in Plasma cell dyscrasias. Poster presented at The 29th Annual Association of Genetic Technologist meeting, June 2004 Anaheim, CA USA.

2. **Khan WA**, Knoll JHM, Rogan PK. Novel reagents to identify classes of segmental duplication rearrangements in Prader-Willi and Angelman syndromes. Poster presented at Margret Moffat Research Day 2008, University of Western Ontario, London, ON Canada.

3. **Khan WA**, Rogan PK, Knoll JHM. Exploiting 15q11.2-q13 segmental duplication structures to distinguish different classes of chromosomal rearrangements *in situ*. Poster presented at The 59th Annual Meeting of the American Society of Human Genetics, October 2009, Honolulu, HI USA.

4. **Khan WA**, Knoll, J, Tarnowski H, Tadayyon S, Chisholm R, Lu Z, Johnston L, Guo L, Norton P, Rogan P. Sequence-based detection of chromosomal disorders: New Frontiers in single copy FISH technology. Poster presented at World Discoveries Research Day, February 2010, London, ON Canada. Poster presentation.

5. **Khan WA**, Knoll JHM, Rogan PK. Delineating chromosomal regions with complex architectures using single and low copy FISH algorithms. Cytogenetics and Genome Research, preprint April 2010. Paper presented at The 41st Biennial American Cytogenetics Conference, May 2010 Niagara Falls, ON Canada.

6. **Khan WA**, Knoll JHM, Rogan, PK. Delineating complex genomic architecture involving chromosome segmental duplications. Paper presented at European Society of Human Genetics, June 2010 Gothenburg, Sweden.

7. Johnston LJ, Chisholm RA, Rogan, PK, **Khan WA**, Knoll, JHM, Tadayyon SM, Norton PR. Nanoscale imaging of FISH probe binding to metaphase chromosomes. Paper presented at Biophysical Society 55th Annual Meeting, March 2011 Baltimore, MD USA. Biophysical Journal 2011; 100:356a.

8. **Khan WA**, Knoll JHM, Rogan PK, Chisholm RA, Johnston LJ, Tadayyon SM, Norton PR, Subasinghe A, Samarabandu J. Visualizing Sister Chromatid Segregation during Metaphase by Nanoscale Imaging. Paper presented at Canadian Institute for Photonics Innovations – CIPI, May 2011, Ottawa, ON Canada.

9. **Khan WA**, Chisholm RA, Tadayyon SM, Subasinghe A, Samarabandu J, Johnston LJ, Norton PR, Rogan PK, Knoll JHM. Nanoscale resolution relates DNA segregation to epigenetic structure on human metaphase chromosomes. Paper presented at Centre for Advanced Materials & Biomaterials Research, CAMBR. Distinguished lecturer & Research Day, June 2011, University of Western Ontario, London, ON Canada.

10. **Khan WA**, Chisholm RA, Tadayyon SM, Subasinghe A, Samarabandu J, Johnston LJ, Norton PR, Rogan PK, Knoll, JHM. Nanoscopic analysis of DNA segregation and chromatin accessibility during metaphase. Poster presented at The 12th International Congress of Human Genetics, October 2011, Montreal, QC Canada.

11. Dorman SN, Shirley BC, Caminsky NG, Mucaki, EJ , **Khan WA**, Guo L, Knoll JHM, Rogan PK. Next generation genomic microarrays and custom FISH probes for molecular cytogenetic analysis designed by *ab initio* sequence analysis. Poster presented at The 12th International Congress of Human Genetics, October 2011, Montreal, QC Canada.

12. **Khan WA**, Chisholm RA, Tadayyon SM, Subasinghe A, Samarabandu J., Johnston LJ., Norton PR., Knoll, JHM., Rogan PK. Relating centromere topography in fixed human chromosomes to alpha-satellite DNA and CENP-B distribution. Paper presented at Great Lakes Chromosome Conference, May 17-18, 2012, Toronto, ON Canada.

13. **Khan WA**, Rogan PK, Knoll JHM. Defining chromatin accessibility and topography in human metaphase chromosomes. Paper presented at Annual Pathology Research Day, University of Western Ontario, April 2013, London, ON Canada.

14. **Khan WA**, Rogan PK, Knoll JHM. Non-random, locus-specific differences in DNA accessibility are present in homologous metaphase chromosomes. Paper presented at 63rd Annual Meeting of The American Society of Human Genetics, October 2013, Boston, MA USA.

15. **Khan WA**, Rogan PK, Knoll JHM. Differences in Chromatin Accessibility are present between Homologous Metaphase Chromosomes. Paper presented at Annual Pathology Research Day, University of Western Ontario, March 2014, London, ON Canada.

16. **Khan WA,** Rogan PK, Knoll JHM. Reversing differences in chromatin accessibility that distinguish homologous mitotic metaphase chromosomes. Poster at The 64th Annual Meeting of The American Society of Human Genetics, October 21, 2014, San Diego, CA USA.

Volunteer Work:

Organization: The Canadian Medical Hall of Fame
Role: Volunteer. TD Discovery Day programs in Health Sciences, assisted in presenting workshops geared towards navigating online bioinformatics resources to Southwestern Ontario high school students
Dates of Service: 2010-2013

Organization: University of Western Ontario, London, ON Canada
Role: Panel of judges for *Annual Pathology & Toxicology undergraduate poster research day competition*
Dates of Service: 2011-2012

Organization: The American Society of Human Genetics
Role: The Annual DNA Day essay contest judge
Dates of Service: 03/2014-present

Organization: University of Western Ontario, London, ON Canada
Role: Graduate and post-doctoral student representative for Pathology Research committee
Dates of Service: 2013-2014